

PHOTON SCIENCE 2013.

Highlights and Annual Report

Accelerators | Photon Science | Particle Physics

Deutsches Elektronen-Synchrotron
A Research Centre of the Helmholtz Association





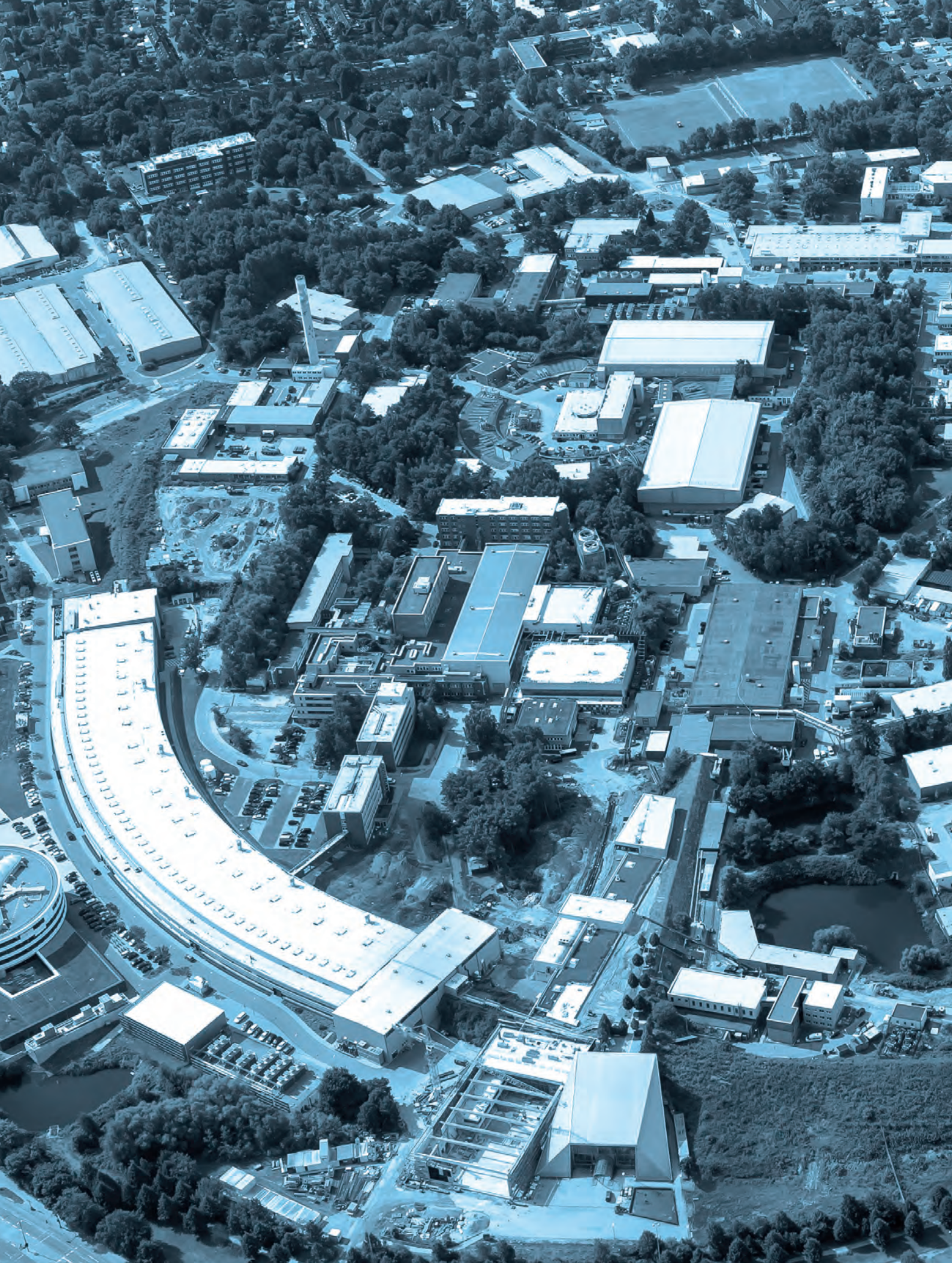
Cover

A view into the first of the three experimental hutches of beamline P09 at PETRA III that is dedicated to resonant scattering and diffraction in the regime of hard X-rays. The second hutch is used for general diffraction experiments and hosts a 14 T split-coil magnet with access to the temperature range from 320 mK to 300 K. The third hutch houses a hard X-ray photoelectron spectroscopy setup. Measurements for the research highlights “Taming electrons at heterointerfaces” page 40 and “The true bulk electronic structure of quasicrystals” page 44 were performed at this beamline and further information is available in the lightsources section on page 94.



PHOTON SCIENCE 2013.

Highlights and Annual Report



Contents.

> Introduction	4
> News and Events	8
> Research Highlights	18
• Quantum and nonlinear optics	20
• Atomic and molecular dynamics	26
• Surfaces and interfaces	36
• Electronic and magnetic structure	44
• Structure and structural dynamics	48
• Macromolecular crystallography	60
• X-ray laser science	70
> Research Platforms and Outstations	76
> Light Sources	88
> New Technologies and Developments	100
> Facts and Numbers	112

User Contributions to the Annual Report.

DESY Photon Science

A deeper insight into the photon science activities at DESY is provided by the several hundreds of annual user experiment and development reports which are available online: http://photon-science.desy.de/annual_report

These users' reports feature all activities and experiments performed by scientists at the DESY light sources PETRA III and FLASH as well as at on-site experimental infrastructure. Contributions for the year 2013 will be published in late spring 2014.

A list of publications based on work done at DESY Photon Science is accessible online: http://photon-science.desy.de/research/publications/list_of_all_publications/index_eng.html

DESY tries to keep this list as complete and as updated as possible, and relies on the support by all users, who are kindly requested to register their publications via DOOR.

The year 2013 at DESY.

Chairman's foreword



European XFEL underground construction completed in June. (From left to right: Stephan Hebgen (ARGE Tunnel XFEL), Helmut Dosch (DESY), Dorothee Stapelfeldt (Senator for Science Hamburg), Christian Scherf (DESY), Beatrix Vierkorn-Rudolph (Head of the Directorate for Large Facilities and Basic Research BMBF), Claudia Burger (European XFEL), Massimo Altarelli (European XFEL).

2013 has again been a very busy as well as successful year for DESY.

There are many new projects on our agenda. The construction of the European XFEL clearly has highest priority. The successful implementation of industrial series production of Niobium cavities within the international XFEL project once again underlines the competence of DESY in accelerator R & D. The superconducting resonators built by DESY are the heart of the Free-Electron Laser. Performance tests of these components at DESY have proven that the technical specifications have been met or even exceeded.

The realization of FLASH II advances according to plan; we are aiming to start commissioning in 2014. After the long shutdown of FLASH, user operation should restart February 2014.



Workers guide the injector klystron into place using a crane in the injector hall at European XFEL's Bahrenfeld site.

The shutdown of DORIS has caused a severe bottleneck for German and European user communities which depend on EXAFS and chemical crystallography. With the additional experimental possibilities in the new PETRA III Extensions these DORIS technologies which are missing at the moment should then become available again providing a much better beam and improved experimental conditions.

Parallel to the development of new user facilities new research centres are established at DESY which exploit the unique properties of the DESY light sources.

Biologists, chemists, medical doctors and physicists in Northern Germany will join forces at the DESY Campus to fight infection on the molecular level. The new Centre for Structural Systems Biology (CSSB) will be an interdisciplinary centre with partners from several universities and research facilities from Hamburg and Lower Saxony. Their common goal is to investigate with atomic resolution how pathogens attack. The building construction was officially launched this year with the traditional groundbreaking ceremony attended by the German Federal Minister of Education and Research, Johanna Wanka, and the Senator for Science and Research of Hamburg, Dorothee Stapelfeldt.

Moreover, DESY currently plans to construct a new Photon Science building that hosts the NanoLab as a facility for in-house research and users providing access to advanced nano-characterization, nano-structuring and nano-synthesis techniques.

The Center for Free-Electron Laser Science (CFEL), which hosts top scientists from the University of Hamburg, the Max Planck Society and DESY further expands its international leading position in the field of free-electron laser science.

With a kickoff meeting at DESY in Hamburg the recently founded German-Russian Ioffe Röntgen Institute (IRI) has commenced operation. This new institution is supposed to establish cooperation between German and Russian scientists on a new strategic basis and offer a common umbrella for future bilateral German-Russian projects in X-ray and neutron science in order to further strengthen and deepen cooperation in this strategically important research area between both countries.

Along with other Helmholtz Centres within the research field *Matter* DESY has been very busy during this year, particularly during the last months, to formulate its research plans for the upcoming funding period 2015-2019. I am confident that we can convince the international reviewers of the outstanding quality of our work. ●



Johanna Wanka, German Federal Minister of Education and Research, speaking at the CSSB groundbreaking ceremony.



Groundbreaking ceremony for the CSSB building on the DESY campus: DESY director Helmut Dosch, Hamburg's Science Senator Dorothee Stapelfeldt, the German Federal Minister of Education and Research Johanna Wanka, Rüdiger Eichel of Lower Saxony's Science Ministry and the head of the CSSB task force, Chris Meier from the University of Hamburg (from left to right).

The reliability of the synchrotron radiation facility PETRA III is continuously improving. Many outstanding projects have been carried out at the various PETRA III experimental stations. I want to congratulate all our users for this impressive success.

A handwritten signature in black ink, which appears to be 'Helmut Dosch'.

Helmut Dosch
Chairman of the DESY Board of Directors

Photon Science at DESY.

Introduction

The year 2013 was one of many changes and challenges for DESY Photon Science. It was the first year during which all 14 PETRA III beamlines were in operation for users. More than 2000 individual scientists carried out experiments at PETRA III during this year in about 5200 h of user operation. Many highlight results have been achieved during this year and some of them are presented in this report. Examples among numerous others are a 5 nm X-ray focus at about 8 keV photon energy obtained at the Coherence Applications Beamline P10 and the formation of Iridium-trihydride at high pressure at the Extreme Conditions Beamline P02.

The preparation work for the PETRA III extension project has significantly been pushed forward. One of the aims of PETRA III extension is to provide those experimental techniques to our user community that are no longer available at DESY after the shutdown of DORIS III in late 2012. Due to the stiff market situation for civil construction in Germany, the extension's civil construction work could not be started as planned and DESY was forced to postpone the shutdown of PETRA III for six months. For this reason a call for proposals was issued on short notice for the second half of 2013 and we would like to thank all our users and members of the review panels for their help and understanding in such a difficult situation. Meanwhile all civil engineering contracts have been signed and the shutdown of PETRA III will start at the beginning of February 2014. According to the present plan commissioning of the rebuilt storage ring will start at the beginning of 2015. After the completion of the extension project in total 27 independent experimental stations will be available at PETRA III.

In May 2013 DESY memorized the scientific achievements at DORIS during 38 years of operation in all fields of science. Experiments with synchrotron radiation alone resulted in about 12000 publications so far and there is certainly still a number to come as more recent examples in this report demonstrates. Also almost 1100 PhD and about 900 Diploma theses are based on experimental work at DORIS. In order to access the impact DORIS had on science and in the socio economic field an impact study has been initiated with first results to be expected in 2014.

FLASH has been shut down most of the year 2013 due to the construction work for the FLASH II project. Nevertheless a number of very exciting publications based on experiments at FLASH have been published during this year like stimulated

soft X-ray emission in Silicon or the ultrafast breakdown of the X-ray magnetic cross section upon optical excitation. Further examples are featured in this report. With some delays the FLASH II civil construction will be completed in January 2014. The new FEL tunnel has been finished in Summer 2013 and since then the installation of the components for the new FEL – FLASH2 - is advancing. Since October the commissioning of FLASH1 is ongoing. Unfortunately, this procedure took much longer than anticipated mainly due to the necessity of a total realignment of the entire facility due to the large ground motions caused by the weight of new FLASH2 buildings. User operation at FLASH is expected to restart at the beginning of 2014. At July 1st the new BMBF Verbundforschung period started. As in previous periods user groups of our facilities were very successful in acquiring significant funds for further improvements of beamline instrumentation and to carry out exciting science. We are looking forward to many successful collaborations and experiments.

Pulsed high repetition rate and high power optical laser became of increasing importance for the operation and the experiments at FELs. This starts with the photo cathode gun laser for the linear accelerator that is important for generating a low emittance electron bunch. It continues with the very powerful laser system needed for external seeding of a FEL in the VUV and soft X-ray regime. And ends with the pump-probe lasers at the experiments. None of these laser systems is commercially available at present. Therefore, DESY has decided to set up its own laser development and operations group, which will closely collaborate with the Helmholtz Institute Jena and the laser group of the Center for Free-Electron Laser Science (CFEL).

Even if slightly delayed the installation work for the superconducting linear accelerator of the European XFEL is ongoing and the industrial production of the accelerator modules is ramping up. Quality control of the first produced modules shows an average gradient well above the design value of 23.6 MV/m. According to the present schedule commissioning with beam is expected for the year 2016.

Scientists from CFEL – a collaboration of scientists from Max-Planck Society, University of Hamburg and DESY – continue to be very successful to carry out experiments at ultra short time scales using FELs around the world and other short pulse photon sources. Prominent examples are to be found in the field of serial femto-second nano crystallography, laser physics



Edgar Weckert
Director Photon Science

and in the theory of radiation-matter interaction at extremely short time scales. CFEL has obtained an additional boost by the foundation of a new Max-Planck Institute for Structure and Dynamics under the roof of CFEL at the beginning of the year 2013. About three years ago European XFEL issued a call for proposals for user consortia to establish new experimental possibilities at European XFEL not covered by the base budget. CFEL scientists and their collaborators were very successful in this process and have already acquired substantial additional funding for these efforts.

The planning for a new Photon Science laboratory and office building housing also a laboratory (NanoLab) for the preparation, characterization and handling of samples at the nano scale in preparation for experiments at PETRA III and FLASH has significantly advanced. Due to budget and capacity boundary conditions the start of this project has been postponed to 2015/2016. Meanwhile, DESY is investigating other locations for suitable laboratory space close to the experimental stations at PETRA III for the realization of a part of the corresponding laboratory infrastructure.

The Centre for Structural Systems Biology (CSSB) – a collaboration of nine institutions in the field of structural biology and infection research – has made a major step forward in 2013. The groundbreaking ceremony took place in September. The planning for the civil engineering of the new building is completed and the call for tender for the bare concrete work has been published in autumn 2013. Hiring of the group leaders for the research teams of the individual institutions has been successfully continued. Meanwhile, two W3 professors have been appointed, another two are in negotiation and a further position is open for applications. In addition five further group heads for W2, W1, young investigators and other teams have been

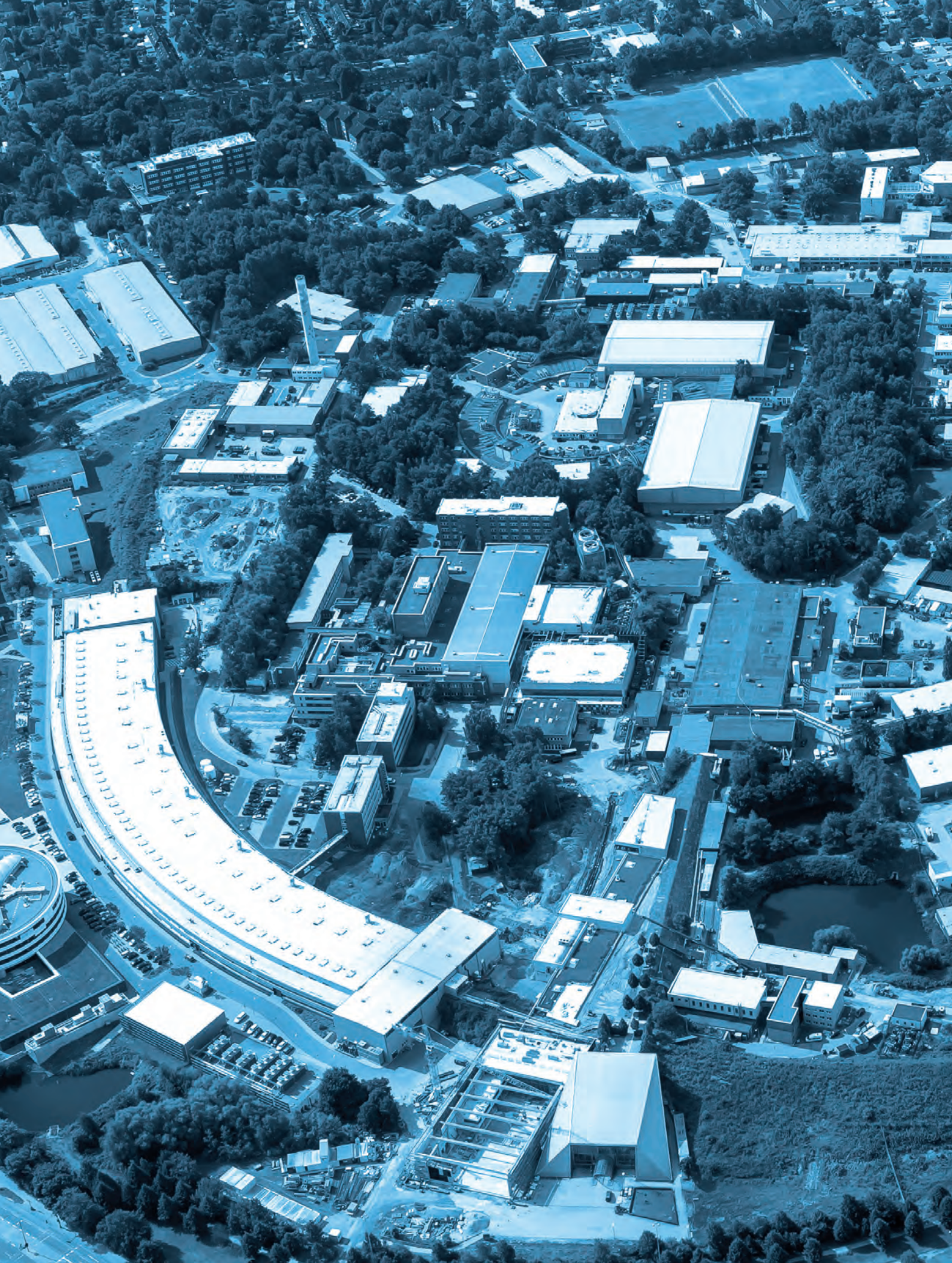
appointed. The newly established CSSB groups are currently located at their home institutions or temporarily in DESY offices and laboratories until the new CSSB building is finished. Many remarkable results have been achieved by DESY Photon Science in-house research scientists. A selection of them can be found in this report. In order to further strengthen in-house research DESY plans to establish three further research groups. One in the field of ‘Structural Biology’ within the frame of CSSB and two further groups in ‘Science at Ultra Short Time Scales’ and in ‘X-ray Optics and Nano Science’. If all these negotiations are successful the new group leaders will join DESY during next year.

2014 will be a very special year for DESY. It is the 50th anniversary of the first synchrotron radiation experiments carried out at the DESY synchrotron in 1964. This pioneering achievement was one of the nuclei for the worldwide success story of research with synchrotron radiation. Since then the brilliance of DESY’s light sources has increased by more than 10 orders of magnitude and the experimental techniques have reached an unprecedented level of sophistication. DESY will celebrate this jubilee, the ‘International Year of Crystallography’ and the subsequent ‘International Year of Light’ in 2015 by several events.

Finally, let me wish all of you a personally and scientifically most successful year 2014. ●

A handwritten signature in black ink, appearing to read 'E. Weckert', written in a cursive style.

Edgar Weckert
Director Photon Science



News and Events.



News and Events.

A busy year 2013

January

23-25 January:

Joint European XFEL and DESY Photon Science Users' Meeting

This year's Users' Meeting of DESY Photon Science and of the European X-ray free-electron laser XFEL set up a new participation record. About 800 users, students and scientists came together to get informed about the latest developments at DESY's light sources FLASH and PETRA III and the advances in the construction of the European XFEL. The 3 day event started on January 23 with the European XFEL Users' Meeting. The second day was devoted to the status of and experiments at the soft X-ray free-electron laser FLASH, a meeting which was jointly organized by DESY and the European XFEL. In the afternoon of the second day 11 satellite meetings were organized which addressed specific topics related to the status of various instruments, experimental techniques, and new projects. On the third day the DESY Photon Science Users' Meeting took place with a general report on the status of Photon Science at DESY, a couple of talks on scientific highlights presented by users. In the afternoon the joint DESY – European XFEL poster session with more than 300 contributions gave a comprehensive overview of the recent activities in the fields of material science, life science, methods and instrumentation and at the free-electron lasers representing an excellent forum for lively discussions among the participants.



The DESY main auditorium during the Photon Science Users' Meeting.

March

18-19 March:

Third German-Swedish Workshop within the Röntgen-Ångström-Cluster on Materials Science

The Röntgen-Ångström-Cluster was launched in summer 2009 by the governments of Sweden and Germany. Its aim is to strengthen research using neutrons and photons in materials and structural biology research and to promote the efficient use of corresponding large facilities available in Sweden and Northern Germany. In the meantime numerous workshops were organized with two of them focusing explicitly on materials science. The third one in this series now was dedicated to *in situ* method development for materials science with neutron and synchrotron radiation. Almost 50 participants attended the meeting.



Participants of the third German-Swedish Workshop of the Röntgen-Ångström-Cluster on Materials Science.

20-22 March:

XII. Research Course on X-Ray Science

The annual DESY Research Course on X-ray science provides basic knowledge about new directions of X-ray research. It addresses Diploma, Master, and PhD students and young research fellows. The 12th course was entitled "Theoretical Foundations of Research with X-ray Free-Electron Lasers and Synchrotron Radiation Sources" and had a focus on the investigation of dynamic processes.

May

14-15 May: DORIS Days – A particle accelerator makes scientific history

With the end of 2012 the particle accelerator DORIS was finally shut down after more than 40 years of operation for particle physics and synchrotron radiation research. The DORIS Days were intended to look back over the history of this exceptionally successful machine and to review its technological, scientific, economic, and social impact. The first day was organized as a ceremony with welcome addresses by Olaf Scholz, First Mayor of the Free and Hanseatic City of Hamburg, and Beatrix Vierkorn-Rudolph from the German Federal Ministry for Education and Research.



Christian Scherf, DESY Director for Administration, thanks Beatrix Vierkorn-Rudolph (middle), German Federal Ministry for Education and Research BMBF, and Olaf Scholz (right), First Mayor of the Free and Hanseatic City of Hamburg after their welcome addresses at the DORIS Days.

Talks given in a first session then highlighted the pioneering role of DORIS in the historical context and a following session savoured the societal and international relevance of DORIS. The sessions which were attended by 450 participants closed with an award ceremony during which the DESY Goldene Ehrennadel was presented to Herwig Schopper, Director General at DESY from 1973 to 1980.

The following day was organized as a symposium on DORIS photon science. Seven talks highlighted ground-breaking applications of DORIS in the fields of spectroscopy and diffraction. Three more talks at the end addressed research topics with obvious impact on economy and society: Industrial catalysis research, tomography, and X-ray imaging on cultural heritage.



DESY Directors awarding the DESY Goldene Ehrennadel to Herwig Schopper, DESY Director General from 1973-1980.



Former DESY Director Herwig Schopper at the DORIS Days.



Talks on the DORIS Days symposium.

June

2-5 June:

Kickoff Meeting for the Helmholtz International Beamline for Extreme Fields at the European XFEL

This workshop served as a founding meeting for the User Consortium of the “Helmholtz International Beamline for Extreme Fields (HIBEF)” to be located at the High Energy Density (HED) instrument of the European XFEL. The initial proposal of the HIBEF User Consortium, coordinated by the Helmholtz-Zentrum Dresden-Rossendorf (HZDR) and DESY, was endorsed by the Scientific Advisory Committee (SAC) and the council of the European XFEL in summer of 2012. The goal of the User Consortium is to bring together the community to establish instrumentation creating “Extreme Fields” including high powered optical lasers and pulsed high-field magnets that would benefit significantly from the probing capabilities of the highly brilliant beam of the European XFEL at the HED instrument. The consortium consists of more than 80 groups from more than 60 institutes in 16 nations. It comprises about 350 scientists and about 300 PhD students. 145 participants registered for the meeting. Pursued research areas are high energy density states of matter, ultra-high-field electrodynamics, structural evolution of processes on atomic timescales, X-ray magnetic absorption and scattering in pulsed high fields, and physics of relativistic interaction between lasers and solid matter. The aims of the workshop were to establish the organization of the User Consortium, to discuss in-kind contributions of the different consortium members, and to finalize the proposal to be submitted for funding major parts of the project.



The participants of the HIBEF kickoff meeting.

6 June:

European XFEL underground construction completed

An important milestone was reached on one of Germany’s largest science construction sites: the underground civil engineering work for the X-ray laser European XFEL has been completed. About 300 guests from politics, academia, administration, and business gathered to celebrate and visit the underground facilities in Schenefeld. The tunnel buildings with a total length of 5.7 km and underground halls will accommodate the more than 2 km long linear accelerator, the XFEL undulator structures, supporting infrastructure, and experimental stations for the new X-ray free-electron laser.



Visiting the main tunnel of the European XFEL (from left to right): Helmut Dosch (Chairman of the DESY Board of Directors), Stephan Hebgen (XFEL tunnel Consortium), Dorothee Stapelfeldt (Hamburg Senator for Science and Research), Christian Scherf (DESY Director for Administration), Beatrix Vierkorn-Rudolph (German Federal Ministry for Education and Research BMBF), Claudia Burger (European XFEL), Massimo Altarelli (European XFEL).



Helmut Dosch (Chairman of the DESY Board of Directors) welcomes guests to the tunnel celebration.

July

11-14 June: Summer School on Ultrafast X-ray Science

The Center for Free-Electron Laser Science (CFEL) at DESY hosted the Ultrafast X-ray Summer School 2013 (UXSS 2013). It was jointly organized by CFEL and the PULSE institute at SLAC National Accelerator Laboratory, Stanford, US. The highly interdisciplinary summer school program covered topics ranging from accelerator physics to molecular biology, and was intended to give doctoral students and postdoctoral researchers the opportunity to get familiar with the latest developments and opportunities in ultrafast X-ray science. About 90 participants from Germany and 15 other countries attended eight lectures given by invited international experts. In smaller groups they worked on mock proposals for the various planned experimental stations at European XFEL.



Teams of students presenting their mock beamtime proposals for experiments at the European XFEL on the last day of the Summer School on Ultrafast X-ray Science.

16 July: Start of DESY Summer Student Program 2013

In total, more than 500 undergraduate students from various fields of natural sciences applied for the DESY Summer Student Program 2013 of which 160 indicated Photon Science as their first preference. 16 female and 17 male students from China, Colombia, Germany, Denmark, Estonia, Great Britain, India, Italy, Poland, Russia, Slovakia, Thailand, and Ukraine were finally accepted for the photon science part of the program. They stayed at DESY from July 16 until September 5.



The DESY summer students 2013.

The students joined the daily work of photon science related research groups at DESY, CFEL, or European XFEL where they carried out own small projects. In addition, they attended a couple of lectures about DESY science in general and a special series of 13 lectures on research with synchrotron radiation.



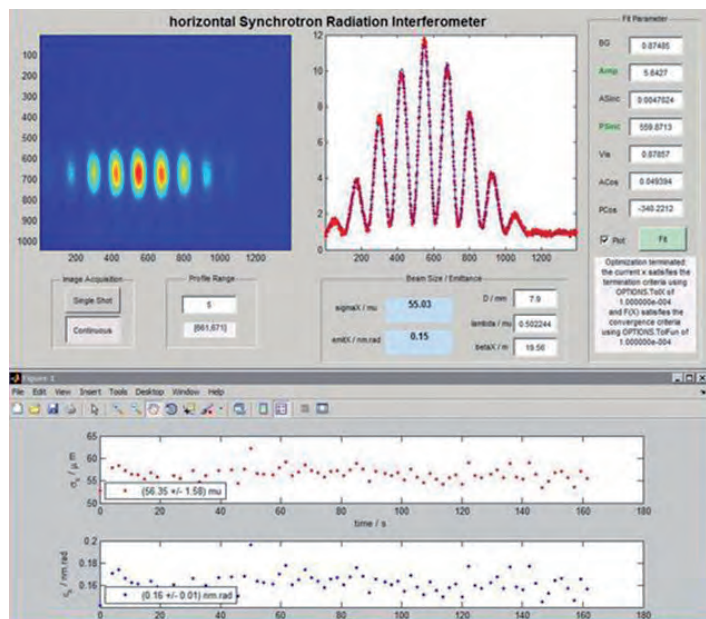
The DESY summer students 2013 in the field of Photon Science.

August

23 August:

PETRA III sets a new emittance world record

PETRA III machine physicists set a new world record. At 3 Giga electron volts beam energy they achieved a horizontal beam emittance of 160 picometer radian, the smallest value ever reached by a storage ring. The emittance is the product of cross-section and divergence of a particle beam in an accelerator, a quantity which dominantly determines the brilliance of the emitted synchrotron radiation.



A screenshot for experts: An interferogram generated with synchrotron radiation from a bending magnet can be used to determine size and emittance of the particle beam in PETRA III.

26 August:

Helmholtz PhD Thesis Prize for CFEL Scientist

Stefan Pabst, who recently completed his PhD thesis at CFEL, was among the first five young researchers to be awarded with the new Helmholtz PhD Thesis Prize. The award comes with 5000 Euros prize money and appreciates his work on „New Theoretical Approaches to Atomic and Molecular Dynamics Triggered by Ultrashort Light Pulses on the Atto- to Picosecond Time Scale“.



Stefan Pabst, awardee of the Helmholtz PhD Thesis Prize 2013.

September

2-6 September:

22nd International Congress on X-Ray Optics and Microanalysis

The International Congress on X-Ray Optics and Microanalysis (ICXOM) is a series of conferences dedicated to the fields of micro- and nano-analysis by means of X-ray beams. ICXOM22 was organized by DESY with special emphasis on synchrotron radiation sources. It addressed the various probing techniques and its application to the fields of chemistry, life, materials, energy, earth and environmental sciences, as well as of archaeometry and cultural heritage. The program was completed by related topics on X-ray optics, detectors, and other instrumentation. Each day keynote and plenary talks in the morning were followed by parallel sessions after the lunch break and a poster session in the afternoon. Most part of the five days event took place at the Hamburg University Campus, except the third day, when the participants, after two keynote talks on photon science at DESY in the morning, moved to the DESY site for a guided tour visiting PETRA III and the European XFEL and for a couple of keynote talks on micro- and nano-analysis at SPring-8, APS, and ESRF. In total the congress featured nine keynote and ten plenary talks, 56 talks in parallel sessions and about 120 posters. It was attended by 230 participants.



Participants of ICXOM22 gathering in front of Hamburg University main lecture building.

4 September: Groundbreaking ceremony for the CSSB Building

The new Centre for Structural Systems Biology (CSSB) – to be established on the DESY campus – is dedicated to research in Structural Biology and Systems Biology with a special focus on infectious diseases. Bringing together the expertise of various scientific disciplines, special emphasis will be on imaging and fundamental processes in cell biology to study molecular interactions which are crucial in determining the course of infections. Up to ten highly interconnected new research groups are going to meet this challenge. DESY offers unique facilities that provide optimal conditions for Structural Biology. Using some of the most advanced light sources such as PETRA III and FLASH or the European XFEL, CSSB scientists will be able to study biological samples in different ways – ranging from the structural analysis of single molecules to the understanding of molecular and dynamic processes.

The CSSB research building will be constructed on the DESY Campus, south of the PETRA III experimental hall and will provide space for 180 scientists, engineers, and technicians. Construction of the building is expected to be finished in 2016.



Johanna Wanka, German Federal Minister of Education and Research speaking at the CSSB groundbreaking ceremony.

8-11 September: IUCr workshop on High Pressure Research

This meeting, attended by 95 participants, was a continuation of a series of workshops supported by the International Union of Crystallography (IUCr) Commission on High Pressure. The primary focus of the meeting was on recent scientific advances in powder and single crystal diffraction at static and dynamic high pressure. Nine sessions covered investigations related to crystal structure, phase transitions and their kinetics, synthesis of new materials, earth and planetary science, soft and biological matter, physical and chemical properties, theory and computation, and new technical developments for high pressure studies.



The attendants of the IUCr Workshop on High Pressure Research.

25 September: Topping-out for FLASH experimental hall

The building shell of the FLASH II experimental hall is finished. On 25 September, DESY, building firms and architects celebrated the completion of the roof of the experimental hall with a traditional topping-out ceremony. The hall construction started in January this year. It is part of the FLASH II project, in which the accelerator of the free-electron laser FLASH is extended by a second lasing beamline which branches off from the existing FLASH tunnel behind the FLASH accelerator and is intended to serve more users with the highly demanded soft X-ray light.



Topping-out for the new FLASH II building. A group photo with members of DESY and of the construction company Züblin.

October

7-9 October: International workshop on Grazing Incidence X-Ray Scattering (GISAXS2013)

GISAXS2013 was the continuation of a very successful series of three international GISAXS workshops held at DESY in 2005, 2007 and 2009.

The workshop, attended by more than 100 participants, brought together scientists from different communities working in the field of thin films, nanostructures, surfaces and interfaces, to gain insights into the powerful method of grazing incidence small angle X-ray scattering. The program was divided in two parts. Basic introductory lectures were combined with talks on specific scientific topics given by international experts in the field of grazing incidence methods and applications. Thereby, the workshop addressed students as well as experienced researchers working in the field of and exploiting the potentials of GISAXS.

The second part of the workshop offered practical exercises. In small groups the participants could practice on-line treatment and simulation of GISAXS data. The workshop was completed by a poster session and a visit to the micro SAXS instrument at PETRA III beamline P03.



The participants of the GISAXS2013 workshop.

9 October: Ioffe Röntgen Institute launched

With a kickoff meeting at DESY the newly founded Russian-German Ioffe Röntgen Institute (IRI) has taken up work. The new institution will serve as an umbrella for cooperation in the development and application of large-scale research infrastructures in the partner countries. For the first IRI meeting around 30 participants from Germany and Russia came to DESY, including the Director of the Kurchatov Institute in Moscow, Mikhail Kovalchuk. The National Research Center Kurchatov Institute is the Russian IRI partner. On the German side Beatrix Vierkorn-Rudolph, Head of the Directorate for Large Facilities and Basic Research of the Federal Ministry of Research (BMBF) and chair of DESY's Administrative Council, and the Chairman of the DESY Board of Directors, Helmut Dosch, welcomed the guests. At the constituent meeting a decision was made upon a first funding round that will be announced in mid 2014. Supported projects should be focused on research with synchrotron radiation and neutrons.



Representatives at the constituent meeting of the Russian-German Ioffe Röntgen Institute.

November

30 October:

PhD thesis prize for Andrej Singer and Johannes Hauk

This year's PhD thesis prize of the *Association of the Friends and Sponsors of DESY* is shared by Andrej Singer and Johannes Hauk. Andrej Singer graduated with his PhD work entitled "Coherence Properties of Third and Fourth Generation X-ray Sources – Theory and Experiment". He performed detailed theoretical studies to derive transversal coherence properties from source operating parameters and analysed experimental data from FLASH at DESY and LCLS in Stanford (US) to compare theory and experiment. He could also determine the coherence properties of FLASH by an intensity correlation method that had been proposed for visible light earlier.

Johannes Hauk worked in the DESY CMS group which is part of the international collaboration at the CMS particle detector at CERN. His PhD thesis provides important insights into interacting electroweak processes and processes involving heavy quarks and how this can be used to analyse Higgs-pair production.

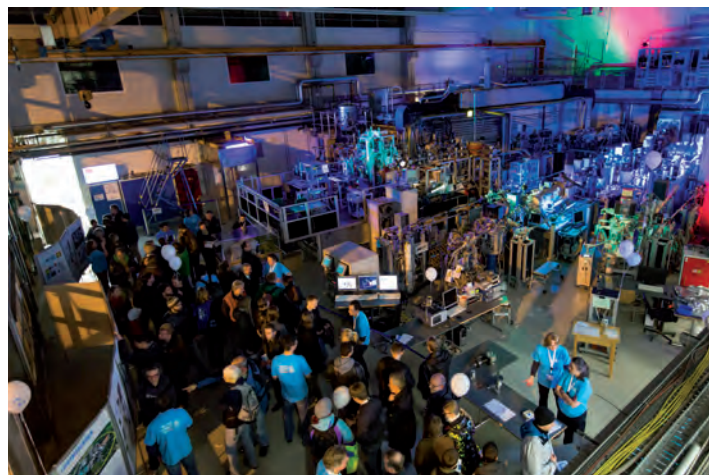


Johannes Hauk (left) and Andrej Singer (right) are the awardees of the 2013 PhD thesis prize of the *Association of the Friends and Sponsors of DESY*.

2 November:

Open Day at DESY and Night of Knowledge in Hamburg

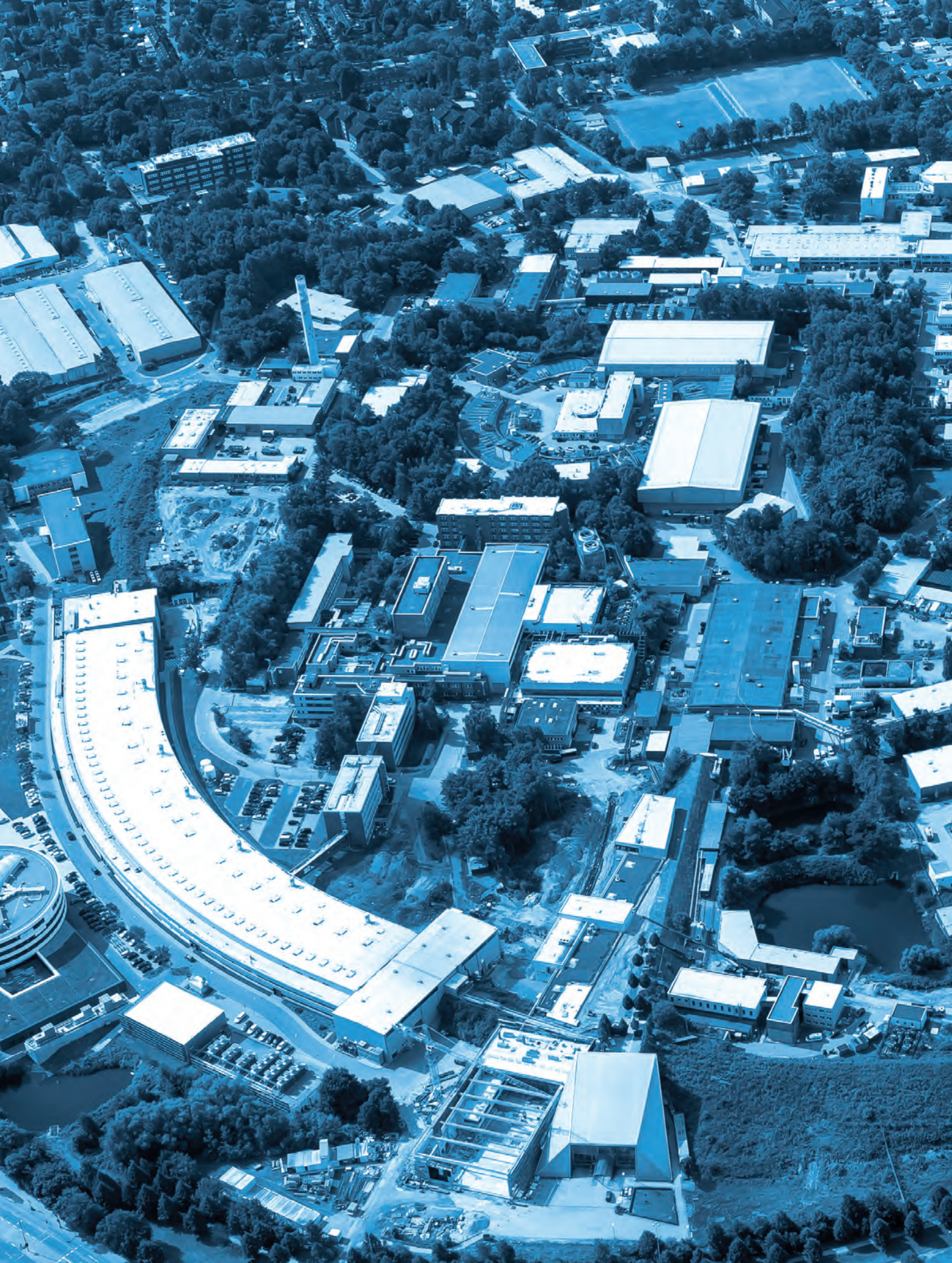
This was the fifth Night of Knowledge in Hamburg and DESY and its partner institutes again took this opportunity to present their facilities and activities to the public. The event was breaking numerous records. DESY opened its doors already at noon and at 5 pm, when the Science Night was officially started, already 11000 visitors were counted on the DESY premises. At midnight finally about 18600 curious people had visited DESY, 4600 more than during the previous Open Day two years ago. 1000 colleagues volunteered to help making the more than 100 attractions, lectures, and hands-on experiments a big success and showed that research at DESY is not only about fascinating high-tech equipment but also about engaged and enthusiastic people. All facets of DESY work were presented, from photon science and particle physics to the library and fire fighting services in the DESY safety group. Many visitors came with their families and especially the many hands-on activities were attractive for all ages, even for the youngest guests. This not only included the famous chocolate marshmallow under vacuum but also for instance building a functioning monochromator from a cardboard tube, a cotton bud, and a piece of compact disc.



Inside the colourfully illuminated FLASH experimental hall at the Hamburg Science Night.



A young visitor at the DESY Open Day joins in one of the numerous hands-on experiments.



Research Highlights.

Quantum and nonlinear optics

- Amplifying X-rays in a solid 20
- Quantum states out of nothing 22
- Hanbury Brown – Twiss interferometry at FLASH 24

Atomic and molecular dynamics

- The ultimately hot gas phase of metals 26
- Atoms team up for faster relaxation 28
- Unraveling the structure-function relationship in chemistry 30
- Filming dancing electrons with a high speed X-ray camera 32
- Ultra efficient ionization 34

Surfaces and interfaces

- From gold atoms to gold layers 36
- At liquid boundaries a crystal is born 38
- Taming electrons at heterointerfaces 40
- Insights in heterojunctions of operational organic electronic devices 42

Electronic and magnetic structure

- The true bulk electronic structure of quasicrystals 44
- Breakdown of the X-ray magnetic scattering cross section 46

Structure and structural dynamics

- Magmas at depth 48
- Unexpected flow behaviour of anisotropic particles 50
- The oldest carnivorous dinosaur clutch with embryos 52
- The liquid and solid character of colloidal liquid crystals 54
- Two liquid states in a strong bulk metallic glass-former 56
- Synthesis of metastable polymorphs 58

Macromolecular crystallography

- Dramatic compaction of a protein complex upon tRNA binding 60
- Linking molecular structure and cellular reprogramming 62
- The innate immune sabotage 64
- First new crystal structure solved using an FEL 66
- Shock freezing of virus crystals 68

X-ray laser science

- FLASH's heartbeat 70
- Extreme ultraviolet and extremely short 72
- Towards few fs resolution movies at XFEL facilities 74

Amplifying X-rays in a solid.

Non-linear stimulated X-ray emission from silicon

X-ray emission spectroscopy (XES) and resonant inelastic X-ray scattering (RIXS) as highly sensitive probes have contributed considerably to the understanding of material's properties and functionality. Unfortunately, low signal levels limit the resolution and make experiments sometimes tedious. For experiments with optical lasers, non-linear techniques have been developed to amplify weak signals and to enhance the information. With X-ray free-electron lasers, it becomes possible now to merge the high sensitivity of X-ray spectroscopy with non-linear laser methods. We studied the X-ray emission signal of silicon after intense excitation from FLASH and observed a non-linear amplification in the signal with a characteristic angular dependence. We explain the observed effects with stimulated emission in the medium with a high density of holes in core electronic states.

RIXS is an X-ray spectroscopy that gains increasing attention because of its ability to study the dispersion of fundamental excitations (phonons, magnons, spinons, orbitons and so on) as well as details of the electronic structure. Combined with the element specificity of soft X-rays this allows for a fundamental understanding of the driving forces behind materials' functions [1].

This enhanced information comes at the cost of a limited signal level. First, only 0.1-1% of the incoming soft X-ray photons get re-emitted as fluorescence photons that are detected in a RIXS experiment. The major part is converted into energetic electrons, which via electron-electron scattering processes ultimately destroy the sample in case of strong X-ray irradiation. Secondly, the fluorescence is nearly isotropically emitted while RIXS spectrometers necessarily have a limited acceptance angle. Thus, they detect often only one out of 10,000 to 1,000,000 fluorescence photons.

We present here a method to overcome these limitations. We use non-linear processes after intense X-ray irradiation [2] to enhance the conversion efficiency from incoming to emitted photons and to form a directed beam that enables higher detection probabilities [3]. The spectroscopic information of RIXS is preserved [4].

The basic mechanism is amplified spontaneous emission (ASE): After the creation of a high density of excited atoms, spontaneously emitted fluorescence photons travel through the excited volume. Either these photons are re-absorbed or they stimulate the fluorescent decay of other excited atoms. If the probability for stimulation is higher than for absorption, there will be gain in the fluorescence signal. And, the stimulated atom will not decay via electron emission thereby reducing the sample damage.

Furthermore, the emitted radiation gets more directed: stimulation

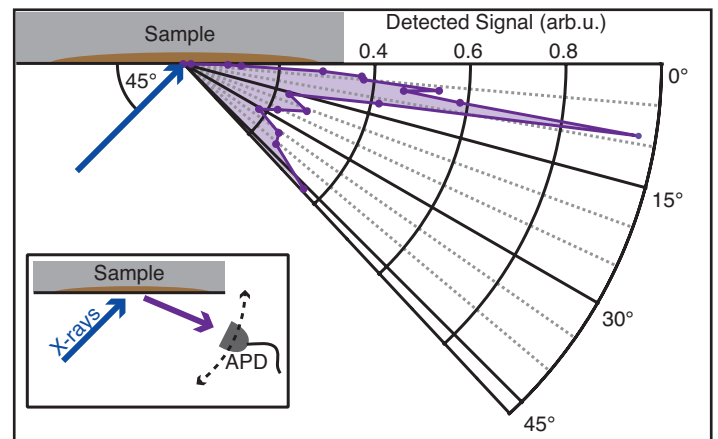


Figure 1

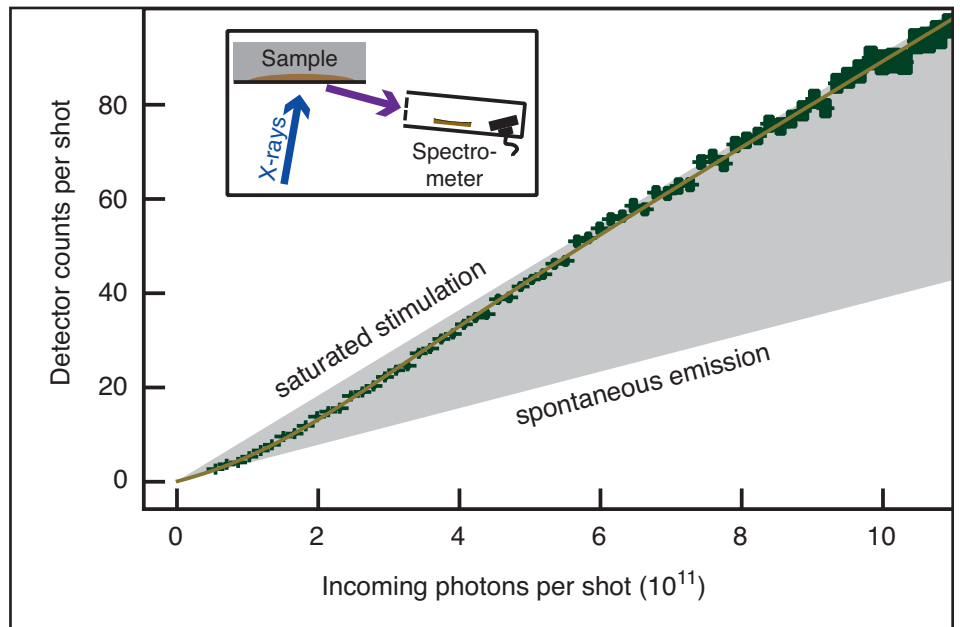
The angular dependence of the emission signal from silicon after intense X-ray irradiation as measured with an avalanche photodiode (APD) at FLASH. Besides a small enhancement close to the reflected beam at 45°, a strong increase of about a factor of five is observed at 9° to the surface. This is characteristic for the described amplification by stimulated emission and is a result of the disk-shaped excited volume.

of fluorescence only occurs when the photons travel a long path through an excited part of the sample. The shape of the excited volume for soft X-rays on solids looks typically like a thin disk (typical focal sizes of tens of micrometers determine the diameter of the disk while its thickness is determined by the penetration depth which is tens of nanometers). The longest paths inside this volume are found along the diameter of the disk parallel to the surface. Since with longer path length the probability for absorption increases, too, it turns out that there is an optimal angle of around 9° to the sample surface where the emission is maximal.

The emitted photons can stimulate emission from other sites and thus an exponential amplification is expected along the

Figure 2

Evolution of the emission signal as a function of the number of incoming photons. The lower limit of the displayed evolution is given by purely spontaneous emission. Through stimulated processes, the emission gets amplified until it reaches saturation, where the signal becomes linear with the incident number of photons again. At this level, stimulated processes in every direction compete for the available excited atoms and only a fraction of the excitations enhances the observed signal. Due to experimental constraints, the detector was placed at 15° to the surface, away from the optimal amplification angle. In this direction, the gain in signal over the spontaneous emission is about a factor of two.



path that the original spontaneous fluorescence photon was travelling. This process starts in parallel from very many fluorescence photons such that all emission directions compete for the available excited atoms. This competition makes the process hard to predict and effectively limits the achievable gain. But the amplification can be optimized through special geometric arrangements. In order to make the amplification most efficient for the one selected direction where the spectrometer will be placed, one can shape the X-ray footprint on the sample and use a grazing incidence geometry.

In our experiment at FLASH we saw a doubling of the emission signal as compared to spontaneous emission since the spectrometer could not be placed in the optimal geometry. By changing the detection angle we observed another five-fold increase such that an increase by one order of magnitude can be achieved at present conditions. We expect even further amplifications by orders of magnitude through optimized beam and experimental conditions.

The described fundamental insights can guide the design of future experiments on more complex sample systems, for example in the international user consortium “Heisenberg RIXS” at the European XFEL. Attention should be paid to have an X-ray pulse that is not substantially longer than the core hole lifetime. When excited atoms decay during the X-ray pulse the effective excitation density and thus the amplification effect is reduced. Most core holes actually decay faster than the silicon 2p-hole that we studied such that this requirement poses a challenge for pulsed X-ray sources.

With the described guiding principles one can fruitfully adopt other non-linear techniques to the X-ray world. The main differences to visible light are the larger linear cross-sections, much shorter excited state lifetimes and the strongly competing electronic decay channels.

Contact: Martin Beye, martin.beye@helmholtz-berlin.de
Alexander Föhlisch, alexander.foehlich@helmholtz-berlin.de

Authors

Martin Beye¹, Simon Schreck^{1,2}, Florian Sorgenfrei^{1,3}, Christoph Trabant^{1,2,4}, Niko Pontius¹, Christian Schüßler-Langeheine¹, Wilfried Wurth³ and Alexander Föhlisch^{1,2}

1. Institute for Methods and Instrumentation of Synchrotron Radiation Research G-ISRR, Helmholtz-Zentrum Berlin für Materialien und Energie GmbH, Albert-Einstein-Straße 15, D-12489 Berlin, Germany
2. Fakultät für Physik und Astronomie, Universität Potsdam, Karl-Liebknecht-Straße 24–25, D-14476 Potsdam, Germany.
3. Institut für Experimentalphysik, Universität Hamburg and Center for Free-Electron Laser Science, Luruper Chaussee 149, D-22761 Hamburg, Germany
4. II. Physikalisches Institut, Universität zu Köln, Zùlpicher Straße 77, D-50937 Köln, Germany

Original publication

“Stimulated X-ray emission for materials science”, *Nature* 501, 191-194 (2013).

References

1. L.J.P. Ament, M. van Veenendaal, T. Devereaux, J. P. Hill, J. van den Brink, “Resonant inelastic x-ray scattering studies of elementary excitations”, *Rev. Mod. Phys.* 83, 705-767 (2011).
2. B. D. Patterson, “Resource Letter on Stimulated Inelastic X-ray Scattering at an XFEL”, SLAC Technical Note SLAC-TN-10-026 (2010).
3. N. Rohringer, D. Ryan, R. A. London, M. Purvis, F. Albert, J. Dunn, J. D. Bozek, C. Bostedt, A. Graf, R. Hill, S. P. Hau-Riege, J. J. Rocca, “Atomic inner-shell X-ray laser at 1.46 nanometres pumped by an X-ray free-electron laser”, *Nature* 481, 488-491 (2012).
4. E. Fill, “Boosting X-ray emission”, *Nature* 501, 172-173 (2013).

Quantum states out of nothing.

Vacuum generates quantum mechanical superposition states

Quantum mechanical objects can exist in multiple states simultaneously, in contrast to everyday experience with classical objects. Such superposition states are important resources for future quantum technologies, but extremely fragile: already the interaction with the vacuum alone can destroy them. We have manipulated the interaction of a large ensemble of nuclei with the vacuum such that this interaction instead produces and even stabilizes superpositions of nuclear quantum states. Probing the system using nuclear resonance scattering, we observed clear signatures of the formed coherences, controlled by a weak external magnetic field. This opens up a variety of future perspectives for quantum optics with novel X-ray light sources.

The success story of optical lasers is founded on coherence, non-linearities and quantum effects. However, it remains a challenge to exploit similar phenomena in the X-ray domain. An important step towards this goal is the generation of coherent superpositions of quantum states. These were crucial in the development of quantum mechanics, as exemplified by the famous thought experiment about the fate of Schrödinger's cat. Nowadays, such coherent superpositions are key resources for quantum technologies. But in experiments, usually inevitable decoherence destroys the superposition states, restricting many applications. An important source of decoherence is spontaneous emission, induced by the interaction with the surrounding vacuum field.

A promising solution in theory is already known for more than 40 years [1]. At that time it was predicted that the interaction with the vacuum may be manipulated in such a way that it produces the desired superpositions instead of destroying them. Unfortunately, this is linked to rigorous conditions which so far hindered the experimental realization. We have circumvented these constraints, and demonstrated the spontaneous generation of coherences between the quantum states of a large ensemble of nuclei, using resonant scattering of X-rays on ^{57}Fe nuclei embedded in a nanoscale planar cavity, which feature a Mössbauer transition at 14.4 keV.

The X-ray cavity was formed by a Pd (5 nm) / C (40 nm) / Pd (20 nm) layer system with the Pd layers acting as the mirrors and the C as guiding layer. The probed ^{57}Fe nuclei were placed as a 2.5 nm thick layer in the centre of the carbon layer. The Fe layer orders ferromagnetically and the magnetization can be aligned and controlled via a weak external field. The internal magnetic hyperfine field at the ^{57}Fe nuclei results in a Zeeman splitting of the ground and excited state, resolving their magnetic sublevels. Already in previous experiments similar cavities had facilitated extending quantum optical concepts into the regime of hard X-rays [2, 3]. In the experiment at the PETRA III Dynamics Beamline P01 we employed nuclear resonance scattering, in which scattered photons are detected in a time- and energy-resolved

way after an initial pulsed broadband excitation. A special feature of our experiment is an X-ray polarimetry setup [4], which consists of two Si (840) polarizer crystals in crossed setting with the sample in between. This allowed us to select transitions between specific magnetic sublevels, and to suppress nonresonant background photons by almost 10 orders of magnitude.

The archetype setup for spontaneously generated coherences (SGC) consists of an atom with a ground and two excited states [1, 6]. If, initially, the atom is in one of the excited states, a photon is emitted upon a transition of the atom from the excited to the ground state. Subsequently, the photon can be reabsorbed

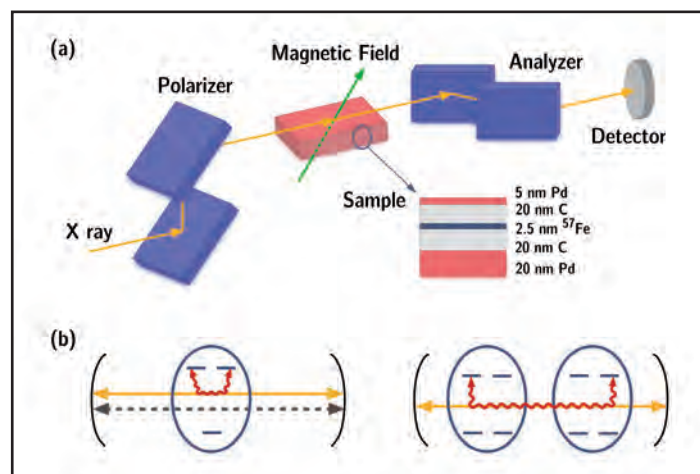


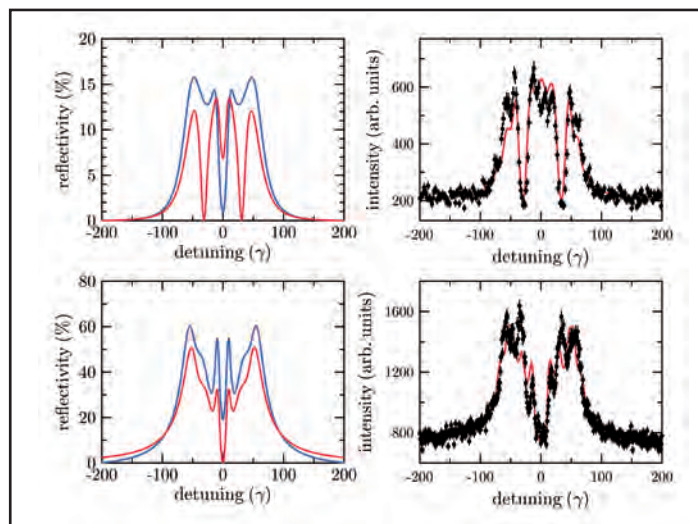
Figure 1

(a) Experimental setup with the sample located between polarizer and analyzer of a high-purity X-ray polarimeter. The inset shows the layer structure of the thin-film nanoscale cavity used in the experiment. The interaction of the resonant X-rays with the Mössbauer nuclei in the cavity can be controlled via the magnetization of the iron layer and the photon polarization.

(b) Illustration of two mechanisms leading to the formation of SGC. In both pictures the outer parentheses symbolize the mirrors of the cavity, the oval shapes stand for the nuclei with their ground and excited levels. In the left panel, the nuclei couple only to one polarization state, on the right panel the X-rays 'see' one effective quantum system formed by different nuclei. As described in the text, both mechanisms lead to SGC mediated by the cavity (curly red lines).

Figure 2

Cavity reflectivity as function of the detuning of the incident X-ray energy from the nuclear resonance energy. The two rows show theoretical predictions (left) and experimental data (right) for two different alignments of incident polarization and magnetization. The theoretical curves compare results with SGC (red) and without SGC (blue). Solid red curves in the right column are theoretical predictions taking into account the precise detection scheme. Deep minima at certain frequencies indicative of SGC are clearly resolved in the experimental data, in good agreement with the theory. Since the minima arise from destructive interference and drop down to the background baseline, we conclude that the system essentially operates decoherence-free.



with a transition of the atom back to the initial state. This leads to a complex energy shift, with real and imaginary parts contributing to the Lamb shift and the spontaneous decay rate. If, however, the reabsorption of the virtual photon can evolve the atom to the other excited state, then the desired SGC are created between the two excited states. For atoms in free space, this process does not occur, since the virtual photon can only be reabsorbed on the emitting transition due to its energy and polarization.

We have circumvented this limitation using two tricks. First, the cavity environment can be engineered in such a way that the virtual photon dominantly couples to one polarization mode only, instead of two in free space. If the transition dipoles of the system are aligned properly using a suitably chosen external magnetic field, then this single polarization mode can couple to both transitions from the ground to the two excited states, such that SGC are created. Second, the different nuclei can also exchange energy via the vacuum. The probing X-ray field, however, cannot distinguish between individual nuclei. Instead, the ensemble of nuclei in the cavity appears as a single quantum system in which the SGC appear due to the coupling between the different nuclei, thus effectively realizing a quantum simulator for a giant atom.

The experimental results are in good agreement with a recently established quantum optical theory [5]. The spectra show the

resonances of up to six transitions between the ground and the excited magnetic sublevels. Without SGC, they would incoherently add up. But due to SGC, interference can occur, which leads to deep interference minima as shown in Fig. 2. The reduction of the reflected intensity at certain detunings can directly be traced back to the presence of non-decaying metastable excited states, formed due to SGC. As the interference minima are nearly perfect, we conclude that our setup operates essentially decoherence-free. All results were obtained with the same cavity, but with different directions of the applied external field. This demonstrates the possibility to externally control the appearance of SGC and thus the X-ray optical properties of the system.

Our method opens up a variety of possibilities for future studies because it enables the realization of undisturbed and highly configurable quantum optical model systems for applications with hard X-rays from synchrotron radiation and X-ray laser sources. Moreover, our approach is not restricted to the X-ray range but also works with visible light. This offers the chance to realize the theoretically proposed applications based on SGC [6] reaching from novel laser mechanisms [7] to the efficiency increase of solar cells [8].

Contact: Jörg Evers, joerg.evers@mpi-hd.mpg.de

Authors

Kilian P. Heeg¹, Hans-Christian Wille², Kai Schlage², Tatyana Guryeva², Daniel Schumacher², Ingo Uschmann^{3,4}, Kai S. Schulze⁴, Berit Marx³, Tino Kämpfer⁴, Gerhard G. Paulus^{3,4}, Ralf Röhlsberger², and Jörg Evers¹

1. Max-Planck-Institut für Kernphysik, Saupfercheckweg 1, D-69117 Heidelberg, Germany
2. Deutsches Elektronen-Synchrotron DESY, Notkestraße 85, D-22607 Hamburg, Germany
3. Institut für Optik und Quantenelektronik, Friedrich-Schiller-Universität Jena, Max-Wien-Platz 1, D-07743 Jena, Germany
4. Helmholtz-Institut Jena, Fröbelstieg 3, D-07743 Jena, Germany

Original publication

“Vacuum-Assisted Generation and Control of Atomic Coherences at X-Ray Energies”, *Phys. Rev. Lett.* **111**, 073601 (2013).

References

1. G. S. Agarwal, “Quantum Statistical Theories of Spontaneous Emission and Their Relation to Other Approaches”, *Springer Tracts in Modern Physics* Vol. **70**, 1-128 (Springer, Berlin, 1974).

2. R. Röhlsberger, K. Schlage, B. Sahoo, S. Couet, and R. Rüffer, “Collective Lamb Shift in Single-Photon Superradiance”, *Science* **328**, 1248-1251 (2010).
3. R. Röhlsberger, H.-C. Wille, K. Schlage, and B. Sahoo, “Electromagnetically induced transparency with resonant nuclei in a cavity”, *Nature (London)* **482**, 199-203 (2012).
4. B. Marx, I. Uschmann, S. Höfer, R. Löttsch, O. Wehrhan, E. Förster, M. Kaluza, T. Stöhlker, H. Gies, C. Detlefs, T. Roth, J. Härtwig, and G. G. Paulus, “Determination of high-purity polarization state of X-rays”, *Opt. Commun.* **284**, 915-918 (2011).
5. K. P. Heeg and J. Evers, “X-ray quantum optics with Mössbauer nuclei embedded in thin film cavities”, *Phys. Rev. A* **88**, 043828 (2013).
6. M. Kiffner, M. Macovei, J. Evers, and C. H. Keitel, “Vacuum-Induced Processes in Multilevel Atoms”, in *Progress in Optics* Vol. **55** (Elsevier, Amsterdam, 2010).
7. S. E. Harris, “Lasers without inversion: Interference of lifetime-broadened resonances”, *Phys. Rev. Lett.* **62**, 1033-1036 (1989).
8. M. O. Scully, K. R. Chapin, K. E. Dorfman, M. B. Kim, and A. Svidzinsky, “Quantum heat engine power can be increased by noise-induced coherence”, *Proc. Natl. Acad. Sci. U.S.A.* **108**, 15097-15100 (2011).

Hanbury Brown – Twiss interferometry at FLASH.

Photon correlations measured at a free-electron laser

X-ray free-electron lasers (FELs) with their unprecedented peak brilliance and ultrashort pulse duration have a revolutionary impact on X-ray science and open the route to a number of ground breaking experiments including femtosecond nano-crystallography and single particle coherent imaging. Many of these experiments exploit the high degree of coherence of FELs. However, the coherence properties of FEL radiation are not yet fully characterized, in particular, the statistical properties of self-amplified spontaneous emission (SASE) FELs. To explore this question Hanbury Brown – Twiss interferometry was performed at FLASH.

In their pioneering experiments, Hanbury Brown and Twiss demonstrated [1, 2] that fundamental information on the statistics of light sources can be acquired by coincidence detection of photons. This intensity interferometry was originally designed to determine the size of stars, but subsequently raised fundamental questions in the field of optical coherence and quantum optics [3].

A defining feature of any laser source is its high degree of coherence. In recent experiments [4, 5], it was demonstrated that FELs based on the SASE generation process have a high degree of transverse coherence, but low temporal coherence. To get a more detailed picture of the statistical properties of these sources, higher-order correlations of the FEL wave fields must be studied. In this work, measurements of second- and higher-order intensity correlation functions were performed at FLASH by implementing Hanbury Brown – Twiss (HBT) interferometry.

The core idea of a HBT experiment is to determine the normalized second-order intensity correlation function $g^{(2)}(r_1, r_2) = \langle I(r_1) \cdot I(r_2) \rangle / (\langle I(r_1) \rangle \langle I(r_2) \rangle)$ by measuring the coincident intensity $I(r_1)$, and $I(r_2)$ of two detectors at separated positions r_1 and r_2 . Averaging is done over a large number of wave fields (i.e. many FEL pulses in our case). Importantly, chaotic light can be completely described in the frame of Gaussian statistics and its statistical properties are determined by the first-order correlation function known as the spectral degree of coherence (SDC) $\mu(r_1, r_2)$. The intensity correlation function then reduces to $g^{(2)}(r_1, r_2) = 1 + \zeta_2(\Delta\omega) \cdot |\mu(r_1, r_2)|^2$, where the contrast $\zeta_2(\Delta\omega) \sim 1 / \Delta\omega T$ is inversely proportional to the bandwidth $\Delta\omega$ and duration T of the radiation pulse.

X-ray FELs, with their pulse durations of a few tens of femtoseconds, are ideal sources for intensity correlation experiments. According to FEL theory [6] these sources should obey Gaussian statistics in the linear and deep nonlinear regime of operation.

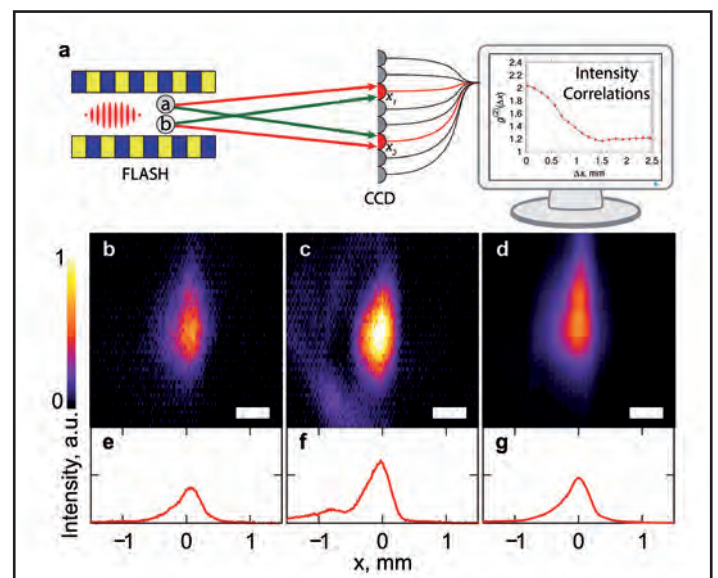


Figure 1

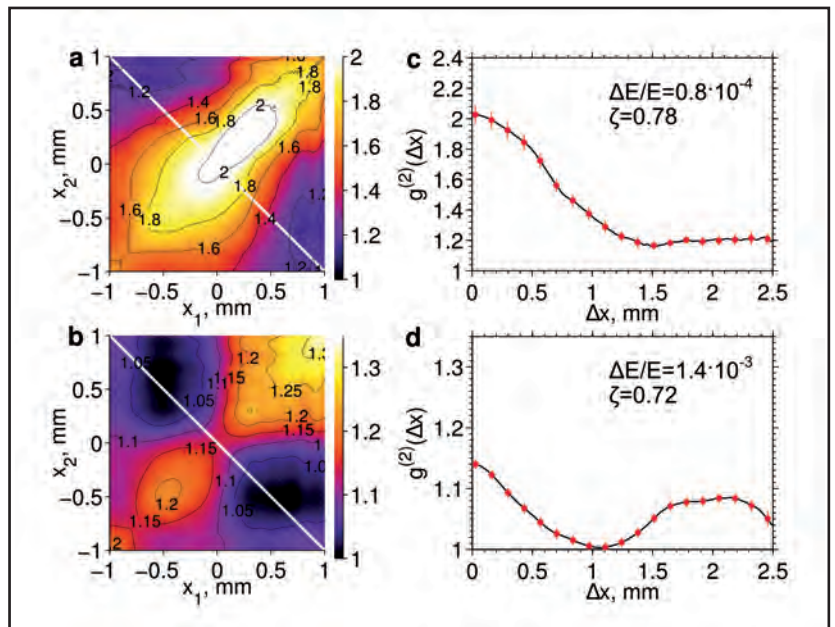
(a) A sketch of Hanbury Brown – Twiss interferometry performed at FLASH. The FEL beam is probed on the detector by correlating intensity values at different positions x_1 and x_2 and averaged over many FEL pulses. (b), (c) Typical single pulse intensity profiles and (d) an average over 2×10^4 pulses for a monochromator bandwidth of $\Delta E/E = 0.8 \times 10^{-4}$. (e) – (g) Projections of the pulse intensities onto the horizontal axis. The scale bar is 0.5 mm long.

Under these conditions, the correlation function $g^{(2)}(r_1, r_2)$ provides access to the transverse coherence properties of an FEL as well as to its pulse duration.

The experiment, shown in Fig. 1(a), was carried out at FLASH at a photon wavelength of $\lambda = 5.5$ nm. The measurements were performed at the plane grating monochromator beamline PG2 for several resolution settings. While the original HBT experiment [1, 2] made use of two separate detectors, we measured the FEL profiles on a pixel detector and correlated intensities recorded on different pixels. This allowed us to determine second- and

Figure 2

Intensity correlation analysis of FEL pulses. Intensity correlation function $g^{(2)}(x_1, x_2)$ for a bandwidth of $\Delta E/E = 0.8 \times 10^{-4}$ (a) and 1.4×10^{-3} (b). Panels (c) and (d) show the intensity correlation function $g^{(2)}(\Delta x)$ taken along the white line around the centre of the beam in (a) and (b) respectively. The values of the bandwidth $\Delta E/E$ and global degree of spatial coherence ζ are indicated in (c) and (d).



higher-order correlation functions at many separation points simultaneously.

The normalized second-order correlation function $g^{(2)}(x_1, x_2)$ for a narrow bandwidth radiation of $\Delta E/E = 0.8 \times 10^{-4}$ is shown in Fig. 2(a). In Fig. 2(c) the intensity correlation function $g^{(2)}(\Delta x)$ taken along the white line in 2(a) is presented. Remarkably, $g^{(2)}(\Delta x)$ reaches the maximum value of two for small separations, which indicates that the beam is Fourier-limited for this monochromator setting. This 100 % contrast also indicates that for these FLASH parameters the averaged coherence is not degraded due to optics imperfections. The second-order correlation function $g^{(2)}(x_1, x_2)$ for a larger bandwidth of $\Delta E/E = 1.4 \times 10^{-3}$ is shown in Fig. 2(b). The corresponding $g^{(2)}(\Delta x)$ is presented in Fig. 2(d) and has a smaller contrast, as expected. Surprisingly, at these conditions $g^{(2)}(\Delta x)$ exhibits an oscillatory behaviour. This may originate from the contribution of two independent sources in the lasing conditions of FLASH. It could also be a more general feature of the nonlinear coupling of the electrons and the emitted SASE radiation.

From our measurements we determined a transverse coherence length of $l_C = 0.93$ mm and global degree of spatial coherence of 78 %. Importantly, we got a value of 10^9 for the degeneracy

parameter, which is the number of photons in a single coherent mode. This value is significantly higher than that of any synchrotron source. These results are in good agreement with previous Young's double pinhole measurements at FLASH [5]. Analyzing the contrast as a function of the bandwidth we determined an average pulse duration of FLASH below 50 fs.

In summary, our measurements of the degree of transverse coherence, degeneracy parameter, and pulse duration indicate that SASE FELs in many aspects exhibit properties similar to optical lasers. At the same time, the measurements of the higher-order correlation functions suggest that SASE FELs are essentially chaotic sources obeying Gaussian statistics. An interesting future application of the methods developed in this work would be the study of seeded FELs. An intriguing question is whether seeded FELs are fully coherent sources in all orders, as described by Glauber [3], and, in this way, are equivalent to conventional single mode lasers, or if they obey Gaussian statistics like SASE FELs. We could also foresee that intensity correlation analysis might be applied to study the dynamics of ultrafast processes at FELs.

Contact: Ivan Vartaniants, Ivan.Vartaniants@desy.de,
Wilfried Wurth, Wilfried.Wurth@desy.de

Authors

A. Singer¹, U. Lorenz¹, F. Sorgenfrei², N. Gerasimova¹, J. Gulden¹, O. M. Yefanov¹, R. P. Kurta¹, A. Shabalin¹, R. Dronyak¹, R. Treusch¹, V. Kocharyan¹, E. Weckert¹, W. Wurth², and I. A. Vartanyants^{1,3}

1. Deutsches Elektronen-Synchrotron DESY, Notkestrasse 85, D-22607 Hamburg, Germany
2. Institut für Experimentalphysik and CFEL, University of Hamburg, Luruper Chaussee 149, D-22603 Hamburg, Germany
3. National Research Nuclear University, "MEPhI", 115409 Moscow, Russia

Original publication

"Hanbury Brown – Twiss Interferometry at a Free-Electron Laser", *Physical Review Letters* 111, 034802 (2013).

References

1. R. Hanbury Brown and R. Q. Twiss, "Correlation between Photons in two Coherent Beams of Light", *Nature (London)* 177, 27 (1956).
2. R. Hanbury Brown and R. Q. Twiss, "A Test of a New Type of Stellar Interferometer on Sirius", *Nature (London)* 178, 1046 (1956).
3. R. J. Glauber, "The Quantum Theory of Optical Coherence", *Phys. Rev.* 130, 2529 (1963).
4. I. A. Vartanyants et al., "Coherence Properties of Individual Femtosecond Pulses of an X-Ray Free-Electron Laser", *Phys. Rev. Lett.* 107, 144801 (2011).
5. A. Singer et al., "Spatial and temporal coherence properties of single free-electron laser pulses", *Opt. Express* 20, 17480 (2012).
6. E. L. Saldin, E. A. Schneidmiller, and M. V. Yurkov, "The Physics of Free Electron Lasers", Springer-Verlag, Berlin (2000).

The ultimately hot gas phase of metals.

X-ray fluorescence of iron ions at nuclear fusion temperatures

Iron ions are essential components of the solar core plasmas at 16 million Kelvin temperatures. In spite of a low concentration of only a few parts per million, or 0.14 % in mass, they scatter more X-rays than any other element including hydrogen, and hence they determine the opacity of those plasmas. Their X-ray lines are also prominent in the spectra of X-ray binary stars and active galactic nuclei. We prepare and trap iron ions typical for those environments, expose them to monochromatic synchrotron radiation, and measure for the first time their ground state absorption and X-ray fluorescence. The new method yields precise transition energies and line widths, thus allowing for detailed tests of atomic theory predictions used in the simulation of astrophysical plasmas.

Energy transport in stellar interiors is governed by X-rays, since they scatter less than electrons or other particles bare the neutrino. The nuclear fusion process requires high temperatures to proceed, yet it delivers, contrary to popular belief, only moderate power densities inside most stars. A paradox arises: the core maintains the high temperature, although only hundreds of watts of power are generated per cubic meter of solar core mass, while the radiative energy should escape at speed of light. The thermal insulation of the fusion core is the answer: X-ray scattering reduces radiation flux by more than ten orders of magnitude even at the boundary of the radiative zone of the Sun, which contains most of its mass. And because light elements are transparent to X-rays, their contribution to the solar opacity – the ability to block radiation – is much smaller than that of heavy elements. In this way, iron, the only heavy element with a significant mass contribution to main sequence stars, acquires an essential role.

Under stellar core conditions, light elements are fully ionized, meaning completely bare of electrons. However, iron, due to its nuclear charge of 26 protons, manages to keep a few bound electrons even at 15.7 MK and enormous pressures leading to a 150 kg/cm³ matter density. Even some of its higher excited orbits, with principal quantum numbers $n = 2, 3$ and 4 are still rather undisturbed by the prevailing collision rates. Transitions between the electronic ground state and higher levels occur constantly: excited levels have lifetimes on the order of few femtoseconds, six orders of magnitude shorter than optical transitions. Moreover, the energy exchanged between the ions and the photon field amounts to more than 6.5 keV in each of those processes, again a factor of thousand higher than in the optical case. Thus, both the ability of iron ions for absorbing and emitting radiation a million times faster than hydrogen, and this in quanta that are thousand times more energetic than the Lyman transitions of hydrogen, more than compensate for the small abundance of iron. The solar iron could be concentrated in an imaginary “iron curtain” of 100 km thickness at two thirds of the solar radius of 700,000 km that would effectively stop

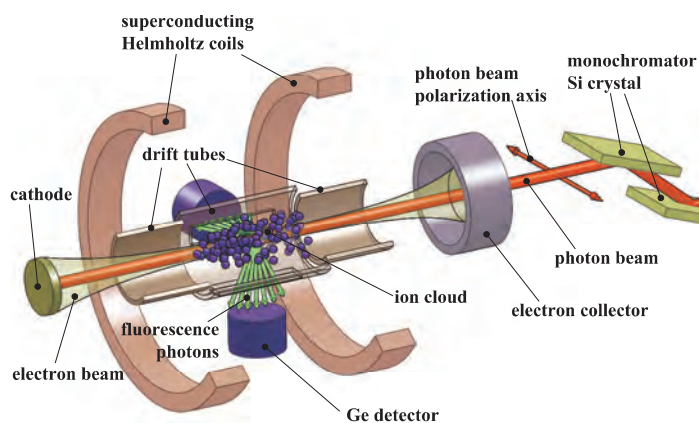


Figure 1

Principle of the experiment. Highly charged iron ions are generated by electron impact ionization of iron atoms, and subsequently trapped by the electron beam negative space charge potential in combination with additional drift tube electrodes. A monochromatic photon beam enters the trap region and excites the ions at characteristic resonance energies. The fluorescence decay follows within femtoseconds, and is detected by photon detectors mounted in directions parallel and perpendicular to the photon polarization plane.

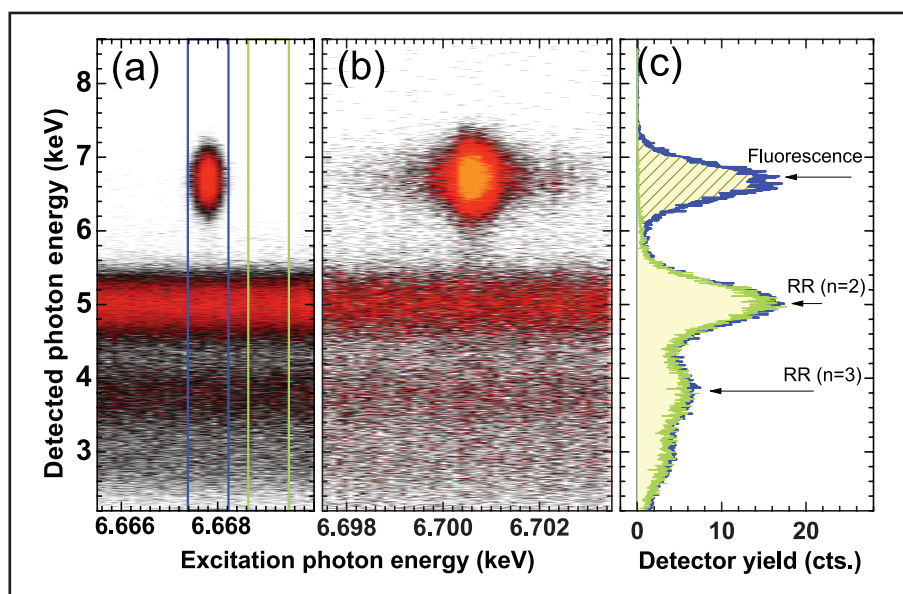
X-rays from leaving the radiative zone. The diluted iron ions achieve the same effect in the plasma.

Modern X-ray astronomy has also discovered a great number of sources showing K_{α} lines of iron. They arise from heating processes due to gravitational matter in-fall in massive binary systems, and from X-ray fluorescence of accretion disks in active galactic nuclei [1]. Dominating the X-ray spectrum of most of those sources, they are key elements for the diagnostics of such objects.

Investigation of X-ray absorption processes of highly charged ions has advanced theoretically for a few decades, but experiments approaching the conditions needed to test them were not possible,

Figure 2

Panels (a) and (b): X-ray emission spectra as a function of the excitation photon energy. The horizontal features are independent thereof, and arise from electron impact excitation and radiative recombination of trapped helium like iron ions (Fe^{24}). The isolated resonances above are due to: (a) an intercombination line $1s^2\ ^1S_0 \rightarrow 1s\ 2p\ ^3P_1$; and (b) an allowed resonance line $1s^2\ ^1S_0 \rightarrow 1s\ 2p\ ^1P_1$; in (c), the projection onto the emission photon energy axis is shown.



until now. Production and trapping of highly charged ions is meanwhile achieved with electron beam ion traps (EBITs). They use a hair-thin, magnetically focused electron beam in order to strip atoms of their outer electrons by collisions (Fig. 1). Additionally, the negative space charge of the beam attracts the positive ions to the beam centre, and traps them tightly. By choosing a certain energy of the electron beam, the maximum achievable charge state is selected. We used FLASH-EBIT, a device developed at the Max-Planck-Institut für Kernphysik for operation at soft X-ray energies at FLASH [2]. Photoionization of highly charged ions with synchrotron radiation [3] and laser spectroscopic studies at soft X-ray energies with it became feasible, addressing open questions in astrophysics [4].

Progress by one additional order of magnitude in photon energy has now been enabled at the P01 beamline of PETRA III. A key factor is its high photon flux, capable of resonantly exciting the trapped iron ions in charge states typical for the solar core, from helium-like (two bound electrons left) to carbon-like (six electrons). X-ray detectors registered the fluorescence photons emitted by the ions while scanning the monochromator. We were able to

investigate the absorption and fluorescence of all the strong K_{α} transitions ($n = 1$ to $n = 2$) of the ions of interest. An example is displayed in Fig. 2.

Resonant excitation by synchrotron radiation constitutes a novel and uniquely sensitive method of determining transition energies. We also resolved their line profiles down to their natural widths, with much more detail than earlier emission studies. These advantages allow for a systematic comparison with transition energies and probabilities calculated within this work using advanced multi-configuration Dirac-Fock methods, as well as with other theoretical predictions.

Future experiments will aim at reaching even higher resolution by using translationally cooled highly charged ions. With their wealth of transitions of various multipolarities and linewidths from the wide to the very narrow, highly charged ions could enable an extension of optical clocks into the much higher frequency domain of X-rays.

Contact: José R. Crespo López-Urrutia, crespojr@mpi-hd.mpg.de

Authors

J.K. Rudolph^{1,2}, S. Bernitt¹, S.W. Epp³, R. Steinbrügge¹, C. Beilmann^{1,4}, G.V. Brown⁵, S. Eberle¹, A. Graf⁵, Z. Harman^{1,6}, N. Hell^{5,7}, M. Leutenegger^{8,9}, A. Müller², K. Schlage¹⁰, H.-C. Wille¹⁰, H. Yavaş¹⁰, J. Ullrich^{1,†}, and J.R. Crespo López-Urrutia¹

1. Max-Planck-Institut für Kernphysik, Saupfercheckweg 1, D-69117 Heidelberg, Germany
 2. Institut für Atom- und Molekülphysik, Justus-Liebig-Universität Gießen, Leihgesterner Weg 217, D-35392 Gießen, Germany
 3. Max Planck Advanced Study Group, CFEL, Notkestraße 85, D-22607 Hamburg, Germany Institute for Nanotechnology, Karlsruhe Institute of Technology (KIT), Karlsruhe D-76021, Germany
 4. Physikalisches Institut, Ruprecht-Karls-Universität Heidelberg, Im Neuenheimer Feld 226, D-69120 Heidelberg, Germany
 5. Lawrence Livermore National Laboratory, 7000 East Avenue, Livermore, California 94550, USA
 6. ExtreMe Matter Institute (EMMI), Planckstraße 1, D-64291 Darmstadt, Germany
 7. Dr. Karl Remels-Observatory and ECAP, Universität Erlangen Nürnberg, Sternwartstraße 7, D-96049 Bamberg, Germany
 8. NASA/Goddard Space Flight Center, 8800 Greenbelt Road, Greenbelt, Maryland 20771, USA
 9. Center for Space Sciences and Technology, University of Maryland, Baltimore County, Baltimore, Maryland 21250, USA
 10. Deutsches Elektronen-Synchrotron DESY, Notkestraße 85, D-22607 Hamburg, Germany
- † Present address: Physikalisches Technische Bundesanstalt (PTB), Bundesallee 100, D-38116 Braunschweig, Germany

Original publication

“X-Ray Resonant Photoexcitation: Linewidths and Energies of K_{α} Transitions in Highly Charged Fe Ions”, *Physical Review Letters* 111, 103002 (2013).

References

1. K. Nandra, *Mon. Not. R. Astron. Soc.* 368, L62 (2006).
2. S.W. Epp, J. R. Crespo López-Urrutia, G. Brenner, V. Mäckel, P. H. Mokler, R. Treusch, M. Kuhlmann, M.V. Yurkov, J. Feldhaus, J. R. Schneider, M. Wellhöfer, M. Martins, W. Wurth, and J. Ullrich, *Phys. Rev. Lett.* 98, 183001 (2007).
3. M. C. Simon, J. R. Crespo López-Urrutia, C. Beilmann, M. Schwarz, Z. Harman, S.W. Epp, B. L. Schmitt, T. M. Baumann, E. Behar, S. Bernitt, R. Follath, R. Ginzel, C.H. Keitel, R. Klawitter, K. Kubiček, V. Mäckel, P.H. Mokler, G. Reichardt, O. Schwarzkopf, and J. Ullrich, *J., Phys. Rev. Lett.* 105, 183001 (2010).
4. S. Bernitt, G.V. Brown, J. K. Rudolph, R. Steinbrügge, A. Graf, M. Leutenegger, S.W. Epp, S. Eberle, K. Kubiček, V. Mäckel, M.C. Simon, E. Träbert, E.W. Magee, C. Beilmann, N. Hell, S. Schippers, A. Müller, S.M. Kahn, A. Surzhykov, Z. Harman, C.H. Keitel, J. Clementson, F.S. Porter, W. Schlotter, J. J. Turner, J. Ullrich, P. Beiersdorfer, and J.R. Crespo López-Urrutia, *Nature* 492, 225 (2012).

Atoms team up for faster relaxation.

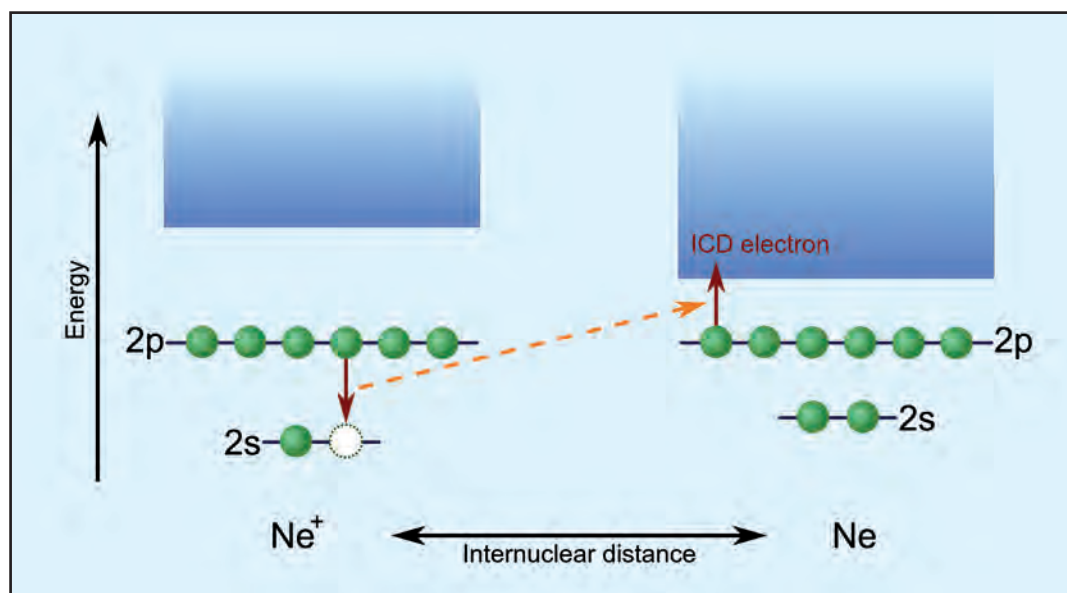
Real-time measurement of interatomic coulombic decay (ICD) in Ne_2

In a XUV-XUV pump-probe experiment at FLASH, the decay time of an efficient non-radiative relaxation process that occurs in weakly bound systems was measured in neon dimers (Ne_2). An isolated excited Ne^{2+} ion with one of its 2s electrons removed needs almost one nanosecond to decay to its ground state by emission of a photon. When a second Ne atom is placed in the vicinity of the first one, as realized in neon dimers, we found that the relaxation is about 10,000 times faster: 150 ± 50 fs. The excitation energy is transferred non-radiatively from the Ne^{2+} to its neutral neighbour, thereby ionizing it. This *atomic teamwork* is known as Interatomic Coulombic Decay (ICD). It is the dominant relaxation process for most van-der-Waals and hydrogen bound systems, the latter being the controlling binding force of large biomolecules.

Figure 1

Illustration of ICD in Ne_2 . Absorption of a single photon leads to the removal of a 2s electron from one of the Ne atoms.

The excited ion relaxes via ICD by transferring its excess energy to the neighbouring Ne atom that consequently ejects one of its 2p electrons. Finally, two singly charged Ne^+ ions are created that repel each other by the Coulomb force.



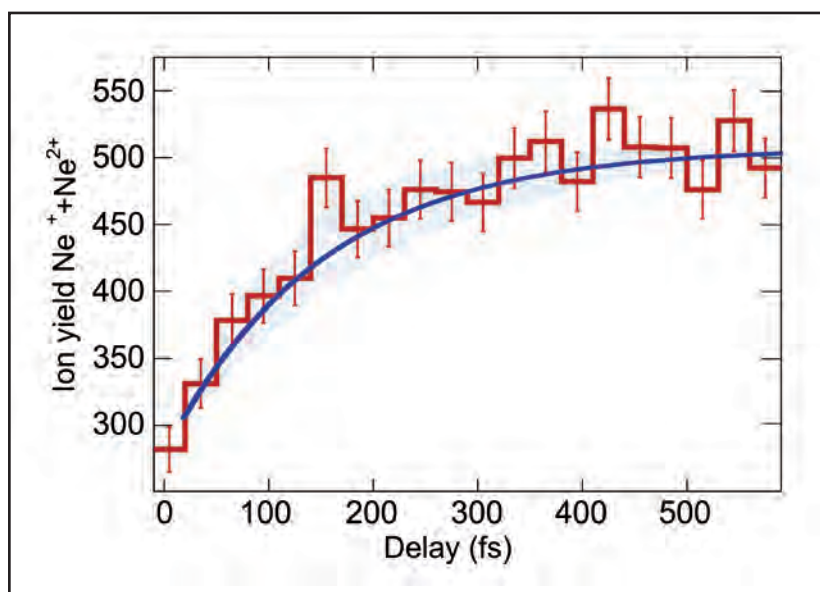
Efficient energy transport within or between molecules plays a crucial role in many chemical and biochemical processes. The redistribution of energy that is deposited in a system at a certain point by absorption of a photon may lead to an internal movement and eventually to the breakage of a chemical bond at another point. In many cases, the energy is transferred by moving electrons or by a rearrangement of charges. Very often the electric force between electrons alone is sufficient for an efficient energy transfer – even over long distances (on the atomic scale).

Interatomic or Intermolecular Coulombic Decay (ICD) is a prime example for such a process. It is an extremely efficient relaxation mechanism that comes into play whenever excited atoms (or molecules) are embedded in a weakly interacting environment. In particular, isolated excited ions that have relaxation times in the order of pico- or nanoseconds after the removal of an inner-valence electron can relax much faster via ICD.

The excess energy is transferred to a neighbouring atom thereby ionizing it. After its theoretical prediction in 1997 [1], ICD has by now been experimentally investigated in van-der-Waals bound rare-gas clusters of various sizes [2] as well as hydrogen bound water clusters [3]. Hydrogen bonds are essential for holding large biomolecules together giving them their characteristic shapes. Once ICD has occurred in such a system the ejected low energetic ICD electron can effectively interact with the environment itself, destroying chemical bonds. This can happen for instance in DNA, which makes the ICD process also relevant for radiation therapy. The aim of our experiment was to determine the ICD lifetime for the first time directly by means of a real-time observation of the decay process in neon dimers (Ne_2). Different theoretical calculations predicted the relaxation to occur on a time scale between some tens to hundreds of femtoseconds [4]. This is about a factor of 10,000 faster than the competing relaxation via fluorescence.

Figure 2

Yield of coincident $\text{Ne}^+ + \text{Ne}^{2+}$ ions measured in the reaction microscope (REMI) as a function of the time delay (red histogram). The blue line indicates an exponential fit resulting in an ICD lifetime of 150 ± 50 fs, with the uncertainty indicated by the light blue area.



An XUV-XUV pump-probe experiment was performed at FLASH using a reaction microscope (REMI) [5] equipped with a split-and-delay stage. The incoming FEL beam at 58.2 eV photon energy with a pulse duration of approximately 60 fs (FWHM) and an intensity of 10^{12} W/cm² is reflected off a multilayer mirror, which geometrically splits the beam into two halves. The two beams are recombined by focussing them onto the same spot in an intrinsically cold beam of Ne_2 . The REMI enables the determination of the ion momentum vectors and in addition an unambiguous identification of those fragment pairs that emerge from the same dimer.

As illustrated in Fig. 1, ICD in Ne_2 is initiated by removing a 2s inner-shell electron from one of the two Ne atoms. The time it takes for the excited ion to relax by transferring its energy to the neighbouring Ne atom, and thereby ionizing it, is referred to as ICD lifetime. It can be determined using a pump-probe scheme. The pump pulse removes a 2s electron and thus populates an intermediate excited $\text{Ne}^{**} + \text{Ne}$ state in the singly-charged dimer. The system will remain in this state until it decays into $\text{Ne}^+ + \text{Ne}^+$ via ICD. Thus, we need a method to determine at what time the neighbouring Ne atom is ionized with respect

to the initial excitation. This is done by probing the dimer's charge state with the second half of the FEL pulse which further ionizes one of the Ne fragments after an adjustable time delay. Only if ICD has already occurred before the arrival of the probe pulse an effectively triply ionized dimer ($\text{Ne}^+ + \text{Ne}^{2+}$) is formed. Hence, the increase of the yield of coincident $\text{Ne}^+ + \text{Ne}^{2+}$ ions for larger delays reflects the ICD lifetime. Fig. 2 shows the recorded ion yield together with an exponential fit resulting in a decay time of 150 ± 50 fs.

The obtained ICD lifetime is in good agreement with theoretical predictions, but only with those that take the nuclear motion into account: The removal of the first electron causes a change of the binding force between the two neon nuclei, which leads to a time-dependent internuclear distance. Nuclear dynamics play a crucial role for the decay process, because the ICD lifetime is predicted to be strongly dependent on this distance. This dependence we intend to investigate in future experiments.

Contact: Kirsten Schnorr, kirsten.schnorr@mpi-hd.mpg.de
Robert Moshhammer, r.moshhammer@mpi-hd.mpg.de

Authors

K. Schnorr¹, A. Senftleben¹, M. Kurka¹, A. Rudenko^{2,3}, L. Foucar^{2,4}, G. Schmid¹, A. Broska¹, T. Pfeifer¹, K. Meyer¹, D. Anielski^{1,2}, R. Boll^{1,2}, D. Rolles^{2,5}, M. Kübel⁶, M.F. Kling^{3,6}, Y.H. Jiang⁷, S. Mondal⁸, T. Tachibana⁸, K. Ueda⁸, T. Marchenko⁹, M. Simon⁹, G. Brenner⁵, R. Treusch⁵, S. Scheit¹⁰, V. Averbukh¹¹, J. Ullrich¹², C.D. Schröter¹ and R. Moshhammer¹

1. Max-Planck-Institut für Kernphysik, D-69117 Heidelberg, Germany
2. Max-Planck Advanced Study Group at CFEL, D-22607 Hamburg, Germany
3. J.R. Macdonald Laboratory, Kansas State University, Manhattan, Kansas 66506, USA
4. Max-Planck-Institut für medizinische Forschung, D-69120 Heidelberg, Germany
5. Deutsches Elektronen-Synchrotron DESY, D-22607 Hamburg, Germany
6. Max-Planck-Institut für Quantenoptik, D-85748 Garching, Germany
7. SARI, CAS, Shanghai 201210, China
8. IMRAM, Tohoku University, Sendai 980-8577, Japan
9. LCPMR, UPMC and CNRS, F-75231 Paris, France
10. Goethe-Universität, D-60438 Frankfurt, Germany
11. Imperial College London, London, SW7 2AZ, United Kingdom
12. Physikalisch-Technische Bundesanstalt, D-38116 Braunschweig, Germany

Original publication

"Time-Resolved Measurement of Interatomic Coulombic Decay in Ne_2 ", *Phys. Rev. Lett.* **111**, 093402 (2013).

References

1. L. S. Cederbaum, J. Zobeley, and F. H. Tarantelli, "Giant Intermolecular Decay and Fragmentation of Clusters", *Phys. Rev. Lett.* **79**, 4778 (1997).
2. S. Marburger et al., "Experimental Evidence for Interatomic Coulombic Decay in Ne Clusters", *Phys. Rev. Lett.* **90**, 203401 (2003).
3. T. Jahnke et al., "Ultrafast energy transfer between water molecules", *Nature Physics* **6**, 139-142 (2010).
4. R. Santra and L. S. Cederbaum, "An efficient combination of computational techniques for investigating electronic resonance states in molecules", *J. Chem. Phys.* **115**, 6853 (2001).
5. J. Ullrich et al., "Recoil-ion and electron momentum spectroscopy: reaction microscopes", *Rep. Prog. Phys.* **66**, 1463-1545 (2003).

Unraveling the structure–function relationship in chemistry.

Specific chemical reactivities of spatially separated 3-aminophenol conformers with cold Ca^+ ions

Most molecules exhibit multiple structural isomers, which have the same chemical formula and connectivities, but differ in the exact positions of their atoms or the orientation of functional groups. These isomers can often interconvert thermally and are difficult to isolate. Consequently, a precise characterization of their role in chemical reactions has proven challenging. We have probed the reactivity of specific conformers – rotational structural isomers – by using an experimental technique based on their spatial separation in a molecular beam using electrostatic deflection. The separated conformers react with a target of trapped laser-cooled ions. In the reaction of Ca^+ with 3-aminophenol, we find a twofold larger rate constant for the *cis* compared to the *trans* conformer, although these conformers differ only in the relative orientation of the O–H bond. This result is explained by conformer specific differences in the long range ion-molecule interaction potentials. Our approach demonstrates the possibility of controlling reactivity through selection of conformational states.

Recent progress in the cooling, manipulation, and control of isolated molecules in the gas phase has paved the way for the study of chemical processes at high levels of sensitivity, selectivity, and detail. Methods for slowing and merging of supersonic molecular beams have enabled precise characterizations of the role of collision energy and of the molecular quantum state in scattering and reactive processes. Recent experiments with trapped, translationally cold molecules and ions have provided insights into the quantum dynamics of chemical reactions and the subtleties of intermolecular interactions. These experiments have thus far been restricted to reactions involving atoms or small molecules with simple geometric and quantum structures. The vast majority of molecules, however, possess a plethora of internal degrees of freedom that are challenging to probe independently. In particular, polyatomic molecules usually exhibit many rotational isomers. These conformers interconvert with low thermal barriers through rotations of covalent bonds. We have developed experimental methods to spatially separate the individual conformers in a molecular beam, consisting of an electric deflector [1], the quadrupole focuser [2], and the alternating gradient decelerator [3]. These are the neutral-molecule equivalents of the bender, the ion guide, and the LINAC for charged particles, respectively.

Here, we exploit the spatially separated conformers to study specific conformational effects in bimolecular reactions with stationary targets of ultra-cold trapped ions [4] to gain insight into fundamental reaction mechanisms in chemistry. We introduce a distinct approach for the study of conformational effects and conformation-dependent reactivities, i.e. rate constants, in bimolecular reactions. A cold beam of 3-aminophenol was created by co-expanding the molecular sample at 150 °C with high pressure helium or neon gas into the vacuum, resulting in cold molecular beams with internal temperatures of about 1 K. We spatially separated the *cis* and *trans* conformers of 3-aminophenol ($\text{C}_6\text{H}_7\text{NO}$) by using the inhomogeneous static electric field

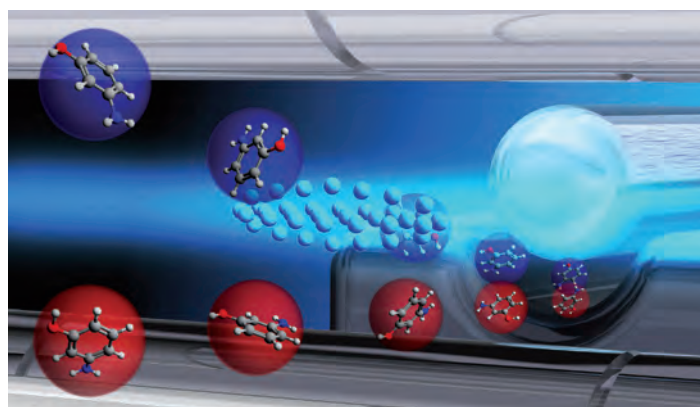


Figure 1

Artists impression of the experiment. A cold molecular beam of 3-aminophenol is dispersed in the electric deflector, samples of the separated *cis* and *trans* conformers are directed at a stationary Ca^+ ion target, and the rate of chemical reaction is recorded individually.

in the deflector and directed the molecules toward the reaction volume. There, they interacted with a stationary target of trapped and laser cooled Ca^+ ions. Reactions of organic molecules with metal ions are prototypical organometallic chemical processes that are relevant for the activation of chemically inert polar bonds, for instance, in catalysis, in atmospheric chemistry, and for the interaction of metal ions with biomolecular building blocks. The experiments were performed at CFEL and at the University of Basel.

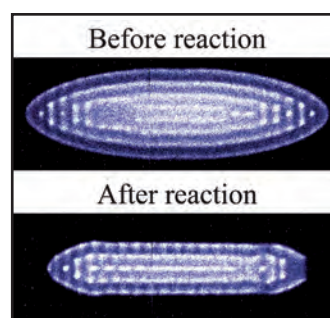


Figure 2

Atomically resolved fluorescence image of laser cooled Ca^+ ions in the trap. Heavier product ions collect at the outside of the Coulomb crystal; they are not resonant to the laser radiation and do not fluoresce.

Fig. 1 shows the experimental layout. The laser cooled Ca^+ ions, depicted by the small light-blue spheres, form a Coulomb crystal that provides a tightly confined reaction target, much smaller in extent than the conformationally separated regions of the dispersed molecular beam. The spatial separation of the conformers is depicted by the different trajectories of *cis* and *trans* 3-aminophenol by blue and red balls, respectively, which are overlaid by the actual molecular structures. The Coulomb crystal also provided a highly sensitive detection of reactions through the fluorescence of laser cooled Ca^+ ions, which was reduced for every single reaction, as the products are not resonant with the cooling lasers. Instead, they are sympathetically cooled to low translational energies. In our experiments, the invisible products accumulated on the outside of the crystal and the Ca^+ ions formed a narrower cylinder in the centre of the crystal. These effects are shown in Fig. 2. The fluorescence depletion gave the reaction rate and the narrowing of the fluorescing volume shows that the reaction products are heavier than Ca^+ .

In our benchmark experiment we applied various voltages to the electric deflector to vary the deflection and the dispersion of the two conformers. In Fig. 3 the data for experiments performed at one specific deflector voltage of 7.5 kV are shown as an example. In Fig. 3 (a) the individual molecular beam profiles for *cis* and *trans* 3-aminophenol are shown in blue and red, respectively, demonstrating the dispersion of the molecular beam. These curves were obtained by selective two-photon-ionization of the conformers using resonant ns laser pulses at 280 nm and vertically scanning the molecular beam across the laser focus. Subsequently, we measured the reactivity of the dispersed molecular beam with the stationary Ca^+ target, this time scanning the beam across the small trapped ion target. The resulting pseudo-first-order reaction rate constants are plotted in Fig. 3(b). The red and blue lines depict the fitted rate constant contributions from the *trans* and *cis* conformer, respectively. The considerably larger relative contribution from the *cis* species, compared to its ion signal in Fig. 3(a), already demonstrates its higher reactivity. A careful calibration of the molecular densities, pulse durations, and the electronic state populations of the Ca^+ ions allowed us to deduce the second order rate constants for the reaction.

The resulting second-order rates across the dispersed molecular beam are shown in Fig. 3(c). From this graph it is obvious that the *cis* conformer reacts about twice as fast as the *trans* conformer. The exact rate constants are $k_{2,\text{cis}} = (3.2 \pm 1.3) \times 10^{-9} \text{ cm}^3 \text{ s}^{-1}$

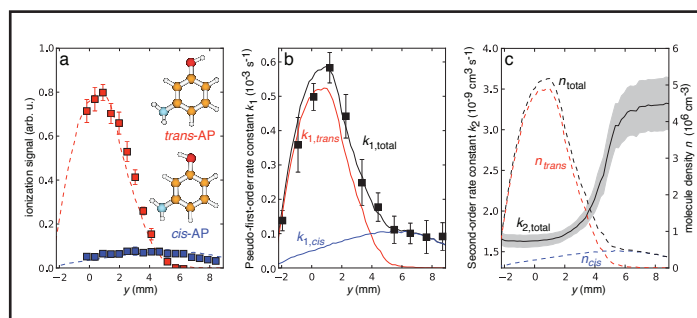


Figure 3

Experimental data: a) Conformer-specific molecular beam deflection profiles for a deflector voltage of 7.5 kV. This demonstrates the spatial dispersion of the conformers in the molecular beam. b) Reactivity as a function of the molecular beam composition. c) Second-order rate constants as derived from the calibrated experiment.

and $k_{2,\text{trans}} = (1.5 \pm 0.6) \times 10^{-9} \text{ cm}^3 \text{ s}^{-1}$ with a *cis:trans* reactivity ratio of 2.1 ± 0.5 . A detailed analysis of the detuning of the cooling laser showed that more than 90 % of the reactions took place with electronically excited Ca^+ ; under these conditions the reaction was barrierless. We could explain the distinct reaction rates by capture rate calculations. These calculations predicted that the collision cross section is 1.5 times larger for *cis* than for *trans* 3-aminophenol due to differences in the respective charge-dipole interactions for the reaction systems.

The present advances in the studies of chemical reactivities have become possible by combining conformer selection control experiments with highly sensitive trapped ion methods. We expect that the current methodology will benefit fundamental reaction-dynamics studies as well as the investigation of a wide range of ion-molecule reactions that are relevant for catalysis and interstellar chemistry. Electrostatic conformer selection is a widely applicable technique whenever the conformers present in the molecular beam possess sufficiently different dipole moments. Even more advanced electric field manipulation techniques for the separation of individual chemical species or individual quantum states have been demonstrated. In addition, sympathetic cooling of ions is a near-universal technique that allows the generation of Coulomb crystals of a wide range of atomic and molecular species with simultaneous preparation of their internal quantum state.

Contact: Jochen Küpper, jochen.kuepper@desy.de

Authors

Yuan-Pin Chang¹, Karol Dlugolecki¹, Jochen Küpper^{1,2,3}, Daniel Rösch⁴, Dieter Wild⁴ and Stefan Willitsch⁴

- Center for Free-Electron Laser Science, DESY, Notkestrasse 85, D-22607 Hamburg, Germany
- The Hamburg Center for Ultrafast Imaging, University of Hamburg, Luruper Chaussee 149, D-22761 Hamburg, Germany
- Dep. of Physics, University of Hamburg, Luruper Chaussee 149, D-22761 Hamburg, Germany
- Department of Chemistry, University of Basel, Klingelbergstrasse 80, CH-4056 Basel, Switzerland

Original publication

“Specific Chemical Reactivities of Spatially Separated 3-Aminophenol Conformers with Cold Ca^+ Ions”, *Science* **342**, 98-101 (2013).

References

- F. Filsinger et al., “Pure samples of individual conformers: the separation of stereoisomers of complex molecules using electric fields”, 6900–6902.
- F. Filsinger, U. Erlekam, G. von Helden, J. Küpper, G. Meijer, “Selector for structural isomers of neutral molecules”, 133003(4) *Phys. Rev. Lett.* **100**, 133003 (2008).
- K. Wohlfart et al., “Alternating gradient focusing and deceleration of large molecules”, 031404(4) *Phys. Rev. A* **77** (2008).
- S. Willitsch, “Coulomb-crystallised molecular ions in traps: methods, applications, prospects”, 175-199 *Int Rev Phys Chem* **31** 175 (2012).

Filming dancing electrons with a high speed X-ray camera.

How to freeze-frame electrons with X-rays

Electrons are the glue that keeps atoms in matter together, and their motion plays a key role in the function and transformation of materials. During complex chemical and biological reactions, electrons undergo ultrafast rearrangements. One challenge is that the motion of electrons is so fast that ordinary light is unsuitable for taking an image. For decades, X-rays have been used to visualize the location of electrons in materials. But only very recently, it has become possible to generate flashes of X-rays that are short enough to take snapshots of the transient positions of these electrons. A second challenge is that, usually when X-rays interact with electrons, they inevitably change the electronic motion while the snapshot is being taken. The focus of our work was to find a way to overcome the problem of these light-induced changes by taking snapshots using the phase variation of X-rays.

Ever since the discovery of X-rays, scattering of X-rays from matter has been used to take images of the microcosm, i.e., to unravel the atomic-scale structure of matter. However, the images generated to date are mostly static: pictures resolve situations in real-space, but not in real-time. The motion of atoms within molecules and solids that is associated with chemical transformations occurs on the femtosecond ($1 \text{ fs} = 10^{-15} \text{ s}$) timescale. The timescale of electronic motion can be even faster, on the order of attoseconds ($1 \text{ as} = 10^{-18} \text{ s}$). In order to see the motion of electrons during ultrafast rearrangement in a complex chemical reaction, matter must be illuminated with flashes of X-rays that are short and bright enough to take stroboscopic snapshots of these moving electrons. A series of such snapshots stitched together results in a movie of the electronic motion with atomic-scale spatial and temporal resolution [1, 2].

One of the key objectives of the new X-ray lasers like FLASH or European XFEL is to film these ultrafast electronic rearrangements in detail, in order to understand and eventually change the behaviour of the reacting partners, to develop new functional materials. For ordinary synchrotron light sources, this motion of electrons has always been too fast for taking an image. But the intense and ultrafast light flashes of X-ray lasers should be able to freeze-frame the electronic motion during a chemical reaction. But such high-speed filming does not only demand new detectors and equipment, it also requires new theoretical approaches: How can one describe and interpret the interaction of ultrafast and highly intense X-rays with a non-stationary electronic system? And how can one be sure that the intense X-ray pulse only probes the current arrangement and does not disturb the sample so much as to destroy the information content of the measurement [3]?

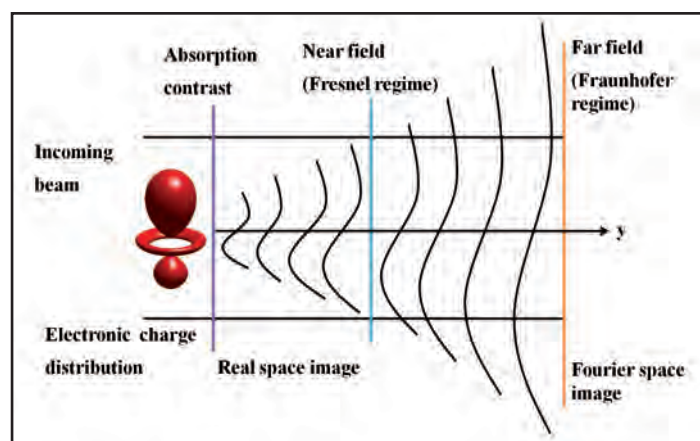
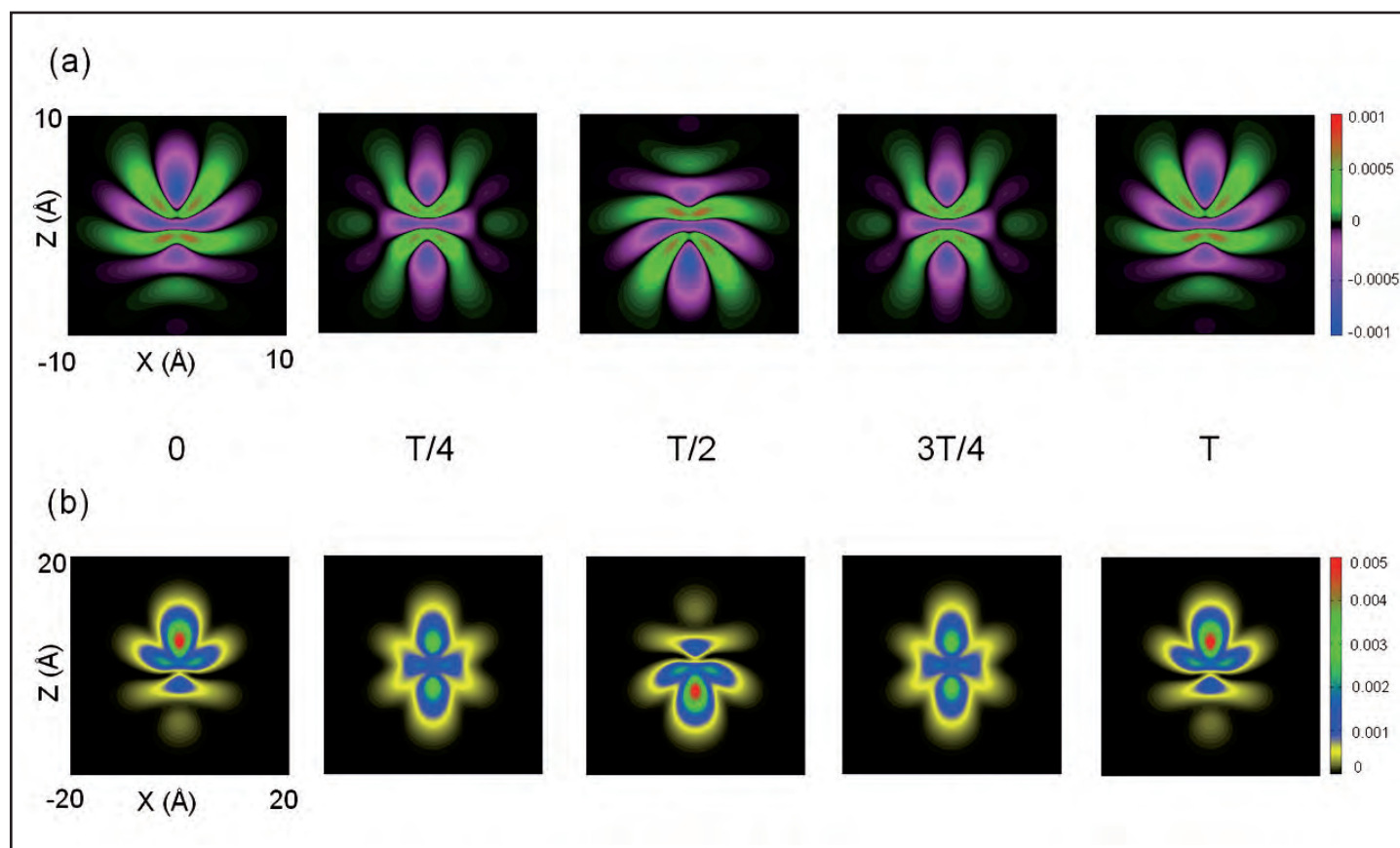


Figure 1

Concept of X-ray matter interaction, where matter is represented by an isosurface of an electronic charge distribution of an electronic wave packet. The real-space phase-contrast image is observed in the near-field region, whereas the Fourier-space scattering pattern is observed in the far-field region. The figure is taken from [G. Dixit, J. M. Slowik, and R. Santra, Phys. Rev. Lett. 110, 137403 (2013)] © 2013 American Physical Society

In our work, we proposed a new strategy to visualize these rearrangements using time-resolved X-ray phase contrast imaging. We simulated a coherent electronic motion, oscillating on a few femtoseconds time-scale. The incoming X-ray flashes are treated as a quantum wave packet interacting with the electrons. We demonstrated that the X-ray pulses are really able to image different states of the ultrafast electronic motion. Also, we visually demonstrated that the problem of light-induced changes during the snapshot of the motion can be overcome by using the phase variation of X-rays (see Fig. 1). Phase contrast imaging is a very



common method for imaging samples with synchrotron light. It makes use of the fact that interaction of light with matter does not only change the intensity of the X-rays but also the phase. The phase difference of the transmitted X-rays and the scattered X-rays can be detected and it contains information on the sample's structure.

In our original publication, a very short pump pulse sets an electron into motion. This electronic motion can be described as an electronic wave packet. The wave packet can be snapshot at various time intervals with an ultrashort X-ray pulse, producing distinctive images that change as the electron moves. Moreover, our study suggests that the proposed method provides information on the curvature of the instantaneous electron density, which can be used to gather details of the internal structure of the wave packet (see Fig. 2). This may be useful for understanding complex bonding and topology of charge distributions in complex systems. Moreover, our present finding is a step towards real-time imaging of microscopic motions, which will enhance our understanding about the working of the microcosm.

Contact: Robin Santra, robin.santra@cfel.de

Figure 2

Phase contrast images and projected instantaneous electron density of the wave packet. (a) Laplacian of the projected instantaneous electron density, and (b) the instantaneous electron density integrated along the direction of propagation of the incident X-rays (y axis) at pump-probe delay times 0, $T/4$, $T/2$, $3T/4$, and T , where the oscillation period of the electronic wave packet is $T = 6.25$ fs. The figure is taken from [G. Dixit, J. M. Slowik, and R. Santra, *Phys. Rev. Lett.* 110, 137403 (2013)] © 2013 American Physical Society

Authors

Gopal Dixit¹, Jan Malte Slowik^{1,2}, and Robin Santra^{1,2}

- Center for Free-Electron Laser Science, DESY, Notkestrasse 85, D-22607 Hamburg, Germany
- Department of Physics, University of Hamburg, D-20355 Hamburg, Germany

Original publication

"Proposed Imaging of the Ultrafast Electronic Motion in Samples using X-ray Phase Contrast", *Phys. Rev. Lett.* 110, 137403 (2013).

References

- F. Krausz and M. Ivanov, "Attosecond physics", *Rev. Mod. Phys.* 81, 163-234 (2009).
- A. Stolow, "The three pillars of photo initiated quantum dynamics", *Faraday Discuss* 163, 9-32 (2013).
- G. Dixit, O. Vendrell, and R. Santra, "Imaging electronic quantum motion with light", *Proc. Nat. Acad. Sci. U.S.A.* 109, 11636-11640 (2012).

Ultra efficient ionization.

Free-Electron Laser pulses create extremely highly charged xenon ions

X-ray Free-Electron Lasers produce unprecedentedly strong X-ray pulses that provide unique opportunities for studying ultrafast dynamics during chemical reactions and for imaging the structure of complex systems such as viruses and nanocrystals. Understanding the response of individual atoms to such intense X-rays is essential for most Free-Electron Laser applications. We studied the ionization of xenon atoms by intense 1.5 and 2 keV X-ray pulses and found that many more electrons could be stripped away by these pulses than existing theories had predicted.

The successful operation of the first VUV and X-ray free-electron lasers FLASH at DESY and LCLS at the SLAC National Accelerator Laboratory has sparked research activities by a broad scientific community ranging from physics, chemistry and material sciences to biology and medicine. Triggered by the demonstration of femtosecond coherent imaging of protein nanocrystals [1] and single viruses [2], radiation damage processes induced by the intense X-ray pulses have received considerable attention because they ultimately set the resolution limits for this potentially ground-breaking technique.

At the atomic level, radiation damage is typically induced by direct photo-ionization and Auger decay, both of which can lead to further secondary damage processes. Substantial theoretical and experimental efforts have therefore been devoted to studying, in detail, the photo-ionization of single atoms and molecules by intense Free-Electron Laser pulses. Early experiments at FLASH showed that more than fifty VUV photons can be combined to strip 21 electrons from a xenon atom [3], triggering an ongoing theoretical discussion of the possible mechanisms for this surprisingly high level of ionization. First experiments in the X-ray domain at LCLS found that for light elements such as neon and molecular nitrogen (N_2), the absorption of multiple X-ray photons within a single, ultra-short X-ray pulse proceeds mainly sequentially and is in good agreement with the corresponding theoretical predictions [4, 5]. In this case, the highest charge state produced is defined by the last ionic state that can be ionized directly with one photon.

In contrast to this, our X-ray experiment on the heavy element xenon has found an unprecedentedly high degree of ionization to charge states up to Xe^{36+} (see Fig. 1), which have ionization potentials far exceeding the photon energy. This is the highest ionization state ever created in an atom with a single electromagnetic pulse (that is, both by photo-absorption and by ion impact), and it is in striking disagreement with state-of-the-art calculations of sequential photo-absorption shown in Fig. 1(b). While our calculations are in good agreement with the experimental findings at 2.0 keV photon energy, they strongly underestimate

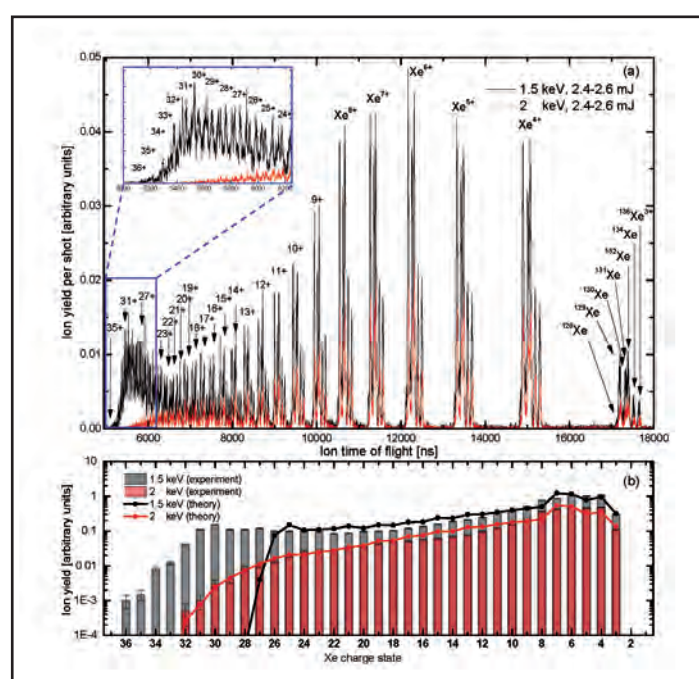


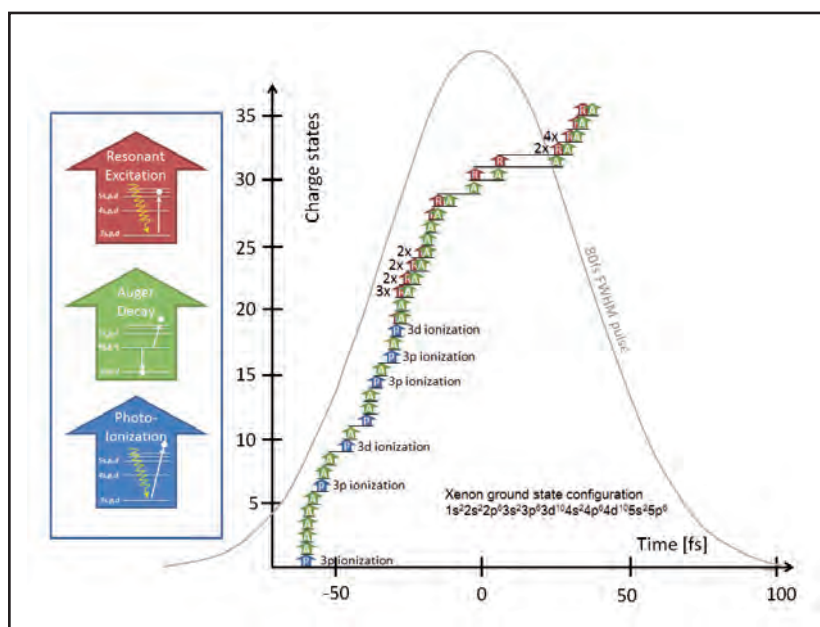
Figure 1 Comparison of experimental and simulated xenon charge state yields. (a) Xenon ion time-of-flight spectra recorded at photon energies of 1.5 keV (black) and 2.0 keV (red) for nominally 80 fs Free-Electron Laser pulses. The inset shows a zoom of the region containing the highest charge states. (b) Experimental xenon charge state distribution (bars) compared to theory (circles with lines) calculated for the experimental parameters given above.

the ionization at 1.5 keV, where the total absorbed energy per atom is more than twice higher than theoretically expected.

In order to explain the occurrence of these surprisingly high charge states at 1.5 keV photon energy, we proposed an ultra efficient, resonance enabled X-ray multiple ionization (REXMI) mechanism, where transient resonances in highly charged ions created during the X-ray pulse enable further photo-absorption beyond the sequential direct ionization limit. As the binding energy of the xenon M shell electrons surpasses the photon energy with

Figure 2

Diagram of an exemplary pathway leading to Xe^{36+} : X-rays with a photon energy of 1.5 keV primarily photo-ionize xenon 3p- and 3d-shell electrons (P, blue arrows), followed by a cascade of Auger decays (A, green arrows). Each of these processes increases the charge state of the xenon ion (vertical axis) by one. Within an ultra-intense 80 femtosecond (FWHM) X-ray pulse (pulse profile shown in grey), a sequence of photo-ionizations and Auger decays quickly lead to charge state Xe^{19+} , where the first resonant excitation (R, red arrows) occurs in the exemplary pathway shown here. The resonant excitations themselves do not increase the charge state but they are followed by Auger decays which do increase the charge state. In some instances, several excitations happen at a single charge state before an Auger decay occurs.



increasing ionic charge, direct single photon ionization from this shell is no longer possible. However, the M shell electrons can still be resonantly excited into densely spaced Rydberg states and unoccupied valence orbitals, and these highly excited states can then be further ionized via Auger decay and other auto-ionizing transitions to the extremely high charge states that are observed experimentally as shown schematically in Fig.2. Our hypothesis is confirmed by X-ray fluorescence measurements, which we performed simultaneously to the ion time-of-flight spectroscopy and which clearly show the presence of core-holes in the xenon 3p shell in highly charged xenon ions, which have a 3p binding energy well beyond the available photon energy. We have also observed similar resonance enhanced ionization in krypton atoms [6] as well as in iodomethane and iodine monochloride molecules, and predict this to be a general mechanism

for multiple ionization of heavy elements induced by intense, short pulse X-rays.

The strong resonant increase in X-ray absorption due to the REXMI mechanism dramatically increases the energy deposition in the target and may be used to efficiently create highly excited, dense plasmas of heavy atoms, e.g. from clusters or condensed matter systems. For imaging applications, the photon energy ranges where REXMI plays a significant role should be avoided in order to avoid increased radiation damage. Alternatively, a narrow band X-ray source (such as a seeded FEL) may be used to reduce the effect because fewer of the densely spaced resonances can be excited.

Contact: Daniel Rolles, daniel.rolles@desy.de

Authors

Benedikt Rudek^{1,2,18}, Sang-Kil Son³, Lutz Foucar^{1,4}, Sascha W. Epp^{1,2,12}, Benjamin Erk^{1,2,12}, Robert Hartmann⁵, Marcus Adolph⁶, Robert Andritschke⁷, Andrew Aquila^{3,8}, Nora Berrah⁸, Christoph Bostedt⁹, John Bozek⁹, Nicola Coppola^{3,8}, Frank Filsinger¹⁰, Hubert Gorke¹¹, Tais Gorkhovec⁶, Heinz Graafsma¹², Lars Gumprecht³, Andreas Hartmann⁵, Günter Hauser^{7,13}, Sven Herrmann⁷, Helmut Hirssemann¹², Peter Holl⁵, André Hömke^{1,2}, Loïc Journé^{1,4}, Christian Kaiser², Nils Kimmel¹³, Faton Krasniqi^{1,4}, Kai-Uwe Kühnel², Michael Matysek¹⁵, Marc Messerschmidt⁹, Danilo Miesner⁷, Thomas Möller⁶, Robert Moshhammer^{1,2}, Kiyonobu Nagaya¹⁶, Björn Nilsson¹², Guillaume Potdevin¹², Daniel Pietschner¹³, Christian Reich⁵, Daniela Rupp⁶, Gerhard Schaller⁷, Ilme Schlichting^{1,4}, Carlo Schmidt^{1,2}, Florian Schopper⁷, Sebastian Schorb^{6,9}, Claus-Dieter Schröter², Joachim Schulz^{3,8}, Marc Simon¹⁴, Heike Soltau⁵, Lothar Strüder^{1,13}, Kiyoshi Ueda¹⁷, Georg Weidenspointner^{7,13}, Robin Santra^{3,15}, Joachim Ullrich^{1,2,18}, Artem Rudenko^{1,2,19}, and Daniel Rolles^{1,4,12}

1. Max-Planck Advanced Study Group at Center for Free-Electron Laser Science (CFEL), D-22607 Hamburg, Germany
2. Max-Planck-Institut für Kernphysik, D-69117 Heidelberg, Germany
3. CFEL, DESY, D-22607 Hamburg, Germany
4. Max-Planck-Institut für medizinische Forschung, D-69120 Heidelberg, Germany
5. PNSensor GmbH, D-81739 München, Germany
6. Institut für Optik und Atomare Physik, Technische Universität Berlin, D-10623 Berlin, Germany
7. Max-Planck-Institut für extraterrestrische Physik, D-85741 Garching, Germany
8. Western Michigan University, Physics Department, Kalamazoo, Michigan 49008, USA
9. Linac Coherent Light Source, Stanford Linear Accelerator Center (SLAC) National Accelerator Laboratory, Menlo Park, California 94025, USA
10. Fritz-Haber-Institut der Max-Planck-Gesellschaft, D-14195 Berlin, Germany
11. Forschungszentrum Jülich, Institut Zentrallabor für Elektronik (ZEL), D-52428 Jülich, Germany
12. Deutsches Elektronen-Synchrotron DESY, D-22607 Hamburg, Germany
13. Max-Planck-Institut Halbleiterlabor, D-81739 München, Germany
14. Laboratoire de Chimie Physique-Matière et Rayonnement, Université Pierre et Marie Curie

and Centre national de la recherche scientifique (CNRS), Unité Mixte de Recherche (UMR) 7614, F-75231 Paris Cedex 05, France

15. Universität Hamburg, D-20355 Hamburg, Germany

16. Kyoto University, Kyoto 606-8501, Japan

17. Tohoku University, Sendai 980-8577, Japan

18. Physikalisch-Technische Bundesanstalt, D-38116 Braunschweig, Germany

19. J.R. Macdonald Laboratory, Department of Physics, Kansas State University, Manhattan, Kansas 66506, USA

Present address: European X-ray Free-Electron Laser (XFEL) GmbH, D-22761 Hamburg, Germany

Original publication

“Ultra-efficient ionization of heavy atoms by intense X-ray free-electron laser pulses”, *Nature Photonics* **6**, 858–865 (2012).

References

1. H. N. Chapman et al., “Femtosecond X-ray protein nanocrystallography”, *Nature* **470**, 73–77 (2011).
2. M. M. Seibert et al., “Single mimivirus particles intercepted and imaged with an X-ray laser”, *Nature* **470**, 78–81 (2011).
3. A. A. Sorokin et al., “Photoelectric Effect at Ultrahigh Intensities”, *Phys. Rev. Lett.* **99**, 213002 (2007).
4. L. Young et al., “Femtosecond electronic response of atoms to ultra-intense X-rays”, *Nature* **466**, 56–61 (2010).
5. M. Hoener et al., “Ultraintense X-ray induced ionization, dissociation and frustrated absorption in molecular nitrogen”, *Phys. Rev. Lett.* **104**, 253001 (2010).
6. B. Rudek et al., “Resonance-enhanced multiple ionization of krypton at an x-ray free-electron laser”, *Phys. Rev. A* **87**, 023413 (2013).

From gold atoms to gold layers.

Real-time study of gold cluster growth during sputter deposition

The tuning of size dependent catalytic, electrical and optical properties of gold cluster assemblies is a very significant issue in modern applied nanotechnology. We present a real-time investigation of the growth kinetics of gold nanostructures from small nuclei to a complete gold layer during sputter deposition with high time resolution. We specify a four stage growth including the thresholds with sub-monolayer resolution and identify phase transitions. Our study allows for deducing the wetting behaviour of gold cluster films on solid substrates and provides a better understanding of the growth kinetics in general, which is essential for optimization of manufacturing parameters, saving energy and resources.

The remarkable manifold properties of gold cluster assemblies are of great interest for fundamental research and promising various potential applications in solar cells, biosensors, anti-reflective coatings and especially in heterogeneous catalysis [1, 2]. The adjustment of the size dependent catalytic, electrical and optical properties of gold cluster assemblies is therefore a very significant topic in modern applied nanotechnology. For an efficient and controlled production of such active nanostructured gold cluster surfaces, the sputter deposition process plays an important role [3]. In order to elucidate and characterize the self-organisation during nanocluster film formation, it is mandatory to control and therefore to understand how the growth kinetics influences the cluster film morphology during sputter deposition [4, 5].

The first real-time investigations of the growth kinetics of gold nanoclusters into a gold layer are enabled by combining sputter deposition and surface sensitive X-ray scattering (μ GISAXS). The scheme in Fig. 1 shows the main characteristics of the experimental setup performed at the PETRA III beamline P03 [6]. High frame-rate two-dimensional X-ray detectors in combination with the high photon flux of micro beam spot size, available at the P03 beamline, enables a non-invasive *in situ* and real-time investigation of gold growth kinetics during sputter deposition. With an acquisition throughput of 67 frames per second, we were able to produce kinetic growth movies of the fast surface processes in reciprocal space and on the nanoscale. The high time resolution in the 10 millisecond regime allows the precise determination of kinetics of initial nucleation and subsequent cluster growth during sputter deposition of gold on an amorphous silicon oxide layer.

We were able to identify four different stages of growth including their thresholds with sub-monolayer resolution and concomitant phase transitions. Each stage can be characterized by a predominant surface process and its intrinsic kinetics: nucleation, diffusion, adsorption and grain growth. Moreover we introduced

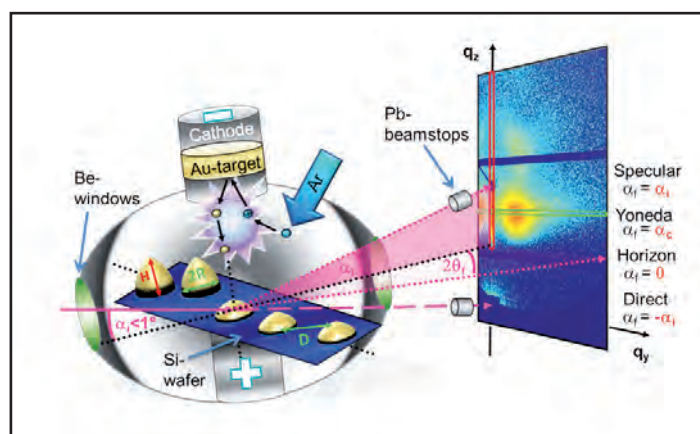


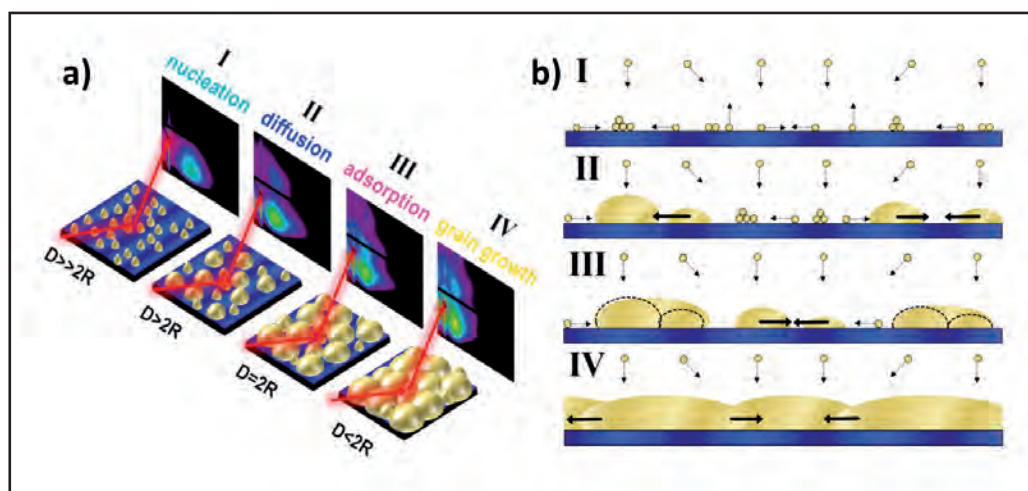
Figure 1

Scheme of the sputter chamber in a microbeam grazing incidence small-angle X-ray scattering (μ GISAXS) setup: At low argon pressure, a voltage is applied to two parallel electrodes resulting in a plasma discharge. The accelerated gas ions impinge onto the cathode (target), gold atoms are emitted and deposited on the Si-wafer leading to cluster formation and growth. During this process, a microfocussed X-ray beam under grazing incident angle α_i scatters by any type of electron contrast variation in the near surface regime. α_i denotes the exit angle, α_c the critical angle and $2\theta_i$ the out-of-plane angle. The direct beam position marks the origin of coordinates of the scattering vector components q_y and q_z . Line cuts were performed on the detected 2D data to extract information on the gold cluster morphology (H = height, R = radius, D = distance) and growth kinetics: a vertical cut along the scattering plane (red) (q_z at $q_y = 0$) and horizontal cuts (green) (q_y at $\alpha_f = \alpha_c$).

a new and flexible geometrical model to extract morphological real space parameters, such as cluster size and shape, correlation distance, layer porosity and surface coverage directly from the reciprocal space scattering data. The model allowed simulating, visualizing and interpreting gold nanocluster growth kinetics in terms of nanoscopic processes. Furthermore, we were able to deduce the wetting angle and the onset of long range connectivity during the deposition process.

Figure 2

(a) Evolution of the scattering patterns and model based morphological parameters (D = distance; R = radius) of gold clusters during sputter deposition in four growth stages: (I) nucleation; (II) diffusion mediated coalescence ($D > 2R$); (III) adsorption mediated cluster growth until percolation threshold ($D = 2R$) and subsequent grain growth (IV) ($D < 2R$). (b) Side view scheme of each growth stage showing the predominant processes. The black arrows indicate the movement of atoms, clusters and grain boundaries.



This approach is a prerequisite for future investigations of the influence of different process parameters on the thin metal film morphology such as surface temperature, deposition rates, catalysis, and optical response. In particular, the traceability of the wetting behaviour and contact angle in the nanoscale regime is a novel concept and important for sputter deposition on polymeric and functionalized surfaces [3-5].

Fig. 2 gives an overview of the temporal evolution of the scattering patterns, the deduced thin film morphology and the four dominant growth stages:

I) Nucleation: Stable nuclei are formed by triple atom collisions and can adsorb diffusing atoms on the surface leading to cluster growth. The rapidly increasing surface coverage promotes an increase of the adsorption probability and consequently a decrease in the nucleation probability.

II) Diffusion: Above the nucleation threshold, the cluster growth is dominated by diffusion controlled merging of small mobile clusters. This so-called coalescence strongly depends on the cluster size, because with increasing size the surface mobility becomes more restricted and fusion of two larger clusters becomes more time consuming.

III) Adsorption: At the diffusion threshold, the clusters mobility

is significantly limited and the probability of direct adsorption from the gaseous phase further increases. Henceforth, the predominating process changes to an adsorption driven growth of immobilized clusters.

IV) Grain growth: At the percolation threshold, the mean cluster distance equals the average diameter leading to a fractal-like cluster with high degree of long range connectivity. Surface mobility is now totally restricted resulting in a grain growth process by a discontinuous movement of cluster boundaries. At a film thickness of 9 nm the surface is fully covered and a porous gold layer grows preferentially in vertical direction due to lateral spatial limitations.

These findings help to efficiently control manufacturing of gold cluster films in multidisciplinary fields ranging from photovoltaic applications, heterogeneous catalysts to semiconductor industry and in general in all nano- and surface-related science. This in turn prevents wasting energy and such unique resources as gold, which is of broad appeal, world wide and ever growing environmental interest.

Contact: Matthias Schwartzkopf, Matthias.Schwartzkopf@desy.de
Stephan V. Roth, Stephan.Roth@desy.de

Authors

Matthias Schwartzkopf^{1,2}, Adeline Buffet¹, Volker Körstgens³, Ezzeldin Metwalli³, Kai Schlage¹, Gunthard Benecke^{1,4}, Jan Perlich¹, Monika Rawolle³, André Rothkirch¹, Berit Heidmann¹, Gerd Herzog¹, Peter Müller-Buschbaum³, Ralf Röhlsberger¹, Rainer Gehrke¹, Norbert Striebeck² and Stephan V. Roth¹

1. Deutsches Elektronen-Synchrotron DESY, Notkestr. 85, D-22607 Hamburg, Germany
2. Universität Hamburg, Institut für Technische und Makromolekulare Chemie, Bundesstr. 45, D-20146 Hamburg, Germany
3. TU München, Physik Department, Lehrstuhl für Funktionelle Materialien, James-Frank-Str. 1, D-85747 Garching, Germany
4. MPIKG, Department of Biomaterials, Am Mühlenberg 1, D-14424 Potsdam-Golm, Germany

Original publication

“From Atoms to Layers: *In Situ* Gold Cluster Growth Kinetics during Sputter Deposition”, *Nanoscale* 5, 5053-5062 (2013).

References

1. P. Pyykkö, “Theoretical Chemistry of Gold”, *Angew. Chemie, Int. Ed.* 116, 4512–4557 (2004)
2. G. Bauer, J. Hassmann, H. Walter, J. Haglmüller, C. Mayer, T. Schalkhammer, “Resonant Nanocluster Technology—from Optical Coding and High Quality Security Features to Biochips”, *Nanotechnology* 14, 1289–1311 (2003).
3. F. Faupel, V. Zaporozhchenko, T. Strunskus, M. Elbahri, “Metal-Polymer Nanocomposites for Functional Applications”, *Adv. Eng. Mater.* 12, 1177–1190 (2010).
4. G. Kaune, M. A. Ruderer, E. Metwalli, W. Wang, S. Couet, K. Schlage, R. Röhlsberger, S. V. Roth, P. Müller-Buschbaum, “*In Situ* GISAXS Study of Gold Film Growth on Conducting Polymer Films”, *ACS Appl. Mater. Interfaces* 1, 353–360 (2009).
5. S. Yu, G. Santoro, K. Sarkar, B. Dicke, P. Wessels, S. Bommel, R. Döhrmann, J. Perlich, M. Kuhlmann, E. Metwalli, “Formation of Al Nanostructures on Alq3: An *in Situ* Grazing Incidence Small Angle X-Ray Scattering Study During RF Sputter Deposition”, *J. Phys. Chem. Lett.* 4, 3170–3175 (2013).
6. A. Buffet, A. Rothkirch, R. Döhrmann, V. Körstgens, M. M. Abul Kashem, J. Perlich, G. Herzog, M. Schwartzkopf, R. Gehrke, P. Müller-Buschbaum et al. “P03, the Microfocus and Nanofocus X-Ray Scattering (MiNaXS) Beamline of the PETRA III Storage Ring: The Microfocus Endstation”, *J. Synchrotron Radiat.* 19, 647–653 (2012).

At liquid boundaries a crystal is born.

In situ X-ray studies of crystal nucleation at the liquid–liquid interface

Paints, milk and mayonnaise – mixtures of immiscible liquids are part of our everyday life. Additionally, liquid–liquid interfaces offer exciting opportunities for material synthesis. To investigate these processes on an atomic level we use *in situ* X-ray surface scattering methods to achieve the first observation of the birth process of a crystal at the fluidic interface. In studies at PETRA III of liquid mercury in contact with a salt solution containing fluorine, bromine and lead ions we found that a nanometre thin crystalline layer forms at the interface, consisting of an atomic layer of fluorine sandwiched between two layers of lead and bromine. This layer then directs the growth of larger PbFBr crystals perfectly aligned on top of this interfacial nano-scale layer.

Liquid–liquid interfaces offer many distinct advantages for material synthesis [1]. They provide soft, smooth, defect- and stress-free interfaces at which the growth of materials can occur in a very controlled way. Consequently, many chemical processes for producing materials and nano-particles employing growth at liquid interfaces have been explored in the last few years. For example, an extremely energy efficient electrochemical deposition process for manufacturing semiconductor germanium at room-temperature from an aqueous germanium oxide solution on liquid mercury has recently been reported [2]. Yet, being inaccessible to most experimental techniques, the atomic-scale structure of liquid–liquid interfaces is almost completely unknown. To date, the understanding of the syntheses at these interfaces relies almost exclusively on *ex situ* studies of post-deposition products, severely hampering development of the underlying phase formation processes.

For *in situ* studies of such interface processes with atomic resolution we have developed in the last years the LISA liquid interface diffractometer at the PETRA III beamline P08 [3, 4], which allows detailed surface scattering studies of liquid–liquid interfaces while the sample remains stationary, providing utmost mechanical stability. Using this instrument as well as a liquid diffractometer at the Advanced Photon Source (Argonne, USA) beamline 9ID we investigated the initial stages of crystal growth at model Hg–electrolyte interfaces. We used a NaF base electrolyte containing Pb^{2+} and Br^- ions and controlled the phase formation reaction electrochemically via a Faradaic reaction. Pb amalgamates into Hg at potentials ≤ 0.70 V, whereas at more positive potentials the amalgamated lead is released into the electrolyte. The potential-dependent variations in the structure of the Hg–electrolyte interface were studied by X-ray reflectivity (XR) measurements (Fig. 1).

During Pb amalgamation the interface structure is identical to that in Pb-free electrolyte. However, drastic changes are observed in the measured XR curves as the potential increases into the dealumination regime. Although the quasi-Bragg

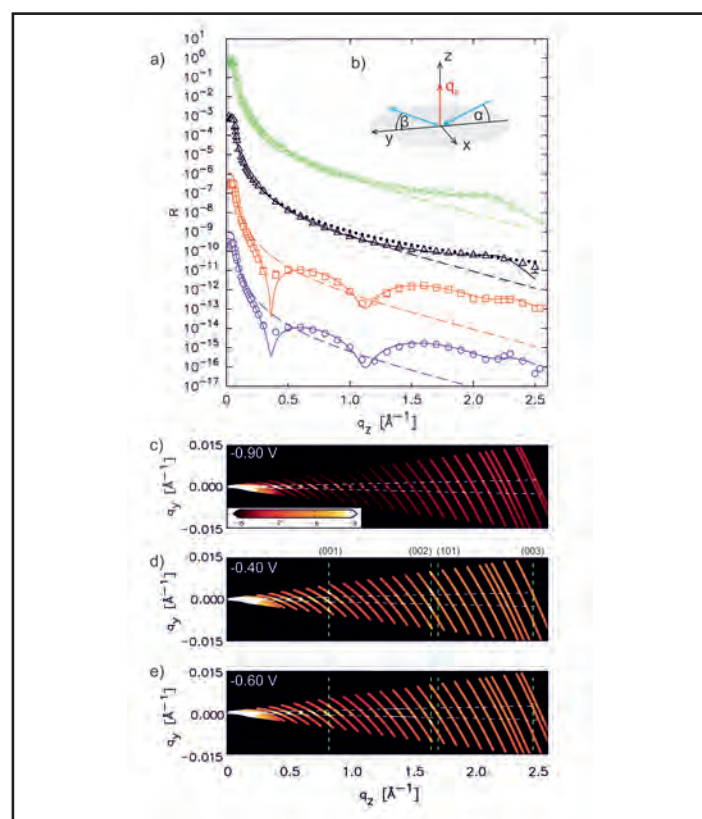


Figure 1

Reflectivity curves at different potentials for liquid Hg in a NaF + NaBr + PbBr₂ solution. a) Measured reflectivity curves at -0.90 V (black triangles), -0.60 V (red squares), and -0.40 V (blue circles). For comparison a reflectivity curve measured at the Hg– 0.01 M NaF interface at -0.90 V is shown (green circles). Solid lines correspond to the best fits by the models, the dotted line to R_p , and the dashed lines to the reflectivity of an interface with a Gaussian roughness of $\sigma = 1.00$ Å. b) Schematic experimental geometry. c–e) Corresponding full intensity maps. Each solid line corresponds to a 1D detector frame at a specific angle where the centre of each line corresponds to $\alpha = \beta$ and the colour indicates the scattered intensity in logarithmic units. Horizontal white dashed lines indicate the angular range used in determining the reflectivity curves in a) and vertical green dashed lines mark the q_z positions of the 3D crystallites' diffraction peaks (bright spots in this figure).

peak due to Hg atomic layering still persists [5], pronounced modulations appear in the reflectivity (Fig. 1a, red squares and blue circles). These indicate significant structural changes at the interface, specifically the presence of a well-defined interfacial adlayer [6]. The modulations' period yields an estimated adlayer thickness of 7.8 Å. The intensity at the modulations' maxima ($q_z \approx 0.8$ and 1.6 \AA^{-1}) exceeds tenfold that measured at -0.90 V and even the Fresnel reflectivity of a perfect interface. These data can only be rationalized by an adlayer with an electron density which significantly exceeds that of the electrolyte and consists of several atomic layers. Quantitative analysis and modelling reveals that this layer corresponds to a one-unit-cell-thick PbFBr film composed of a stack of 5 ionic layers (Fig. 2).

Accompanying these changes in the reflectivity, Bragg-reflections also emerge. These appear in the 1-dimensional detector data, which records the intensity distribution along a varying-length arc in the (q_y , q_z) plane at each XR point (shown in Fig. 1 c–e). The sharp, intense diffraction peaks imply the presence of 3D crystallites at the interface in addition to the adlayer. This has been confirmed in grazing incidence scattering measurements. The diffraction peaks observed indicate the formation of a highly ordered PbFBr phase with sharply-defined orientation of the c-axis along the surface normal of the interface. This process may be viewed as a controlled precipitation, where the electrochemical dealumination reaction increases the Pb^{2+} concentration near the surface, promoting formation of the solid adlayer.

Macroscopic data on similar systems, obtained in previous electrochemical studies, suggest high surface excess concentrations of these species, from which the presence of a close-packed, vertically ordered stack of PbBr_2 layer at the interface was argued [7, 8]. However, rather than merely verifying these predictions our experiments reveal much more complex phenomena, specifically the formation of an ultrathin precursor layer that acts as a template for subsequent growth of highly aligned 3D crystalline deposits – a behaviour which may help to explain previous indirect observations for quasi epitaxial growth at liquid–

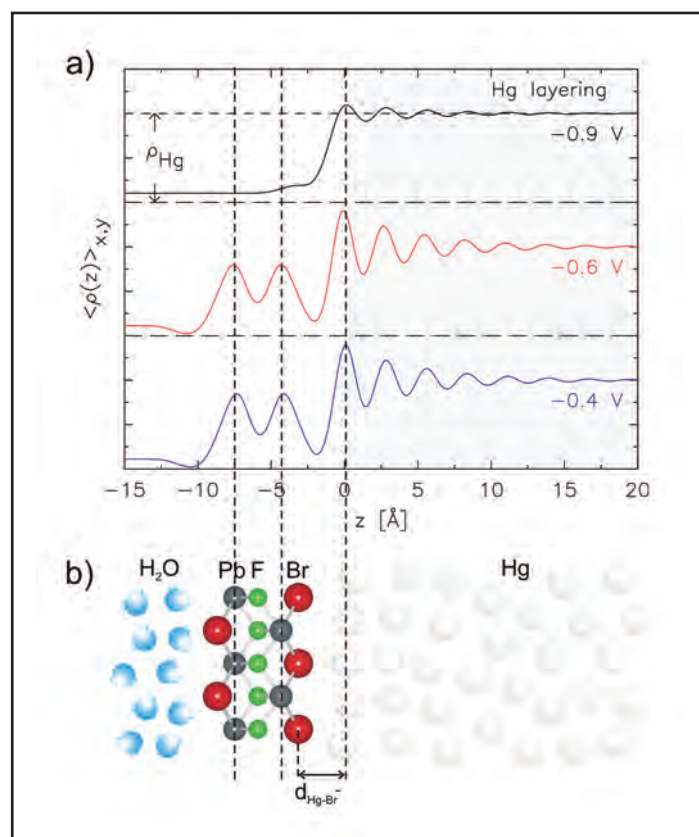


Figure 2

a) Electron density profiles for different potentials, corresponding to the best fits to the reflectivity data shown in Fig. 1a. b) Schematic structural model of the PbFBr adlayer. Dashed lines indicate the positions of the two sheets of Pb ions and the topmost Hg layer.

liquid interfaces. In order to achieve this, a better understanding on the atomic scale is required. This work is a first step in this direction.

Contact: Bridget Murphy, murphy@physik.uni-kiel.de

Authors

Annika Elsen¹, Sven Festersen¹, Benjamin Runge¹, Christian T. Koops¹, Benjamin M. Ocko², Moshe Deutsch³, Oliver H. Seeck⁴, Bridget M. Murphy^{1,5} and Olaf M. Magnussen^{1,5}

1. Institute for Experimental and Applied Physics, Christian-Albrechts-University Kiel, D-24098 Kiel, Germany
2. Condensed Matter Physics and Materials Science Department, Brookhaven National Laboratory, Upton, NY 11973
3. Physics Department, and Institute of Nanotechnology and Advanced Materials, Bar-Ilan University, Ramat-Gan 52900, Israel

Original publication

"In situ x-ray studies of adlayer-induced crystal nucleation at the liquid-liquid interface" *Proc. Nat. Acad. Sci.* **110**, 6663–6668 (2013)

Online at: www.pnas.org/cgi/doi/10.1073/pnas.1301800110

References

1. R. Krishnaswamy, A. K. Sood, "Growth, self-assembly and dynamics of nano-scale films at fluid interfaces", *J. Mater. Chem.* **20**, 3539–3552 (2010).
2. A. I. Carim, S. M. Collins, J. M. Foley, S. Maldonado, "Benchtop electrochemical liquid-liquid-solid growth of nanostructured crystalline germanium", *J. Am. Chem. Soc.* **133**, 13292–13295 (2011).

3. O. H. Seeck, C. Deiter, K. Pflaum, F. Bertram, A. Beerlink, H. Franz, J. Horbach, H. Schulte-Schrepping, B. M. Murphy, M. Greve and O. Magnussen, "The high-resolution diffraction beamline P08 at PETRA III", *J. Synchrotron Radiat.* **19**, 30–38 (2012).
4. B. M. Murphy, M. Greve, B. Runge, C. T. Koops, A. Elsen, J. Stettner, O. H. Seeck and O. M. Magnussen, "A novel X-ray diffractometer for studies of liquid-liquid interfaces", *J. Synchrotron Radiat.* in print (2013).
5. A. Elsen, B. M. Murphy, B. M. Ocko, L. Tamam, M. Deutsch, I. Kumenko and O. M. Magnussen, "Surface layering at the Mercury-electrolyte Interface", *Phys. Rev. Lett.* **104**:105501 (2010).
6. P. S. Pershan, M. L. Schlossman, "Liquid Surfaces and Interfaces: Synchrotron X-Ray Methods", Cambridge Univ Press, Cambridge, UK (2012).
7. H. B. Herman, R. L. McNeely, P. Surana, C. M. Elliott, R. W. Murray, "Surface solubility and reaction inhibition in lead bromide and iodide adsorbed on mercury electrodes", *Anal. Chem.* **46**, 1258–1265 (1974).
8. M. Lovrić, S. Komorsky-Lovrić, "Adsorption of PbBr_2 complex on mercury electrodes", *Langmuir* **11**, 1784–1790 (1995).

Taming electrons at heterointerfaces.

Electric field effect in $\text{LaAlO}_3/\text{SrTiO}_3$ heterostructures

Mobile electrons are confined at the interface between SrTiO_3 and a LaAlO_3 layer with a thickness of only a few unit cells. With infrared ellipsometry, X-ray diffraction, and resistance measurements we have investigated the electric field induced effects on the confined electrons at the $\text{LaAlO}_3/\text{SrTiO}_3$ heterostructure interface. We have found evidence that the charge carrier localization at negative gate voltage is enhanced, or even induced, by a polar phase transition that takes place in SrTiO_3 close to the heterointerface. This phase transition reduces the polarizability of the lattice and subsequently the screening of defects at the interface. We have shown that the charge localization and the polar order appear below $T \approx 50$ K and both phenomena exhibit a similar unipolar hysteretic behaviour as function of the applied gate voltage.

In the last years, the particular properties of the mobile charge carriers at the interface between insulating SrTiO_3 (STO) and thin (insulating) LaAlO_3 (LAO) layers with a thickness of $n \geq 4$ unit cells have been thoroughly investigated [1, 2]. The conductivity of these interfacial charge carriers can be modified by an applied gate voltage, V_g , and even insulating samples with $n = 3$ can be switched into a metallic state with moderate gate voltages [2]. A superconducting phase of the charge carriers has also been observed at very low temperatures of $T_c \leq 0.4$ K. This superconducting state can be suppressed by an external gate voltage which results in a localized state of the charge carriers at negative bias [3]. The mechanism by which the electric field leads to the confined state is still under discussion. Our infrared ellipsometry measurements together with X-ray diffraction experiments and resistance measurements suggest that a polar phase transition in the STO close to the heterointerface plays an important role.

Metallic LAO/STO heterostructures with $n = 4.5$ have been prepared by pulsed laser deposition of LAO on TiO_2 -terminated STO substrates as explained in [2]. The structure of the samples, i.e. the contact arrangement and the polarity of the applied gate voltage, is shown in Fig. 1(a). Ellipsometry spectra of the LAO/STO sample have been obtained at $T = 10$ K and at different V_g . The spectra are displayed in Fig. 2(a) in terms of the real part of the optical conductivity, σ_1 . The measurements reveal that a splitting of the STO phonon mode centred at 438 cm^{-1} occurs as the gate voltage is swept from positive towards negative gate voltages. This phonon involves a rotation of the oxygen octahedra (see Fig. 1(b)) that is modulated by the long-wavelength infrared radiation. Figure 2(b) shows that the mode splitting as function of V_g exhibits an unipolar and hysteretic behaviour. The splitting starts to develop at $V_g \approx +50$ V as V_g is swept from +250 V towards -250 V. In Fig. 2(d), we show the temperature dependence of the phonon mode splitting at $V_g = -150$ V by the open circles. It is important to note that the presence of the remanent phonon peak at 438 cm^{-1} even at $V_g = -250$ V indicates that not the whole

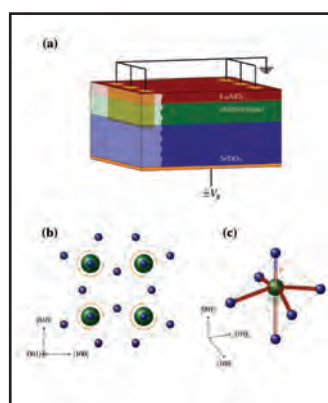


Figure 1

(a) Sketch of the LAO/STO structure and electrodes used to apply the gate voltages. (b) Antiphase rotation of the oxygen octahedral in STO which give rise to the 438 cm^{-1} phonon mode. (c) Polar displacement of the Ti ion in the STO unit cell showing the effect of the bond length change.

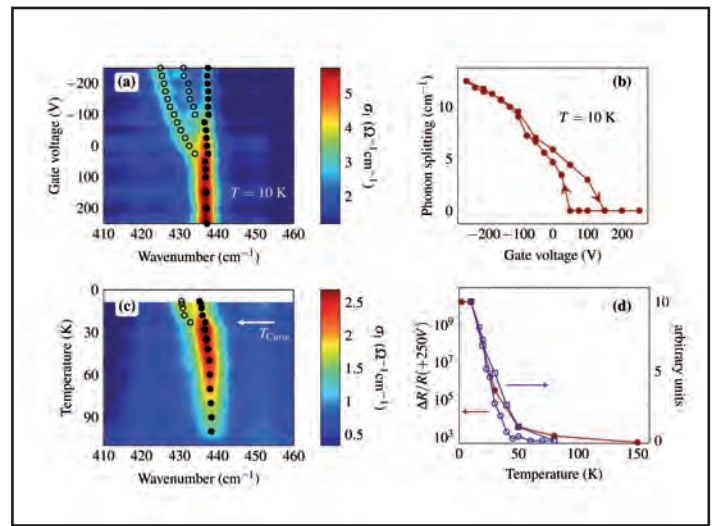
STO substrate undergoes a structural transition. This allows us to estimate the thickness of the distorted layer to be on the order of $1 \mu\text{m}$ at $V_g = -250$ V.

A corresponding splitting of the 438 cm^{-1} phonon mode has been observed in ferroelectric $\text{SrTi}^{18}\text{O}_3$ crystals where ^{16}O has been exchanged with the heavier ^{18}O isotope. These samples become ferroelectric at $T_{\text{Curie}} \approx 25$ K [4] and the phonon splitting appears below T_{Curie} as shown in Fig. 2(c). The softening of the phonon in the polar phase can be understood in terms of the polar off-centre displacement of the Ti cation as it is schematically shown in Fig. 1(c). The length change of the Ti-O bonds results in an anisotropic softening of the bonds shown in red. This leads to the observed splitting of the phonon in the ferroelectric state of $\text{SrTi}^{18}\text{O}_3$ and for the LAO/STO heterostructures at negative bias.

In Fig. 3, we show k -space maps of the (002) Bragg reflection of the STO substrate at different gate voltages and temperatures. These k -space maps have been measured at the PETRA III/P09 beamline and show that the main (002) reflection is not influenced by the application of $V_g = -250$ V. However, additional satellite reflections appear symmetrically to the main Bragg reflection along the $[110]_c$ direction parallel to the heterointerface. Their spacing of $\Delta Q = 0.0063$ reciprocal lattice units (rlu) corresponds

Figure 2

(a) Contour plot of the ellipsometry spectra at 10 K showing the voltage induced splitting of the 438 cm^{-1} phonon mode of STO. (b) Hysteretic voltage dependence of the splitting of the phonon mode at 10 K. (c) Ellipsometry spectra of $\text{SrTi}^{18}\text{O}_3$ showing the splitting of the 438 cm^{-1} phonon in the ferroelectric phase below T_{Curie} . (d) Comparison of the temperature dependence of the phonon splitting at $V_g = -150\text{ V}$ (open circles), the satellite Bragg reflex intensity at $V_g = -250\text{ V}$ (open squares), and the increase of the sample resistance (full squares) of the LAO/STO heterostructure.



to a long range modulation period of $\approx 60\text{ nm}$. Similar superlattice peaks have previously been observed in ferroelectric thin films due to the formation of alternating antiphase stripe domains [5, 6]. In the case of the LAO/STO heterostructures,

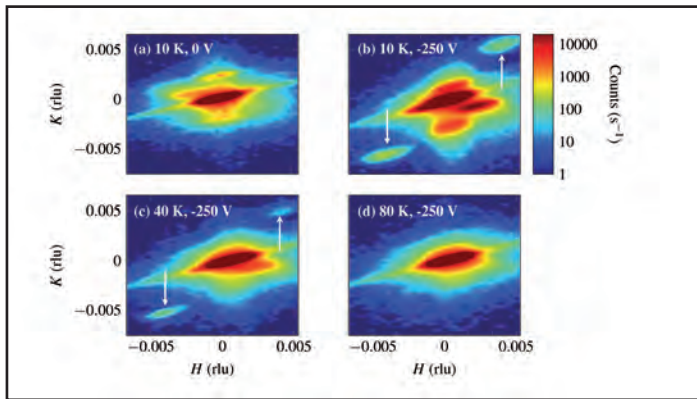


Figure 3

Field induced satellite Bragg reflections in the polar domain state of the LAO/STO heterostructure. (a) and (b), Gate voltage dependence of the k -space map of the (002) Bragg reflex of STO at 10 K. The arrows mark the appearance of two satellite reflections at $(\hbar k/2)$ and $(hk/2)$ with $h = 0.004$ and $k = 0.005$. (c) and (d), Temperature evolution of the satellite reflections at $V_g = -250\text{ V}$.

the satellite peaks likely arise from a modulation of the in-plane component of the tilted polarization or from a modulation of the amplitude of the normal component. In Fig. 2(d), we compare the normalized temperature dependence of the phonon splitting with the normalized intensity of the satellite peaks (blue open squares). Both features exhibit the same temperature dependence and disappear at temperatures above $T \approx 50\text{ K}$. The measurement of the sample resistance exhibits a unipolar and hysteretic behaviour as function of V_g , similarly to the phonon splitting shown before. In Fig. 2(d), we show that the normalized increase of the resistance (red, full symbols) as function of temperature starts below $T \approx 50\text{ K}$.

Our observations suggest that the electric field induced localization of the charge carriers in LAO/STO heterostructures is induced, or at least strongly enhanced, by a polar phase transition of the STO layer in the vicinity of the conducting interface. This field induced phase transition leads to a reduction of the dielectric constant and thus of the screening of defects that tend to localize the charge carriers.

Contact: Christian Bernhard, christian.bernhard@unifr.ch
Matthias Rössle, matthias.roessle@uni-potsdam.de

Authors

M. Rössle¹, K. W. Kim^{1,2}, A. Dubroka^{1,3}, P. Marsik¹, C. N. Wang¹, R. Jany⁴, C. Richter^{4,5}, J. Mannhart⁶, C. W. Schneider⁶, A. Frano^{5,7}, P. Wochner⁸, Y. Lu⁵, B. Keimer⁵, D. K. Shukla⁹, J. Strepfner⁹ and C. Bernhard¹

- University of Fribourg, Department of Physics and Fribourg Center for Nanomaterials, Chemin du Musée 3, CH-1700 Fribourg, Switzerland
- Department of Physics, Chungbuk National University, Cheongju 361-763, Korea
- Department of Condensed Matter Physics, Faculty of Science, Masaryk University and Central European Institute of Technology, Kotlářská 2, CZ-61137 Brno, Czech Republic
- Experimental Physics VI, Center for Electronic Correlations and Magnetism, Institute of Physics, University of Augsburg, D-86135 Augsburg, Germany
- Max-Planck-Institut für Festkörperforschung, Heisenbergstrasse 1, D-70569 Stuttgart, Germany
- Paul Scherrer Institut, CH-5232 Villigen, Switzerland
- Helmholtz-Zentrum Berlin für Materialien und Energie, Albert-Einstein-Strasse 15, D-12489 Berlin, Germany
- Max-Planck-Institut für Intelligente Systeme, Heisenbergstrasse 3, D-70569 Stuttgart, Germany
- Deutsches Elektronen-Synchrotron DESY, Notkestrasse 85, D-22603 Hamburg, Germany

Original publication

“Electric-Field-Induced Polar Order and Localization of the Confined Electrons in $\text{LaAlO}_3/\text{SrTiO}_3$ Heterostructures”, *Physical Review Letters* 110, 136805 (2013).

References

- A. Ohtomo, H. Y. Hwang, “A high-mobility electron gas at the $\text{LaAlO}_3/\text{SrTiO}_3$ heterointerface”, *Nature* 427, 423-426 (2004).
- S. Thiel, G. Hammerl, A. Schmehl, C. W. Schneider, J. Mannhart, “Tunable quasi-two-dimensional electron gases in oxide heterostructures”, *Science* 313, 1942-1945 (2006).
- A. Caviglia, S. Gariglio, N. Reyren, D. Jaccard, T. Schneider, M. Gabay, S. Thiel, G. Hammerl, J. Mannhart, J. M. Triscone, “Electric field control of the $\text{LaAlO}_3/\text{SrTiO}_3$ interface ground state”, *Nature* 456, 624-6247 (2008).
- M. Itoh, R. Wang, Y. Inaguma, T. Yamaguchi, Y.-J. Shan, T. Nakamura, “Ferroelectricity Induced by Oxygen Isotope Exchange in Strontium Titanate Perovskite” *Phys. Rev. Lett.*, 82, 3540-3543 (1999).
- S. K. Streiffer, J. A. Eastman, D. D. Fong, C. Thompson, A. Munkholm, M. V. Ramana Murty, O. Auciello, G. Bai, G. B. Stephenson, “Observation of Nanoscale 180° Stripe Domains in Ferroelectric PbTiO_3 Thin Films”, *Phys. Rev. Lett.* 89, 067601 (2002).
- D. D. Fong, G. B. Stephenson, S. K. Streiffer, J. A. Eastman, O. Auciello, P. H. Fuoss, C. Thompson, “Ferroelectricity in Ultrathin Perovskite Films”, *Science* 304, 1650-1653 (2004).

Insights in heterojunctions of operational organic electronic devices.

In situ characterization of a pentacene - C₆₀ ambipolar thin film transistor

Increasing the performance and efficiency of organic electronic devices such as ambipolar thin film transistors and organic solar cells requires the understanding and tailoring of interfaces. Although the structure and morphology of interfaces is subject to thorough studies, their impact on electronic processes has not been fully comprehended. Here, we utilize the tunability of charge carrier densities in field effect transistors to gain access to charging phenomena at organic interfaces. *In situ* measurements which track interface charging, here for the example of a pentacene - C₆₀ heterojunction, are complemented by grazing incidence X-ray scattering performed at the W1 beamline at DORIS III.

The energetic landscape at organic interfaces is complex due to a wealth of electrostatic phenomena such as charge transfer, dipole generation, and doping, all related to aspects of the molecular structure, e.g. molecular orientation, crystallinity, interdiffusion, and domain size.

The performance of electronic devices, however, also depends crucially on the balance of Debye length, depletion width, film thickness, and in particular the spatial location of trap states. Therefore, it is mandatory to track the changes of device characteristics with film thickness. The inherent lateral geometry of thin film transistors (TFTs) allows for the *in situ* acquisition of characteristic curves before and during semiconductor deposition [1]. Here we deposit an electron conducting semiconductor (C₆₀) on top of a fully developed p-channel TFT (pentacene) to observe the changes of the device characteristics due to the evolution of an additional n-channel.

In order to exclude structural or morphological changes within the organic films during deposition we performed structural analysis of the system using atomic force microscopy (AFM) and grazing incidence X-ray scattering (GIXS). The AFM images show that the fullerene coating clearly retraces the pyramid like topography of the underlying pentacene film (Fig. 1a). However, it exhibits drop-like growth with a grain size much smaller than the pentacene grains. In addition to morphological studies via AFM we also investigated the crystalline structure of the bilayer. The resulting diffraction pattern, see Fig. 1(b), shows well known Bragg peaks stemming from ordered thin film growth of pentacene in [00L] direction [2, 3]. In addition, this pattern is superimposed by a second set of Bragg features which we have identified to originate from C₆₀ face centred cubic (fcc) growth in [111] direction with a lattice constant of $a = 14.14 \text{ \AA}$. The C₆₀ growth corresponds to the well known fcc structure of single crystals at room temperature [4]. The absence of additional, not indexed features allows us to exclude a lying down phase of pentacene at the interface or a crystalline interdiffusion layer.

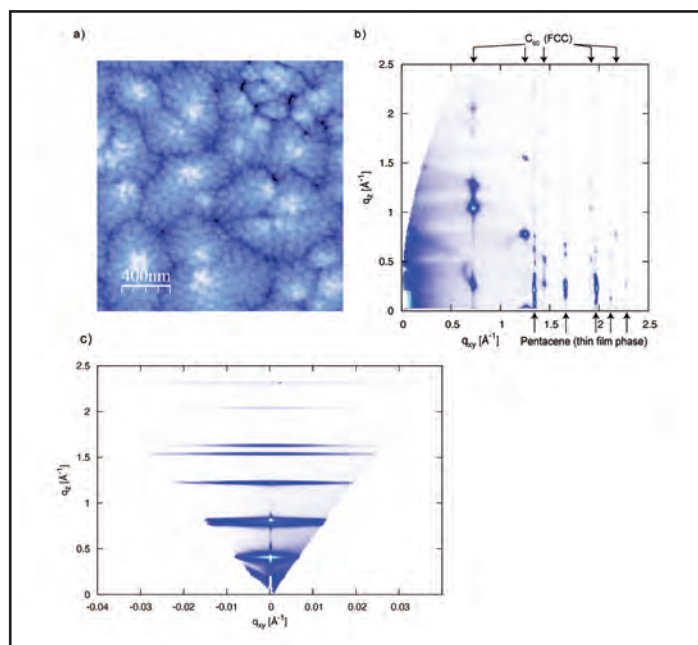


Figure 1

a) AFM height image ($2 \mu\text{m} \times 2 \mu\text{m}$) of 25 nm C₆₀ coating a 20 nm pentacene thin film layer. b) GIXS measurement of a pentacene-C₆₀ bilayer. All diffraction features can be accounted for by a standing up pentacene thin film phase and [111] fcc C₆₀. c) Off-specular reflectometry X-ray measurement, demonstrating high crystallinity.

Additional off-specular reflectometry X-ray measurements, shown in Fig. 1(c), confirm the pentacene thin film growth in [00L] direction as well as the C₆₀ fcc growth in [111] direction and indicate high crystallinity of the organic thin films.

To explore the electrostatic changes during the heterojunction formation, we performed C₆₀ film thickness dependent measurements by recording gate sweeps for positive source-drain voltages during fullerene deposition, while the ambipolar TFT develops (Fig 2a).

During the first 50 Å of deposition, which corresponds to about 6 monolayers (ML) C₆₀, the characteristic curves hardly change. Then, at around 55 Å C₆₀ film thickness, the device suddenly begins to show electron conducting characteristics as well. The thickness resolved values for the respective threshold voltages for hole and electron conduction channel and the electron mobility are plotted in Fig. 2(b). Beyond 55 Å, the electron mobility starts to rise quickly with increasing film thickness, until it saturates at thicknesses higher than about 150 Å, i.e. well beyond the Debye length. From unipolar devices it is known that the onset of conduction goes along with percolation of the semiconductor layer [1]. The threshold voltages show similar behaviour. Beyond 6 ML fullerene, both, the hole and the electron threshold voltages shift oppositely to more positive and more negative values, respectively. This means that both channels open earlier with respect to their onset voltage.

The shift of the p-channel threshold shift leads to an important finding. The Fermi levels of pentacene and C₆₀ are expected to align via interface charging, i.e. by formation of depletion zones or accumulation of charges, depending on the direction of the shift. From literature values for the highest occupied molecular orbital (HOMO) and the lowest unoccupied molecular orbital (LUMO) energy levels of the two semiconductors we expect the Fermi level of pentacene to lie above the Fermi level of C₆₀ [5], which means that the pentacene side of the interface is to be charged positively, while the C₆₀ side is charged negatively. Sweeping the bottom gate voltage to more positive values will at one point switch the pentacene bottom interface from accumulation to depletion, which would lead to a vanishing hole current flow. Here however, the pentacene layer has to be depleted entirely by the bottom gate in order to compensate for the extra top charge at the pentacene-C₆₀ interface. Thus, the effective threshold voltage is expected to shift to more positive values, which matches the observed direction of the threshold shift in our device.

Remarkably, the shifts of both threshold voltages set in with C₆₀ percolation. Obviously, not only the C₆₀ n-channel requires percolation, but also the pentacene top channel. The dropletlike growth behaviour of C₆₀ on pentacene suggests that the heterojunction is confined to the pentacene-C₆₀ contact area. Thus, before percolation, the inhomogeneous heterojunction landscape resembles a plane of disconnected patches of electrons and holes confined to the interface of the fullerene droplets with the pentacene surface.

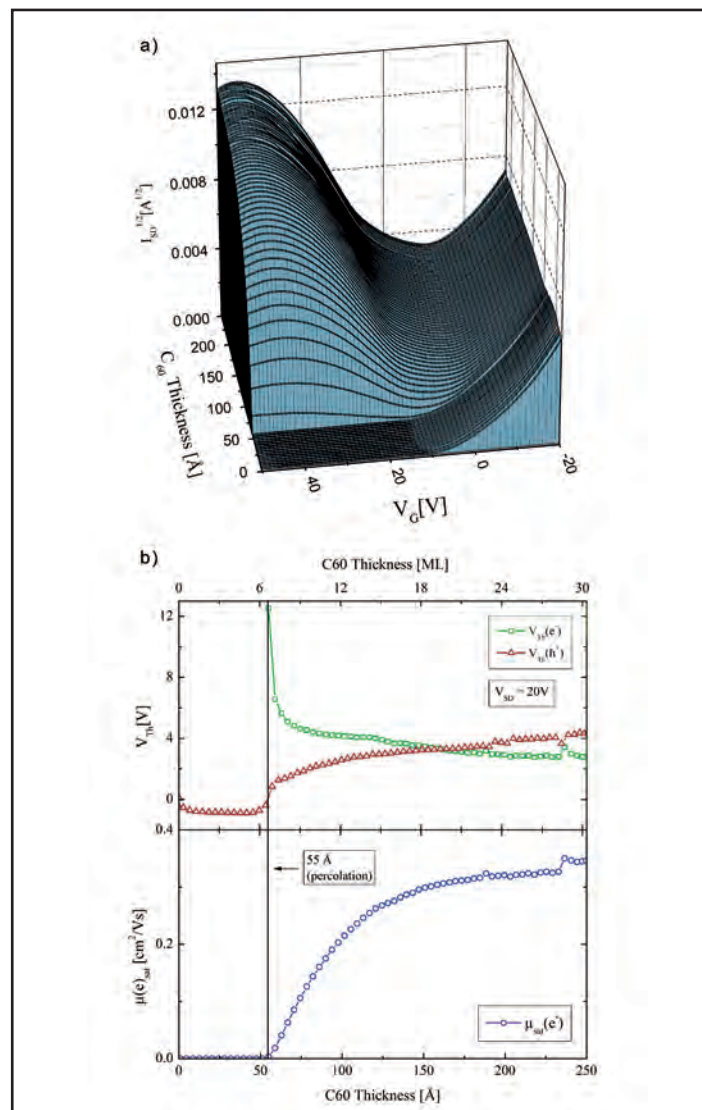


Figure 2

Thickness resolved measurements of an ambipolar FET during C₆₀ growth. a) *In situ* transconductance curves of an ambipolar TFT. b) Thickness resolved threshold voltages and electron saturation mobilities. Percolation of the electron channel is indicated.

In summary, the combination of structural and electronic characterization allowed us to quantify the evolution of the organic heterojunctions in detail. Such experiments will enhance the understanding of the relation between molecular arrangement and electrostatic properties of devices based on organic heterojunctions such as organic solar cells.

Contact: Bert Nickel, nickel@lmu.de

Authors

Simon J. Noever¹, Stefan Fischer¹, and Bert Nickel¹

1. Ludwig-Maximilians-Universität München, Fakultät für Physik and CeNS, Geschwister-Scholl-Platz 1, D-80539 Munich, Germany

Original publication

“Dual Channel Operation Upon n-Channel Percolation in a Pentacene-C₆₀ Ambipolar Organic Thin Film Transistor”, *Adv.Mater.* 25, 2147–2151 (2013).

References

1. M. Fiebig, D. Beckmeier, B. Nickel, “Thickness-dependent *in situ* studies of trap states in pentacene thin film transistors”, *Appl. Phys. Lett.* 66, 083304 (2010).

2. S. Schiefer, M. Huth, A. Dobrinevski, B. Nickel, “Determination of the crystal structure of substrate-induced pentacene polymorphs in fiber structured thin films”, *J. Am. Chem. Soc.* 129, 10316 – 10317 (2007).
3. M. Göllner, M. Huth, B. Nickel, “Pentacene thin-film transistors encapsulated by a thin alkane layer operated in an aqueous ionic environment”, *Adv. Mater.* 22, 4350–4354 (2010).
4. P. A. Heiney et al., “Orientational ordering transition in solid C₆₀”, *Phys. Rev. Lett.* 66, 2911–2914 (1991).
5. S. D. Wang, K. Kanai, Y. Ouchi, K. Seki, “Bottom contact ambipolar organic thin film transistor and organic inverter based on C₆₀/pentacene heterostructure”, *Org. Electron.* 7, 457–464 (2006). 89, 1237–1250 (2005).

The true bulk electronic structure of quasicrystals.

Pseudogap in the valence band observed by hard X-ray photoemission

The discovery of aperiodic ordering in solids has changed our concept of how atoms may arrange in solids, and has led to a new definition of what constitutes a crystal. Many quasicrystalline metallic alloys have been discovered, yet the question why they order in this manner is still subject of controversy. Here we use hard X-ray photoemission (HAXPES), which gives access to the true bulk electronic structure, to resolve a controversial issue regarding the electronic driving mechanism for their formation, i.e. the existence of a pseudogap at the Fermi level. Our data from icosahedral Al-Pd-Mn and Al-Cu-Fe clearly demonstrate the presence of a pseudogap in the bulk, which is masked in soft X-ray photoemission because of a metallic surface phase. In Al-Cu-Fe the pseudogap reaches a very low density of states at the Fermi level, indicating that this material is close to a metal-insulator phase boundary.

Quasicrystals belong to a class of novel materials whose structure fundamentally differs from other two known forms of solids, crystalline and amorphous, because they combine long-range translational order and forbidden rotational symmetries. Such properties were thought to be incompatible up to 30 years ago, until Dan Shechtman demonstrated the existence of quasicrystals (Nobel Prize in Chemistry in 2011). Quasicrystals exhibit many unusual physical properties such as high electrical resistivity, a negative temperature coefficient of resistance, and a low electronic contribution to specific heat. Many (~100) aperiodically ordered alloys have been synthesized to date, and even naturally occurring quasicrystals have been reported. The question “where are the atoms” in a quasicrystal has been successfully answered for a few of them. However, the fundamental question of why nature prefers quasicrystalline order, as shown for icosahedral Al-Cu-Fe in Fig. 1, in some parts of the alloy phase diagram has remained controversial.

This has been ascribed to a mechanism that predicts the existence of a pseudogap in the electronic density of states at the Fermi level (E_F) due to quasi-Brillouin zone and Fermi surface interaction (i.e. Hume-Rothery mechanism) [1]. Surface sensitive photoemission [2, 3] of icosahedral i-Al-Pd-Mn and i-Al-Cu-Fe show a clearly developed metallic Fermi edge with a rounded shape near E_F , which was considered as an indirect evidence of the pseudogap [2, 3]. On the other hand, the explanation of bulk transport properties of quasicrystals such as high resistivity, negative temperature coefficient of resistivity, and low electronic specific heat requires a pseudogap at E_F . This discrepancy was ascribed to an enhanced surface metallicity compared to the bulk [3], which masks the pseudogap in low energy (i.e., surface sensitive) photoemission.

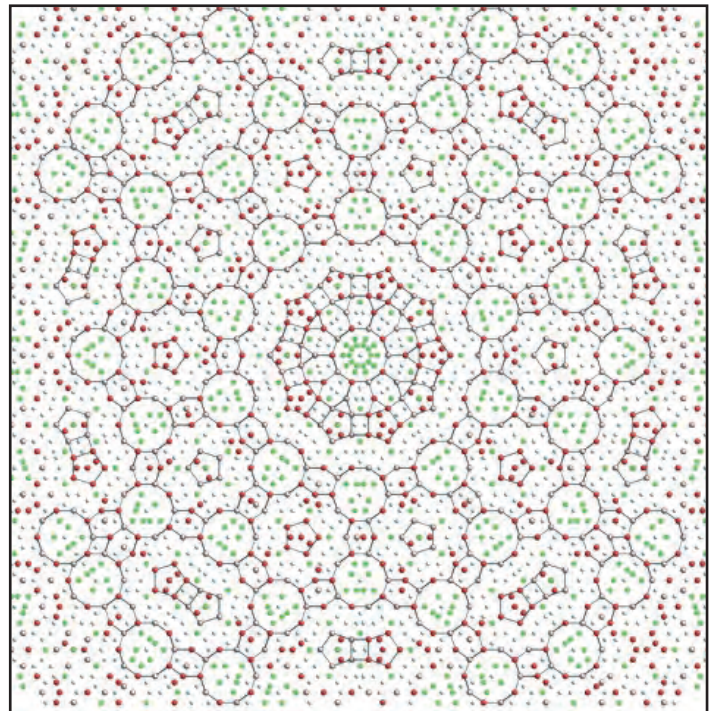


Figure 1

Section of the structure of i-Al-Cu-Fe based on a model by Steurer and Deloudi. Grey atoms are Al, Cu is red, Fe green. This figure is reproduced from Ref. 4 with permission.

Our HAXPES data, recorded at the P09 beamline at PETRA III, DESY, Hamburg and at the ID32 beamline at ESRF, Grenoble using 7.93 and 5.95 keV X-rays at 300 K and 40 K, clearly show the well-developed pseudogap at E_F that has been predicted by theory and required to explain the transport data (Fig. 2).

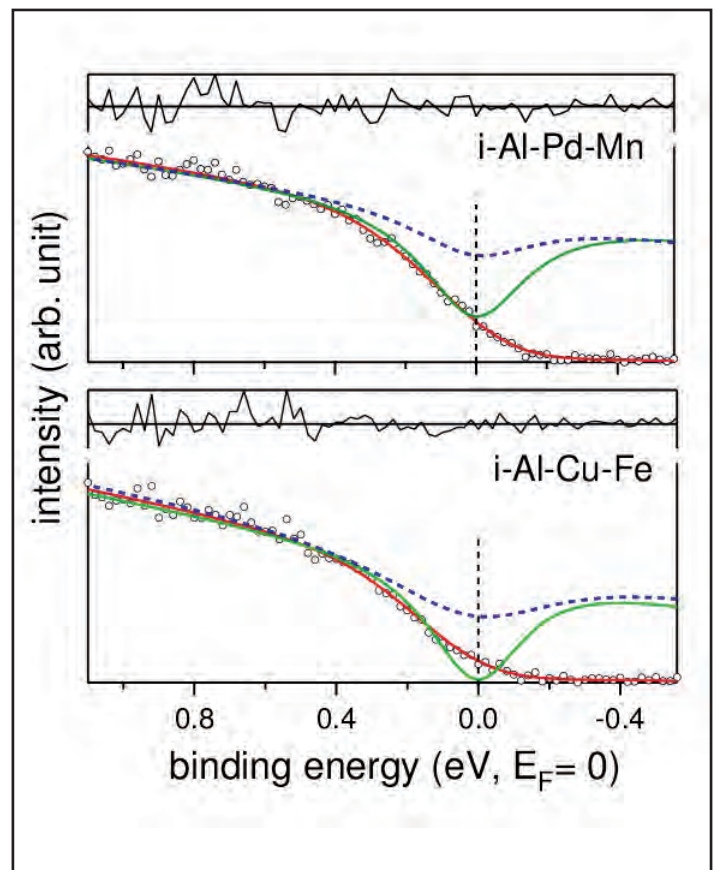


Figure 2

HAXPES valence band spectra of i-Al-Pd-Mn and i-Al-Cu-Fe close to the Fermi level (E_F) measured at 40 K using 7.93 keV photon energy. The experimental valence band spectra (black open circles), which have been fitted with a Lorentzian function (green line) broadened by the instrumental resolution and multiplied by the Fermi function, show a deep pseudogap at the Fermi level. The resulting fitted curve is shown as a red line. In contrast, low energy photoemission [2] (dashed blue line) fails to show the pseudogap. This figure is taken from the original publication (Phys. Rev. Lett. 109, 216403, 2012) with permission.

This shows the important advantage of using high energy photons to examine the true bulk electronic structure using HAXPES; in spite of the low cross sections in this region, the effect is clear, and shows considerable differences between the two materials. In order to quantitatively evaluate the depth and width of the pseudogap, we analyze the line shape through a Lorentzian function convoluted by a Gaussian to represent the instrumental influence (green line in Fig. 2). A well-developed pseudogap in the bulk is thus unambiguously observed in i-Al-Pd-Mn. For i-Al-Cu-Fe, the pseudogap is even more pronounced in the bulk, with the minimum of the spectral function reaching zero; in both cases, this is in marked contrast to the surface sensitive data (dashed blue line, from [2]). The line shape analysis suggests that the pseudogap is not only deeper but also narrower in the bulk compared to the surface. In fact, for i-Al-Cu-Fe, the line shape analysis shows that the density of states is zero at E_F , which indicates that it is close to the metal-insulator phase boundary, in agreement with the specific heat and transport measurements [5].

Contact: Sudipta Roy Barman, barmansr@gmail.com

Authors

J. Nayak¹, M. Maniraj¹, Abhishek Rai¹, Sanjay Singh¹, Parasmani Rajput², A. Gloskovskii³, J. Zegenhagen², D. L. Schlagel⁴, T. A. Lograsso⁴, K. Horn⁵ and S. R. Barman¹

1. UGC-DAE Consortium for Scientific Research, Khandwa Road, Indore 452001, India
2. European Synchrotron Radiation Facility, 6 rue Jules Horowitz, F-38043 Grenoble, France
3. Deutsches Elektronen-Synchrotron DESY, Notkestraße 85, D-22607 Hamburg, Germany
4. Ames Laboratory U. S. DOE, Iowa State University, Ames, Iowa 50011-3020, USA
5. Fritz-Haber-Institut der Max-Planck-Gesellschaft, Faradayweg 4-6, D-14195 Berlin, Germany

Original publication

“Bulk electronic structure of quasicrystals”, Phys. Rev. Lett. 109, 216403 (2012).

References

1. J. Hafner and M. Krajčí, Phys. Rev. Lett. 68, 2321 (1992).
2. Z. M. Stadnik, D. Purdie, M. Garnier, Y. Baer, A.-P. Tsai, A. Inoue, K. Edagawa, S. Takeuchi, and K. H. J. Buschow, Phys. Rev. B 55, 10 938 (1997).
3. G. Neuhold, S. R. Barman, K. Horn, W. Theis, P. Ebert, and K. Urban, Phys. Rev. B 58, 734 (1998).
4. M. Quiquandon and D. Gratias, Phys. Rev. B 74, 214205 (2006).
5. T. Klein, C. Berger, D. Mayou, F. Cyrot-Lackmann, Phys. Rev. Lett. 66, 2907 (1991).

Breakdown of the X-ray magnetic scattering cross section.

Rendering magnetism invisible

Free-electron laser sources provide radiation with unprecedented parameters in terms of ultrashort pulse length and high photon flux, making them ideal tools for studying ultrafast phenomena in matter on a previously inaccessible level. Here, we report on an ultrafast breakdown of the resonant magnetic scattering channel in a magnetic cobalt/platinum multilayer system, exposed to 100-fs-long ultraintense extreme ultraviolet (XUV) pulses from FLASH. We find that already during the first few femtoseconds of the XUV pulse the electronic state of the sample is strongly perturbed, leading to a shift in the energy levels, such that the incoming photon energy no longer matches the condition for resonant scattering.

The use of X-ray scattering for studying electronic and magnetic structures of matter is based on the premise that the scattered X-rays provide information on an as-prepared state. Free-electron laser (FEL) sources providing ultraintense and ultrashort radiation pulses challenge this premise, especially with regard to electron transitions probed in resonant scattering experiments.

We present here the results of a resonant magnetic scattering experiment at FLASH, see also [1, 2], comparing magnetic scattering from a cobalt/platinum multilayer sample at non-destructive low and destructive high fluences. As for resonant magnetic scattering a specific quantum transition within the electronic system is probed, radiation damage can manifest itself on timescales even shorter than those found for (non-resonant) charge scattering of nanocrystals [3].

For the experiment, the photon pulse length was estimated to be 100 fs and the focal spot size 20 μm . Different fluences were set by solid-state absorbers. The photon energy was tuned to the magneto-dichroic transition of cobalt at 59.6 eV (M-edge) which yields the magnetic scattering contrast, see Ref. [1, 2] and references therein. However, this leads also to strongly enhanced absorption and hence to increased radiation damage to both the electronic and, on longer timescales, the atomic systems. The altered electronic states can result in different properties, like enhanced transmission, as shown e.g. for aluminium [4].

We show magnetic scattering data of a thin cobalt/platinum multilayer film deposited on a free-standing silicon nitride membrane. Due to its perpendicular magnetic anisotropy the film exhibits a domain pattern with out-of-plane magnetic domains which have been aligned in stripes by an in-plane magnetic field before the experiment. The scattering pattern shown in Fig. 1(a) results from accumulating the scattering signal from 1000 FEL pulses with an average fluence of 7.5 mJ/cm² and at a repetition rate of 10 Hz. A diffraction pattern with the magnetic scattering con-

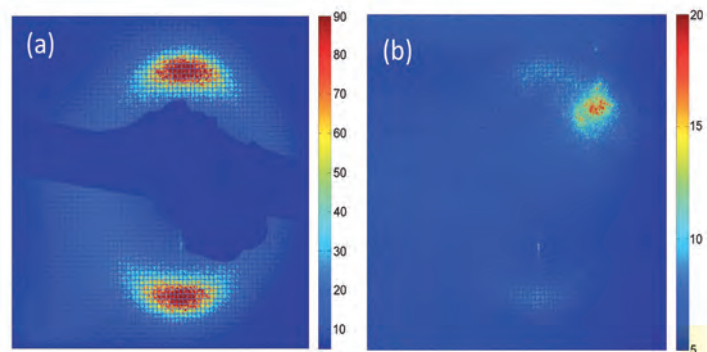
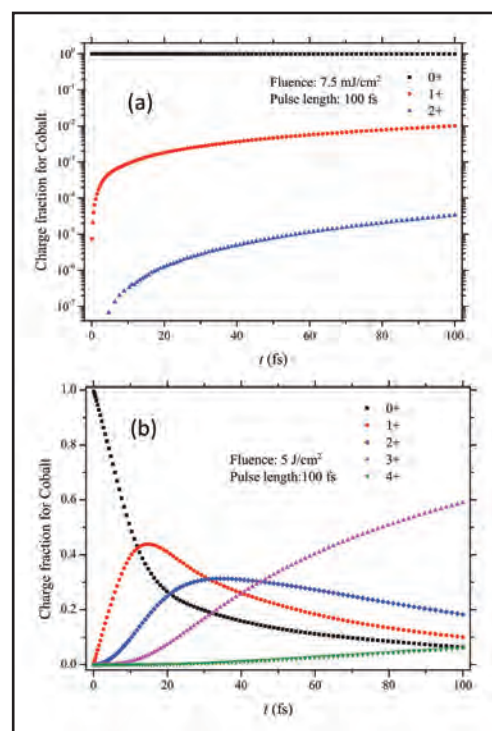


Figure 1 Scattering images of a magnetic sample with domains partially aligned into stripes. The FEL is tuned to the Co M edge at 20.8 nm. (a) Scattering pattern from 1000 low fluence shots with a total fluence of 7.5 J/cm². (b) Single shot scattering pattern from a single pulse with a fluence of 5 J/cm². The scale bar indicates the number of photons per pixel. The scattering intensity is decreased by a factor of 20 in the high fluence case. Furthermore, a parasitic signal originating from the destruction of the sample is visible.

centrated in two intensity lobes is observed. We note that this indicates the absence of heat load effects, as the meta-stable state of linearly aligned magnetic domains would become disordered towards a 2-D labyrinth state upon heating and the scattering pattern would evolve into a ring. The scattering pattern shown in Fig. 1(b) has been recorded from the same sample with a single FEL pulse reaching a fluence of 5 J/cm². Although the total number of photons is rather comparable, the scattering patterns show pronounced differences: the scattering intensity in the previously intense magnetic scattering lobes is strongly reduced and an additional signal appears on the detector. For the latter signal it can be excluded that it originates from scattering due to its shape and lack of point symmetry; it is attributed to the Coulomb explosion of the sample. The striking observation is the strong reduction of the resonant magnetic scattering intensity by a factor of 20, relative to the low fluence case.

Figure 2

Simulation results for the evolution of charge states of cobalt for the cobalt/platinum multilayer system during exposure to a 100 fs long FEL pulse. For the low fluence (a) only a small fraction of cobalt 1+ and cobalt 2+ ions are present. Therefore the electronic system is essentially unperturbed and the magnetic scattering can be observed as expected (Fig. 1a). In the high fluence case (b), in contrast, a large amount of differently charged cobalt ions are present in the sample. Already within the first 10 fs of the FEL pulse more ions than neutral cobalt atoms remain. Therefore, the electronic structure has changed such that no more resonant magnetic scattering takes place. The total observed scattering intensity drops (Fig. 1b).



We attribute the loss in scattering intensity to a reduced rate of the resonant magnetic scattering process. We expect that this intensity reduction is due, to a large extent, to the efficient absorption of the X-rays which leads to significant changes in the irradiated material's electronic structure. Especially, the photoionization of weakly bound 3d and 4s electrons are of relevance.

To confirm this idea, we have performed simulations of the non-equilibrium evolution of the cobalt/platinum multilayer sample, using a non-equilibrium code based on kinetic Boltzmann equations, see e.g. [5]. Those simulations yield quantitative insight into the ultrafast electronic processes occurring during the intense FEL irradiation, so that the evolution of the electronic and atomic system starting from the neutral state through all stages of the progressing ionization and sample damage can be followed. In the case of low fluence only minor changes are induced to the electronic system: the average ionization degree per atom is ~ 0.01 and Co +1 states appear mostly within the

sample (Fig. 2a). In contrast, in the high fluence case, the electronic system and the average ionization degree per atom change dramatically after a few up to tens of femtoseconds (Fig. 2b). The average degree of ionization is close to 1 already after the first 10 fs of the exposure to the FEL pulse. Using the Hartree-Fock-Slater model, implemented in the XATOM package [6], it was estimated that the resonant transition energies of cobalt +1 to +3 ions shift by 1, 1.5 and 2 eV with respect to those of neutral cobalt. The FEL photon energy staying tuned to the cobalt $0+$ bulk transition energy and having a bandwidth of ~ 0.6 eV is therefore out of resonance for ions which consequently reduces the observed scattering intensity. As the resonant scattering process is then quenched during the first few femtoseconds of the exposure, this result implies an existence of an upper fluence limit for the ultrafast resonant magnetic scattering.

Contact: Leonard Müller, Leonard.Mueller@desy.de

Authors

L. Müller¹, C. Gutt¹, B. Pfau², S. Schaffert², J. Geilhufe³, F. Büttner², J. Mohanty², S. Flewett², R. Treusch¹, S. Düsterer¹, H. Redlin¹, A. Al-Shemmary¹, M. Hille⁴, A. Kobs⁴, R. Frömter⁴, H. P. Oepen⁴, B. Ziaja^{1,5,6}, N. Medvedev^{1,5}, S.-K. Son^{1,5}, R. Thiele^{1,5}, R. Santra^{1,5,7}, B. Vodungbo⁸, J. Lüning⁸, S. Eisebitt^{2,3} and G. Grübel¹

1. Deutsches Elektronen-Synchrotron DESY, D-22607 Hamburg, Germany
2. Technische Universität Berlin, Institut für Optik und Atomare Physik, D-10623 Berlin, Germany
3. Helmholtz-Zentrum Berlin für Materialien und Energie GmbH, D-14109 Berlin, Germany
4. Universität Hamburg, Institut für Angewandte Physik, D-20355 Hamburg, Germany
5. Center for Free-Electron Laser Science, DESY, D-22607 Hamburg, Germany
6. Institute of Nuclear Physics, Polish Academy of Sciences, Radzikowskiego 152, P-31-342, Krakow, Poland
7. Universität Hamburg, I. Institut für Theoretische Physik, D-20355 Hamburg, Germany
8. Université Pierre et Marie Curie, Laboratoire de Chimie Physique - Matière et Rayonnement - CNRS UMR 7614, F-75005 Paris, France

Original publication

"Breakdown of the X-ray resonant magnetic scattering signal during intense pulses of XUV FEL radiation", *Physical Review Letters* **110**, 234801 (2013).

References

1. C. Gutt et al., "Single-pulse resonant magnetic scattering using a soft X-ray free-electron laser", *Phys. Rev. B* **81**, 100401(R) (2010).
2. L. Müller, C. Gutt et al., "Endstation for ultrafast magnetic scattering experiments at the free-electron laser in Hamburg", *Rev. Sci. Instrum.* **84**, 013906 (2013).
3. A. Barty et al., "Self-terminating diffraction gates femtosecond X-ray nanocrystallography measurements", *Nat. Phot.* **6**, 35-40 (2012).
4. B. Nagler, U. Zastra, R.R. Fäustlin, S. M. Vinko, T. Whitcher, A.J. Nelson, R. Sobierajski, J. Krzywinski, J. Chalupsky, E. Abreu et al., "Turning solid aluminium transparent by intense soft X-ray photoionization", *Nat. Phys.* **5**, 693-696, (2009).
5. B. Ziaja, H. Wabnitz, E. Weckert, T. Möller, "Femtosecond non-equilibrium dynamics of clusters irradiated with short intense VUV pulses", *New J. Phys.* **10**, 043003 (2008).
6. S.-K. Son, L. Young, and R. Santra, "Impact of hollow-atom formation on coherent x-ray scattering at high intensity", *Phys. Rev. A* **83**, 033402 (2011).

Magmas at depth.

Structural change in basalt at deep mantle conditions

Silicate liquids, i.e. magmas, play a key part at all stages of deep Earth evolution, ranging from core and crust formation billions of years ago to present-day volcanic activity. Quantitative models of these processes require knowledge of the structural changes and compression mechanisms that take place in magmas at the high pressures and temperatures in the Earth's interior. However, obtaining that has long been impeded by the challenging nature of the experiments. We measured the structure and density of molten basalt up to 60 GPa by means of *in situ* X-ray diffraction.

Density measurements of silicate melts are much sought after, because density is the primary factor controlling the evolution of magmas at depth. Pioneering results have been obtained using shock-wave [1] at upper-mantle conditions, demonstrating that basaltic magmas are more compressible than their crystalline counterparts, which implies that density inversion between magmas and crystals must occur at depth. This behaviour can be explained by the different compression mechanisms available in liquid silicates, compared to the crystalline structures, including the collapse of ring structures at low pressure and gradual coordination changes.

A key point to be investigated is how and where the transition from fourfold- to sixfold-coordinated silicon occurs in magmas at depth, and in turn, how that affects melt compressibility. Si coordination change occurs in the crystalline phases at 25 GPa (i.e. 660 km depth); it is the major phenomenon affecting the Earth's mantle and defines its reservoirs, the upper and lower mantles.

In recent years, structural and density information for silica glass was obtained at record pressures of up to 100 GPa [2], a major step towards obtaining data on the molten state. But so far, only shock-wave experiments have been able to probe the properties of magmas at deep mantle conditions, with data reported up to 127 GPa [3]. However, these data are difficult to interpret in terms of an isothermal equation of state as the temperatures generated during the shock ramp from 2000 K to 8000 K, exceeding by far the mantle temperature profile.

We collected *in situ* X-ray diffraction data on molten basalt, the most commonly produced magma, using laser-heated diamond anvil cells at the Extreme Conditions Beamline P02.2 at PETRA III (Fig. 1). A structural change is observed between 10 and 35 GPa and attributed to Si undergoing a coordination change from 4 to 6. We measured the density of melts from the same set of data, using the X-ray-diffraction-based method [4]. Above the



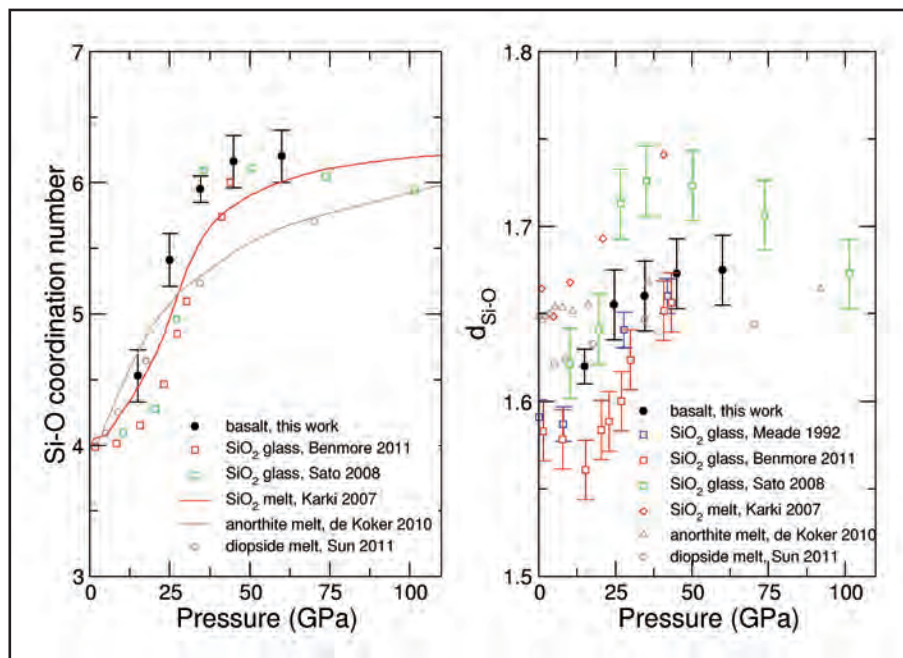
Figure 1

Photograph of a laser heated sample inside a diamond-anvil cell at 35 GPa. Three laser-heated spots are visible. Sample size: 100 microns.

structural transition, there is a clear stiffening of the melt. This stiffening is related to the fact that Si is the last of the major elements to undergo a coordination increase, so that above 35 GPa, bond-length shortening gradually overtakes coordination change as the dominant compression mechanism (Fig. 2).

Our data provide the first *in situ* experimental insight into the behaviour of a magma ocean at depth. Planets were indeed born molten, e.g. the so-called magma ocean stage. In the context of the crystallization of a magma ocean, the difference in density between melts and crystals will be at its highest at the bottom of the upper mantle, that is, above the fourfold-to-sixfold Si-coordination transition in crystals, and above the bottom of the lower mantle atop the core. We should therefore expect a layered magma ocean with a crystalline layer separating

Figure 2
Pressure-evolution of Si-O coordination number. Present data are compared to theoretical calculations on silicate melts [6, 7] and to experimental data on SiO₂ glass [2].



an upper magma ocean from a basal one, as posited by thermal evolution models [5]. The existence of two separate magma oceans has been postulated to reconcile geochronological estimates for the duration of the magma ocean era of a few tens of Myrs with cooling models, as a single magma ocean would otherwise have cooled within one Myr only. Today, there are still remnants of the basal magma ocean in the form of melt pockets detected atop the Earth's core by seismology.

The structural change thus affects the physical properties of magmas at depth, but it also affects their chemical properties. Strikingly, the reported structural and compressibility changes coincide with a marked change in the pressure evolution of the distribution of nickel between metal and silicate melts. The depth of a magma ocean is classically estimated based on the measured pressure-dependency of siderophile elements (such as Ni) partitioning between molten silicate and metal. Recent estimates exceed 30 GPa and range up to 60 GPa, with most models relying on extrapolations of experimental data restricted to lower pressures (<25 GPa). The coincidence between the change in silicate melt compressibility and nickel partitioning

implies that data obtained below 35 GPa should not be used to constrain partitioning at deeper mantle pressures. Partitioning of an element between two phases is controlled by its coordination geometry and site compressibility in each phase. Silicate melt stiffening implies a convergence of site compressibility between silicate and metal melts, resulting in a weak pressure-dependence of Ni partitioning above 35 GPa. An unfortunate consequence of this weak pressure-dependence is that error bars on magma ocean depths need to be revised upwards, if they can be determined at all. These examples illustrate that models of the magma ocean era, including segregation of the molten Fe core and crystallization of the magma ocean, must incorporate pressure-induced structural changes in melts.

This study shows that it is possible to study magmas *in situ* at the high pressure and temperature conditions of their formation. This opens the way to more systematic studies for the wide range of compositions of natural magmas, and in particular, to the effect of volatile elements on their properties.

Contact: *Chrystèle Sanloup*, chrystèle.sanloup@ed.ac.uk

Authors

Chrystèle Sanloup^{1,2}, James W. E. Drewitt¹, Zuzana Konôpková³, Philip Dalladay-Simpson¹, Donna M. Morton¹, Nachiketa Rai⁴, Wim van Westrenen⁴ and Wolfgang Morgenroth^{3,5}

1. School of Physics and Astronomy, University of Edinburgh, EH9 3JZ Edinburgh, United Kingdom
2. Institut des Sciences de la Terre Paris, Université Pierre et Marie Curie, F-75252 Paris, France
3. Deutsches Elektronen-Synchrotron DESY, Notkestrasse 85, D-22607 Hamburg, Germany
4. Faculty of Earth and Life Sciences, Vrije Universiteit, NL-1081 HV Amsterdam, The Netherlands
5. Institut für Geowissenschaften, Goethe-Universität Frankfurt, D-60438 Frankfurt am Main, Germany

Original publication

"Structural change in molten basalt at deep mantle conditions", *Nature* 503, 104 - 107 (2013).

References

1. S. M. Rigden, T. J. Ahrens, E. M. Stolper, "Densities of liquid silicate at high pressures", *Science* 226, 1071-1074 (1984).
2. T. Sato, N. Funamori, "Sixfold-coordinated amorphous polymorph of SiO₂ under high pressure", *Phys. Rev. Lett.* 101, 255502 (2008).
3. P. D. Asimow, T. Ahrens, "Shock compression of liquid silicates up to 125 GPa: the anorthite–diopside join", *J. Geophys. Res.* 115, B10209 (2010).
4. J. H. Eggert, G. Weck, P. Loubeyre, M. Mezouar, "Quantitative structure factor and density measurements of high-pressure in diamond anvil cells by X-ray diffraction: argon and water", *Phys. Rev. B* 65, 174105 (2002).
5. S. Labrosse, J. W. Hernlund, N. Coltice, "A crystallizing dense magma ocean at the base of the Earth's mantle", *Nature* 450, 866-869 (2007).
6. B. B. Karki, D. Bhattarai, L. Strixrude, "First-principles simulations of liquid silica: structural and dynamical behavior at high pressure" *Phys. Rev. B* 76, 104205 (2007).
7. N. de Koker, "Structure, thermodynamics, and diffusion in CaAl₂Si₂O₈ liquid from first-principles molecular dynamics", *Geochim. Cosmochim. Acta* 74, 5657-5671 (2010).

Unexpected flow behaviour of anisotropic particles.

Perpendicular orientation of cylindrical micelles behind a tapering

Flow orientation of anisotropic particles is of importance in many fields, ranging from the production of polymer fibres to the flow of cells and proteins through thin capillaries or pipes. It is commonly assumed that anisotropic particles align parallel to the flow, whereas in narrow channel sections one expects the increased flow rate to improve parallel particle alignment. However, we discovered that anisotropic colloidal particles generally realign perpendicular to the flow after passing a narrow channel section. Realignment occurs in the expansion after a narrow channel section in a region with significant extensional flow which is promoted by shear thinning, a typical property of complex fluids. This reorientation is of high relevance in fibre production and a possible thrombogenic mechanism in blood capillaries.

In situ investigations of the flow orientation of colloids in solution under very well-defined conditions have recently become possible with the development of X-ray transparent microfluidic devices and high-brilliance micro-focused X-ray beams at dedicated synchrotron beamlines [1]. Due to their small dimensions, fluid flow in microchannels is mostly laminar, even for high flow rates, with a well-defined flow velocity profile. Such conditions are ideal to perform detailed investigations of the flow orientation of anisotropic colloids.

Of many different types of anisotropic particles that are of high relevance for such studies, including semi-flexible polymer chains, carbon nanotubes, fibrous proteins, rod-like nanoparticles, and DNA [2,3], we chose aqueous solutions of cylindrical block copolymer micelles. Their flow-orientation behaviour can be well studied in microfluidic devices using polarized microscopy and micro-focus synchrotron small-angle X-ray scattering (μ SAXS), as sketched in Figure 1. The cylindrical micelles have diameters of 25 nm and contour lengths of several micrometers, as shown by the AFM-image in Figure 1b. In our studies we focused on the orientation behaviour of the cylindrical micelles when flowing through narrow channel sections.

We performed synchrotron X-ray measurements to scan the contraction/expansion zone of the narrow microchannel section and to map the orientation of the cylindrical micelles, as shown in Fig. 2 together with a polarized optical micrograph of the channel section. When flowing into the contraction zone of the narrow section, the micelles remain aligned in flow direction, as indicated by the blue birefringence interference colour and the azimuthal positions of the Bragg peaks, which appear on the meridian of the detector. As expected, the azimuthal peak widths become smaller, indicating improved alignment of the micelles in flow direction. When scanning with the X-ray beam downstream into the channel expansion zone, we observe a surprising behaviour. First, in a region directly behind the exit of the microchannel narrowing, there is no preferred orientation as apparent from the observed Debye-Scherrer rings (Fig. 2b). Further downstream, the micelles become oriented perpendicular to the flow direction. We observe an interference colour change

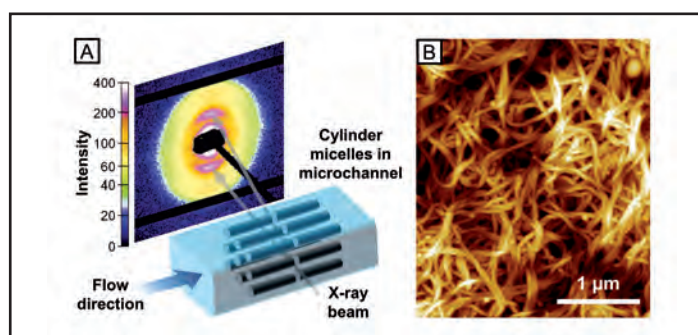


Figure 1

Schematic of the experimental setup for studying the orientation of cylindrical micelles in microchannels using μ SAXS. a) X-ray beam alignment and SAXS pattern measured for a stream of cylindrical micelles flowing in a microchannel. b) Atomic force microscopy image of an isotropic assembly of cylindrical micelles used in this study.

from blue to orange in the polarized microscopy image, and the Bragg reflections now appear on the equator of the detector. This orientation is stable along the remaining part of the channel and does not even change in a subsequent curved section of the microfluidic device. Only close to the channel walls, the wormlike micelles are aligned parallel to the flow direction, as indicated by the blue interference colour close to the channel walls. When the wormlike micelles are subjected to planar extensional flow in x-direction in a subsequent narrow channel section, they again become aligned in flow direction in the contraction zone and perpendicularly aligned in the subsequent expansion zone. To compare the results of the micro-focus X-ray diffraction scanning experiments to the polarized optical micrographs, we mapped the diffracted intensity on the equatorial region of the diffraction patterns onto the corresponding position of the X-ray beam (Fig. 2c). The intensity map corresponds very well to the birefringence interference colours, as shown in Figure 3a. We have reproduced this behaviour for wormlike polymer micelles of different block copolymers, different concentrations (5 – 30 % w/w) and width ratios of the main channel and the narrow section diameter (10:1 – 2.5:1) and always found the same behaviour.

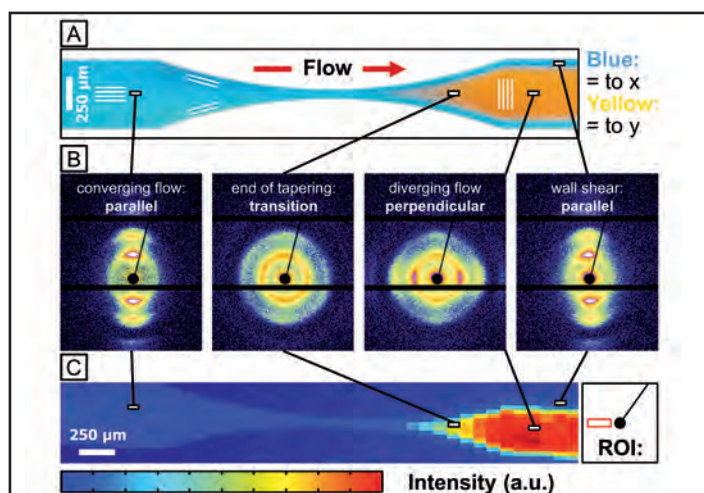


Figure 2

Orientation of cylindrical micelles determined by scanning micro-focus X-ray diffraction. a) Alignment of cylindrical micelles in a narrow channel section visualized by polarized optical microscopy. b) X-ray diffraction patterns measured at the positions indicated in a and c. c) Pixel map of the equatorial intensity of the diffraction patterns at different positions in the channel tapering. The high intensity in the expansion zone corresponds to micelles with an orientation perpendicular to the flow direction. ROI depicts the region of interest.

Ongoing experiments on cylindrical micelles with much higher bending rigidity, on disk-like micelles and very flexible worm-like surfactant micelles show that this phenomenon is generally occurring.

To obtain more insight we performed computational fluid dynamics (CFD) simulations to calculate shear rates and extensional rates in the contraction / expansion zone of the tapering. The calculations were performed for non-Newtonian liquids, as solutions of cylindrical micelles are known to be strongly shear-thinning [5]. The calculated velocity field in the contraction/expansion zone for a typical channel geometry and flow rate used in the experiments is presented in Fig. 3a. Figure 3b shows the calculated velocity profiles across the channel at position I before entering the contraction zone, and at position III after the expansion zone. The velocity profiles are both non-parabolic, as expected for shear thinning fluids, with an almost constant flow velocity in the central part of the channel and a strongly decreasing flow velocity close to the channel walls. Fig. 3c shows the calculated velocity components v_x and v_y , and Fig. 3d the corresponding

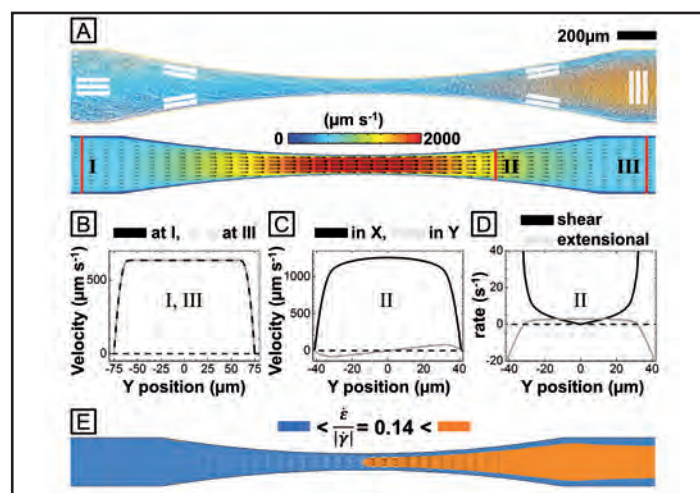


Figure 3

Calculation of the velocity field as well as shear and extensional rates for the flow of cylindrical micelles through a narrow channel section. a) Alignment of cylindrical micelles visualized by polarized optical microscopy and the corresponding calculated velocity field highlighting three points of interest (I, II, III). b) Calculated velocity profiles $v_x(y)$ before (solid black line) and after (dashed grey line) the microchannel tapering (I, III). c) Velocity profiles $v_x(y)$ (solid black line) and $v_y(y)$ (solid grey line) in the expansion zone (II). d) Shear rate $|\dot{\gamma}(y)|$ (solid black line) and extensional rate $\dot{\epsilon}(y)$ (solid grey line) in the expanding micro-channel behind the tapering. e) Map of the ratio $\frac{\dot{\epsilon}}{|\dot{\gamma}|}$ in the wide and narrow channel sections. In the orange regions, $\frac{\dot{\epsilon}}{|\dot{\gamma}|} > 0.14$, whereas in the blue regions, $\frac{\dot{\epsilon}}{|\dot{\gamma}|} < 0.14$. The resulting colour map shows good agreement with the polarized optical micrograph in Fig. 2a, the X-ray intensity map in Fig. 2c, and measured velocity maps.

shear rate $\dot{\gamma} = \nabla_y v_x$ and the extensional rate $\dot{\epsilon} = -\nabla_y v_y$ along the line across the expansion zone indicated in Fig. 3a. We observe, that over the major centre part of the cross section in the expansion zone, the extensional rate $\dot{\epsilon}$ is larger or at least of the same order of magnitude as the shear rate $\dot{\gamma}$. Fig. 3e shows the calculated ratio $\frac{\dot{\epsilon}}{|\dot{\gamma}|}$ over the contraction / expansion zone with a colour scale adjusted such that orange colour indicates areas with $\frac{\dot{\epsilon}}{|\dot{\gamma}|} > 0.14$, whereas blue colour indicates the results of the micro-focus SAXS experiments. This shows that the perpendicular orientation is caused by strong extensional fluid flow amplified by shear thinning.

Contact: Julian Thiele, j.thiele@science.ru.nl; Stephan Förster, stephan.foerster@uni-bayreuth.de

Authors

Martin Trebbin¹, Dagmar Steinhauser^{2,3}, Jan Perlich⁴, Adeline Buffet⁴, Stephan V. Roth⁴, Walter Zimmermann⁵, Julian Thiele⁶ and Stephan Förster¹

1. Physical Chemistry I, University of Bayreuth, D-95447 Bayreuth, Germany
2. Max-Planck-Institute for Dynamics and Self-Organization, D-37073 Göttingen, Germany
3. Deutsches Institut für Kautschuktechnologie e.V., D-30519 Hannover, Germany
4. Deutsches Elektronen-Synchrotron DESY, D-22607 Hamburg, Germany
5. Theoretical Physics I, University of Bayreuth, D-95447 Bayreuth, Germany
6. Institute for Molecules and Materials, Radboud University Nijmegen, NL-6525 AJ, Nijmegen, Netherlands

Original publication

"Anisotropic particles align perpendicular to the flow direction in narrow microchannels", *Proc. Natl. Acad. Sci. U.S.A.* **10.1073/pnas.1219340110** (2013).

References

1. R. Barrett, M. Faucon, J. Lopez, G. Cristobal, F. Destremaut, A. Dodge, P. Guillot, P. Laval, C. Masselon, J. B. Salmon, "X-ray microfocussing combined with microfluidics for on-chip X-ray scattering measurements", *Lab Chip* **6**, 494–499 (2006).
2. S. Rammensee, U. Slotta, T. Scheibel, A. R. Bausch, "Assembly mechanism of recombinant spider silk proteins", *Proc. Natl. Acad. Sci. USA* **105**, 6590–6595 (2008).
3. E. T. Dimalanta, R. Runnheim, C. Lamers, C. Churas, D. K. Forrest, J. J. de Pablo, M. D. Graham, S. N. Coppersmith, S. Goldstein, D. C. Schwartz, "A microfluidic system for large DNA molecule arrays", *Anal. Chem.* **76**, 5293–5301 (2004).
4. M. E. Cates, S. J. Candau, "Statics and dynamics of worm-like surfactant micelles", *J. Phys. Condens. Matter* **2**, 6869–6892 (1990).
5. S. Förster, M. Konrad, P. Lindner, "Shear thinning and orientational ordering of worm-like micelles", *Phys. Rev. Lett.* **94**, 017803 (2005).

The oldest carnivorous dinosaur clutch with embryos.

Fossilized eggshells revealed by synchrotron radiation micro-computed tomography

A clutch of crushed eggs and embryonic material ascribed to the megalosaurid theropod *Torvosaurus*, a primitive carnivorous bipedal dinosaur, has been discovered in the Lourinhã Formation in Portugal. The find represents the only unequivocal evidence of early theropod embryos discovered to date, furthering our understanding of dinosaur eggshell morphology and structure, and bridging a phylogenetic gap in the evolutionary framework among the theropods.

The Lourinhã Formation, central west Portugal, is very rich in dinosaur fossils of the Late Jurassic. In 2005, a large number of clustered eggshell fragments forming an assemblage containing embryonic bones and teeth (Fig. 1 - ML1188), was discovered on a grey mudstone layer. In what concerns dinosaurs, the Museum of Lourinhã hosts one of the most varied and best-preserved paleontological collections in the country and in Europe.

The discovery of fossilized eggs associated with embryos is rare and, thus, the Museum of Lourinhã has been using non-destructive techniques for the study of these exceptionally preserved dinosaur fossils. The purpose of this work is to link a new eggshell morphology to the osteology of a particular group of basal theropod dinosaurs, as well as to evaluate the extension of the diagenesis (the geochemical alterations during the lithification process, thus, the changes of chemistry when an eggshell transforms from a living tissue to a rock) on the morphology of the eggshell. We employed synchrotron radiation-based micro-computed tomography (SR- μ CT), scanning electron microscopy (SEM), and optical microscopy techniques to study the morphology and microstructure of the fossilized eggshell fragments. Additionally, eggshells and surrounding sediment characterization was performed by using an array of complementary techniques in order to assess the extension of the diagenesis, namely micro-proton induced X-ray emission (μ -PIXE), synchrotron radiation-based X-ray diffraction (SR-XRD) and cathodoluminescence (CL).

Several eggshell fragments have been studied by SR- μ CT at the HARWI II beamline at the DORIS III synchrotron storage ring. The samples were imaged in absorption mode with a photon energy of 37 keV. SR-XRD data were acquired at the High Energy Materials Science beamline (HEMS) at PETRA III [1] in transmission mode using a beam spot of 100 μ m in vertical and 300 μ m in horizontal with an energy of 87 keV. The results presented in Fig. 2 show that SR- μ CT is a useful technique for nondestructive imaging of the eggshell's morphology. They bear (i) anastomizing ornamentation resembling to some degree the patterns of linear [2] ornamentation, consisting of subcircular to subelliptical grooves separated by intercon-

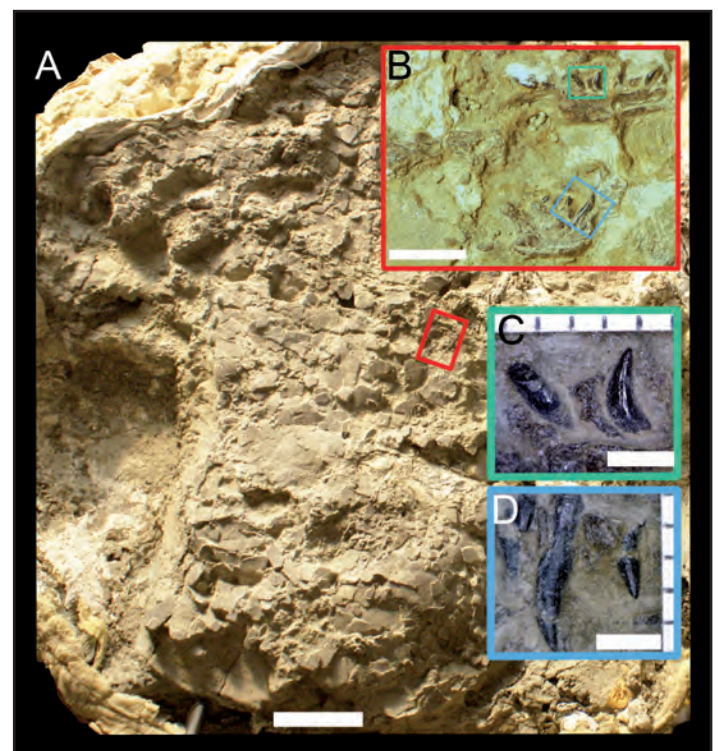


Figure 1

A) Clutch of *Torvosaurus* eggs (ML1188). B) Dentary and maxilla in medial view of *Torvosaurus*. C) Second and third dentary teeth, separated by interdental plate in medial view. D) Second and third maxillary teeth, separated by interdental plate in medial view. Scale bars 100 mm (A), 5 mm (B), 2 mm (C, D).

nected sharp ridges, (ii) needlelike, elongated bladeshaped, calcite (CaCO_3) crystals radiating from the base of the mammillae to the outermost part of the eggshell, and (iii) only one primary layer. Importantly, the ML1188 eggshells are highly porous. The morphology of the pores is provided by the SR- μ CT high-quality data, difficult to visualize by SEM or thin-sections. The pores are irregular canals that branch out, vary in width along their length, and reconnect close to the outer surface. In fact, the pores seem to form an interconnected system (Fig. 2 – bottom). Furthermore, all eggshells have equivalent pore density, which indicates that all the eggs were buried under a homogenous incubating medium [3].

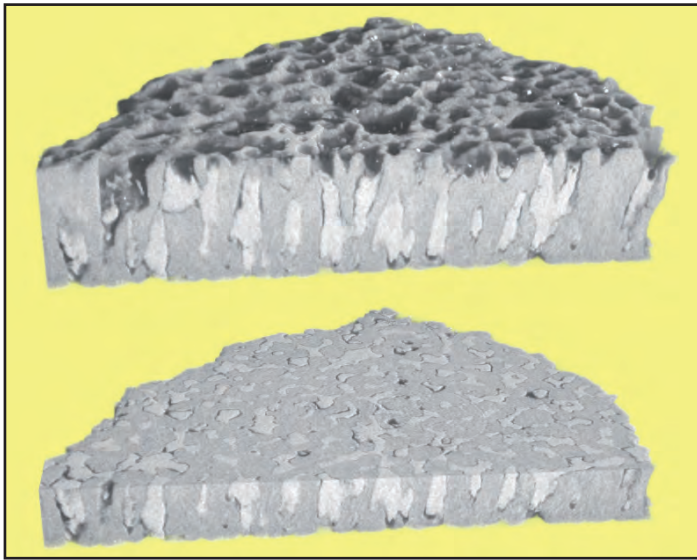


Figure 2
SR- μ CT image of a fossilized eggshell from ML1188 in (top) external and (bottom) transverse view. The total thickness of the eggshell is approximately 1.2 mm.

SR-XRD shows that the major compound of the eggshell is calcite (Fig. 3). The analysis of the external and internal surface zones of the eggshell fragments shows the presence of quartz and phyllosilicates. Furthermore, SR-XRD and μ -PIXE data recorded for the zone between the outer and inner surface layers (middle of the shell) indicate that sediment mainly composed of phyllosilicates is filling in the pores. ML1188 eggshells represent the first report of theropod eggs with a single structural layer, the “primitive” condition for Theropoda, in contrast to more complex eggshells with two or even three layers of advanced theropods, including modern birds, which are practically “living dinosaurs”. It was known that primitive dinosaurs from other non-theropod clades had single-layered eggs, but theropods were the missing piece in the puzzle.

The clutch was not significantly taphonomically disturbed (Fig. 1), meaning the environmental context from the burial of the nest by the progenitors and the deposition of the subsequent sediment layers has remained the same. This nearly undisturbed scenario can be explained by deliberate burial from the progenitor, analogously to the behaviour seen in extant sea turtles. Furthermore, the eggshells are highly porous and, thus, indicative of eggs buried for incubation within the substrate. Thus, ML1188

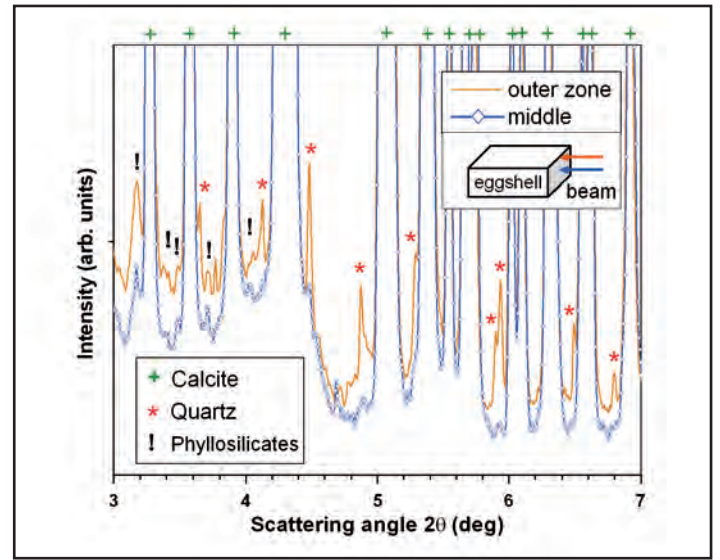


Figure 3
SR-XRD patterns obtained for an eggshell from ML1188 at the topmost zone (external surface zone) and at the middle zone of the eggshell.

could have been buried by the progenitor because of the high porosity of the eggshells, undisturbed taphonomic setting, and low energy geological context.

The non-avian saurischians, including e.g. the longnecked herbivores and the T-rex lookalikes, that have associated eggshells and embryos are represented only by *Massospondylus* and “advanced” theropods *Coelurosauria*, thus missing the basal theropod representatives.

The dinosaur clutch described here encompasses several crushed eggs and embryonic material ascribed to the megalosaurid theropod *Torvosaurus*. It represents the first associated eggshells and embryos of megalosauroids, thus filling an important phylogenetic gap between two distantly related groups of dinosaurs. These fossils represent the only unequivocal basal theropod embryos found to date. Furthermore, these fossils allow unambiguous association of basal theropod osteology with a specific and unique new eggshell morphology. The morphological, microstructural and chemical characterization of the eggshell fragments indicate very mild diagenesis.

Contact: Ricardo Araújo, rmaraujo@smu.edu
Rui M.S. Martins, rmsm@fct.unl.pt

Authors

Ricardo Araújo^{1,2}, Rui Castanhinha^{2,3}, Rui M. S. Martins^{2,4,5,6}, Octávio Mateus^{2,7}, Christophe Hendrickx^{2,7}, Felix Beckmann⁸, Norbert Schell⁸ and Luís C. Alves^{4,6}

- Huffington Department of Earth Sciences, Southern Methodist University, 75275-0395, Dallas, Texas, USA
- Museu da Lourinhã, Rua João Luís de Moura, 95, P-2530-158 Lourinhã, Portugal
- Instituto Gulbenkian de Ciência, Rua da Quinta Grande, N°6, P-2780-156 Oeiras, Portugal
- IST/CTN, Campus Tecnológico e Nuclear, EN10 ao km 139.7, P-2695-066 Bobadela LRS, Portugal
- CENIMAT/13N, Faculdade de Ciências e Tecnologia da Universidade Nova de Lisboa, Quinta da Torre, P-2829-516 Caparica, Portugal
- Centro de Física Nuclear da Universidade de Lisboa (CFNUL), Av. Prof. Gama Pinto 2, P-1649-003 Lisboa, Portugal
- Centro de Investigação em Ciência e Engenharia Geológica (CICEGe), Faculdade de Ciências e Tecnologia da Universidade Nova de Lisboa, Quinta da Torre, P-2829-516 Caparica, Portugal
- Helmholtz-Zentrum Geesthacht (HZG), Max-Planck-Str. 1, D-21502 Geesthacht, Germany

Original publication

“Filling the gaps of dinosaur eggshell phylogeny: Late Jurassic Theropod clutch with embryos from Portugal”, *Scientific Reports* 3, 1924 (2013).

References

- N. Schell et al., “The high energy materials science beamline (HEMS) at PETRA III”, *AIP Conf. Proc.* 1234, 391–394 (2010).
- K. Carpenter, “Eggs, nests and baby dinosaurs: A look at dinosaur reproduction”, (Indiana Press, 1999).
- F. D. Jackson, J. R. Horner, D. J. Varricchio, “A study of a Troodon egg containing embryonic remains using epifluorescence microscopy and other techniques”, *Cretac. Res.* 31, 255–262 (2010).
- G. Grellet-Tinner, “Phylogenetic interpretation of eggs and eggshells: implications for phylogeny of Palaeognathae”, *Alcheringa* 30, 141–182 (2006).
- R. S. Seymour, “Dinosaur Eggs: Gas conductance through the shell, water loss during incubation and clutch size”, *Paleobiol* 5, 1–11 (1979).

The liquid and solid character of colloidal liquid crystals.

Nanoplatelets in shear flow

Most soft matter materials cannot be classified as fluids or solids because they possess a dual character: they can have a response that is solid-like or fluid-like, depending on the mechanical deformation. This dual visco-elastic character can also be found in an important class of soft matter systems, namely liquid crystals. Liquid crystals can be formed by small 'colloidal' platelets, such as clay particles, which all have similar orientation. Thus they are in a nematic phase despite of their Brownian motion, which makes them colloidal. We subjected these dispersions of platelets to an oscillating shear field, squeezing the dispersions between two moving plates. By combining this geometry with X-ray scattering, we uncover the structural origin of the transformation between solid and liquid-like behaviour. These new insights might change the view on the origin of visco-elastic behaviour in complex fluids.

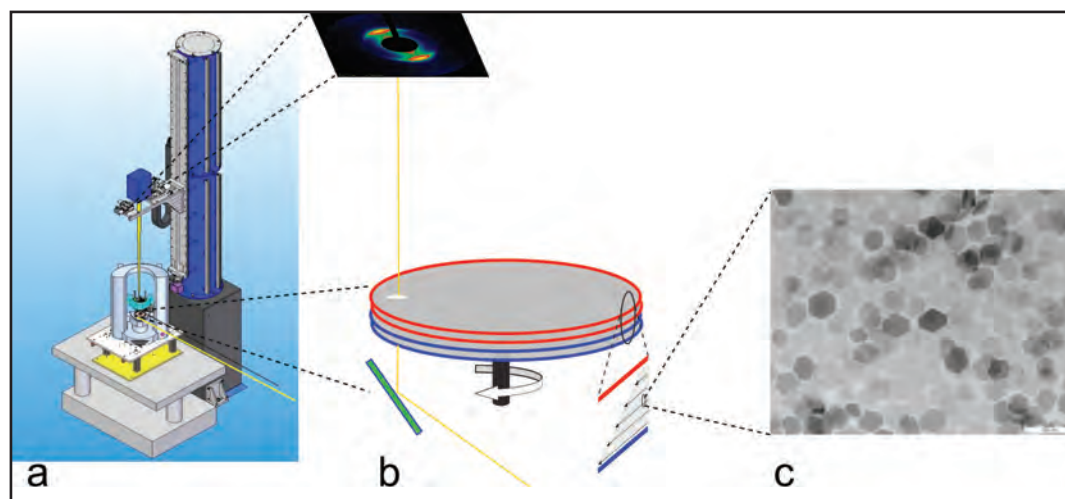


Figure 1

(a) Cartoon of the Rheo-SAXS set-up, with the deflected beam, vertical detection line and the shear cell. (b) The geometry of the plate-plate shear cell showing the light-path of the X-ray beam. (c) Gibbsite platelets that were used in the experiment. Scale bar 500 nm.

Bread dough, yoghurt, tomato ketchup, paints, cement are all complex fluids which behave like a fluid or a solid depending on the rate at which they are deformed. The reason for this behaviour can be found in the response of the structures that constitute the materials. Shear deformation can cause structures to break up so that the system can flow as is the case with tomato ketchup. On the other hand, shear deformation can also enhance interactions, so that the material stiffens, as is the case with silly putty. This 'non-linear' behaviour can cause flow instabilities where the fluid breaks up into regions with, for example, different viscosities [1]. The structural changes underlying such flow instabilities have been our interest in the past. There are two requirements to successfully study such changes. First, the moment in time where the changes take place must be isolated. Second, the structure must be probed *in situ* by a suitable technique. The first requirement is achieved by applying Large Amplitude Oscillatory Shear (LAOS) flow where material states are probed which are inaccessible to standard methodologies. We fulfilled the second requirement in the past for several soft matter systems by combining LAOS with time-resolved

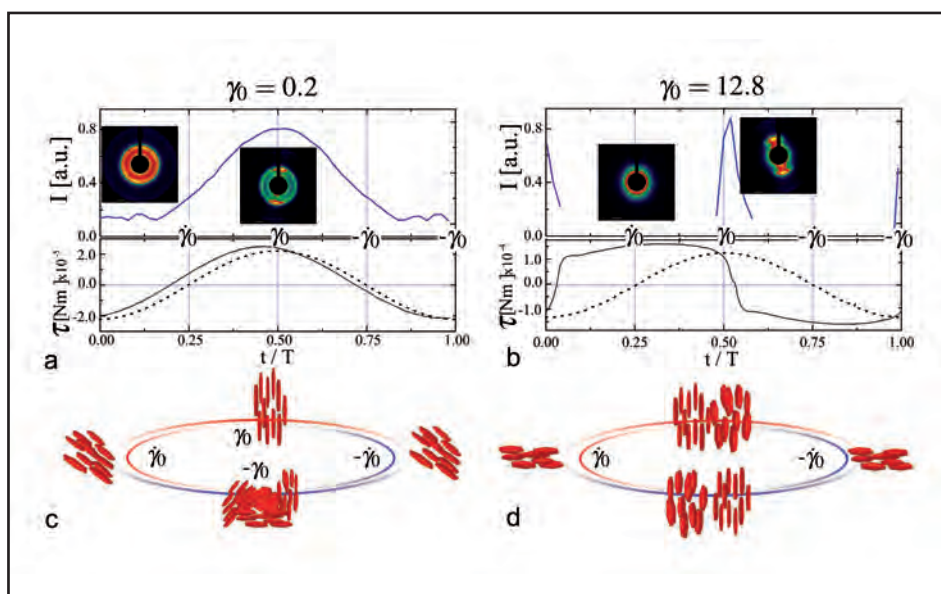
Small Angle Neutron Scattering, simultaneously probing the macroscopic mechanical response and the microscopic structural response [2, 3].

Liquid crystals form a unique class of materials due to the combination of highly ordered structure with low mechanical modulus. This feature is typically used in liquid crystal displays, where orientations of rod-like molecules are quickly switched by electric fields. Clay platelets, the most present colloids in nature, can also display liquid crystalline phases. Moreover, clay dispersions exactly display the flow behaviour that was discussed above and that is for example used in the oil industry to switch from a state in which it flows to a state in which its motion freezes. Here we use a newly developed combination of a rheometer with powerful X-ray light sources such as PETRA III at beamline P10, which ensures sufficient temporal resolution to follow the response of the system to the applied field, see Fig. 1 [4].

We found in this way that the simple elastic response of nematic platelets at small strain amplitudes is accompanied by an

Figure 2

Response to an oscillatory shear field at low strain (a) and high (b) strain amplitudes throughout one period T . Top panels: the peak intensity of the scattering; Bottom panels: the applied strain (dotted line) and the measured torque (solid line). The insets show typical scatter patterns. For low strain we observe a transition from a powder-like scattering to a typical scatter peak, going from minimum to maximum strain. The fact that the corresponding torque almost overlaps with the applied strain exemplifies the elastic response. For high strain amplitudes we observe diffuse isotropic scattering, except for the point when there is a stress overshoot, the platelets flip and we observe a sharp nematic structure peak. (c,d) The corresponding cartoons of dynamic behaviour during one period for different strain amplitudes.



anomalous structural response. Commonly it is assumed that the structural response to oscillatory shear is independent of the direction of deformation. As a consequence the structural response should have twice the frequency of the applied oscillatory shear field. Nematic platelets undergo however a structural symmetry breaking: a preferential direction of deformation is selected which induces off-plane orientation of the platelets. As a result the increase and decrease of the structure peak takes the full period of the oscillation, see Fig. 2(a). We can rationalize the transition to a symmetry-broken state by noting that the total strain acquired between the two most extreme positions of the moving plate is only enough to tilt the director towards the flow direction, but no further. When the flow is reversed, then the director is pushed back, so that it returns to its initial orientation, as indicated in Fig. 2(c).

This anomalous structural response disappears at sufficiently large strain amplitudes. The system then displays a cycle of elastic-like and fluid-like behaviour. Analysing both the mechanical and stress response during the oscillation, we can connect the elastic part of the cycle with the tilting of the platelets away from the wall towards the flow direction and the fluid part with sliding of the platelets Fig. 2(b, d). The transition between the different responses is connected with a rich dynamical behaviour of the nematic ordering.

This study has implications on several levels. It demonstrates the subtleties that are involved in the processing of liquid crystals. This is especially true for colloidal platelets which display a much more complex behaviour than rods [5]. Hence, this paper also urges theoreticians to develop more refined theories where the full reorientational motion of platelets is incorporated as well as the effect of wall anchoring. Finally, we pose that the transition between a structural response of the same frequency as the applied field at low strains to the double frequency at high strains could be at the origin of the non-linear shear thinning of many soft matter systems, like the paints and ketchups described above. That this transition went unnoticed up to now can be attributed to the fact that the combination of LAOS with in situ probing techniques like the set up at DESY is very rare.

We want to close with an outlook on the wealth of possibilities of the set-up that are presently being worked on. High brilliancy light sources can produce coherent beams, which have the advantage that the velocity of colloids can be characterized. We thus envision possibilities to probe velocity and structure at the same time.

Contact: Pavlik Lettinga, p.lettinga@fz-juelich.de

Authors

Minne Paul Lettinga^{1,2}, Simon Rogers^{1,3}, Dzina Kleshchanok⁴, Peter Holmqvist¹ and Bernd Struth⁵

1. ICS-3, Institut Weiche Materie, Forschungszentrum Jülich, D-52425 Jülich, Germany
2. Department of Physics and Astronomy, Laboratory for Acoustics and Thermal Physics, Katholieke Universiteit Leuven, Celestijnenlaan 200D, Leuven B-3001, Belgium
3. Present address: Chemical & Biomolecular Engineering, University of Delaware Newark, Delaware, 19716
4. Van 't Hoff Laboratory for Physical and Colloid Chemistry, Debye Institute for Nanomaterials Science, Utrecht University, NL-584CH Utrecht, The Netherlands
5. CFEL at DESY, Notkestr. 85, D-22607 Hamburg, German

Original publication

“Nonlinear Behavior of Nematic Platelet Dispersions in Shear Flow”, *Phys. Rev. Lett.* **109**, 246001 (2012).

References

1. R. G. Larson, “The Structure and Rheology of Complex Fluids”. *Topics in Chemical Engineering*, Oxford University Press, (1998).
2. S. A. Rogers, J. Kohlbrecher and M. P. Lettinga, “The molecular origin of stress generation in worm-like micelles, using a rheo-SANS LAOS approach”, *Soft Matter*, **8**, 7831-7839, (2012).
3. B. Lonetti, J. Kohlbrecher, L. Willner, J. K. G. Dhont and M. P. Lettinga, “Dynamic response of block copolymer wormlike micelles to shear flow”, *J. Phys.: Condens. Matter*, **20**, 404207, (2008).
4. B. Struth, K. Hyun, E. Kats, T. Meins, M. Walther, M. Wilhelm, and G. Grübel, “Observation of New States of Liquid Crystal 8CB under Nonlinear Shear Conditions as Observed via a Novel and Unique Rheology/Small-Angle X-ray Scattering Combination”, *Langmuir* **27**, 2880 (2011).
5. M. P. Lettinga, Z. Dogic, H. Wang, and J. Vermant, “Flow behaviour of colloidal rodlike viruses in the nematic phase”, *Langmuir*, **21**, 8048-8057, (2005).

Two liquid states in a strong bulk metallic glass-former.

A liquid transforms itself

Polymorphic transitions are common in crystalline solids. Recent studies suggested that phase transitions may also exist between two different amorphous or liquid phases. However, it is difficult to detect such a polyamorphic transition experimentally due to the difficulties in avoiding crystallization and/or measuring at high temperatures/pressures. In this work, we studied the bulk metallic glass-forming liquid $\text{Zr}_{41.2}\text{Ti}_{13.8}\text{Cu}_{12.5}\text{Ni}_{10}\text{Be}_{22.5}$ using calorimetry, synchrotron X-ray scattering and electrostatic levitation. We found thermodynamic, dynamic and structural anomalies that suggest a liquid-liquid transition in this system.

A polyamorphic transition refers to a phase transformation between two liquid (or solid amorphous) phases having identical chemical composition but different structures and physical properties (e.g. thermodynamic and rheological properties). A polyamorphic transition in liquid states is known as liquid-liquid transition. Polyamorphic transitions have been suggested in various systems [1], including water, SiO_2 , BeF_2 , Ge, Si, molten P and $\text{Al}_2\text{O}_3\text{-Y}_2\text{O}_3$ as well as Ce-Al metallic glasses. However, the nature of the transitions has been debated due to crystallization problems that hamper experiments in the desired super-cooled regime.

Recent viscosity measurements of the bulk metallic glass-former $\text{Zr}_{41.2}\text{Ti}_{13.8}\text{Cu}_{12.5}\text{Ni}_{10}\text{Be}_{22.5}$ (in short: "Vit.1") revealed two distinct dynamic states by Vogel-Fulcher-Tammann fits of viscosity data [2]. The low-temperature state exhibits Arrhenius-like behaviour, so-called strong liquid, while the high-temperature state is non-Arrhenius, so-called fragile liquid. A viscosity hysteresis was observed (Fig. 1), where the viscosity changes anomalously by ~ 2 orders of magnitude upon heating above the liquidus temperature and during undercooling. The kinetic strong-fragile transition resembles the dynamic crossovers in water and network glass-formers.

To study the thermodynamic and structural origin of the strong-fragile crossover, we carried out high-temperature calorimetric experiments and *in situ* synchrotron X-ray scattering at beam-line BW5 at DORIS in contactless environment using an electrostatic levitator (ESL). Figure 1 shows the heat capacity c_p of Vit.1 measured in reference to sapphire. A c_p peak is observed on heating between 1100 K and 1200 K, above the reported liquidus temperature 1026 K. The heat gain of the c_p peak is ~ 1 kJ g-atom^{-1} , about 10% of the enthalpy of fusion. The result of *in situ* X-ray diffraction shows no sharp Bragg peaks between 1100 K and 1200 K, indicating that the c_p peak occurs in the liquid state and cannot be attributed to melting of crystals. The dash-dot line in the lower part of Fig. 1 is the deeply super-cooled c_p data from $c_p/\text{emissivity}$ measured in an ESL by Ohsaka et al. [3].

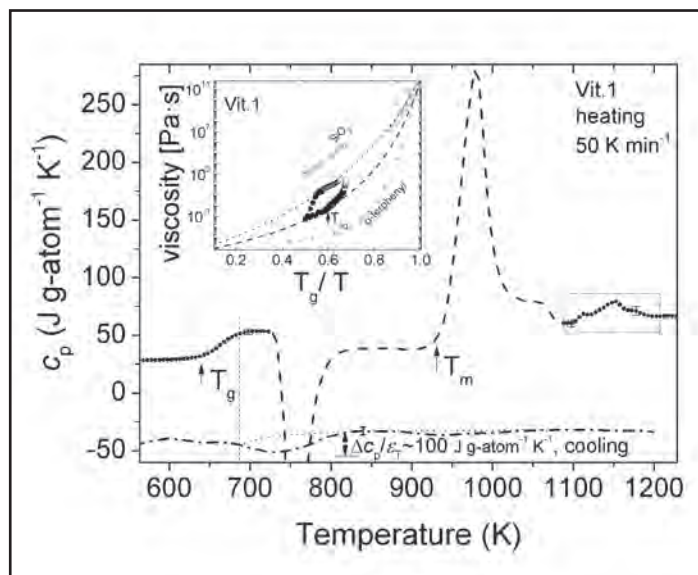


Figure 1

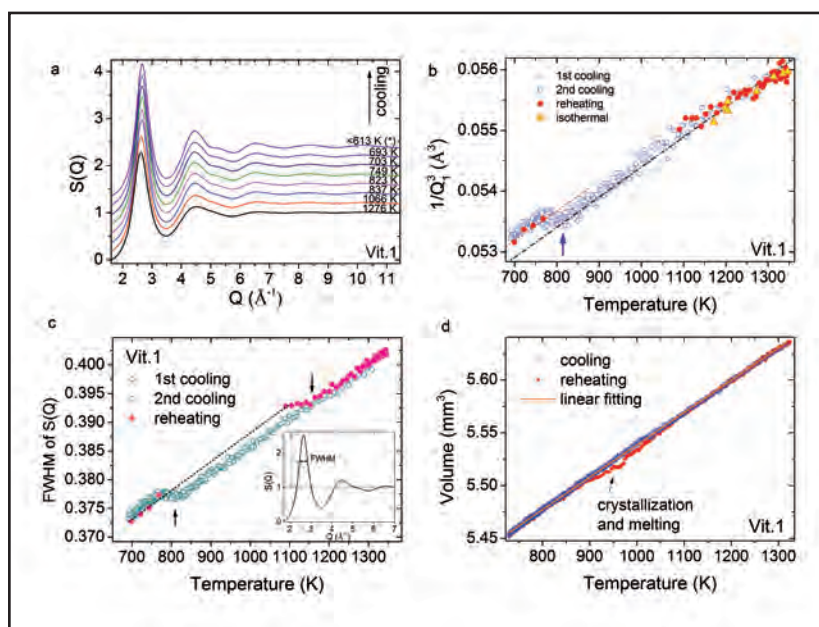
Heat capacity c_p of Vit.1. Solid dots represent the c_p for glassy and liquid states; the dashed curve is c_p for crystallization and melting processes. A c_p peak is observed at around 1150 K. In the lower part, the dash-dot curve represents the heat capacity during cooling, plotted as negative values to indicate the heat release around 700 - 800 K in the supercooled liquid [3]. Inset: viscosity hysteresis observed in the melt.

An exothermic peak was reported around 700-800 K with an enthalpy release ~ 900 J g-atom^{-1} , which appeared to be associated with the c_p peak on heating (1100 - 1200 K) when the viscosity hysteresis and structural measurements were taken into account.

Synchrotron X-ray scattering combined with ESL allows us to study the structural changes of liquids in the deeply super-cooled regime due to the absence of heterogeneous nucleation sites. The total structure factors $S(Q)$ (Fig. 2a) were extracted from the diffracted intensity data. In Fig. 2b, the first peak position of $S(Q)$ is denoted as Q_1 , which is plotted as $1/Q_1^3$ in the volume dimension (\AA^3) against temperature. A sudden

Figure 2

Structural changes in the liquid and volume measurements. a) Examples of $S(Q)$ on cooling from about 1300 K to ~610 K. $S(Q)$ are vertically shifted for clarity. b) $1/Q_1^3$ (\AA^3) on cooling (open symbols) and on heating (red dots). c) FWHM of 1st peaks of $S(Q)$ (see Inset) during thermal cycles. d) Liquid volume measured in ESL during cooling and reheating. The deviation of the macroscopic volume (density) data on reheating (arrow) from the data on cooling is due to partial crystallization and re-melting around 800 - 1100 K, which is the temperature range where the XRD data for the liquid state are not available on reheating, seen as a data-gap between the solid dots in Fig. 2b, c.



change in the temperature dependence of $1/Q_1^3$ is observed at around 830 K during undercooling (open symbols). The sudden shift in $1/Q_1^3$ suggests a medium-range-order change in the Zr-dominant interatomic correlations in real space. The solid symbols represent $1/Q_1^3$ on reheating, which reproduce the values during cooling, except for the range from 770 to 1091 K. In this temperature interval, the sample devitrified on heating and measurements on the liquid state are not possible.

Fig. 2c shows the full width at half maximum (FWHM) of the first peak of $S(Q)$. An abrupt change of the FWHM during cooling (open symbols) occurred around 760 - 830 K. This is the same feature as the sudden change observed in $1/Q_1^3$ in Fig. 2b. On reheating, after the system returns to the liquid state at high temperature (~1100 K), the data points exhibit a clear change of slope at around ~1150 K, which corresponds to the temperature range where the c_p peak is observed in the calorimeter (Fig. 1). The changes on cooling and reheating appear as a reversible phenomenon and the data in Fig. 2c display a form of three quarters of a hysteresis when the missing data gap is extrapolated as the dashed line from the lower temperature data.

Both c_p peaks in Fig. 1 correspond to a similar enthalpy change (~1 kJ g-atom⁻¹) and form a hysteresis with respect to tem-

perature, which is comparable to the viscosity hysteresis of the strong-fragile crossover [2]. The correlation between thermodynamics and kinetics is suggested by Adam-Gibbs theory, at least, qualitatively. These hysteresis are consistent with the hysteresis-like behaviour in $1/Q_1^3$ and FWHM of the structure factors $S(Q)$ (Fig. 2b, c). These findings suggest that there exists a reversible weak first-order liquid-liquid transition between two liquid phases with different entropies, fragilities and local structures in the investigated system.

Furthermore, volume measurements (Fig. 2d) using ESL showed no anomalous change at the temperature range of 750 - 830 K and 1100 - 1200 K. This indicates that the entropy fluctuation is the dominant term in the liquid-liquid transition instead of a density fluctuation.

In summary, our study provides an important contribution to experimental studies of liquid-liquid transitions in bulk metallic glass-forming systems. We expect to find liquid-liquid transitions also in other strong liquids above their respective T_g [4], including Zr-based bulk metallic glass-formers [5], if crystallization is avoided.

Contact: Shuai Wei, shuai.wei@mx.uni-saarland.de

Authors

Shuai Wei¹, Fan Yang², Jozef Bednarcik³, Ivan Kaban⁴, Olga Shuleshova⁴, Andreas Meyer² and Ralf Busch¹

1. Materials Science and Engineering Department, Saarland University, Campus C63, D-66123 Saarbrücken, Germany
2. Institut für Materialphysik im Weltraum, Deutsches Zentrum für Luft- und Raumfahrt (DLR), D-51147 Köln, Germany
3. Deutsches Elektronen-Synchrotron DESY, Notkestrasse 85, D-22603 Hamburg, Germany
4. IFW Dresden, Institute for Complex Materials P.O. Box 270116, D-01171 Dresden, Germany

Original publication

"Liquid-liquid transition in a strong bulk metallic glass-forming liquid", *Nat. Commun.* DOI: 10.1038/ncomms3083.

References

1. C. A. Angell, "Insights into Phases of Liquid Water from Study of Its Unusual Glass-Forming Properties", *Science* 319, 582-587 (2008).
2. C. Way, P. Wadhwa, and R. Busch, "The influence of shear rate and temperature on the viscosity and fragility of the $Zr_{41.2}Ti_{13.8}Cu_{12.5}Ni_{10}Be_{22.5}$ metallic-glass-forming liquid", *Acta Mater.* 55, 2977-2983 (2007).
3. K. Ohsaka et al., "Specific volumes of the $Zr_{41.2}Ti_{13.8}Cu_{12.5}Ni_{10}Be_{22.5}$ alloy in the liquid, glass, and crystalline states", *Appl. Phys. Lett.* 70, 726-728 (1997).
4. S. Wei, I. Gallino, R. Busch, and C. A. Angell, "Glass transition with decreasing correlation length during cooling of $Fe_{50}Co_{50}$ superlattice and strong liquids", *Nature Phys.* 7, 178-182 (2011).
5. Z. Evenson, T. Schmitt, M. Nicola, I. Gallino, and R. Busch, "High temperature melt viscosity and fragile-to-strong transition in Zr-Cu-Ni-Al-Nb(Ti) and $Cu_{47}Ti_{34}Zr_{11}Ni_8$ bulk metallic glasses", *Acta Mater.* 60, 4712-4719 (2012).

Synthesis of metastable polymorphs.

New way of producing an orthorhombic In_2O_3 polymorph

Indium oxide In_2O_3 – a transparent semiconductor with intrinsic n-type character – serves as a prototypical material for diverse applications including touch displays, solar cells, thermoelectrics and gas sensors. Fundamental studies of different In_2O_3 polymorphs will significantly enhance the structure–property understanding in indium oxide; the latter, in turn, will allow for guiding synthetic approaches towards improved optical and electronic properties of transparent conductive oxides and development of improved electronic devices. The way is now open for the physico-chemical characterization and for growing single crystals of a new orthorhombic σ' - In_2O_3 polymorph which is synthesized from rhombohedral corundum-type $\text{rh-In}_2\text{O}_3$ at moderate high-pressure (8 - 9 GPa) and high-temperature conditions (600 - 1100 °C) and recovered to ambient pressure and temperature. The crystals structure data at ambient conditions confirm unambiguously the Rh_2O_3 -II-type structure.

Four In_2O_3 polymorphs have been synthesized so far. Cubic bixbyite-type $\text{c-In}_2\text{O}_3$ (C-type structure of rare-earth oxides, $Ia-3$, No. 206) and rhombohedral corundum-type $\text{rh-In}_2\text{O}_3$ (space group $R-3c$, No. 167) are accessible through solution-based and solvo-thermal routes [1]. Orthorhombic Rh_2O_3 -II-type σ' - In_2O_3 ($Pbcn$, No. 60) and $\alpha\text{-Gd}_2\text{S}_3$ -type σ'' - In_2O_3 ($Pnma$, No. 62) polymorphs were observed at pressures over 8.1 and 19.9 GPa, respectively. Upon decompression they transformed to $\text{rh-In}_2\text{O}_3$ [2, 3]. In our previous work we succeeded to recover σ' - In_2O_3 to ambient pressure and temperature from a laser heated diamond anvil cell experiment [4]. However, due to a very limited amount of the specimen, only a few crystals of the size $< 10^{-4} \text{ mm}^3$ were available, the crystal structure of σ' - In_2O_3 at ambient conditions was not unambiguously confirmed.

In this work we explore alternative high pressure routes towards producing large amounts of the σ' - In_2O_3 polymorph. In contrast to previous studies [2, 3, 4], we used corundum-type $\text{rh-In}_2\text{O}_3$ as a starting material. The reasons are as follows: Firstly, we are guided by theoretical calculations that suggest using the metastable corundum-type $\text{rh-In}_2\text{O}_3$ as starting material for the high pressure synthesis of the orthorhombic σ' - In_2O_3 polymorph. The rh- to σ' - In_2O_3 transition occurs above 6.4 GPa (arrow 1 in Fig. 1(a)) and thus below the c- to σ' - In_2O_3 (arrow 2 in Fig. 1(a)). Secondly, the computed activation barrier for the collective transition $\text{rh-In}_2\text{O}_3 \rightarrow \sigma'$ - In_2O_3 is 0.4 eV per In_2O_3 (i.e. ~ 650 °C) at the transition pressure 6.4 GPa (Fig. 1b); consequently, we expect a fast transition. Thirdly, even if other corundum-type oxides including Cr_2O_3 , Fe_2O_3 and Al_2O_3 transform to Rh_2O_3 -II-type structure under high pressure, none of them have been recovered to ambient conditions so far. Hence, the availability of Rh_2O_3 -II-type σ' - In_2O_3 at ambient conditions will contribute to a better understanding of the structural chemistry and properties of other binary oxides, too.

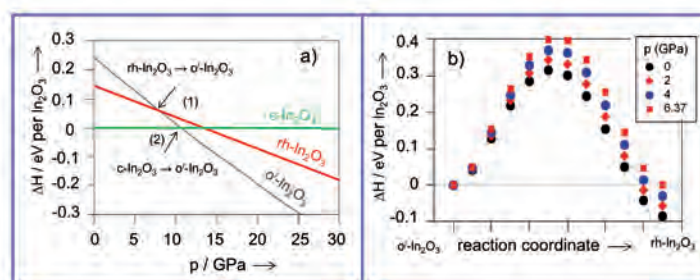


Figure 1

(a) A part of the enthalpy-pressure (ΔH - p) diagram for indium oxide polymorphs, $\text{c-In}_2\text{O}_3$ is a reference structure. Arrows indicate transitions (1) $\text{rh-In}_2\text{O}_3 \rightarrow \sigma'$ - In_2O_3 and (2) $\text{c-In}_2\text{O}_3 \rightarrow \sigma'$ - In_2O_3 . (b) The relative enthalpy (per f.u. In_2O_3) between σ' - In_2O_3 and $\text{rh-In}_2\text{O}_3$ polymorphs at 0, 2, 4, and 6.4 GPa.

In the first step, we followed the phase transitions in indium oxide *in situ* under high pressure high temperature conditions in multi-anvil assemblies by energy-dispersive X-ray diffractometry at the two stage 6-8 MAX200X multi-anvil press at beamline W2 at DORIS III. To avoid reflections from the sample environment we used a new multi-anvil assembly with low X-ray absorption [5]. Fig. 2(a) displays the *in situ* energy dispersive X-ray diffraction patterns of In_2O_3 compressed to 9.0 GPa and heated up to 600 °C. At room temperature $\text{rh-In}_2\text{O}_3$ remains stable upon compression up to 9.0 GPa. The broadening of the XRD reflections, which is due to the deviatoric stress, is reduced by heating the specimen at 9.0 GPa. At 600 °C, the reflections, corresponding to $\text{rh-In}_2\text{O}_3$, start to vanish and a series of new reflections appears. These reflections represent a characteristic pattern of an orthorhombic σ' - In_2O_3 polymorph.

The complete transformation from $\text{rh-In}_2\text{O}_3$ to σ' - In_2O_3 takes less than 20 seconds at 600 °C and 9 GPa, indicating fast kinetics for a diffusionless transition (Fig. 1b). The XRD pattern of

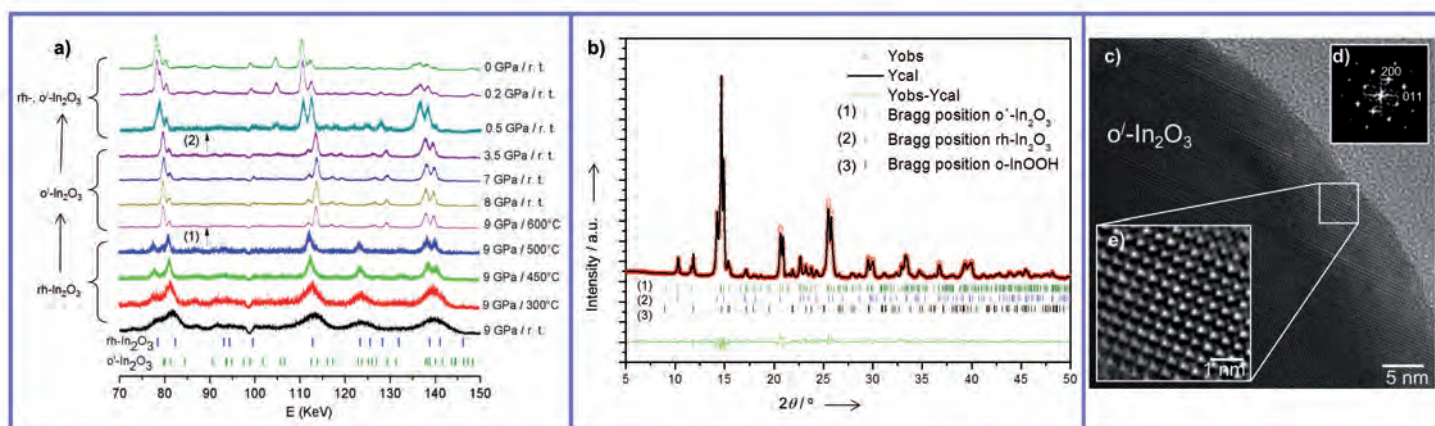


Figure 2

a rapidly quenched specimen from 600 °C to room temperature at 9.0 GPa possesses only σ' - In_2O_3 reflections. During decompression at room temperature, σ' - In_2O_3 partially transforms to corundum $\text{rh-In}_2\text{O}_3$ at a pressure below 1.0 GPa (arrow 2 in Fig. 2a). The structure refinement of the specimen recovered to ambient pressure confirms the coexistence of σ' - In_2O_3 (fraction: 80.0 wt.%), $\text{rh-In}_2\text{O}_3$ (15.9 wt.%) and o-InOOH (4.1 wt.%) as a side phase (Fig. 2b).

In the second step, the crystal structure of σ' - In_2O_3 has been confirmed by High Resolution Transmission Electron Microscopy. Fig. 2(c) shows a HRTEM micrograph of a small area ($\sim 300 \text{ nm}^2$) of an individual σ' - In_2O_3 crystal. The diffraction pattern (Fig. 2d) obtained from the boxed area by means of Fourier Filtered Transform (FFT) of the (200) and (011) reflections of the orthorhombic structure and the Fourier-filtered image (Fig. 2e) from the same boxed area have been used to determine the d -spacings. The d -spacings related to the (200) and (011) reflections (3.96 Å and 3.92 Å, respectively) shown in the inset with the diffraction pattern are well resolved in the Fourier-filtered image, confirming unambiguously the σ' - In_2O_3 ($Pbcn$, No. 60, $a = 7.9295(1)$, $b = 5.4821(2)$, $c = 5.5898(6)$ Å) structure. These results are in a perfect agreement with refinement of the structure (Fig. 2b).

In the next step we confirmed the synthesis of σ' - In_2O_3 in a toroid type high pressure device that allows for obtaining larger material quantities as well as fast compression/decompression rates and less experimental preparation times compared to multi-anvil

a) *In situ* energy-dispersive XRD patterns in multi-anvil assemblies of a $\text{rh-In}_2\text{O}_3$ specimen compressed at 9.0 GPa and heated up to 600 °C. Arrows indicate the complete phase transition $\text{rh-In}_2\text{O}_3 \rightarrow \sigma'$ - In_2O_3 (1) and the partial σ' - In_2O_3 transformation to $\text{rh-In}_2\text{O}_3$ (2). (b) Structure refinement of a specimen recovered from the *in situ* multi-anvil cell experiment showing observed (red dots) and calculated (black solid line) intensities. Tick marks refer to positions of σ' - In_2O_3 , $\text{rh-In}_2\text{O}_3$ and o-InOOH Bragg reflections. (c) HRTEM of a small area ($\sim 300 \text{ nm}^2$) of an individual σ' - In_2O_3 crystal. (d) The diffraction pattern obtained from the boxed area by means of Fourier Filtered Transform (FFT) of the (200) and (011) reflections of the orthorhombic structure. (e) Fourier-filtered image from the boxed area. The d -spacings related to the (200) and (011) reflections (3.96 Å and 3.92 Å, respectively) are well resolved.

devices. The starting material ($\text{rh-In}_2\text{O}_3$) is compressed to 8 GPa and heated at $\sim 1000 - 1100$ °C for 10 min. The structure refinement (not shown here) confirms our finding from the *in situ* multi-anvil experiments and shows the coexistence of σ' - In_2O_3 (fraction: 63.8 wt.%), $\text{rh-In}_2\text{O}_3$ (31.5 wt.%) and o-InOOH (4.7 wt.%) as a side phase in the recovered sample.

Our study shows that orthorhombic σ' - In_2O_3 can be synthesized from rhombohedral corundum-type $\text{rh-In}_2\text{O}_3$ at moderate high pressure and high temperature conditions (8 - 9 GPa, 600 - 1100 °C) in a multi-anvil and toroid press and recovered to ambient conditions. Our experimental setup makes the orthorhombic σ' - In_2O_3 polymorph available in large quantities for further physico-chemical characterization and provides an opportunity for growing σ' - In_2O_3 as single crystals.

Contact: Aleksander Gurlo, gurlo@materials.tu-darmstadt.de

Authors

Maged F. Bekheet¹, Marcus Schwarz², Stefan Lauterbach¹, Hans-Joachim Kleebe¹, Peter Kroll³, Ralf Riedel¹ and Aleksander Gurlo¹

- Fachbereich Material- und Geowissenschaften, Technische Universität Darmstadt, D-64287 Darmstadt, Germany
- Technische Universität Bergakademie Freiberg, Freiberg High Pressure Research Centre, Institut für Anorganische Chemie, D-09599 Freiberg, Germany
- Department of Chemistry and Biochemistry, The University of Texas at Arlington, Arlington, Texas 76019-0065, USA

Original publication

"Orthorhombic In_2O_3 : A Metastable Polymorph of Indium Sesquioxide", *Angew. Chem. Int. Ed.*, 52: 6531–6535 (2013).

References

- A. Gurlo, P. Kroll, R. Riedel, "Metastability of corundum-type In_2O_3 ", *Chem. - Eur. J.* 2008, 14, 3306-3310 (2008).
- H. Yusa, T. Tsuchiya, N. Sata, Y. Ohishi, "Rh₂O₃(II)-type structures in Ga₂O₃ and In₂O₃ under high pressure: Experiment and theory", *Phys. Rev. B*, 77, 064107 (2008).
- H. Yusa, T. Tsuchiya, J. Tsuchiya, N. Sata, Y. Ohishi, "α-Gd₂S₃-type structure in In₂O₃: Experiments and theoretical confirmation of a high-pressure polymorph in sesquioxide", *Phys. Rev. B*, 78, 092107 (2008).
- A. Gurlo, D. Dzivenko, P. Kroll, R. Riedel, "High-pressure high-temperature synthesis of Rh₂O₃-II-type In₂O₃ polymorph", *Phys. Stat. Sol. - RRL*, 2, 269-271 (2008).
- M. Schwarz, T. Barsukova, C. Schimpf, D. Šimek, C. Lathe, D. Rafaja, E. Kroke, (Poster) HASYLAB Users' Meeting, Hamburg, Germany, 2010.

Dramatic compaction of a protein complex upon tRNA binding.

Synchrotron light reveals a spectacular quaternary structure transition

Yeast bacterial proteins, aminoacyl-tRNA synthetases (aaRS) GluRS and MetRS, form a complex with an auxiliary protein Arc1p, and the ternary complex further binds two transfer RNA (tRNA) molecules. We have analyzed the yeast Arc1p-complexes in solution by small-angle X-ray scattering (SAXS). The ternary complex of MetRS and GluRS with Arc1p displays a peculiar extended star-like shape, implying possible flexibility of the complex. Binding of the tRNAs leads to a dramatic compaction of the pentameric complex compared to the ternary one. A hybrid model of the pentameric complex is constructed rationalizing the compaction effect by the interactions of negatively charged tRNA backbones with the positively charged tRNA-binding domains of the synthetases.

Aminoacyl tRNA synthetases (aaRS) play an essential role during protein translation. They are enzymes catalyzing aminoacylation or “charging”, i.e. addition of a specific amino acid onto the corresponding tRNA molecule to form an aminoacyl-tRNA. The aaRSs ensure the accuracy of the aminoacylation of the appropriate tRNA *via* nucleotide determinants, which define the identity of the tRNA [1]. Upon charging of the tRNA the amino acid can further be transferred from the tRNA onto the protein molecule being synthesized.

Whereas prokaryotic aaRS typically function as monomers or homo-dimers, eukaryotic aaRS show heteromeric interactions because of the more complicated organization of the eukaryotic cells. The eukaryotic aaRS possess additional protein-tRNA binding domains and form higher order complexes compared to the prokaryotic aaRS. In yeast, the aminoacyl tRNA synthetase complex is formed by two class I synthetases, MetRS and GluRS and the aminoacyl cofactor Arc1p. While the biochemistry of yeast Arc1p-complex is well characterized [2], the structural information is available only on the enzymatic domains of the individual aaRSs but not on their complexes. Both MetRS and GluRS bind through their N-terminal domains to the N-terminal domain of Arc1p and the synthetases bind to largely independent sites. tRNA^{Met} and tRNA^{Glu} simultaneously bind to their cognate synthetase as well as to Arc1p, whereby the synthetases bind their cognate tRNAs via their C-terminal domains [1].

In the present work, synchrotron small-angle X-ray scattering (SAXS) was employed to elucidate the quaternary structure of the ternary Arc1p complex and of the full pentameric assembly with the two tRNAs in solution. To characterize the peculiarities of the yeast Arc1p-complexes we have studied the three individual proteins (MetRS, GluRS and Arc1p), two binary complexes MetRS:Arc1p and GluRS:Arc1p, the ternary complex and the pentameric complex containing the two RNA molecules, tRNA^{Met} and tRNA^{Glu}. The complexes were reconstituted *in vitro* from the purified components and the complex formation and in-

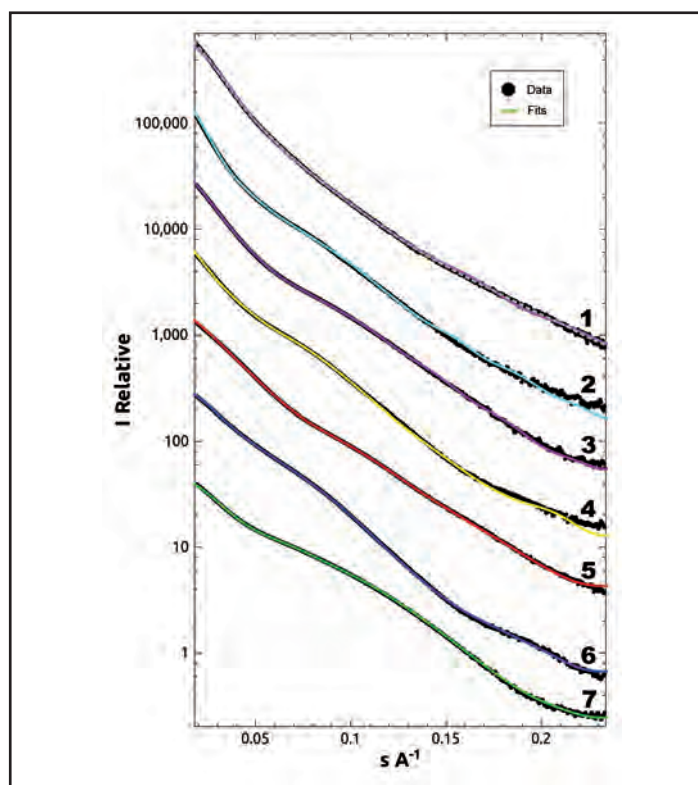


Figure 1

Experimental SAXS curves and the scattering from the structural models of the Arc1p complexes and individual proteins. The experimental data are shown in black dots, the ab-initio fits for each data set and the final rigid body fit for the pentameric complex as lines. 1: Pentameric complex MetRS:GluRS:Arc1p:tRNAs (gray dashed line: ab initio fit, purple: SASREF refined rigid body fit); 2: Trimeric complex (yellow); 3: GluRS:Arc1p (ilac); 4: MetRS:Arc1p complex (yellow); 5: GluRS (red) 6: MetRS (blue); 7: Arc1p (green).

Logarithms of the scattering intensity are displayed as functions of momentum transfer $s = 4\pi \sin(\theta)/\lambda$, where $\lambda = 1.5 \text{ \AA}$ is the X-ray wavelength and 2θ is the scattering angle.

The scattering patterns are appropriately displaced along the logarithmic axis for clarity.

corporation of the relevant tRNA molecules was controlled by gel filtration chromatography, SDS-PAGE and radioactive electro-

phoretic mobility shift assay. The processed SAXS data recorded at the EMBL beamline X33 on the DORIS III storage ring at DESY using a robotic sample changer [3] are presented in Fig. 1.

An advanced multiphase *ab initio* model of the ternary complex was built using the program MONSA [4]. Here, the ternary complex is represented by three “phases” (assemblies of beads), belonging to Arc1p, MetRS and GluRS, and simulated annealing is employed to distribute these beads in such a way that the measured data from the individual proteins, binary and ternary complexes are simultaneously fitted by a single model. A typical MONSA reconstruction in Fig. 2A, B, reveals a distinct star-like assembly of the elongated individual proteins. The available structures of the N-termini and the homologs of the C-termini of the individual proteins are well fitted within the appropriate envelopes (Fig. 2A, B) where the individual domains interact with each other in agreement with previous biochemical and structural data [2].

These data indicate that the extended conformations of the free protein subunits are preserved in the trimeric complex. This is not the case for the pentameric complex, whose *ab initio* shape (Fig. 2C, D) appears as a globular particle, significantly more compact than the trimeric complex. To further understand this result, available high resolution fragments of the protein termini were fitted in the envelope of the pentameric complex accounting for the surface charges and the tRNA binding sites of the proteins. The tentative model was further refined by rigid body modelling using the program SASREF [5] by fitting the data while keeping the major protein-RNA interfaces. The refined model is displayed together with the *ab initio* shape in Fig. 2C, D. Analysis of the electrostatic interactions indicates that the synthetases and Arc1p show positive surface charges at the binding sites of the negatively charged tRNAs.

The use of synchrotron SAXS thus allowed us to observe a totally unexpected effect, a drastic compaction of a protein complex upon tRNA binding. A compaction effect of such magnitude, literally a collapse, has, to our knowledge, not been reported before for nucleoprotein complexes. These impressive rearrangements of the subunits are most probably due to the surface charges of the individual protein domains. Electrostatic repulsion

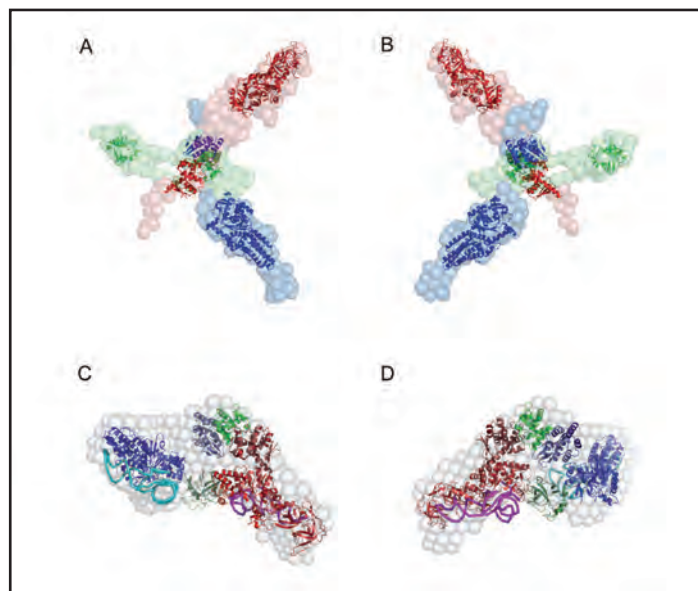


Figure 2

Low resolution shapes and hybrid models of Arc1p complexes. The *ab initio* models are displayed as beads, the high resolution structures and homology models as cartoons. (A, B): two views of the trimeric complex (GluRS, red; MetRS, blue and Arc1p, green). (C, D), two views of the pentameric complex (*ab initio* model, gray protein colours as in (A,B), tRNA^{Glu} is depicted in magenta and tRNA^{Met} in cyan.

of the positively charged tRNA-binding domains of the synthetases as well as Arc1p may cause the star-like arrangement of the proteins in the trimeric complex. In the pentamer, the negatively charged tRNA backbones induce the contraction of these domains. The flexible links connecting the protein domains facilitate these rearrangements.

In yeast as well as in eukaryotic cells, it is important to have an effective translation machinery because of the size and complexity of the cell. The pentameric complex has a higher affinity and specificity of binding the tRNAs and ensures faster aminoacylation compared to binary synthetase-tRNA complexes as observed in prokaryotes. The present structural results have therefore clear functional implications in the context of the efficiency of the translational mechanism.

Contact: Dmitri Svergun, Svergun@embl-hamburg.de

Authors

Christine Koehler¹, Adam Round², Hannes Simader³, Dietrich Suck¹ and Dmitri Svergun⁴

1. Structural and Computational Biology Unit, European Molecular Biology Laboratory EMBL, D-69117 Heidelberg, Germany

2. EMBL UVHCI, F-38042 Grenoble, Cedex 9, France

3. Proteros Biostructure, D-82152 Martinsried-München, Germany

4. EMBL Outstation Hamburg, c/o DESY, European Molecular Biology Laboratory, D-22603 Hamburg, Germany

The first two authors should be regarded as joint First Authors.

Original publication

“Quaternary structure of the yeast Arc1p-aminoacyl-tRNA synthetase complex in solution and its compaction upon binding of tRNAs”, *Nucleic Acids Res* 7, 667-676 (2013).

References

1. M. Ibba, D. Söll, “Aminoacyl-tRNA Synthesis”, *Annu. Rev. Biochem.* 69, 617-650 (2000).
2. G. Simos, A. Sauer, F. Fasiolo, E. C. Hurt “A conserved domain within Arc1p delivers tRNA to aminoacyl-tRNA synthetases”, *Mol. Cell.* 1, 235-242 (1998).
3. C. E. Blanchet, A. V. Zozulya, A. G. Kikhney, D. Franke, P. V. Konarev, W. Shang, R. Klaering, B. Robrahn, C. Hermes, F. Cipriani, D. I. Svergun and M. Roessle, “Instrumental setup for high-throughput small- and wide-angle solution scattering at the X33 beamline of EMBL Hamburg”, *J. Appl. Crystallogr.* 45, 489-495 (2012).
4. D. I. Svergun, “Restoring low resolution structure of biological macromolecules from solution scattering using simulated annealing”, *Biophys. J.* 76, 2879-2886 (1999).
5. M. V. Petoukhov, D. I. Svergun, “Global rigid body modelling of macromolecular complexes against small-angle scattering data”, *Biophys. J.* 89, 1237-1250 (2005).

Linking molecular structure and cellular reprogramming.

Learning from the Oct4 crystal

Mature cells can be reprogrammed to pluripotency and thus reacquire the ability to divide and differentiate into specialized cell types. Reprogramming can be achieved by induced expression of a cocktail of a few specific transcription factors, including Oct4. Many of the biochemical events that underlie the reprogramming process, however, are still not understood. We shed new light on this process revealing important details about the structure of the transcription factor Oct4. The crystal structure of Oct4 in complex with specific DNA allowed identifying residues located at a linker region between the two DNA binding sub-domains that are essential to its reprogramming activity.

Induced pluripotent stem (iPS) cells are a type of stem cell artificially derived from a differentiated adult cell by inducing the expression of specific genes. The first generations of iPS cells were obtained by the expression of four transcription factors (Oct4, Sox2, c-Myc, and Klf4) in mouse and human fibroblasts [1, 2]. Important hopes have germinated on employing this type of stem cells for medical applications. Proof-of-principle evidence of using iPS cells to produce human organs usable for transplantation has been established [3]. Nevertheless, some technical limitations indicate that the first clinical tests are not yet in near reach. Indeed, the reprogramming process is slow and has a low success rate. More worrisome is the propensity of the iPS cells to form tumours since some of the expressed transcription factors present oncogene activity. Insights into the molecular events that govern these processes are extremely valuable since they provide mechanistic information allowing the cell reprogramming to be refined, thus rendering them potentially powerful medical instruments.

The transcription factor Oct4, a member of the POU family, binds to DNA and controls various genes involved in reprogramming the cells. Interestingly, all proteins of the reprogramming cocktail except Oct4 are replaceable, indicating a very crucial role of Oct4. The DNA binding domain is highly conserved within the POU family except a short residue stretch linking the two DNA binding elements that is highly variable in sequence and length. Up to now, most of the structural data on the POU family were obtained on the functionally unrelated Oct1 transcription factor and its linker region could not be observed [4, 5].

To address the specific role of the domain/domain linker sequence in Oct4, we have determined the crystal structure of Oct4 using high intensity X-ray synchrotron radiation beamlines at the

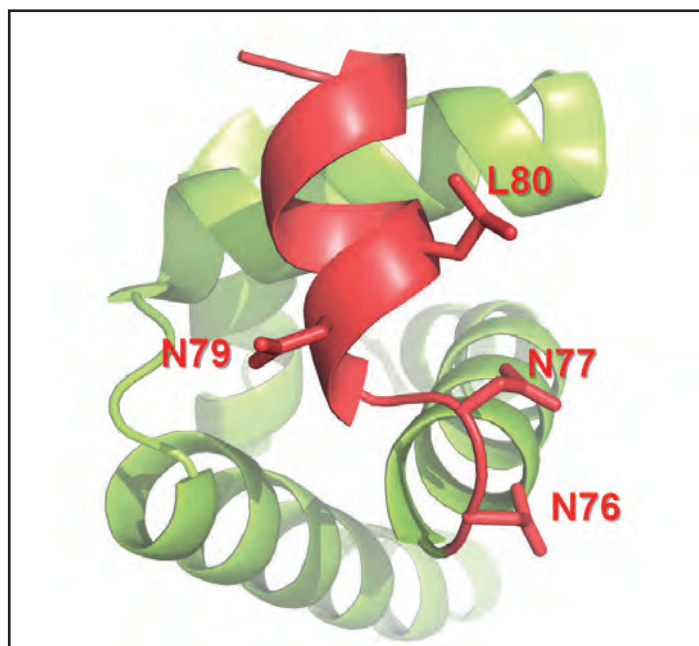


Figure 2

Close-up of the linker region. Reprogramming is impaired by the replacement of the shown residues by alanines.

ESRF in Grenoble and EMBL/DORIS in Hamburg. Contrary to previous structures of Oct1, in Oct4 the linker region has a helical structure and is exposed at the surface of the protein (Fig. 1). Based on these structural findings, we designed several substitutions to elucidate the importance of several residue positions in the linker. Replacement of the human Oct4 linker by the sequence either from mouse or xenopus (a species of frog) keeps Oct4 capable of reprogramming cells. Conversely, when the human Oct4 linker is replaced with that from zebrafish

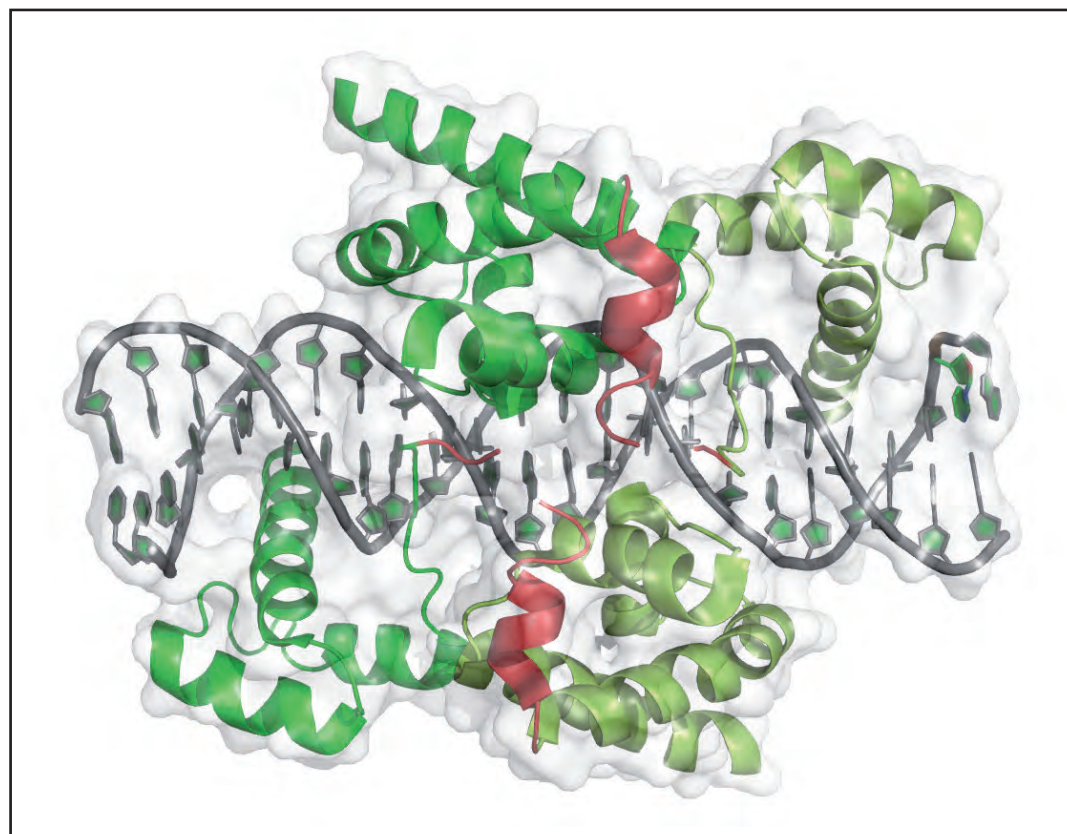


Figure 1

In the crystal structure, two Oct4 molecules (green, pale green) interact with a DNA recognition element. The linker exposed at the surface of the protein is depicted in red.

or medaka, two species of fish representing more distantly related organisms, reprogramming does not occur any further. Based on these data, we systematically mutated exposed linker residues and observed that these mutations although not affecting the basic activity of the protein such as the DNA binding, impaired the cell reprogramming function of Oct4 (Fig. 2). Conversely, mutations of the buried residues of the linker did not affect reprogramming negatively.

Based on these findings, we hypothesized that the linker may recruit key partners to Oct4 target genes, without which the process of reprogramming cannot be completed. Investigation of the interactome of one of the selected mutants (L80A) by mass spectrometry indeed demonstrated that it lost the ability to recruit essential protein partners. One of them, Smarca4 is a regulator of both the epigenetic repression and activation that improves reprogramming efficiency [6]. Another one, Chd4, is

part of the chromatin remodelling complex NuRD, which was shown to safeguard pluripotency in embryonic stem cells (ES cells). All these data indicate that Oct4 may serve as a recruiting platform during the epigenetic transition from a differentiated to a pluripotent cell state. Future research will help determining an integrated picture on how Oct4 acts in the context of many other protein components in stem cell pluripotency. Structural biology will play an important role to further investigate the molecular mechanisms associated with binding to these protein partners.

Contact: Matthias Wilmanns, Wilmanns@embl-hamburg.de

Authors

Daniel Esch¹, Juha Vahokoski², Matthew R. Groves², Vivian Pogenberg², Vlad Cojocaru¹, Hermann vom Bruch¹, Dong Han¹, Hannes C. A. Drexler¹, Marcos J. Araúzo-Bravo¹, Calista K. L. Ng³, Ralf Jauch³, Matthias Wilmanns² and Hans R. Schöler¹

1. Department for Cell and Developmental Biology, Max Planck Institute for Molecular Biomedicine, Röntgenstrasse 20, D-48149 Münster, Germany
2. EMBL-Hamburg, Notkestrasse 85, D-22603 Hamburg, Germany
3. Laboratory for Structural Biochemistry, Genome Institute of Singapore, 60 Biopolis Street, 138672 Singapore, Singapore

Original publication

"A unique Oct4 interface is crucial for reprogramming to pluripotency", *Nature Cell Biol.* 15, 295 (2013).

References

1. K. Takahashi and S. Yamanaka, "Induction of pluripotent stem cells from mouse embryonic and adult fibroblast cultures by defined factors", *Cell* 126, 663-767 (2006).
2. K. Takahashi et al., "Induction of pluripotent stem cells from adult human fibroblasts by defined factors", *Cell* 131, 861-872 (2007).
3. T. Takebe et al., "Vascularized and functional human liver from an iPSC-derived organ bud transplant", *Nature* 499, 481-484 (2013).
4. A. Reményi et al., "Differential Dimer Activities of the Transcription Factor Oct-1 by DNA-Induced Interface Swapping", *Mol. Cell.* 8, 569-580 (2001).
5. A. Reményi, K. Lins, L. J. Nissen, R. Reinbold, H.R. Schöler and M. Wilmanns, "Crystal structure of a POU/HMG/DNA ternary complex suggests differential assembly of Oct4 and Sox2 on two enhancers", *Genes Dev.* 15, 2048-2059 (2003).
6. N. Singhal et al., "Chromatin-remodeling components of the BAF complex facilitate reprogramming", *Cell* 141, 943-955 (2010).

The innate immune sabotage.

A viral protein captures the host immune response

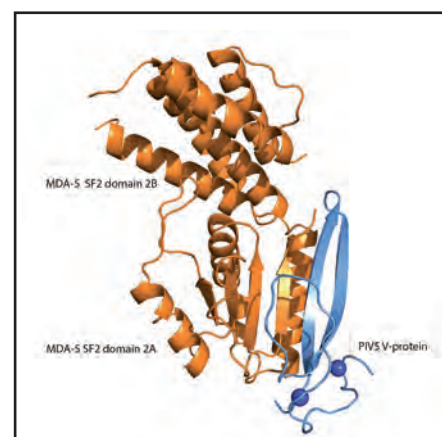
Viruses have developed strategies to escape from or disturb the innate immune response of the host cell. One of the key steps in the detection of intruders is done by pattern recognition receptors, sensing patterns of the intruder and upon this switching on the cellular defence mechanisms. We studied the inhibition of the RIG-I-like pattern recognition receptor MDA-5 by the viral V-protein in a hybrid method approach using X-ray crystallography, small-angle X-ray scattering, electron microscopy and biochemical assays.

The innate immune system is the first line of defence against pathogens entering the cell. These invaders are usually recognized by pattern recognition receptors (PRR) identifying the potential threats via a characteristic molecular pattern, e.g. DNA outside of the nucleus, viral 5'-triphosphate RNA or other specific molecules such as bacterial second messengers and many more. After recognition of these patterns, the innate immune response of the host cell is activated, for instance by stimulating interferon production.

One important class of PRRs are the RIG-I-like receptors comprising RIG-I (retinoic acid-inducible gene I), melanoma differentiation-associated protein 5 (MDA-5) and LGP2 (laboratory of genetics and physiology 2). The domain architecture of RIG-I and MDA-5 is similar: both proteins consist of N-terminal tandem CARD domains needed for downstream signalling, followed by a superfamily-2 ATPase domain (SF2) and a C-terminal RNA-binding motif (regulatory domain, RD) responsible for binding of the viral RNA. Upon binding of the intruders RNA, MDA-5 and RIG-I undergo conformational changes or form multimers leading to exposure and increased local concentration of the CARD-domains. These CARDS then activate downstream signalling leading to interferon response of the cell [1]. On the other side also pathogens evolved strategies to interfere with the activation of the innate immune pathways. For instance, measles virus (and other paramyxoviruses) are producing “V-protein” that enhances pathogenicity and limits interferon response of the host cell by inhibiting MDA-5 and LGP2 (but not RIG-I). Binding of the V-protein abolishes the ATPase-activity of these proteins [2, 3].

We analyzed the interaction between porcine MDA-5 and parainfluenza virus 5 V-protein (PIV5) in a hybrid method approach to understand the structural and biochemical basis of the MDA-5 silencing by the PIV5. We first obtained high-resolution data using protein crystallography. We were able to solve the 2.3 Å resolution crystal structure of the SF2 domain of MDA-5 (residues

Figure 1
Overview of the complex structure of porcine MDA-5 (orange) and PIV5 V-protein (blue). The V-protein has replaced parts of the MDA5 beta sheet region in SF2-domain 2A and structurally disrupted the integrity of the SF2 domain.

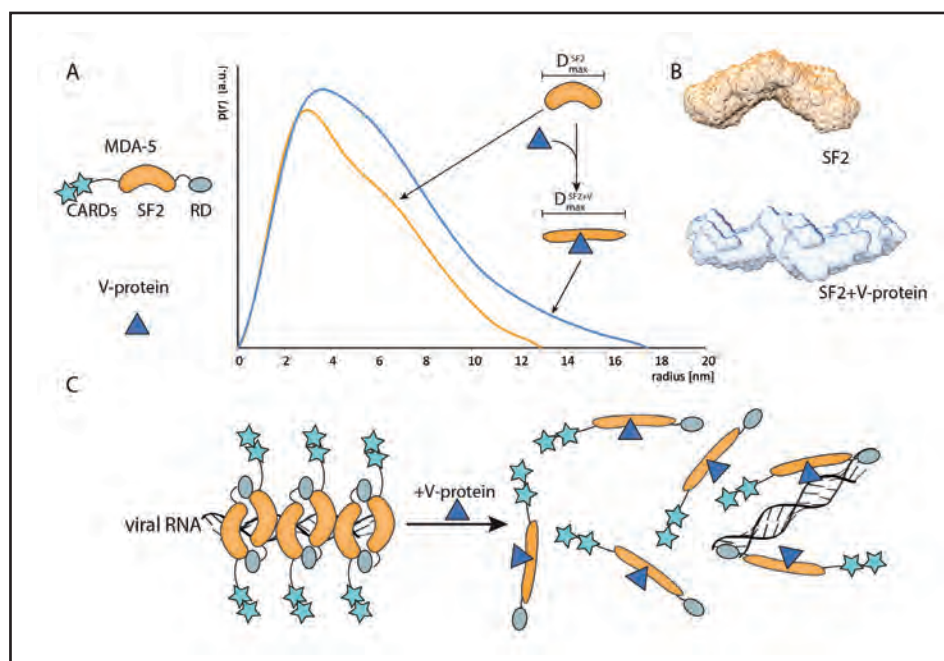


546-808) in complex with PIV5 V-protein (residues 168-219) using diffraction data collected at the ESRF beamline ID23-1. These parts of the two proteins have already been biochemically described to function as the core of the MDA-5/V-protein interaction [4] – and our structure shows how a specific complex is formed. Importantly, two beta strands of the MDA-5 – SF2 ATPase domain 2A have been replaced by the beta-hairpin of the V-protein – leading to a partial disruption of the ATPase motifs and rearrangement of the whole SF2 domain architecture (Fig. 1). This disruption readily explains the reduction of ATPase activity upon binding of the V-protein to MDA-5.

Moreover, taking a closer look at the interface between MDA-5 and PIV5 V-protein reveals the structural basis for the recognition of MDA-5 and LGP2 by the V-protein and also explains why RIG-I is not targeted as two key residues of the interface are not present in RIG-I. Using site directed mutagenesis of these two residues in the SF2 domain of RIG-I we were able to induce robust binding of the V-protein.

However, since the crystal structure of the complex only comprises parts of both proteins, we were interested in the overall structural changes caused by the induced unfolding of the SF2

Figure 2
 A) Schematic depiction of the unfolding of the SF2-domain by the V-protein with corresponding pair-distribution functions from SAXS data and *ab initio* models (B). C) Proposed model for the disruption of MDA-5 filaments by the V-protein and inhibition of the signalosome complex



domain by the V-protein. To monitor these changes in solution small-angle X-ray scattering is the method of choice and thus we performed experiments at the Biological SAXS beamline X33 of the EMBL at DORIS III at DESY. We obtained high quality scattering data at X33 and the results of the SAXS experiments clearly support the idea that unfolding of the MDA-5 SF2 domain, visible on the small-scale in our crystal structure, is translated over the whole molecule. This drastic conformational change is reflected in changes of the overall parameters like maximum particle diameter (D_{max}) and radius of gyration (R_g) – and of course in the shape of the *ab initio* models calculated using the SAXS data.

We first analyzed constructs comprising the complete SF2 domain only. This domain resembles a C-shape in solution as known from homologous crystal structures and also from *ab initio* modelling using the MDA-5 solution scattering data. Upon binding of the V-protein the overall complex is rather elongated, visible in a substantial increase in D_{max} from $D_{max}^{SF2} = 13$ nm to $D_{max}^{SF2+V-protein} = 17.5$ nm, and also supported by changes in the shapes of the *ab initio* models (Fig. 2). Even in the full-length constructs of MDA-5 comprising all domains the changes are still obvious, even though only one of four domains is potentially disrupted by the V-protein.

So how does the unfolding on the small scale affect the downstream signalling of MDA-5? In a proposed model, MDA-5 recognizes viral RNA and forms large filaments that are recognized by the MAVS-proteins on the mitochondrial membrane to form a so called “signalosome” that triggers downstream processes [5]. In presence of the V-protein the MDA-5 SF2-domain is disrupted leading to filament breakdown and thus transmission of the signal is inhibited. We could visualize filament formation of MDA-5 upon binding to RNA and lack of filaments in the presence of the V-protein using negative stain electron microscopy. These data suggest that the V-protein disrupts MDA-5 filaments formation to prevent downstream signalling. Our hybrid methods study provides molecular details of the inhibition of MDA-5 signalling by the viral V-protein and show that V disrupts the SF2 domain of MDA-5. This disruption is affecting the whole MDA-5 architecture as could be shown by SAXS experiments and prevents formation of MDA-5/RNA signalosomes.

Contact: Karl-Peter Hopfner, hopfner@genzentrum.lmu.de
 Gregor Witte, witte@genzentrum.lmu.de

Authors

Carina Motz^{1,‡}, Kerstin Monika Schuhmann², Axel Kirchhofer^{1,†}, Manuela Moldt¹, Gregor Witte¹, Karl-Klaus Conzelmann² and Karl-Peter Hopfner^{1,3}

1. Department of Biochemistry and Gene Center, Ludwig-Maximilians-University, Munich

2. Max von Pettenkofer-Institute and Gene Center, Ludwig-Maximilians-University, Munich

3. Center for Integrated Protein Sciences, Munich

‡ Present address: MRC Laboratory of Molecular Biology, Cambridge

† Present address: Business Consulting, Bayer Business Services GmbH, Leverkusen

Original publication

“Paramyxovirus V proteins disrupt the fold of the RNA sensor MDA5 to inhibit antiviral signaling”, *Science* 339, 690-693 (2013).

References

1. L. A. O’Neill, A. G. Bowie, “The powerstroke and camshaft of the RIG-I antiviral RNA detection machine”, *Cell* 147, 259-261 (2011).
2. J. Andrejeva et al. “The V proteins of paramyxoviruses bind the IFN-inducible RNA helicase, mda-5, and inhibit its activation of the IFN-beta promoter”, *PNAS* 101, 17264-17269 (2004).
3. K. Childs et al. “mda-5, but not RIG-I, is a common target for paramyxovirus V proteins”, *Virology* 359, 190-200 (2007).
4. J. P. Parisien et al. “A shared interface mediates paramyxovirus interference with antiviral RNA helicases MDA5 and LGP2”, *J. Virol.* 83, 7252-7260 (2009).
5. B. Wu et al. “Structural basis for dsRNA recognition, filament formation, and antiviral signal activation by MDA5”, *Cell* 152, 276-289 (2013).

First new crystal structure solved using an FEL.

Natively inhibited *Trypanosoma brucei* cathepsin B

Serial femtosecond crystallography (SFX), allows diffraction data to be acquired from a stream of very small crystals. This new technique has found particular use for studying proteins which do not easily form large crystals, suffer radiation damage when exposed to X-rays, undergo very fast reactions, or perhaps all three at the same time. Until recently, the work using SFX has focused almost entirely on systems with known structures so that the validity of the technique could be assessed. Last year, we reported the first new protein structure obtained using SFX data: a natively inhibited form of an enzyme from a parasite responsible for African sleeping sickness.

The structure of proteins is most often determined by growing crystals of the protein and then studying the diffraction patterns which result from their irradiation by X-rays. The crystalline form scatters X-rays very strongly and provides a convenient repeating arrangement of a very large number of molecules so that the radiation dose can be divided between them. Many proteins form crystals with relative ease, while others are still difficult to form large crystals from, and unfortunately this category includes many proteins which we would be most interested in the structures of. When the crystal size is small, diffraction patterns can be obtained by increasing the intensity of the X-ray beam, by focusing the beam to a smaller size (ideally equal to the size of the crystal) or both. However, very often the crystals cannot withstand the intensity of the X-ray illumination and quickly become damaged or destroyed and unusable.

By using an X-ray free-electron laser instead of a conventional synchrotron beamline or laboratory source, the flux density of the X-ray beam can be increased by many orders of magnitude. Under these conditions, a small crystal of a few microns size can produce a diffraction pattern from a single pulse of only a few tens of femtoseconds duration. The crystal is still destroyed, but now the rate at which the irradiation occurs can be so fast that damage to the crystal structure does not contribute strongly. This technique is called serial femtosecond crystallography (SFX). SFX is also of particular interest for the study of fast chemical reactions, because a diffraction pattern can be acquired from each crystal in such a short period of time.

Until recently, the work performed using SFX has concentrated on validating the technique by applying it to proteins with known structures. The first new structure solved using SFX was published last year. The protein studied was the enzyme cathepsin B from *Trypanosoma brucei*, the parasite responsible for human African sleeping sickness, a disease which causes around

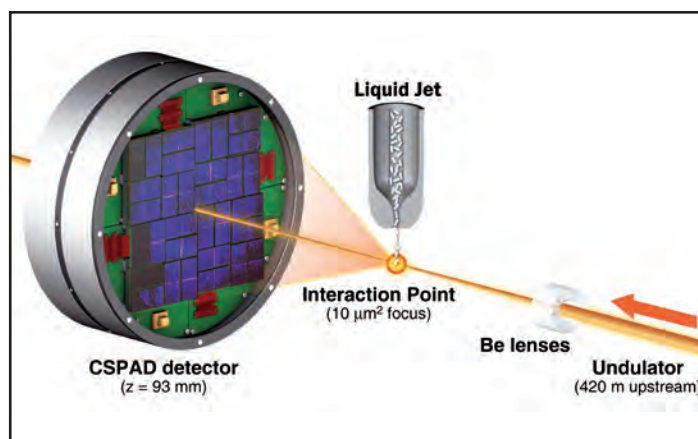


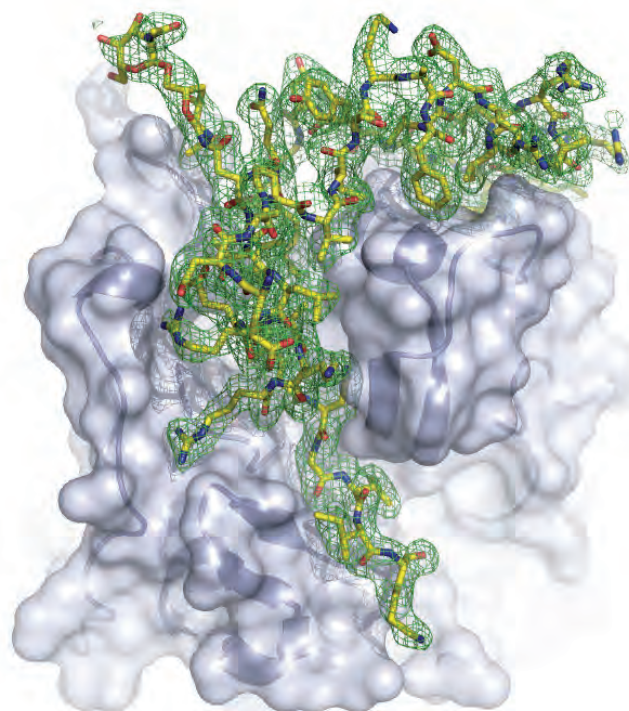
Figure 1

Experimental setup for serial femtosecond crystallography using the CXI instrument at LCLS/SLAC (USA). Reproduced from [2].

30,000 deaths per year, mainly in central Africa. In an earlier article, the formation of crystals of this protein inside living insect cells was described, and initial low-resolution SFX diffraction data was shown [1]. The resolution and data quality in the previous work were both too low to allow the structure to be solved. Now that the first hard X-ray FEL beamlines are available - such as the coherent X-ray imaging (CXI) instrument at the Linac Coherent Light Source (LCLS) where this new work was performed - diffraction data can be acquired with much higher spatial resolution. A high-resolution validity test was previously performed using lysozyme microcrystals [2], and apart from a slightly different distance between the interaction point and the detector, the *in vivo* grown crystals were studied using the same experimental setup, shown in Fig. 1.

Figure 2

Structure of TbCatB determined using X-ray crystallography data from LCLS, showing (in green) the electron density corresponding to the inhibitory propeptide.



The crystals were found to have exceptional compatibility with the injection technique used for SFX, and 293,195 diffraction patterns were acquired in around nine hours of data acquisition at the LCLS pulse rate of 120 pulses per second. 178,875 of these patterns could be processed using the software suite CrystFEL, which was developed at CFEL [3]. This number of patterns is much larger than usual for an SFX experiment, and so the resulting data quality was excellent because of the beneficial averaging effect of increasing the number of measurements.

Although the structure of the cathepsin B molecule itself had been previously determined, its crystal packing was different for the *in vivo* form and had to be newly determined. In addition, carbohydrate molecules bound to the protein were observed, which were not present in the previously determined structural model. We expected this to be the final result of the experiment, but a region of excess electron density was observed close to the substrate binding site of the molecule which was not accounted for by the model. On closer inspection, this density was determined to correspond to a part of the protein molecule which would naturally be removed by the cell during activation.

The function of this “propeptide” is to prevent the enzyme from functioning until it reaches the appropriate part of the cell. This structural information did not appear in the known structure of cathepsin B because the previous work had used the fully functional “mature” form of the enzyme with the propeptide removed. The unexpected visibility of this part of the molecule was therefore very exciting. Since cathepsin B is a protease – a protein which breaks chemical bonds in other proteins – the consequences of it being active in the wrong part of the cell could be very serious and deadly. The direct observation of the way in which nature inhibits the protease is of great potential interest for future drug design efforts, because by mimicking the manner in which the occluding loop binds to the molecule, we might be able to intelligently design a pharmaceutical substance which also inhibits it, preventing the parasite from functioning.

Contact: Thomas White, thomas.white@desy.de
Henry Chapman, henry.chapman@desy.de
Lars Redecke, Lars.Redecke@chemie.uni-hamburg.de

Authors

Lars Redecke, Karol Nass, Daniel P. DePonte, Thomas A. White, Dirk Rehders, Anton Barty, Francesco Stellato, Mengning Liang, Thomas R.M. Barends, Sébastien Boutet, Garth J. Williams, Marc Messerschmidt, M. Marvin Seibert, Andrew Aquila, David Amlund, Sasa Bajt, Torsten Barth, Michael J. Bogan, Carl Caleman, Tzu-Chiao Chao, R. Bruce Doak, Holger Fleckenstein, Matthias Frank, Raimund Fromme, Lorenzo Galli, Ingo Grotjohann, Mark S. Hunter, Linda C. Johansson, Stephan Kasse Meyer, Gergely Katona, Richard A. Kirian, Rudolf Koopmann, Chris Kupitz, Lukas Lomb, Andrew V. Martin, Stefan Mogk, Richard Neutze, Robert L. Shoeman, Jan Steinbrener, Nicusor Timneanu, Dingjie Wang, Uwe Weierstall, Nadia A. Zatsepin, John C. H. Spence, Petra Fromme, Ilme Schlichting, Michael Duszenko, Christian Betzel, Henry N. Chapman
Full author and affiliation details at <http://www.sciencemag.org/content/339/6116/227>.

Original publication

“Natively Inhibited *Trypanosoma brucei* Cathepsin B Structure Determined by Using an X-ray Laser”, *Science* 339, 227-230 (2012).

References

1. R. Koopmann, K. Cupelli, L. Redecke, K. Nass et al., “In vivo protein crystallization opens new routes in structural biology”, *Nature Methods* 9, 259-262 (2012).
2. S. Boutet, L. Lomb, G.J. Williams, T.R.M. Barends et al., “High-Resolution Protein Structure Determination by Serial Femtosecond Crystallography”, *Science* 337, 363-265 (2012).
3. T.A. White, R.A. Kirian, A.V. Martin, A. Aquila, K. Nass, A. Barty and H.N. Chapman. “CrystFEL: a software suite for snapshot serial crystallography”. *J. Appl. Cryst.* 45, 335-341 (2012).

Shock freezing of virus crystals.

Structure determination from a single virus crystal at 100 K

Viruses typically crystallize with large unit cells. As a consequence, successful structure determination requires high X-ray doses, which cause significant radiation damage to the crystals. X-ray data collection at cryogenic temperatures, however, reduces radiation damage effects. Unfortunately, cooling macromolecular crystals to such temperatures is not always possible, especially for large unit cell systems. We have for the first time successfully applied the method of high pressure freezing to virus crystals. Using this technique, a virus structure was determined from one single crystal instead from 28 larger ones, which were required for a room temperature structure determination.



Figure 1

Experimental procedure for fast high pressure freezing of macromolecular crystals. a) BEV2 crystals of less than 50 μm in size are drawn into thin walled quartz capillaries and cut into approx. 2 mm long segments. The capillaries containing the virus crystals in their mother liquor are transferred to an aluminium platelet which is filled with 1-hexadecene. The platelet is sandwiched with another platelet and inserted into the Baltec HPM 010 device (b) via a specimen holder. c) The pressure chamber of the high pressure freezer is filled with ethanol at room temperature. Subsequently, liquid nitrogen pressurized to 210 MPa is 'shot' onto both sides of the containment and the sample is 'shock frozen' at 77 K.

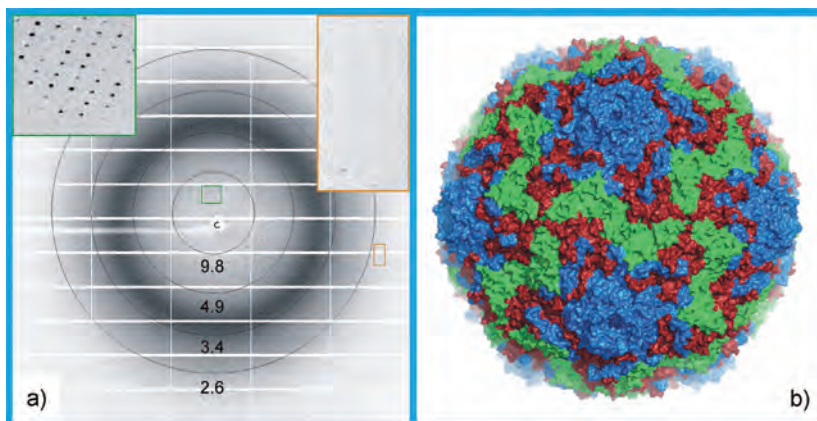
X-ray induced radiation damage is one of the major impediments for the successful structure determination of protein crystals and large molecular complexes. At room temperature, macromolecular crystals can typically withstand the intense X-ray beam of a third generation synchrotron source, such as PETRA III, for less than a second before being severely radiation damaged. Thus, only a few diffraction images can be collected from a single crystal. A standard technique to reduce radiation damage is to cool the crystals to cryogenic temperatures around 100 K during the experiment.

Macromolecular crystals typically contain between 30 and 80 % solvent (mainly water) and are surrounded by their aqueous growth solution (mother liquor). Direct cryocooling, for example by plunging the crystals into liquid nitrogen, leads to the formation of hexagonal ice within the crystal that destroys the crystal lattice. Instead, successful cryocooling requires the conversion of the solvent water to amorphous ice (vitrification). This is usually achieved by exposing the crystals to cryoprotectants such as ethylene glycol or glycerol. The search for optimal cryoconditions can be very crystal- and time-consuming and the crystal quality is often degraded upon cryoprotection. For large unit cell systems such as virus crystals, finding suitable cryoprotectants is often impossible and the majority of X-ray structure determinations is still performed at room temperature.

An alternative approach, which allows sample cooling without any cryoprotectants, is high pressure freezing. This method is well established in cryo-electron microscopy for vitrification of biological samples [1]. High pressure freezing was introduced into macromolecular crystallography in 1973 [2] and further developed by Kim et al. [3]. In their approach, the crystals are cooled with cooling rates of 1 – 2 K/s. Although their method has been successfully applied to several protein crystals, more challenging systems such as virus crystals could not be vitrified. By using much faster cooling rates of several thousand Kelvins per second it became possible to high pressure freeze larger unit cell systems such as membrane proteins [4, 5].

Figure 2

a) Diffraction pattern from a high pressure frozen crystal of BEV2 collected on beamline I24 at Diamond Light Source, UK. The green-framed rectangle shows an enlarged picture of the low-resolution data, the orange-framed rectangle shows an enlarged picture of the high-resolution reflections around 2.5 Å. b) Overall structure of BEV2 viewed along the icosahedral twofold axis.



We report on the first successful high pressure freezing of a virus crystal. Bovine enterovirus 2 (BEV2) is a widespread virus among cattle and may cause miscarriages. Cubic BEV2 crystals were grown by sitting-drop vapour diffusion. To date, suitable cryoconditions could not be established. Various attempts to cryoprotect these crystals with glycerol, ethylene glycol or paraffin oil have failed to yield diffraction data of sufficient quality.

In our work, BEV2 crystals were high pressure frozen at 210 MPa and 77 K using a Baltec HPM 010 instrument. The very high cooling rates achievable with this device allow direct freezing of the crystals in their mother liquor. Further sample preparation such as oil immersion, which can be detrimental to fragile crystals, is avoided.

The BEV2 crystals were first drawn into thin walled quartz capillaries. The capillaries were cut into shorter pieces and sandwiched between two aluminium platelets which were filled with 1-hexadecene (Fig. 1a). The sample containment was transferred to the Baltec HPM 010 device (Fig. 1b) and rapidly cooled to 77 K while being subjected to a pressure of 210 MPa (Fig. 1c). Subsequent sample handling was performed at cryogenic temperatures below 135 K to suppress the possible conversion of vitrified water to hexagonal ice. The capillary segments were removed from the sample containment and mounted on magnetic sample holders for data collection.

Diffraction data from high pressure frozen BEV2 crystals were collected at 100 K and 0.9686 Å using a $10 \times 10 \mu\text{m}^2$ beam at beamline I24 at Diamond Light Source, UK (Fig. 2a). Diffraction rings due to hexagonal ice were not observed in the images, indicating complete sample vitrification. The crystal diffracted to a resolution of 2.4 Å. Bragg reflections were well defined and separated (a hallmark of good data quality), which is manifested in the low mosaic spread of 0.26° . The quality of the cryogenic data is similar to that collected at room temperature, but at 100 K the BEV2 crystals withstand the unattenuated X-ray beam for about 12 s before showing severe signs of radiation damage. This is on average more than a hundred times longer than for crystals measured at room temperature. Thus, high pressure freezing allowed structure determination from a single position of a single BEV2 crystal (Fig. 2b), whereas at room temperature 28 larger crystals were exposed at 76 positions to obtain a complete data set.

Our high pressure freezing protocol is applicable to all kinds of macromolecular crystals. The crystals can be directly cryo-cooled in their mother liquor, and the time-consuming search for cryoprotectants is eliminated.

Contact: Anja Burkhardt, anja.burkhardt@desy.de

Authors

Anja Burkhardt¹, Armin Wagner², Martin Warmer³, Rudolph Reimer³, Heinrich Hohenberg³, Jingshan Ren⁴, Elisabeth E. Fry⁴, David I. Stuart^{2, 4} and Alke Meents¹

1. Deutsches Elektronen-Synchrotron DESY, Notkestraße 85, D-22607 Hamburg, Germany
2. Diamond Light Source, Didcot, Oxfordshire OX11 0DE, United Kingdom
3. Heinrich Pette Institute, Leibniz Institute for Experimental Virology, Martinistraße 52, D-20251 Hamburg, Germany
4. University of Oxford, Division of Structural Biology, The Henry Wellcome Building for Genomic Medicine, Headington, Oxford OX3 7BN, United Kingdom

Original publication

"Structure determination from a single high-pressure frozen virus crystal", *Acta Cryst. D* **69**, 308–312 (2013).

References

1. H. Hohenberg, K. Mannweiler, M. Müller, "High pressure freezing of cell suspensions in cellulose capillary tubes", *J. Microsc.* **175**, 34–43 (1994).
2. U. F. Thomanek, F. Parak, R. L. Mössbauer, H. Formanek, P. Schwager, W. Hoppe, "Freezing of myoglobin crystals at high pressure", *Acta Cryst. A* **29**, 263–265 (1973).
3. C. U. Kim, R. Kupfer, S. M. Gruner, "High pressure cooling of protein crystals without cryoprotectants", *Acta Cryst. D* **61**, 881–890 (2005).
4. M. Kurz, B. Blattmann, A. Kaeck, C. Briand, P. Reardon, U. Ziegler, M. C. Gruetter, "High-throughput counter-diffusion capillary crystallization and *in situ* diffraction using high-pressure freezing in protein crystallography", *J. Appl. Cryst.*, 999–1008 (2012).
5. A. Burkhardt, M. Warmer, S. Panneerselvam, A. Wagner, A. Zouni, C. Glöckner, R. Reimer, H. Hohenberg, A. Meents, "Fast high-pressure freezing of protein crystals in their mother liquor", *Acta Cryst. F* **68**, 495–500 (2012).

FLASH's heartbeat.

Ultrafast stopwatch determines duration of femtosecond FLASH pulses

Many fundamental processes in nature can occur on extremely small lengthscales (few nm) and ultrashort timescales (few fs). X-ray FELs are the future light sources that promise insight in the atomic and molecular world and their characteristic timescales. FELs merge the success of synchrotrons in resolving structure of matter down to an atomic level and ultrafast femtosecond lasers for exploration of ultrafast phenomena. However, temporal resolution of studies performed at X-ray FELs is still limited by shot-to-shot variations of the temporal pulse characteristics. We present a versatile temporal diagnostic tool that allows us to measure the FEL pulse duration and relative arrival time with respect to an external pump-probe laser pulse, even parasitically along with the experiment.

Many fundamental processes in nature, including chemical and biological reactions, occur on very short time- and lengthscales. Researchers have been dreaming for the opportunity to film these fast processes in real time and to understand their underlying principles. As it is well established in photography, the quicker a process occurs, the shorter the exposure must be to resolve it. Another principle in physics says that the wavelength of the radiation used to make an image should be shorter or at least comparable to the size of the imaged structures. Because of that, ideally, for experiments that study intrinsic processes in matter on atomic and molecular timescales, one would use ultrashort X-ray pulses.

X-ray free-electron lasers (FEL), with their intense light bundled into femtosecond pulses, hold the key for unlocking the technologies in ultrafast sciences. Using these large-scale photon facilities, scientists already study ultrafast dynamics on a nanometer lengthscale, within atoms, molecules and solids. In order to take the full advantage of the ultra-short FEL pulses, complete knowledge of their temporal structure, i.e. arrival time and pulse duration is needed. While several arrival time schemes have been successfully used in the past [1-4], pulse duration remains a challenge and topic of intense investigation. Existing techniques for measuring the pulse duration give promising results, however particularly in the case of XUV and soft X-rays radiation, experiments have to be performed in high vacuum, rendering these techniques challenging experiments on their own [4-6]. Using the worldwide first X-ray FEL, FLASH at DESY, we have developed a novel pulse duration monitor, which allows the characterization of FEL pulses while simultaneously performing ultrafast experiments. This technique requires a comparably simple experimental setup. In contrast to previous techniques, it has the potential to be applied in an extremely wide spectral range, from ultraviolet (UV) to hard X-rays.

The method is based on transmission changes in a transparent target caused by the FEL radiation. We irradiate a target sample with infrared laser pulses, e.g. fused silica or silicon nitride. A CCD-camera behind the target detects the transmitted intensity.

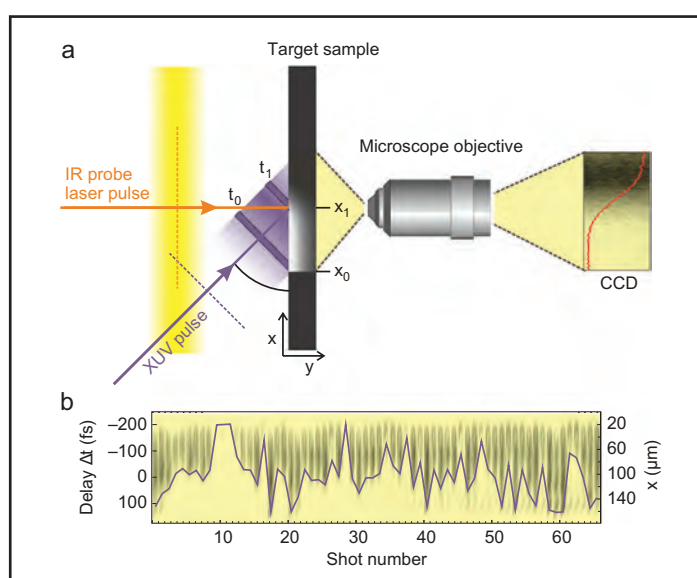


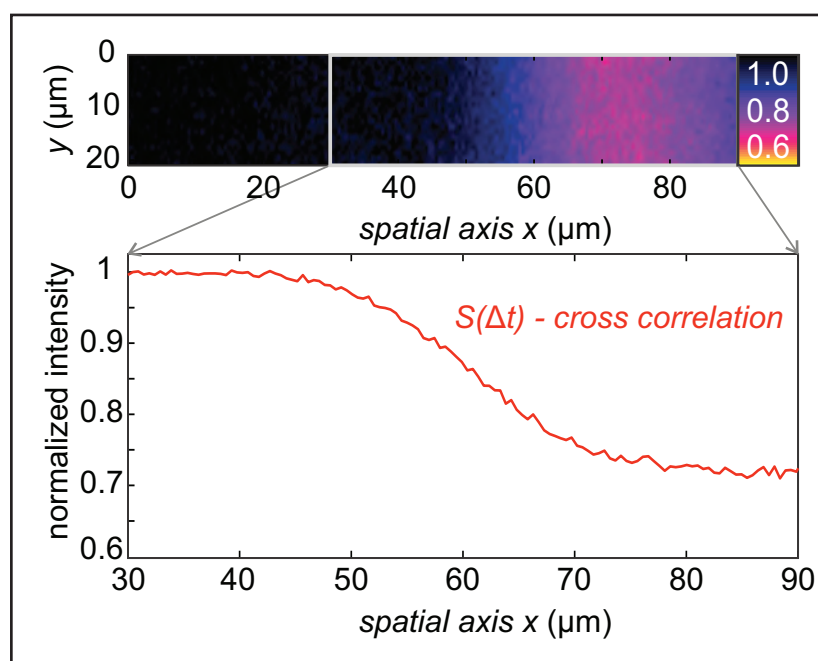
Figure 1

Schematic of the experimental set-up. The XUV pulse is incident under an angle with respect to the sample surface. Within a single shot, different temporal parts t_0 , t_1 of the XUV wavefront are absorbed at different spatial positions x_0 , x_1 on the sample, providing a spatio-temporal decoding. A largely collimated near-infrared pulse under normal incidence is used to probe the optical transmission change within the surface during the absorption. The transmitted light is imaged onto a CCD. (b) Series of single shots recorded with 10Hz acquisition rate. The black shading represents the increased optical opacity due to an increased electron density within the conduction band of the sample surface. The spatial position of the transient bottom edge on the x axis is dependent on the relative arrival time between the probe laser and the FEL pulse. The solid line indicates the extracted arrival time.

When we simultaneously send an X-ray pulse through the sample, we observe an attenuation of the transmitted light. The absorption of the X-ray pulse in the material creates an electron plasma, which acts like a mirror for the optical laser light. Thus, the target becomes less transparent for infrared radiation under the influence of the FEL pulse.

Figure 2

Optical transmission map along the sample during irradiation by FEL pulse. Graph shows extracted cross-correlation between optical laser and FEL. Position of the edge gives FEL arrival time, while slope of the edge is determined by a FEL pulse duration.



The X-ray pulse slants through the target and reaches different spatial positions on the target sample at different times (Fig. 1). Consequently, different locations on the target transmit the optical laser light differently as well. In other words, the time structure of the X-ray pulse translates into a spatial variation of the target's reflectivity (Fig. 2). From the transition between dark and light areas on the camera, we can derive the duration of the X-ray pulse. The key to this analysis is an experimental observation that each X-ray photon absorbed in the target is directly converted into a well-defined number of electrons. The implication is that the number of free electrons in the target scales linearly with the number of absorbed photons. This result allowed us to exclude other excitation processes in the material and ascribe the reflectivity change exclusively to the X-ray pulse. This finding has been confirmed by theoretical calculations at the Center for Free-Electron Laser Science (CFEL).

We have used the pulse duration monitor to characterize FLASH pulses from 21 - 184 femtoseconds duration at two different FEL wavelengths. With our method, users can directly measure the FEL pulse length in their experiment, and they can do so for every individual pulse. Moreover, silicon nitride targets can be

manufactured into very thin membranes. In this particular experiment we have used a membrane that was a mere 20 nanometers thick. The thin material absorbs only fifty to eighty percent of the FEL radiation, therefore part of the beam (or pulse) is transmitting through the sample for other FEL experiments. This should make possible to perform ultrafast pump-probe experiments and pulse duration measurements simultaneously. The technique is easily transferable to other FEL sources operating with ultrashort electron bunches and is therefore of high general interest. With the new method, we have measured femtosecond pulses from FLASH, which produces light in the extreme ultraviolet (XUV) and soft X-ray energy range. Furthermore, calculations show that the technique can be extended to harder X-rays. Consequently, the present timing tool will also be of interest for FELs that operate at higher photon energies such as the Linac Coherent Light Source (SLAC National Accelerator Laboratory) and the future European XFEL currently under construction in Hamburg.

Contact: Nikola Stojanovic, nikola.stojanovic@desy.de
Robert Riedel, riedel@mail.desy.de

Authors

R. Riedel^{1,2}, A. Al-Shemmary³, M. Gensch⁴, T. Golz³, M. Harmand³, N. Medvedev⁵, M. J. Prandolini², K. Sokolowski-Tinten⁶, S. Toleikis³, U. Wegner³, B. Zizaja^{5,7}, N. Stojanovic³ and F. Tavella²

1. Universität Hamburg, Luruper Chaussee 149, D-22761 Hamburg, Germany
2. Helmholtz-Institut Jena, Max-Wien-Platz 1, D-07743 Jena, Germany
3. Deutsches Elektronen-Synchrotron DESY, Notkestraße 85, D-22607 Hamburg, Germany
4. Helmholtz-Zentrum Dresden-Rossendorf, Bautzner Landstrasse 400, D-01328 Dresden, Germany
5. Center for Free-Electron Laser Science/DESY, Notkestraße 85, D-22607 Hamburg, Germany
6. Faculty of Physics and Center for Nanointegration Duisburg-Essen (CENIDE), University of Duisburg-Essen, D-47048 Duisburg, Germany
7. Institute of Nuclear Physics, PAN, Radzikowskiego 152, P-31-342 Kraków, Poland

Original publication

"Single-shot pulse duration monitor for extreme ultraviolet and X-ray free-electron lasers"; *Nature Communications* 4, 1731 (2013). DOI: 10.1038/ncomms2754

References

1. A. Azima et al., "Time-resolved pump-probe experiments beyond the jitter limitations at FLASH", *Appl. Phys. Lett.* 94, 144102 (2009).
2. F. Tavella, N. Stojanovic, G. Geloni, M. Gensch, "Few-femtosecond timing at fourth-generation X-ray light sources", *Nature Photonics* 5, 162-165 (2011).
3. U. Frühling et al., "Light-field streaking for FELs", *J. Phys. B*: 243001 (2011).
4. I. Grguraš et al., "Ultrafast X-ray pulse characterization at free-electron lasers", *Nature Photonics* 6, 852-857 (2012).
5. R. Mitzner et al., "Direct autocorrelation of soft-x-ray free-electron-laser pulses by time-resolved two-photon double ionization of He", *Phys. Rev. A* 80, 025402 (2009).
6. T. Pfeifer et al., "Partial-coherence method to model experimental free-electron laser pulse statistics", *Opt. Lett.* 35, 3441-3443 (2010).

Extreme ultraviolet and extremely short.

Direct FEL seeding at 38.2 nm

Intense radiation pulses generated in free-electron lasers (FEL) allow investigations in various scientific disciplines over a broad spectral region, especially in the high photon energy limit from the extreme ultraviolet into the hard X-ray regime, where no conventional lasers are available. When operated in the self-amplified spontaneous emission mode (SASE), the FEL radiation has a poor temporal coherence in contrast to conventional lasers. This can be improved by operating the FEL as an amplifier seeded by ultrashort and fully coherent laser pulses.

One of the dreams in the free-electron laser community is the generation of fully coherent radiation pulses over a broad spectral region. Important applications for such light sources are e.g. ultrafast spectroscopy which aims for sub-femtosecond X-ray pulses as well as all techniques in high resolution spectroscopy which need as many photons as possible in a narrow spectral bandwidth. A breakthrough in the field would be the full control of the spectral amplitude and phase of the radiation pulses from the FEL in order to tailor the pulses for the experiments. Several techniques have been proposed in the past which have been also experimentally demonstrated in different spectral regions [1, 2, 3]. All schemes using external radiation sources have in common that they suffer from the lack of appropriate radiation sources with sufficient power at short wavelengths.

Recently, it could be demonstrated at FLASH that it is possible to operate an FEL as a direct amplifier for extreme ultraviolet (EUV) radiation pulses at 38.2 nm, which have been produced by means of high-harmonic generation (HHG) from near-infrared laser pulses. The challenge for direct FEL seeding at these wavelengths is to overcome the background emission of the amplifier in order to get a sufficient signal-to-noise ratio.

The seeding experiment at FLASH (sFLASH) was driven by a collaboration of the University of Hamburg and DESY under the lead of Jörg Rossbach, Markus Drescher, and Tim Laarmann. Together with their research teams and the support by the technical groups from the research campus they redesigned a large section of FLASH to accommodate a new variable-gap undulator, as well as all hardware for injection and extraction of the seed and FEL radiation. Details about the experimental setup can be found in [4, 5].

After commissioning the HHG source and all diagnostic tools to setup the six-dimensional laser-electron overlap in space and time we were able to enhance the FEL pulse energy by a factor of five over the SASE background. Fig. 1 shows the measured

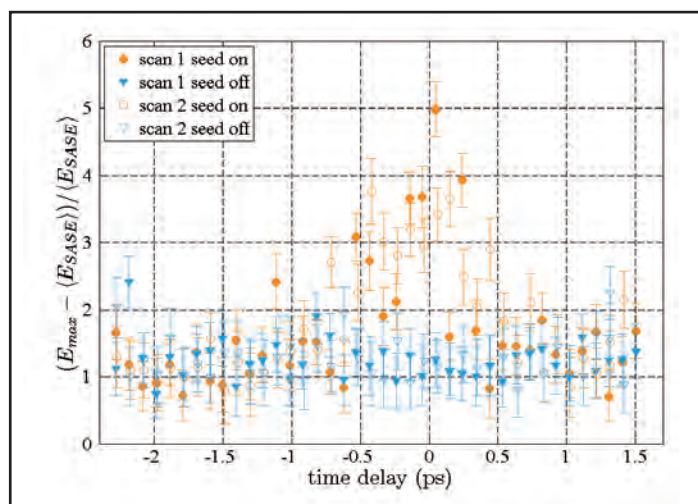


Figure 1

Contrast of the maximum pulse energy relative to the averaged pulse energy of SASE for each time delay between laser pulses and electron bunches as obtained in two independent scans. The seed laser has been toggled every 20 shots. The circles show the data when the laser was on, the triangles show the data where the laser was off.

energy contrast as a function of the time delay between seed pulses and electron bunches. Because the seed pulses have durations of only 15 fs ($1 \text{ fs} = 10^{-15} \text{ s}$) compared to the 50 fs in which SASE is generated, the contrast in the temporal domain is expected to be higher. In addition to this, a significant enhancement of the second harmonic emission of the FEL radiation at 19.1 nm could be detected (Fig. 2). A ratio of up to 36 between the seeded and unseeded case was measured. We note that the pulse duration is given as root mean square throughout the text.

The EUV seed pulse duration of 15 fs and the coherence time of the FEL amplifier of 7.4 fs leads to the conclusion that the ultra-short FEL pulses have a high degree of temporal coherence which is a measure of the monochromaticity of a photon source.

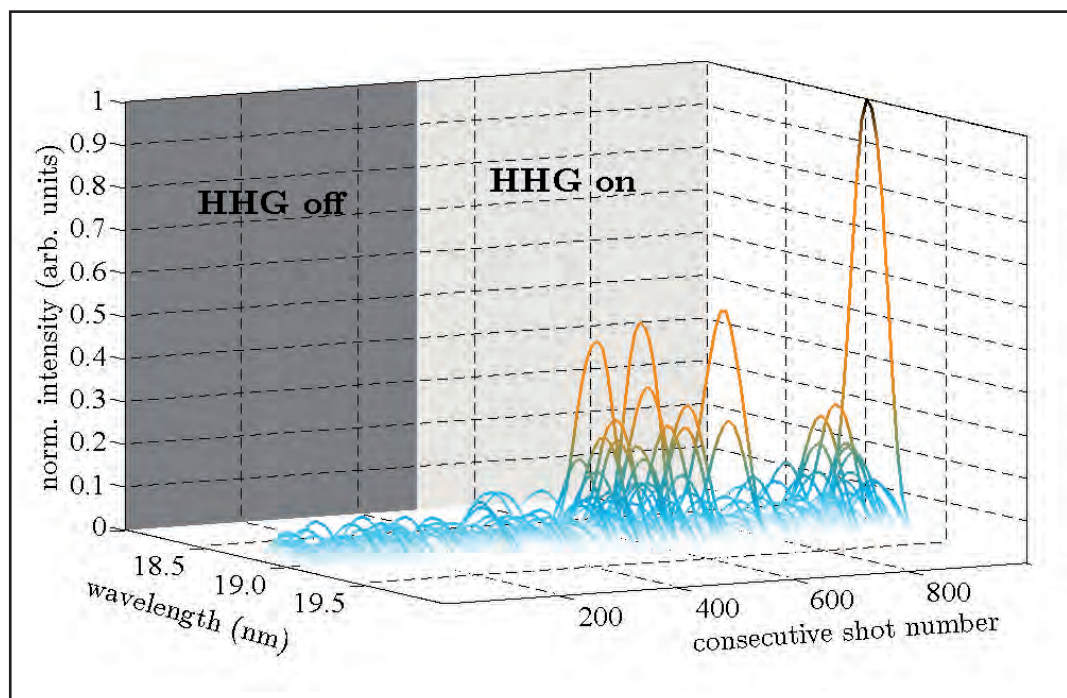


Figure 2

1000 consecutive spectra of the second harmonic emission of the FEL at 19.1 nm. For the first 500 spectra the seed laser was blocked, for the following 500 spectra the seed laser was on.

Thus, the amplified laser pulses must exhibit very good spatial and temporal coherence.

A technical challenge for the seeding setup was the implementation of the hardware in the existing FLASH infrastructure. Given that the HHG source is outside the radiation shielding of FLASH, trade-offs in the injection efficiency had to be made by using five mirrors. Due to the resulting transport efficiency of 5 %, about 1 nJ of seed pulse energy is available at the undulator. The gain in pulse energy from the HHG source to the exit of the FEL is about 3 orders of magnitude and therefore interesting for pilot experiments.

A practical benefit of the external FEL seeding scheme is the intrinsic synchronisation of the seeded part of the FEL pulse with the external laser sources. This allows for pushing the time resolution for precise pump-probe experiments to the limits, i.e. it is only governed by the respective durations of pump- and probe pulses. The sFLASH setup has the capability to test these benefits. A dedicated temporal diagnostic tool is currently set

up to investigate the unique properties of seeding during the next study periods.

Another approach for FEL seeding uses much longer initial laser wavelengths where the frequency up-conversion is generated by manipulation of the electron charge distribution which allows FEL lasing at high harmonics of the seed wavelength. The so called high-gain harmonic generation (HG) concept is successfully applied at FERMI@Elettra [2] generating FEL pulses in the deep EUV and soft X-ray wavelength range. However, the seed pulses and therefore also the FEL pulses are about three times longer than what has been used at FLASH.

In the future, the sFLASH setup will be used for tests of HG, as well as more advanced seeding schemes which have the potential to reach much higher harmonics for pushing the limits of externally seeded FEL technology to even shorter wavelengths.

Contact: Jörn Bödewadt, joern.boedewadt@desy.de

Authors

Sven Ackermann^{1,2}, Armin Azima^{1,5,6}, Sasa Bajt², Jörn Bödewadt¹, Francesca Curbis¹, Hatem Dachraoui², Hossein Delsim-Hashemi², Markus Drescher^{1,5,6}, Stefan Düsterer², Bart Faatz², Matthias Felber², Josef Feldhaus², Eugen Hass¹, Ulrich Hipp¹, Katja Honkavaara², Rasmus Ischebeck⁴, Shaikat Khan³, Christoph Lechner¹, Tim Laarmann^{2,6}, Theophilos Maltezopoulos^{1,5}, Velizar Miltchev¹, Manuel Mittenzwey¹, Marie Rehders^{1,5}, Juliane Rönsch-Schulenburg^{1,5}, Jörg Rossbach^{1,5}, Holger Schlarb², Siegfried Schreiber², Lasse Schroedter², Michael Schulz^{1,2}, Sebastian Schulz², Roxana Tarkeshian¹, Markus Tischer², Violetta Wacker¹, and Marek Wieland^{1,5,6}

1. Department of Physics, University of Hamburg, D-22761 Hamburg, Germany
2. Deutsches Elektronen-Synchrotron DESY, D-22607 Hamburg, Germany
3. Technische Universität Dortmund, D-44227 Dortmund, Germany
4. Paul Scherrer Institut, CH-5323 Villigen, Switzerland
5. Center for Free-Electron Laser Science CFEL, DESY, D-22607 Hamburg, Germany
6. The Hamburg Centre for Ultrafast Imaging CUI, D-22761 Hamburg, Germany

Original publication

“Generation of Coherent 19- and 38-nm Radiation at a Free-Electron Laser Directly Seeded at 38 nm”, *Phys. Rev. Lett.* **111**, 114801 (2013).

References

1. J. Amann et al., “Demonstration of self-seeding in a hard-X-ray free-electron laser”, *Nature Photonics* **6**, 693-698 (2012).
2. E. Allaria et al., “Highly coherent and stable pulses from the FERMI seeded free-electron laser in the extreme ultraviolet”, *Nature Photonics* **6**, 699-704 (2012).
3. G. Lambert et al., “Injection of harmonics generated in gas in a free-electron laser providing intense and coherent extreme-ultraviolet light”, *Nature Physics* **4**, 296-300 (2008).
4. Th. Maltezopoulos et al., “A high-harmonic generation source for seeding a free-electron laser at 38 nm”, *Appl. Phys. B*, DOI: 10.1007/s00340-013-5571-6 (2013)
5. C. Lechner et al., “First direct Seeding at 38 nm”, *Proceedings of the 2010 Free-Electron Laser Conference (JACoW, Nara)*, 197-199 (2012).

Towards few fs resolution movies at XFEL facilities.

Arrival time diagnostics for pump-probe experiments involving FEL and lasers

Studying matter at atomic resolution and at the femtosecond time scale is today becoming possible using an X-ray free-electron laser. Coupled with the available sub-10 fs optical pulses within pump-probe schemes, investigations could give access to the few-femtosecond range. Unfortunately, these kilometre long accelerator based X-ray sources suffer from significant jitter and drifts between optical and X-ray pulses. We have recently demonstrated that a ‘measure-and-sort’ approach of the relative arrival time between the FEL and optical pulse can afford sub-10 fs root-mean-squared (r.m.s.) error measurement, far beyond the common jitter of 100–200 fs r.m.s. This timing diagnostic, now routinely available at the Linac Coherent Light Source (LCLS), is based on ultrafast free-carrier generation in optically transparent materials. Correlation between two independent measurements enables unambiguous demonstration of ~6 fs r.m.s. error in reporting the optical/X-ray delay, with single shot error suggesting the possibility of reaching few-femtosecond resolution.

The advent of femtosecond optical lasers has opened the way to study matter at very high time resolution (tens of femtoseconds). Within a pump-probe scheme [1], a first ultrafast pulse triggers dynamics with sub-10 fs pulse excitations while a second ultrafast pulse probes matter. Unfortunately the link between optical properties and atomic structures is not direct thus preventing a direct visualization of matter in motion. Being able to film matter at the natural time scale of atomic motions is one of the reasons why X-ray free-electron laser are being built. Currently, the temporal precision of the FEL – optical laser synchronisation is limited by shot-to-shot jitter (≥ 100 fs r.m.s.). New schemes are suggesting future synchronization with optical lasers at the sub-100 fs level [2]. Despite these achievements, the question of how to reach sub-10 fs synchronization remains to be answered. To overcome such limitations, many research groups developed ways to directly measure the relative time delay between laser and X-ray thus being able to post-analyze the data and remove the jitter effect from experimental data [3,4]. By correlating the relative arrival times measured with two different timing tools at different position along the FEL beam path, we achieve the first demonstration of a sub-10 fs RMS timing tool on a hard X-ray FEL.

To do so, we use the ultrafast change in optical properties of transparent materials induced by intense irradiation. This results from the rapid change in the free-electron density in the sample [5]. The process is commonly used in laser physics. In the present case, the change of the free-electron density is induced by intense X-ray photons from the FEL pulse. Photoionization, and subsequently collisional ionization, increase the free-electron density within a fs time scale [5]. This technique, pioneered at FLASH and recently developed at LCLS, has been demonstrated for soft X-rays [3, 4]. Derived from such techniques and by using several independent arrival time monitors simultaneously, we are able to directly measure the accuracy of such diagnostics,

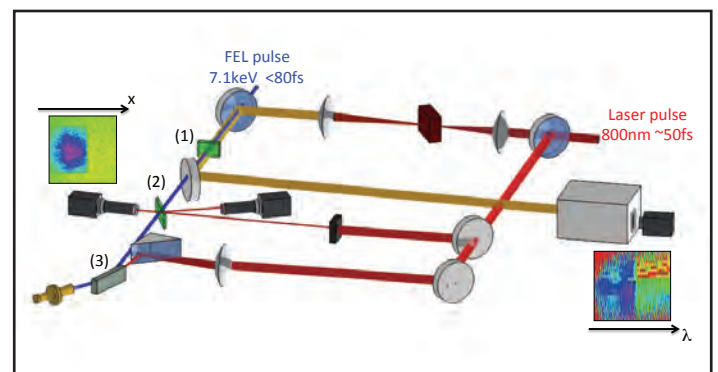


Figure 1

Sketch of the experimental setup at LCLS. The FEL beam propagates from top to bottom. The 800 nm laser beam propagating from right to left is split into three beams: (1) the relative delay between laser and X-ray is encoded into wavelength by using a broadband chirped supercontinuum; (2) the temporal delay is spatially encoded; (3) the coherent phonon motion in bismuth provides an experimental test of time-sorting with the timing tools (1 and 2)

overcoming the inherent limitations due to the currently used X-ray and laser pulse duration. We propose a simple, almost non-invasive method, extended to the hard X-ray regime and based on a non-damaging interaction mode allowing a sub-10 fs accuracy measurement of the arrival time delay between an optical laser and an XFEL.

The experiment was performed at the XPP X-ray Pump-probe station at LCLS. In order to measure the accuracy of the developed techniques and to validate our experimental procedure, we used simultaneously two timing tools and performed in parallel a pump-probe experiment to validate our jitter correction method.

Temporal mapping was achieved spatially via a crossed beam

geometry, or spectrally via a chirped white light continuum. The experimental set up, shown in Fig. 1, is therefore composed of three simultaneous experiments, noted (1), (2) and (3), mounted at three different points along the FEL beam path: (1) a spectral encoding timing tool, (2) a spatial encoding timing tool, and (3) a scientific application based on coherent optical phonons in bismuth. The spatial encoding is placed 1 m after the spectral encoding diagnostic. Each timing tool has been fully characterized by scanning their respective delay line for a fine time calibration. The FEL pulses were characterized by a photon energy of 7.1 keV, with a pulse length <80 fs. The pulse length of the Ti:Sapphire optical laser system was ~50 fs and the optical laser system was split in three paths equipped with individual delay stages for independent pump-probe scans. For both timing tools (1) and (2), we overlapped the unfocused FEL beam with the optical laser pulse on thin transparent membranes.

Fig. 1 shows single shot 2D-images obtained with the spatial (left) and the spectral (right) encoding timing tools. In that case, both diagnostics are used with 1 μm Si₃N₄ membranes and the unfocused FEL beam. Such thin membranes ensure X-ray transmission higher than 90 %. The X-ray photons generate free carriers by an ultrafast ionization process, which induces a change in the optical properties (reflectivity, transmission) directly detected by our independent timing tools [5]. A transmission change of a few percent allows the signal extraction. Variations in the position of the transmission change indicate stochastic fluctuations of the relative arrival time between the optical laser and FEL. Typical error bars are 1.5 fs and 4.5 fs for the spatial and spectral timing tools, respectively.

Contrary to previous experiments in the soft X-ray regime, we observed a non-damaging interaction, allowing high resolution measurements and a permanent implementation of our diagnostics as beam line equipment. Indeed a damaging mode has the disadvantage of requiring that the sample is replaced after every thousand shots. As well as the evident drawback of an intervention during series of shots, this means that the accuracy of the results may be limited by variations between samples, and the reproducibility of target positioning.

The arrival time difference between the FEL and the optical laser pulses is then extracted for each diagnostics and for each single shot. Assuming the difference of the measured arrival time should be equal to zero, the correlation of the two diagnostics is used to estimate the uncertainty in the arrival time determination as well as to optimize the arrival time measurements. Indeed,

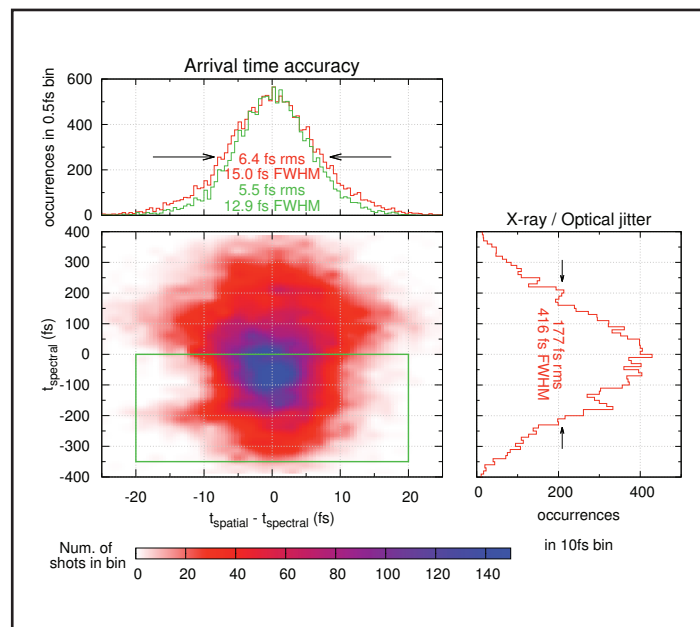


Figure 2

Correlation of spectral and spatial encoding timing tools: the central two-dimensional image shows single-shot spectral encoding arrival times plotted over the arrival time difference between the spatial and spectral encoding ($t_{\text{spatial}} - t_{\text{spectral}}$), after correction of systematic errors. Right panel: histogram of the spectrally encoded arrival time, indicating the jitter between X-ray and optical pulses. Upper panel: histogram of the arrival time difference ($t_{\text{spatial}} - t_{\text{spectral}}$) obtained for a restricted (green, data restricted to area in green box) or full (red) time window, indicating the overall accuracy of the measurements and unambiguously proving a few-femtosecond r.m.s. resolution.

systematic errors due to uncertainty in calibration can be corrected by minimizing the difference between the two timing tools measurements. The final correlation shown in fig. 2 demonstrate unambiguously an uncertainty on the arrival time determination of 6.4 fs r.m.s after correction.

Our measurements demonstrate that the optical response of the Si₃N₄ membrane provides sub-10 fs r.m.s. accuracy in determining the arrival time of the XFEL pulse relative to the optical laser pulse and suggest that the uncertainty could be reduced to just a few femtoseconds.

Contact: Marion Harmand, marion.harmand@polytechnique.edu

Authors

M. Harmand^{1†}, R. Coffee², M. R. Bionta², M. Chollet², D. French², D. Zhu², D. M. Fritz², H. T. Lemke², N. Medvedev³, B. Ziaja^{3,4}, S. Toleikis¹ and M. Cammarata⁵

1. Deutsches Elektronen-Synchrotron DESY, Notkestr. 85, D-22607 Hamburg, Germany

2. LCLS, SLAC National Accelerator Laboratory, Menlo Park, California, USA

3. Center for Free Electron Laser Science, DESY, Hamburg, Germany

4. Institute of Nuclear Physics, Polish Academy of Sciences, Krakow, Poland

5. Institut de Physique de Rennes, CNRS, Université de Rennes 1, Rennes, France

† Present address: LULI, Ecole polytechnique, CNRS, CEA, UPMC, route de Saclay,

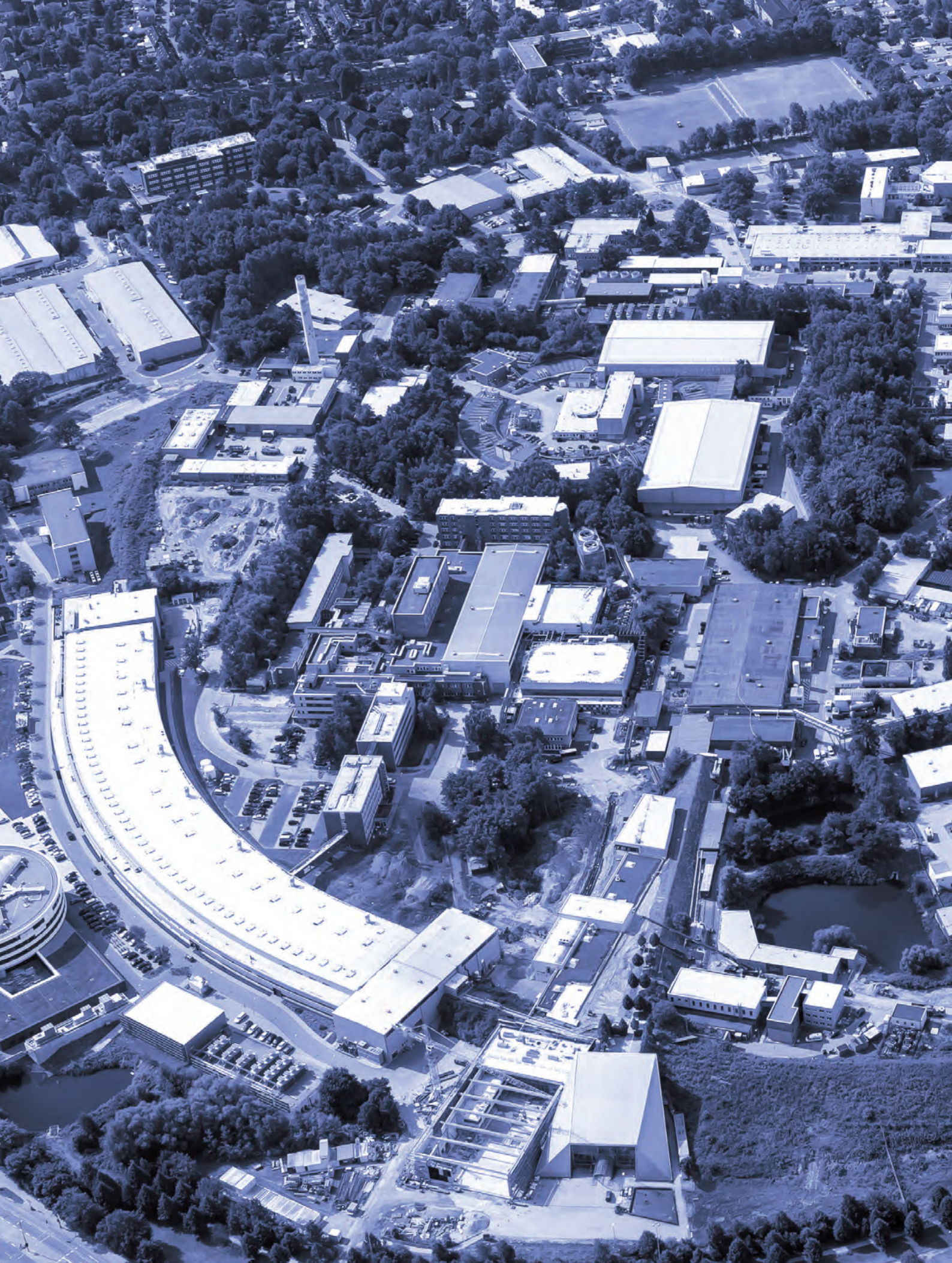
91128 Palaiseau, France

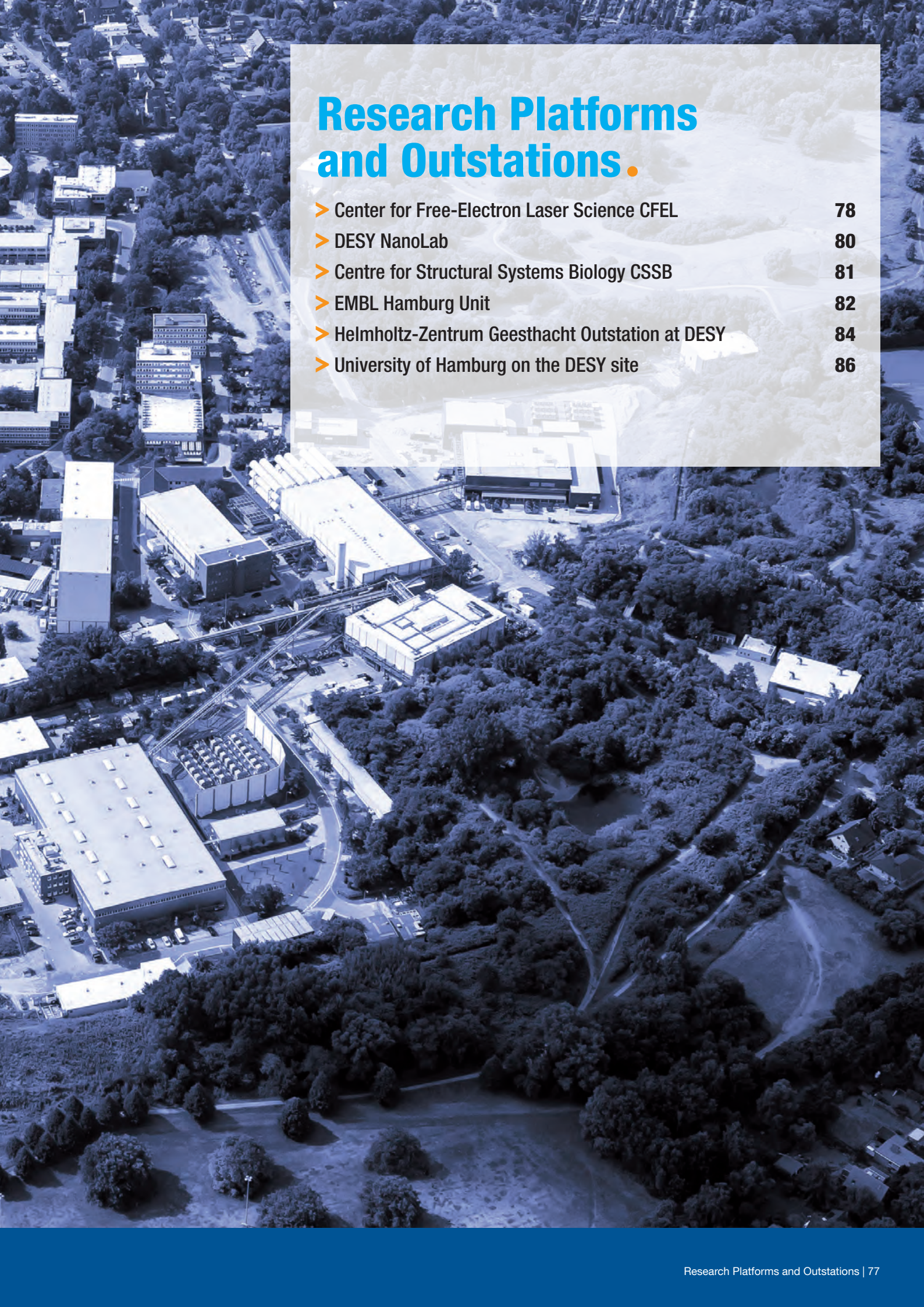
Original publication

"Achieving few-femtosecond time-sorting at hard X-ray free-electron lasers", *Nature Photonics* 7, 215-218 (2013).

References

1. A. H. Zewail, "Femtochemistry. Past, present, and future", *Pure Appl. Chem.* 72, 2219–2231 (2000).
2. F. Lohl et al., "Electron bunch timing with femtosecond precision in a superconducting free-electron laser", *Phys. Rev. Lett.* 104, 144801 (2010).
3. M. R. Bionta et al., "Spectral encoding of X-ray/optical relative delay", *Opt. Express* 19, 21855–21865 (2011).
4. T. Maltezopoulos et al., "Single-shot timing measurement of extreme-ultraviolet free-electron laser pulses", *New J. Phys.* 10, 033026 (2008).
5. N. Medvedev et al., "Electron kinetics in femtosecond X-ray irradiated SiO₂", *Contrib. Plasma Phys.* In press (2013).





Research Platforms and Outstations.

- Center for Free-Electron Laser Science CFEL 78
- DESY NanoLab 80
- Centre for Structural Systems Biology CSSB 81
- EMBL Hamburg Unit 82
- Helmholtz-Zentrum Geesthacht Outstation at DESY 84
- University of Hamburg on the DESY site 86

Center for Free-Electron Laser Science CFEL.

Three institutions working successfully together within CFEL

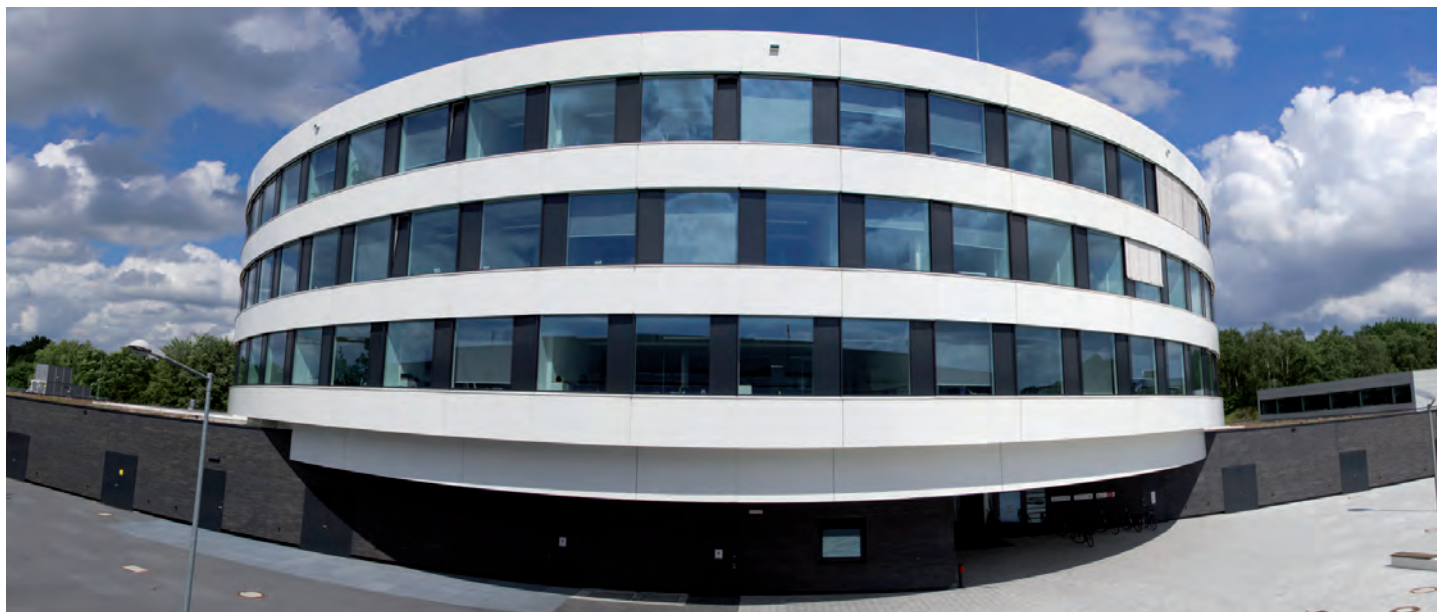


Figure 1

Wide angle front view of the CFEL building.

In 2013, the number of researchers at CFEL has significantly increased in the building and keeps still growing. With the rising number of scientists the scientific output has prospered as well with significant publications over the year from all three institutions that joined their forces in CFEL: Deutsches Elektronen-Synchrotron DESY, Max Planck Society (MPG) and the University of Hamburg (UHH), which is also the owner of the new research complex. On Monday, 17th of June 2013, the new CFEL research building was inaugurated with a scientific symposium followed by a celebration reception with over 350 participants in the CFEL foyer. The group of internationally renowned speakers consisting of Tamar Seideman, Paul B. Corkum, Paul Emma, Eberhard K. U. Gross, Keith A. Nugent and Stuart S. P. Parkin gave a wide overview of the CFEL research fields. The official inauguration ceremony continued in the late afternoon with addresses from prominent guests representing German and Hamburg government and scientific leaders from University of Hamburg, Max Planck Society, Helmholtz Association and DESY. The reception that followed in the evening offered the opportunity for long and lively discussions among the participants and guests.

The official start of the new Max Planck Institute for the Structure and Dynamics of Matter (MPSD) on the 27th of February marked another highlight at CFEL in 2013. The first two directors are

Andrea Cavalleri and Dwayne Miller, both former division heads of the Max Planck Research Department for Structural Dynamics at CFEL. In the course of the year the two research departments were fully integrated into the new MPI. Further directors for the new MPI will be appointed in the future and an extra building will be erected in addition to the space the MPI activities already use in the CFEL building.

Apart from initiatives within the Photon and Nano Science focus in Hamburg, the unique CFEL conception was instrumental in the successful application of the cluster of excellence "The Hamburg Centre for Ultrafast Imaging (CUI)" in 2012. Within CUI, the University of Hamburg and its partners DESY, the Max Planck Society, European XFEL and European Molecular Biology Laboratory Hamburg Unit (EMBL) strive to shoot molecular movies, one of the dream experiments in physics, chemistry, and biology. Many CFEL scientists work within CUI and focus on dynamics on the atomic level to bridge research into such diverse problems like quantum dynamics of small molecules, cooperative and collective phenomena in matter as well as structure-function relations in biomolecules.

CFEL successfully hosted the second Ultrafast X-Ray Summer School (UXSS 2013) in Hamburg, a highly interdisciplinary program with topics ranging from accelerator physics to molecular biology, and intended to give doctoral students and postdoctoral



Figure 2

Official CFEL Inauguration on Monday, 17th of June 2013 (photo courtesy of Lars Berg). Dorothee Stapelfeldt, Second Mayor and State Minister of Science and Research in Hamburg, Georg Schütte, State Secretary at the Federal Ministry of Education and Research, Dieter Lenzen, President of the University of Hamburg, Helmut Dosch, Chairman of the DESY Board of Directors, Martin Stratmann, Vice President of the Max Planck Society, Jürgen Mlynek, President of the Helmholtz Association and Robin Santra, Chair of the CFEL Management Board joined the event with addresses from their respective institutions.

researchers the opportunity to familiarize themselves with the latest developments and methods in ultrafast X-ray science. This summer school has been taking place annually at the PULSE institute at SLAC National Accelerator Laboratory till 2010 and was now, for the second time after 2011, organized in Hamburg by Oriol Vendrell, a senior scientist in the CFEL Theory Division. The learning experience at this year's UXSS 2013 was further enhanced through tutorial groups led by scientists from the European XFEL. The UXSS was financially supported by the Volkswagen Stiftung and will be back in Hamburg in 2015. Since September 3rd, 2012 the CFEL building is operating and is continuously filling with scientists and new experiments. At the end of 2013, over 300 scientists, students, technicians and administrative staff were active in the new CFEL building and the other CFEL operated laboratories on the Bahrenfeld Campus. The visible result of this work is over 100 peer reviewed publications including several full papers in major journals such as Nature and Science.

Another success in the past year was the start of the ERC Synergy Grant on Frontiers in Quantum Materials' Control (Q-MAC) on the 1st of October. Andrea Cavalleri is the speaker of this research consortium that was awarded approximately 10 M€ by the European Research Council for the next 6 years. In addition, Jochen Küpper recently received an ERC Consolidator Grant of

almost 2 M€ for the next 5 years for his research on Controlling the Motion of Complex Molecules and Particles (COMOTION). The Advanced Study Group of UHH (Florian Grüner, Jörg Rossbach, Wilfried Wurth) was able to attract close to 3 M€ for the next three years in the framework of the BMBF Verbundforschung within the priority program FSP-302: Free-Electron Lasers. A new international user consortium initiated and led by Henry Chapman was awarded initial funding to deploy a Serial Femtosecond Crystallography (SFX) instrument at the European XFEL. The instrument is designed for high-throughput structure determination, and takes advantage of the higher repetition rate of the European XFEL compared with other sources. The consortium includes DESY, the UHH, and members from the UK, Sweden, Slovakia, Switzerland, and USA who have raised and already committed over 12 M€ towards the project. This includes 2.7 M€ awarded to the UHH from the BMBF (to Christian Betzel and Henry Chapman), and 5.4 M€ funded by the Wellcome Trust in the UK. Other members include the Max Planck Society and EMBL. A small selection of the CFEL many scientific successes can be found in the "Research Highlights" section of this report. More examples can be found at: http://www.cfel.de/publications/2013/index_eng.html

Contact: Ralf Köhn, ralf.koehn@cfel.de

Towards nanoscience user support at DESY

In 2013, the planning of the DESY NanoLab as complementary facility for DESY Photon Science users made significant progress: during a satellite workshop at the DESY Photon Science User Meeting 2013 entitled “Nanoscience at large scale facilities: discussion of the DESY Nanolab” scientists from various areas presented their work combining synchrotron radiation results with auxiliary nanoscale characterization and preparation methods, demonstrating the necessity and power of this approach.

In a second onsite workshop entitled “Nanostructuring at DESY” the activities of the different institutions on the campus Bahrenfeld (DESY, University of Hamburg, Helmholtz Center Geesthacht (HZG), Max Planck Society, European XFEL GmbH) were highlighted, giving clear evidence for the need of a more compact bundling of the onsite needs and resources across institutional borders.

In both workshops the users expressed the urgent need for instruments such as high resolution scanning electron and atomic force microscopes, dual focussed ion beam and nanostructuring techniques such as e-beam lithography. Especially, implementation of reproducible sample transfer protocols for single nano-objects from NanoLab instruments to nanofocussing beamlines and back was requested. Together with laboratory space for these instruments and techniques, labs for optical microscopy, magnetic characterization and preconditioning, X-ray diffraction and wet chemistry are planned to accommodate the needs for in-house research and user activities.

The NanoLab is planned to be located in the new Photon Science building, which is a joint project between DESY and HZG. During the planning phase of the Photon Science building in 2013, the compatibility of its envisaged location with the requirements for low electromagnetic fields was assessed and a concept for a low vibrational floor in the basement of the building was developed. It consists of 1 m thick concrete plates, which rest on 10 m deep pillars. At the same time, the building’s outer shell rests on independent pillars, ensuring a minimum vibrational coupling towards the low vibration floor.

With progressing planning it became evident that a building fulfilling the initial requirements for office and high-quality laboratory space cannot be realized in the framework of the initial budget. At present, a solution in line with budget is envisaged, still comprising the requirement of low vibration surfaces for sensitive equipment.

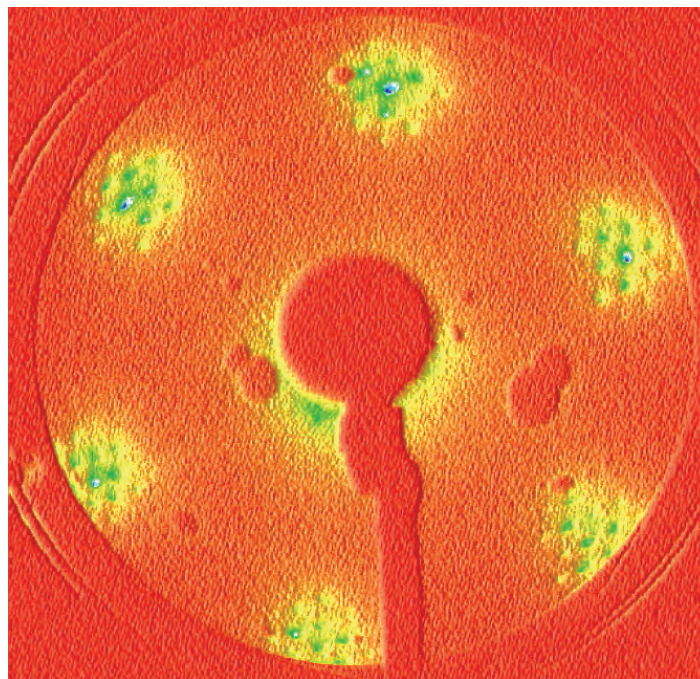


Figure 1

Low energy electron diffraction pattern from a graphene monolayer on Ir(111) grown in the DESY NanoLab.

To bridge the gap until the final realization of the new building, the NanoLab is providing limited service in its current temporary location in building 3, where a UHV lab with growth facilities, scanning probe microscopy, Fourier transform infrared spectroscopy and X-ray photo emission is currently being set up. An example for current research activities is given in Fig.1. In addition, an X-ray diffraction lab equipped with a reflectometer and a six-circle diffractometer is in the commissioning phase. Furthermore, an in-air atomic force microscope is available.

Contact: *Andreas Stierle, andreas.stierle@desy.de*

Centre for Structural Systems Biology CSSB.

A further step in the DESY long-standing tradition in structural biology

The Centre for Structural Systems Biology (CSSB) is taking shape – step by step: The multidisciplinary centre with partners from several universities and research institutes located in Hamburg and Lower Saxony will bundle resources and methods of infection research, structural and systems biology in one nationally leading and internationally competitive centre. At the CSSB, scientists from all natural sciences as well as engineers will join forces to investigate the interaction of pathogens with their hosts. DESY offers unique facilities in Germany that provide optimal conditions for structural biology: PETRA III, FLASH, and – in future – European XFEL. The CSSB will act as a catalyst for cooperations on-campus, particularly with the Center for Free-Electron Laser Science (CFEL), as well as with universities and research organizations in Northern Germany and beyond. It is also expected to substantially contribute to teaching and advanced multidisciplinary training.

In 2013, the construction process of the new CSSB building – south of the PETRA III experimental hall on the DESY campus – made some progress: the construction preparations are running since last spring; in October partial permit for excavation and foundation was granted; construction work will be tendered soon. The groundbreaking ceremony took place on September 4th, 2013, and in the next few months excavators will take over command of the construction site. The completion of the building is expected in 2016. Now that CSSB is slowly developing into reality, newly recruited colleagues are offered a perspective, on which laboratories and experimental infrastructure can be planned and realized.

Most important for the CSSB building design is an operational and communicative environment, leading the groups to interact with each other. There will be seminar rooms and/or meeting points on every floor except for the basement; the lecture hall (1st floor) will have a capacity for 150 persons and the entrance hall will provide enough space for poster sessions during scientific meetings. Additionally, a direct access to PETRA III from the 1st floor is planned. In the basement, installations for handling infectious agents, also hosting a cryo electron microscope, are planned, allowing for biosafety up to the S3 level. In addition, the basement will accommodate the main storage rooms for long term cryo storage of samples as well as a second cryo electron microscope facility.

Soon, three new group leaders will join CSSB: a full professorship for “Cellular Biology of Human Parasites” was jointly filled by the University of Hamburg and the Bernhard Nocht Institute, a second one for “Structural and Systems Biology of Bacteria” by the University Medical Center Hamburg-Eppendorf; a further position as research group leader was appointed for the EMBL topic “Membrane Protein Structural Biology”. Currently, nego-



Figure 1

Groundbreaking ceremony for the construction of CSSB. From left: Helmut Dosch (Chairman of the DESY Board of Directors), Dorothee Stapelfeld (Hamburg Senator for Science and Research), Johanna Wanka (German Federal Minister of Education and Research), Rüdiger Eichel (Head of Scientific Commission of Niedersachsen), and Chris Meier (Vice Dean for Research MIN Faculty of the University of Hamburg and spokesman of the CSSB Task Force).

tiations take place with candidates for two more full professorships: “Structural Biology of Viruses” (HPI/UHH; dedicated to cryo EM and virus infections), and “Biophysical Chemistry of Membrane Proteins” which DESY has been successfully granted by the Helmholtz Recruiting Initiative. The partner institutions will provide interim lab space for CSSB scientists, so that they can join the CSSB groups already established and start their scientific work. In total, the partner institutions will provide support for 11 “CSSB groups”.

CSSB partner institutions

- Bernhard Nocht Institute for Tropical Medicine BNI
- Deutsches Elektronen-Synchrotron DESY
- European Molecular Biology Laboratory EMBL
- Forschungszentrum Jülich FZJ
- Hannover Medical School MHH
- Heinrich Pette Institute, Leibniz Institute for Experimental Virology HPI
- Helmholtz Centre for Infection Research HZI
- University of Hamburg UHH
- University Medical Center Hamburg-Eppendorf UKE

Associated partners:

- Karolinska Institutet, Sweden (Röntgen-Ångström Cluster)

Contact: Ina Plettner, ina.plettner@verw.uni-hamburg.de
Edgar Weckert, edgar.weckert@desy.de

EMBL Hamburg Unit.

Integrated structural biology services and research with synchrotron radiation

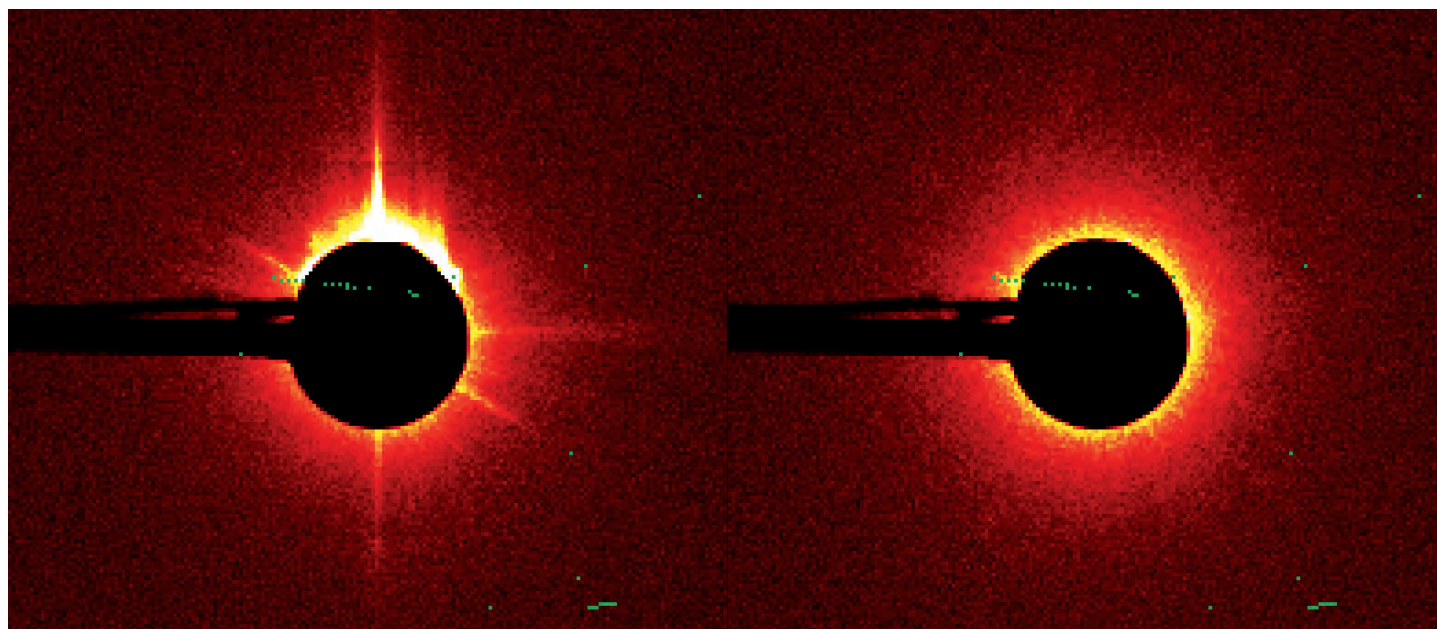


Figure 1

Improvement of the background at P12 due to the scatterless slits. Left and right panels represent the central portion of the scattering pattern around the beamstop without and with the scatterless slits, respectively.

The EMBL Hamburg Unit is a major provider of research services in structural biology, specifically for synchrotron radiation beamlines, preparation and crystallization facilities for biological samples, and the provision of computational services. In 2012/13, the three new EMBL beamlines for applications in structural biology at the PETRA III storage ring – P12, P13 and P14 – have been provided to a large external user community. Details of the quantity of our services are listed in Table 1.

Research Services		Jan-Dec 2012	Jan-Jun 2013
EMBL beamlines	user visits	348	287
	projects	154	125
	external research groups	122	100
EMBL software	users	5117	n.a.
	research groups	2091	n.a.
EMBL crystallization	users	51	36
	crystallization plates	703*	756

*High Throughput Crystallization (HTX) facility was not operational between April-August 2012

Table 1

Research services provided by EMBL Hamburg to the external user community.

At the BioSAXS beamline P12 about 200 external user projects were performed in 2013. Slashing down the measurement times from minutes on the previous DORIS BioSAXS beamline to less than a second, together with full automation of data acquisition and analysis, allowed the users to conduct much more experiments in much shorter times. The new on-line purification and biophysical characterization setup with size exclusion chromatography and light scattering and refraction detectors was made routinely available to external users, and over 15 % of the visitors were making use of this possibility.

A total of eight commissioning weeks helped to further improve the performance and to consolidate the existing installation. In collaboration with the Helmholtz Zentrum Geesthacht, a new small (2 mm diameter) active beamstop and a pair of scatterless slits (Xenocs) were commissioned. These improvements allowed access to yet smaller scattering angles (spatial resolution of up to 3000 Å in a standard configuration) with a dramatically reduced parasitic background, leading to significantly enhanced data quality (Fig. 1). Time resolved activities have been started

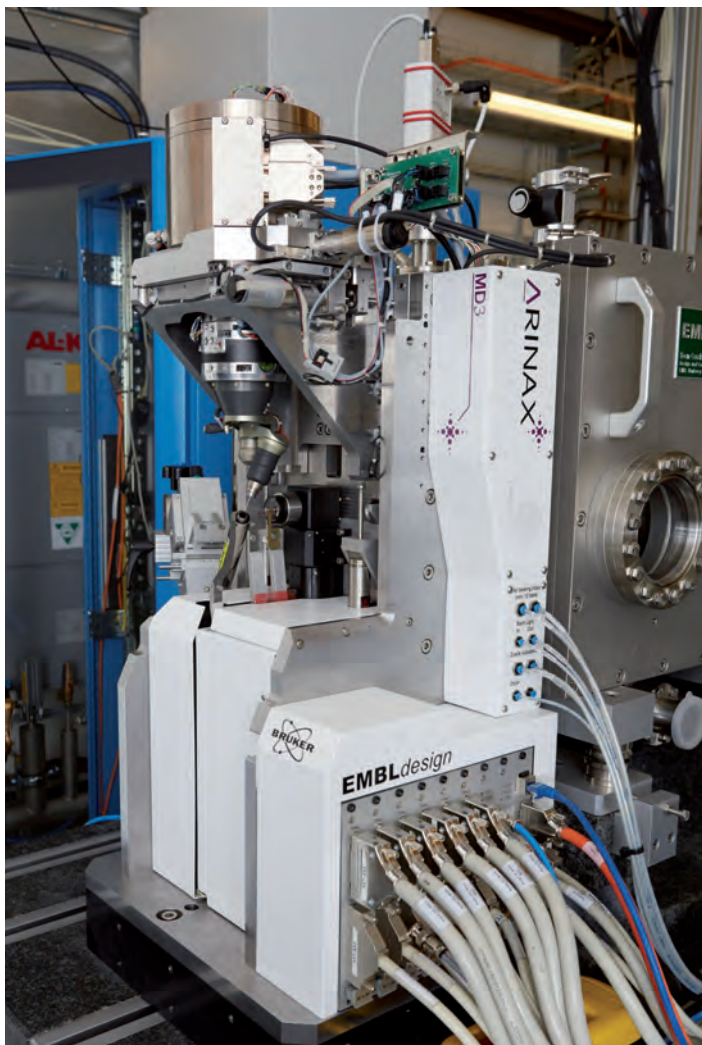


Figure 2

A new high-precision diffractometer 'MD3' has been developed in collaboration between EMBL-Hamburg and EMBL-Grenoble and has been installed on P14. By placing the rotation axis vertically the sphere of confusion was improved by a factor of 10 from 1 μm to 100 nm.

at P12 using a rapid mixing device. The tuning procedure of the front end was optimized to minimize the heat load on the monochromator and improve the beam stability and flux.

On both protein crystallography beamlines P13 and P14 adaptive mirror systems were commissioned. On P13 the smallest focus size achieved is 20 x 30 μm^2 (FWHM), with a flux of 10^{13} ph/s. The focus size can be changed to up to 100 x 150 μm easily. On P14, the smallest focus size achieved is 4 x 5 μm^2 , with a flux of 10^{12} ph/s. Again, the focus can be switched rapidly (30 s) between a fully focused and an unfocused beam with a size of 700 x 1300 μm^2 . This option is very much appreciated by the users as it allows the beam properties to be adjusted to the sample properties while a crystal remains mounted. On P13, the necessary hardware and software was installed to perform MAD experiments and since September 2013 a MARVIN sample changer robot is available. A number of protein structures were solved on P13 via Single-wavelength Anomalous Diffraction (SAD) phasing, in particular by exploiting energies between 4 and 6 keV for data collection. On P14 an 'MD3' high precision diffractometer

with a vertical spindle axis was installed in late 2012 (Fig.2). This diffractometer features a sphere of confusion, with a mini-kappa goniostat mounted, of less than 100 nm and was instrumental in performing a successful serial-crystallography experiment on *in vivo* grown micro-crystals of Cathepsin B, in collaboration with L. Redecke, Univ. Lübeck, and H. Chapman, CFEL. In August 2013, the 'MD3' was equipped with a holder for CrystalDirect™-crystallization trays providing the capability for *in situ* diffraction testing and data collection at room temperature, in collaboration with F. Cipriani, J. Marquez, EMBL-Grenoble.

The sample preparation and characterization (SPC) facility provides a laboratory for synchrotron users to prepare biological samples for characterization at the EMBL beamlines at PETRA III. The facility helps visitors to prepare their samples from cell pellet, through purification and quality control so that they can be crystallized or analyzed as a monodisperse sample in solution for SAXS characterization. The crystallization of proteins is further facilitated by the recent purchase of a MOSQUITO liquid handling robot, and a comprehensive web interface called CRIMS that allows users to check their crystallization experiments from home. The SPC also runs a visitor program that is supported by the FP7 infrastructure grant Biostruct-X, to allow users from the European research area to send samples remotely for characterization. Within this support scheme, the SPC staff takes the samples through a series of quality control and optimization protocols. Once this is completed, the researcher who runs the project is invited to EMBL Hamburg to combine different characterization techniques including SAXS and crystallography to obtain a comprehensive picture of his sample.

EMBL Hamburg is the coordinator of the BioStruct-X I3 consortium funded by the European Commission, which has been running since September 2011. BioStruct-X allows transnational access to X-ray based methods in structural biology. The second annual project meeting was held in Hamburg in September 2013, combined with the midterm project review. BioStruct-X works closely with other I3 projects and the ESFRI project INSTRUCT to coordinate relevant future projects in structural biology.

EMBL is a partner of the future Centre for Structural Systems Biology (CSSB, see separate article). A EMBL/CSSB group leader position, with a scientific focus in membrane protein crystallography, has been recently appointed.

In September 2013, the 11th International "Biology and Synchrotron Radiation" conference was hosted by the EMBL Hamburg Unit in the city centre. Extending the scope of previous conferences, the meeting offered its 330 participants additional sessions dedicated to biological sample preparation, hybrid structural biology approaches, and emerging free-electron laser applications in life sciences. More than one half of the participants joined a tour to the synchrotron and free-electron laser facilities on DESY campus.

Publication highlights in 2013 from EMBL Hamburg research groups can be seen here:

http://www.embl-hamburg.de/research/research_highlights/index.html

Contact: Matthias Wilmanns, matthias.wilmanns@embl-hamburg.de

Helmholtz-Zentrum Geesthacht Outstation at DESY.

See it as it is

The performance of the experimental facilities of the Helmholtz-Zentrum Geesthacht outstation as part of the German Engineering Materials Science Centre (GEMS) has seen a further positive development in the past year. The focus of GEMS on measuring “real-world” processes *in situ*, particularly in the field of engineering materials research, has been further strengthened. The first year of user operation of the new imaging instruments at the GEMS beamlines, covering a very broad energy range of currently 7 to 120 keV for the investigation of materials with different X-ray absorption properties, has been very successful. Selected results will be shown in the present report; they demonstrate the importance of real-space “X-ray vision” in understanding materials properties and in particular “seeing” processes inside those materials.

The High-Energy Materials Science Beamline (HEMS, P07, operated jointly with DESY) has reached an overbooking factor of nearly five at all experimental stations. The demand for complex *in situ* experiments has further increased; e.g. experiments with the popular modified quenching and deformation dilatometer (“FlexiTherm”) and with the in-house developed laser welding chamber (“FlexiLas”) account for nearly a quarter of the scheduled HZG beamtime in the second half of 2013. Ten per cent of the overall scheduled HZG user beamtime is spent on industrial research directly paid by our customers or supported within the Science Link project (see below). Instrumental improvements include the commissioning of a prototype Risø grain mapping reconstruction 2D-detector for the 3D-XRD grain mapper and tests of its optics with polymer compound refractive lenses (custom made by KIT, Karlsruhe) with a line focus of $< 1.5 \mu\text{m}$ (v) x 1 mm (h). Furthermore, high energy tomography (so far, the energy range from 35 to 120 keV has been exploited) is in user operation and enables imaging of engineering materials with high absorption such as WC/Co with μm resolution (Fig. 1). Phase contrast tomography at high energies has been tested and will be developed further.

In 2013, the Imaging Beamline (IBL, P05) has been in regular user operation for the absorption contrast-based tomography. With this method, spatial resolutions down to $1.2 \mu\text{m}$ have been achieved and high quality, low noise tomograms with high density contrast can be provided to the users routinely at different energies in the range of 7 to 32 keV, with applications ranging from natural materials such as wood and bone to metallic catalysts. The phase contrast and the nano tomography setups

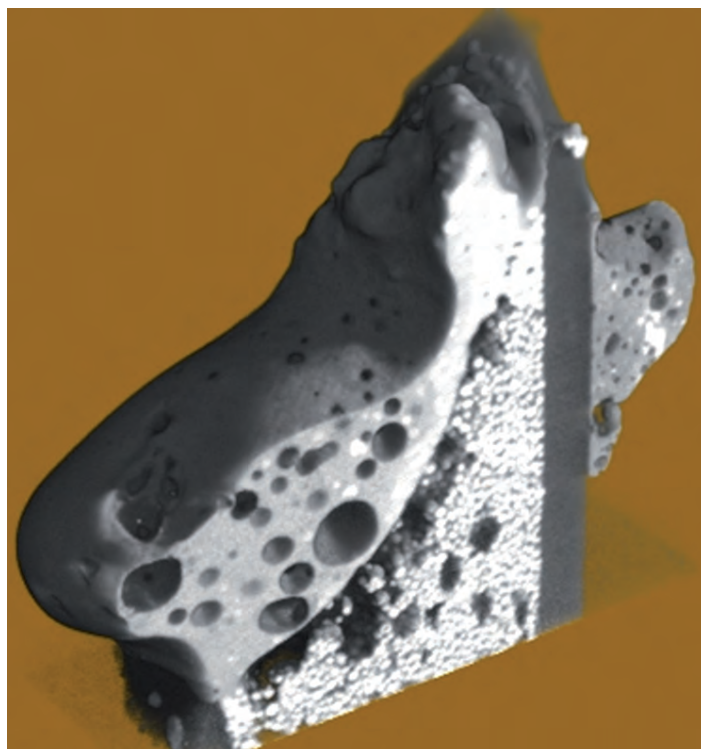


Figure 1

High energy SR μ CT for the understanding of the twin wire arc spraying process in cooperation with J. Nellesen (TU Dortmund), measured at HEMS with 120 keV X-rays and a spatial resolution of $5 \mu\text{m}$. WC/Co particles of 25 - $45 \mu\text{m}$ in diameter are visualized inside a Ni velum.

are under commissioning and first test experiments have been performed. The flexible design of the micro tomography instrument was already used for the installation of various *in situ* sample environments, like stress rigs, flow chambers and corrosion cells (Fig. 2: *in situ* corrosion of Mg biomaterials). An *in situ* furnace (for temperatures up to $800 \text{ }^\circ\text{C}$) has been built and was commissioned in November 2013. Furthermore, a sample changing robot has been installed in the micro tomography hutch and was successfully tested. The installation of the new IBL double multilayer monochromator in 2014 will boost the photon flux by two orders of magnitude. Fast (with high spatial and high density resolution) and high-speed μCT (for the *in situ* visualisation of processes) will thus be made available.

BioSAXS (P12, operated by EMBL together with HZG) started offering a focussed beam (size $110 \times 200 \mu\text{m}^2$ and flux 10^{13} ph/s)

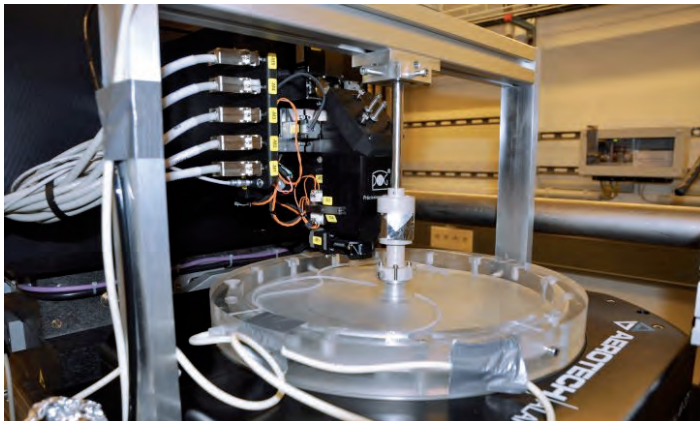
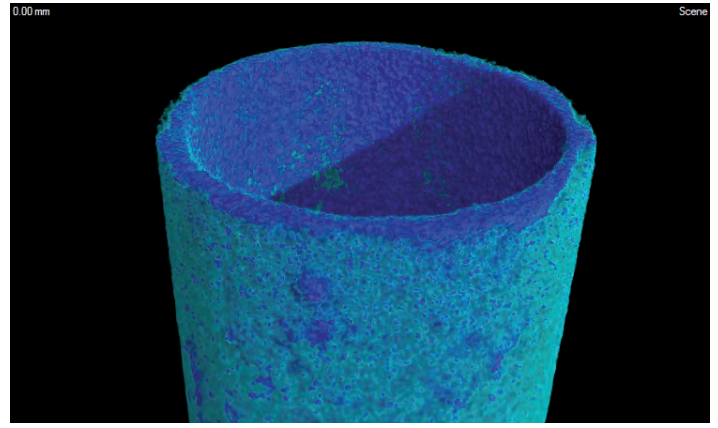


Figure 2

In situ corrosion cell mounted on the IBL micro tomography setup (left). Reconstruction of a corroded Mg tube (2 mm diameter). Projections were taken at 23 keV with a resolution of 4.25 μm . The sample was immersed for 48 hours in a body-like fluid (DMEM). Light blue shades display the corroded surface of the tube whereas darker blue shades depict intact Mg.



to users in December 2012. The further development of the instrument includes the extension of the scattering angle range by improvements of the beamstop design and an improved signal-to-noise ratio by the implementation of scatterless slits. The high throughput mode using the automatic sample changer where only 10 microliters of solution are required for a single measurement was efficiently used for describing the formation pathways of drug delivery nano vehicles such as cubosomes and hexasomes (Fig. 3). Unique beam parameters (small size, high flux and low divergence) have been used for microfluidic measurements of nanoparticles dispersed in a biopolymer matrix under different flow conditions and for investigations of microcrystals formed in butterfly wings (biophotonics). For these experiments the precise positioning of the sample including rotation has been achieved by a hexapod. Construction of a multilayer monochromator for a high flux mode (~ 100 times more flux) has been started.

The Christian-Albrechts University in Kiel (CAU) and HZG agreed to jointly contribute to the operation of the Nanofocus Endstation of P03 (in collaboration with DESY), which had been constructed as a “Verbundinstrument” by the CAU. The combination of a high flux nanobeam of $250 \times 350 \text{ nm}^2$ optimized for diffraction experiments with a working distance of 80 mm will be further exploited in the field of engineering materials science.

GEMS has not only been offering full support to international scientific users. As the experimental possibilities of GEMS are particularly relevant for companies with questions from engineering materials science, we have been traditionally successful in the acquisition of industrial users. Still, there is always room for improvement. During the EU-supported INTERREG programme for the Baltic Sea region, “Science Link”, several industry measurements were performed. The applicants were companies from the industrial fields of mining, metal processing and the automotive industry as well as from medical technology. They have been granted in total eight beamtimes between 8 hours and 2 days including additional data analysis and interpretation. The measurements were or will soon be performed at the GEMS beamlines. Three companies will come back for beamtime as regular industry customers.

Within our central project of the Collaborative Research Centre SFB 986 (“Tailor-Made Multi-Scale Systems – M3”) a number of successful experiments were carried out in 2013. There is an excellent match between the diffraction and imaging possibilities at the GEMS beamlines and the scientific questions related to hierarchically structured materials in the focus of the SFB.

The GEMS activities (including those with neutrons at the FRM II in Garching and in preparation for instrumentation at the European Spallation Source in Lund) were very positively reviewed last April at the site of the outstation at DESY (mid-term review of the respective Helmholtz programme activities). Still, we want to offer even better service in the future and for this reason we started last year a series of GEMS Satellite Workshops to the DESY Photon Science Users’ Meeting. The workshops will take place every year, with the aim of deepening the fruitful discussion with our users.

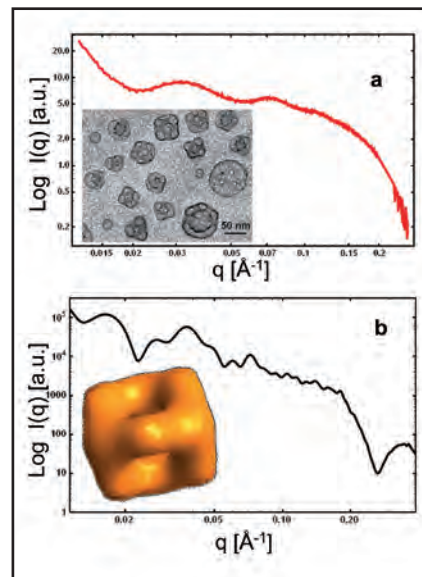


Figure 3

Experimental SAXS curve recorded at the BioSAXS beamline at 25 °C for MO/EPA/DOPE-PEG2000 (79/19/2 mol%) nanoparticles in excess buffer solution (insert: cryo TEM picture); (b) calculated SAXS pattern for a ten-nodes cubosome [B. Angelov *et al.*, *Langmuir* 28, 16647 (2012)].

Contact: Martin Müller, martin.mueller@hzg.de
Andreas Schreyer, andreas.schreyer@hzg.de

University of Hamburg on the DESY site.

Excellent students – excellent science



Figure 1

At the CUI International Symposium 2013, world leading scientists met at CFEL to present and discuss the latest results and developments in photon and nanoscience.

Photon Science is one of the key science areas of the University of Hamburg. The strong commitment to excellence in photon science, life sciences and nanoscience of the University of Hamburg and DESY together with partners from the Max-Planck Society and EMBL was the basis for establishing the Cluster of Excellence – "Hamburg Center for Ultrafast Imaging (CUI): Structure, Dynamics and Control of Materials on the Atomic Scale", (<http://www.cui.uni-hamburg.de/en/>). Within CUI up to three new full professorships and up to six professor positions on the junior level are in the process of being filled. CUI organized its first big international symposium in November 2013 with key note speakers presenting the latest results and developments in all relevant fields from experimental and theoretical ultra-fast physics to X-ray and laser science, solid state physics, quantum optics and nanoscience (Fig. 1). Among the highlights was the award ceremony for the Hamburg Prize in Theoretical Physics sponsored by the Joachim Herz Foundation which was given to Chris H. Greene, Purdue University, for his outstanding pioneering theoretical contributions to atomic and molecular physics.

In 2011 DESY and the University of Hamburg established PIER – Partnership for Innovation, Education and Research as a new platform to foster their long-standing collaboration. One of the strong pillars of PIER is the PIER Helmholtz Graduate School which had its official kick-off meeting in October. The goal of the PIER Helmholtz Graduate School is to combine the unique scientific opportunities on the Campus in Bahrenfeld with excellent PhD training for candidates from Germany and

abroad. In a very tight competition up to six outstanding students are granted PhD scholarships by the private Joachim Herz Foundation. The activities within PIER complement the strong network of excellence in education on the graduate level between the University and DESY. In photon science this is manifested for example through joint master courses in modern X-ray physics and accelerator based photon sources, jointly supervised Master and PhD thesis work, and joint teaching activities in the DFG funded Collaborative Research Centre SFB 925 and Research Training Group GRK 1355.



Figure 2

The spectroscopy chamber of the University of Hamburg on its way to the PG2 beam-line in the FLASH experimental hall.



Figure 3

Dorothee Stapelfeldt, Second Mayor and Senator for Science and Research in Hamburg, speaking to the participants during the CFEL inauguration.

BMBF Verbundforschung strongly supports university activities at large scale facilities with the goal to develop new instrumentation and methods, to use the special expertise of university groups for research, to educate young scientists and engineers and to attract young academics for future research infrastructures. In the round which started July 2013 the research activities in photon science and accelerator science of the University of Hamburg at DESY have led to a very significant number of new projects centred around PETRA III, FLASH and the European XFEL. In total, projects with principal investigators from the University have attracted funding of more than 4.5 M€ over the next three years. Among the highlights are the activities in the framework of the BMBF Priority Program FSP-302 “Free-Electron Lasers” (coordinator: Markus Drescher) which evolved out of the very successful FSP 301 “FLASH: Matter in the Light of Ultrashort and Extremely Intense X-ray Pulses”. Also with support of BMBF Verbundforschung the University of Hamburg continues its involvement at PETRA III and actively contributes to the construction of the “Chemical Crystallography Beamline” P24 at the PETRA III extension.

2013 has also seen the groundbreaking ceremony for the new Centre for Structural Systems Biology (CSSB) which – in the area of life sciences – will soon complement the joint research activities on the DESY campus. DESY and the University of Hamburg together are going to appoint a new full professorship for the CSSB, also conceived to create a strong bond in photon science and a fruitful scientific cooperation with the Center

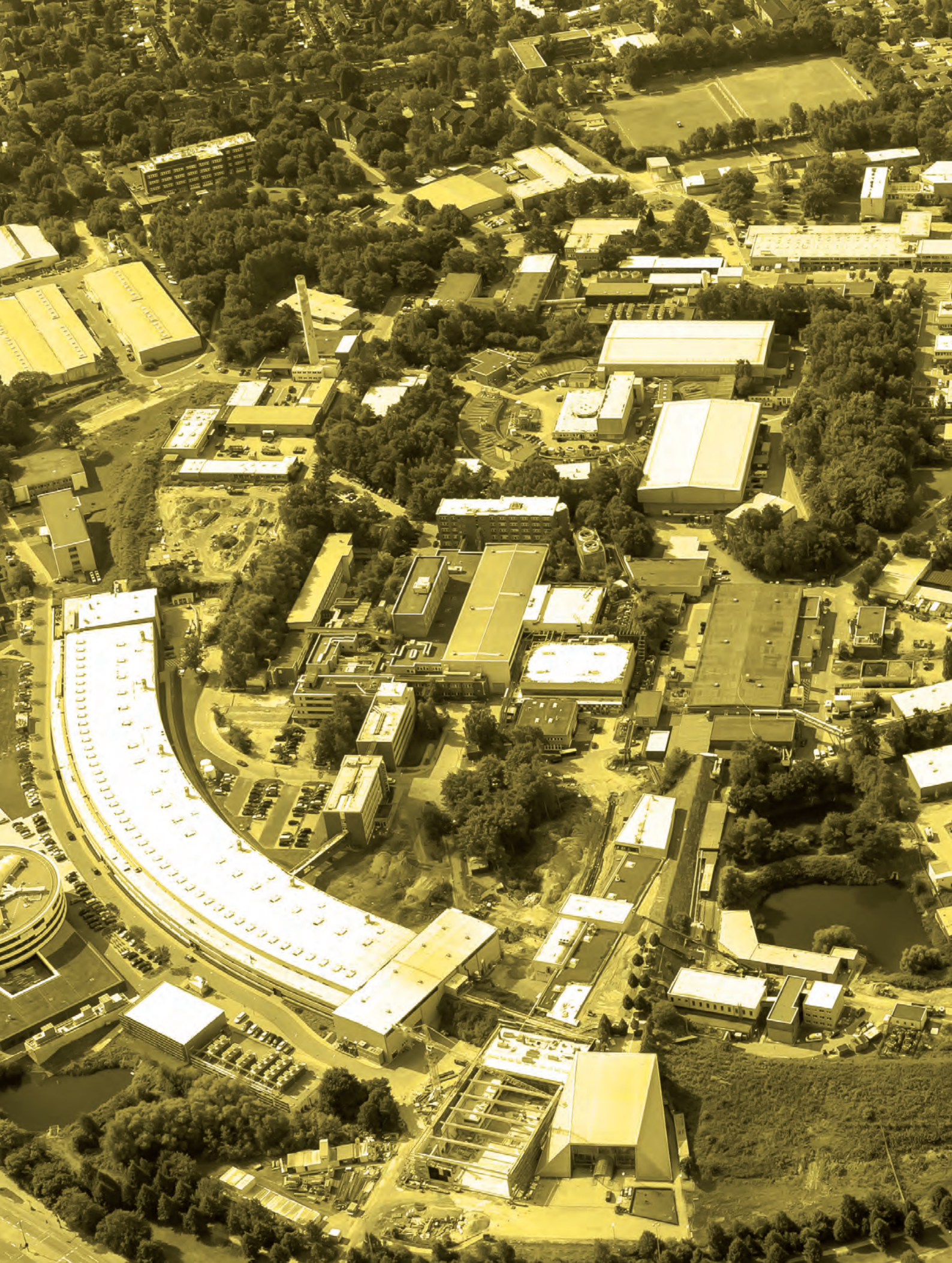
for Free-Electron Laser Science (CFEL). The CFEL celebrated its official inauguration in the new building on June 17th (Fig. 3). In addition, the activities in nanoscience will be boosted in the next years by new centres established by the University (Center for Hybrid Nanostructures – CHYN, coordinator: Robert Blick, Fig. 4) and DESY (NanoLab, coordinator: Andreas Stierle) which will combine efforts to use the photon sources on the Campus for cutting-edge research in nanoscience.

Contact: Wilfried Wurth, wilfried.wurth@desy.de



Figure 4

The future Center for Hybrid Nanostructures (CHYN) of the University of Hamburg on the Bahrenfeld Campus. (Courtesy of Reiner Becker Architekten Berlin)



Light Sources.

- **FLASH** 90
- **PETRA III** 92
- **European XFEL** 96



Figure 1

Aerial view of the FLASH facility in early August 2013 including the FLASH2 tunnel and the new experimental hall under construction.

The year 2013 was mainly centred on the extension of the FLASH facility, including building a separate tunnel for the additional FEL undulator line and a new experimental hall (Fig. 1). After the 4th beamtime period for user experiments was finished in February 2013, the accelerator was shut down until July in order to cut out the required opening between the two tunnels. Moreover all the electron beamline components were installed in the extraction area (Fig. 2). The 14 m stretch between the last accelerator module and the septum was modified accordingly in May and June, and the FLASH2 extraction beamline installed in June and July. In parallel, also many of the subsystems have

been changed during the shutdown to improve their performance or to make them compatible with the systems of the European XFEL. These include the control system of the magnets and the RF system, as well as the personnel interlock system, which had to be modified for FLASH2.

The re-commissioning of FLASH1 started mid-August in order to prepare for the 5th user period, while construction work in the FLASH2 tunnel was continued in parallel. Unfortunately, the area between the old and the new tunnel could only be filled with sand at this time, causing the FLASH1 tunnel floor

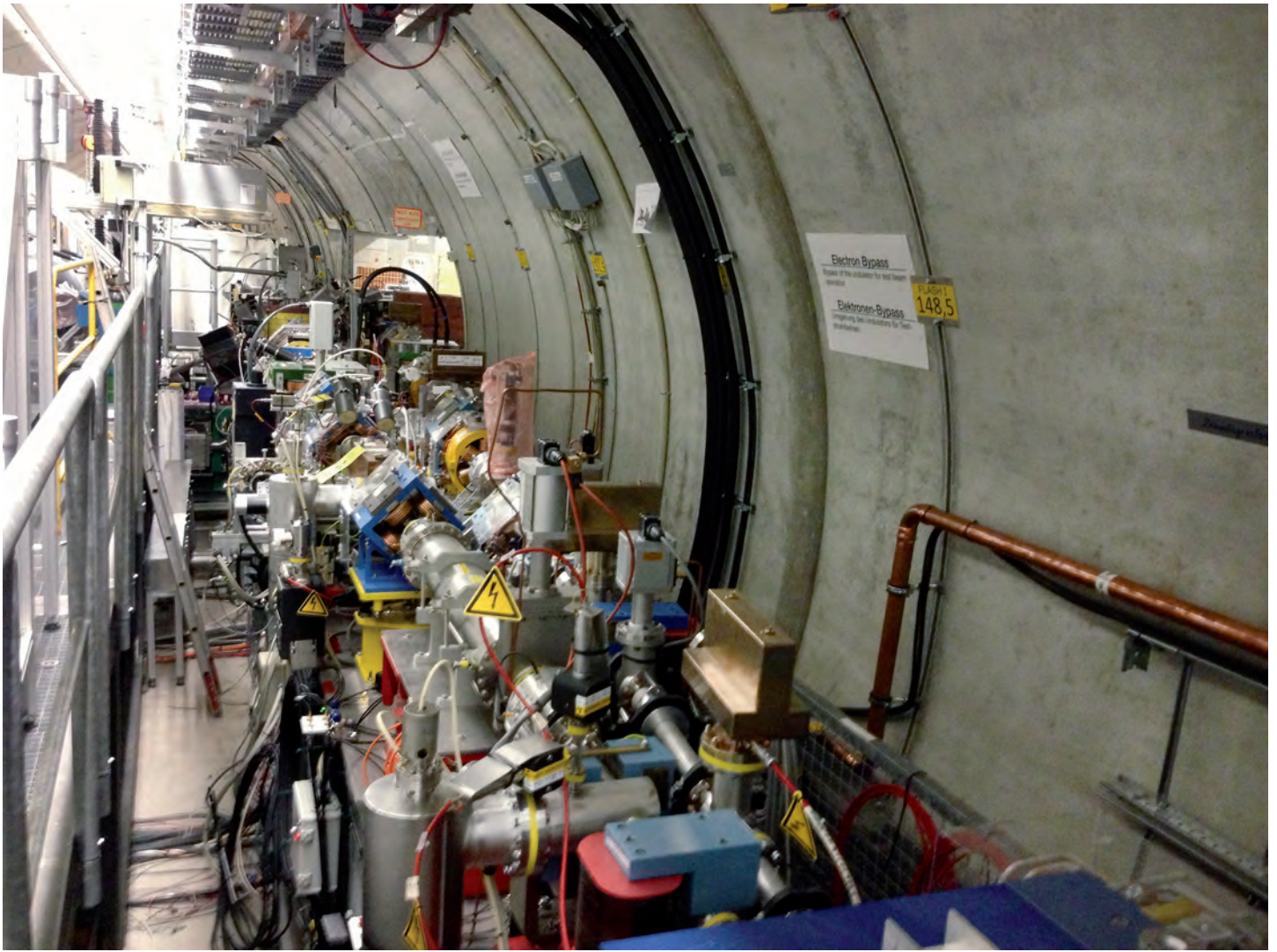


Figure 2
The modified FLASH1 and the new FLASH2 electron beamlines in the extraction area were nearly completed by the end of July 2013. Note the opening in the tunnel wall on the right through which the new beamline enters the FLASH2 tunnel.

to settle by up to 8 mm. The triangle of sand is visible in the middle of the aerial picture (Fig. 1), which was taken at that time. The expected settlement meant survey and alignment of all beamline components over a distance of 130 m, including the undulators and parts of the photon diagnostics. The remaining time for commissioning was not sufficient to guarantee stable FEL beam conditions for the first user experiments originally planned to start in late October 2013. Consequently, the complete user period had to be shifted by almost four months; it will now start by the end of February 2014.

By the end of 2013 the installation of the technical infrastructure in the FLASH2 tunnel and the corridors for the electronics is completed and most beamline components in the main tunnel are installed. Also 11 out of 12 undulator modules are mounted, the last one will be installed in January 2014 (Fig. 3). The commissioning of the FLASH2 beamline (components see Fig. 5) will start at the end of January 2014, after the test and formal approval of the personnel interlock system.

At this time, also the new experimental hall (Fig. 6) will be ready for installation of the technical infrastructure, whereas the photon diagnostics and a first photon beamline will be mounted in the first half of 2014. First photons are expected to reach the new hall in the second half of the year. Extensive tests are planned to establish parallel operation of FLASH1 and FLASH2 and to explore the parameter ranges of the FLASH2 FEL that can be achieved under practical conditions simultaneously with FLASH1 user operation. Regular user experiments in the new experimental hall are expected to start in summer 2015 on two to three beamlines. On one of them a permanent end station for atomic and molecular physics will be available. It is planned to build a total of six to seven beamlines on FLASH2. All beamlines will be equipped with suitable focusing optics and standard differential pumping stages with integrated laser ports, which will be connected to the pump-probe laser system via separate evacuated transport lines. Two to three of the beamlines will have permanent end stations and at least one beamline is foreseen to combine FEL and THz radiation.



Figure 3
 Eleven FLASH2 undulators are already mounted to the beamline (December 2013). Behind them, near the end of the tunnel, vacuum work is continuing.

At the beginning of 2013, before the shutdown of FLASH, machine studies were made in order to test the possibility of producing FEL pulse trains with different pulse lengths quasi-simultaneously on FLASH1 and FLASH2. The lasing of the present FLASH1 FEL was successfully tested with two different bunch charges generated by two separate injector laser systems; the results are shown in Fig. 4. The fast switching of the electron beam and the possibility to have different electron bunch lengths and small wavelength changes for the two trains were already shown in earlier studies.

The operation of FLASH2 will start in SASE mode, however the facility has been designed such that different seeding schemes can be implemented in order to provide FEL beams with improved performance. Most of these schemes require a strong optical laser with high repetition rate and a pulse pattern that matches the bunch pattern of the FLASH linac. Therefore, a strong research and development effort has been made at DESY together with Helmholtz Institute Jena to develop a suitable high-power, few-cycle optical laser system. The seed laser will be installed in a special room foreseen in the FLASH2 tunnel building. Presently the most promising seeding scheme is high-gain

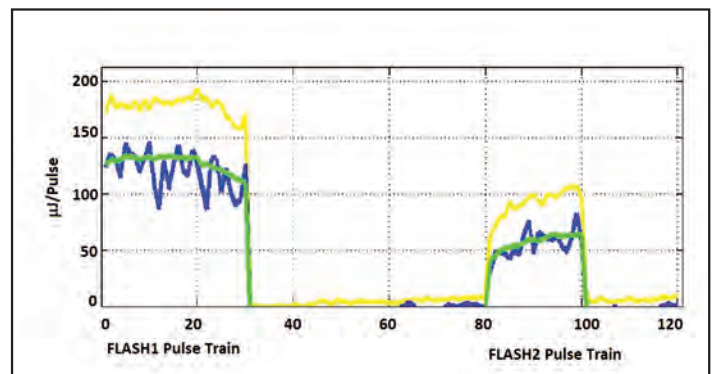


Figure 4
 Lasing with two different bunch charges in a single RF pulse. Two short FEL pulse trains are shown: bunches 1 - 30 with a charge of 0.5 nC, and bunches 81 - 100 with 0.25 nC (blue: pulse energy of the current pulse train; green: pulse energy averaged over all measured pulse trains; yellow: maximum pulse energy of measured pulse trains).

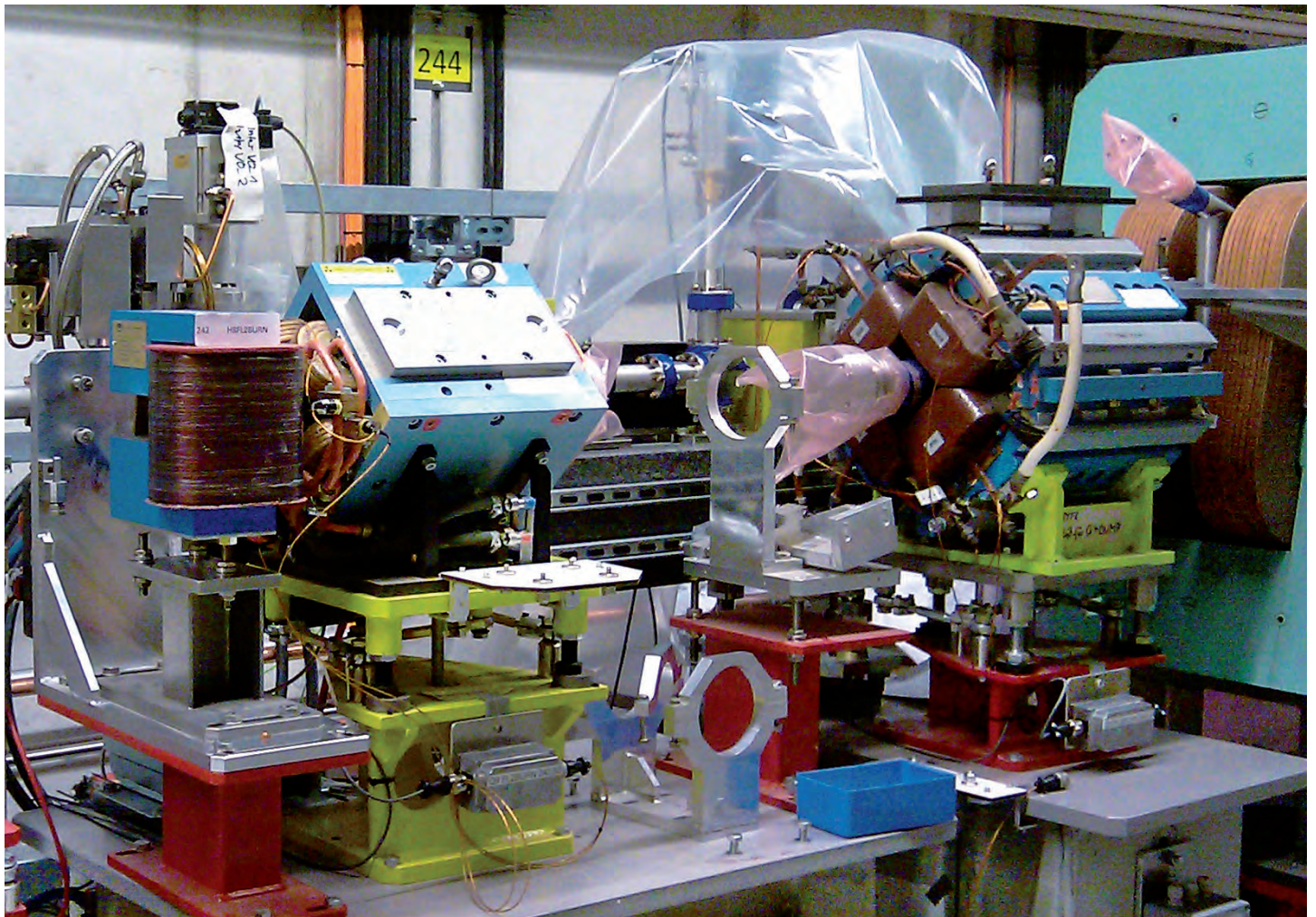


Figure 5

Close-up of FLASH2 beamline components just in front of the large dipole magnet (on the right) that diverts the electron beam to the beam dump. The FEL photon beam passes behind the magnets. It is separated from the electron beam by another bending magnet further left (upstream) in this picture (December 2013).



Figure 6

The FLASH2 experimental hall end of October 2013.

harmonic generation (HG). In this case the electron beam is seeded with an optical laser in a short undulator, called modulator, and high harmonics of the seed radiation are then selected and amplified by the tunable FEL undulator. HG has been successfully implemented at FERMI@Elettra (Trieste, Italy): intense seeded FEL pulses with high stability and narrow bandwidth down to 20 nm wavelength are available for user experiments, while a further beamline (FEL-2) using a second HG cascade is under commissioning and has demonstrated FEL pulses at 4 nm, although at reduced intensity. Other seeding schemes are currently under study at DESY. One of them makes use of high laser harmonics produced by a strong optical laser in a gas target (HHG). HHG seeding at 38 nm wavelength was successfully tested by the sFLASH project on FLASH1, however, with low gain due to low seed power. HHG seeding is currently not expected to work below 10 nm wavelength due to the low efficiency of the HHG source. It is planned to implement seeding shortly after full commissioning and first experience with FLASH2 user operation in SASE mode, i.e. 2016-2017.

Contact: Josef Feldhaus, josef.feldhaus@desy.de (FLASH)
Bart Faatz, bart.faatz@desy.de (FLASH II)

In 2013 for the first time all PETRA III beamlines were in full swing. With 5200 hours of user operation and 820 experiments a new record for user access could be achieved. In parallel to the successful user operation, all beamlines improved their performance; some examples of technical innovations are described below. A number of examples of high profile experiments are featured in the highlight section of this Annual Report.

The only call for proposals this year resulted in 458 proposals submitted for the beamlines P01-P11, additional 254 applications for life-science beamlines have been submitted to EMBL. The average overbooking factor of non-PX beamlines reached 3.1 for the second run period in 2013. The overbooking factor reached a maximum of 4.7 at the resonant scattering and diffraction/hard X-ray photo-electron spectroscopy beamline P09 (see Fig. 1), for which the demand was particularly high. For the first time a new application procedure for category I proposals was applied, now each proposal refers to one beamtime only. Starting with the first run after the extension shutdown also long term projects will be accepted. However, these will be very limited in number and linked to the development of beamlines or instruments. Details will be communicated well in advance.

Until mid of December 2013, over 2000 individual users came to work at PETRA III with an average number of 2 visits per person. The number of users originating from international institutions further increased to now 36 %. These users came from 32 different countries of which India sent the largest group.

Storage ring

In 2013 PETRA III was running almost all year long starting in January and ending December 19th. The operation has been interrupted by two shutdowns, caused mainly by preparation work for the FLASH extension. As in previous years around 50 % of the user time at PETRA III was provided in the timing mode with 40 or 60 equally distributed bunches. The other 50 % were mainly operated in the newly established 960 bunch mode.

The transition from positron to electron operation, which was established during the winter break 2012/2013, went smoothly. Since October 2013 the standard operation with a current of 100 mA could be achieved also in timing mode with 40 bunches. After the replacement of bellows close to the narrow undulator vacuum chambers and some modifications to the feedback system, a bunch current of 2.5 mA could be stored. In recent runs this value was limited to 2.0 mA. A major achievement during machine studies was the operation with a horizontal emittance of 160 pmrad at a particle energy of 3 GeV. This is the lowest value ever achieved in a storage ring. The goal was to find conditions to operate PETRA III as an ultimate storage ring in the future; i.e. operating at extremely low emittance without compromising the performance of the beamlines.

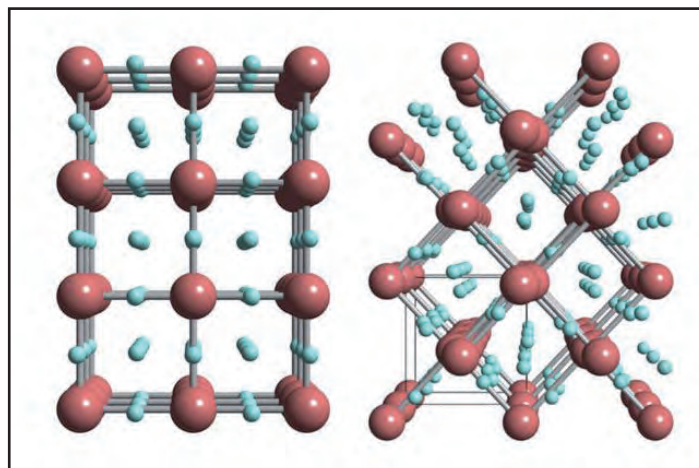


Figure 2

The new material forms at a pressure of 55 GPa (Gigapascal) and has an unexpected structure. Left: Iridium atoms (red) form a simple cubic lattice with hydrogen atoms (blue) occupying the centres of the cubes' faces. Each iridium atom is surrounded by three hydrogen atoms, resulting in an iridium trihydride phase. Right: Theoretical calculations support the presence of a distorted simple cubic metal host lattice in iridium trihydride.

While the availability of the machine has been improving steadily during the first half of the year, some major problems caused a step back during the second half. A severe problem caused by the booster DESY II and a broken coupler in one of the cavities, which had to be replaced, resulted in a loss of several days of scheduled beamtime. Despite the successful start the overall availability in 2013 will be again below 95 % (see section 'Facts and Numbers' at the end of this report).

Beamlines and Experiments

At the beamlines, a couple of technical improvements have been achieved.

An outstanding highlight was certainly a result of the collaboration with the group of T. Salditt from Göttingen University. In an experiment at the coherence beamline P10 they were able to obtain an almost perfectly circular focus of 5 nm. This is the worldwide smallest X-ray beam ever produced. It has been achieved by combining a KB mirror system as pre-focusing device with a multilayer Laue lens (MLL). In this way the overall efficiency of the system is very high in spite of the low acceptance of the MLLs.

The technical progress relating to optics further includes

- A high resolution monochromator with 0.7 meV resolution for nuclear resonance scattering with ¹¹⁹Sn at beamline P01.
- First tests of the multilayer monochromator at the nano-probe beamline P06.

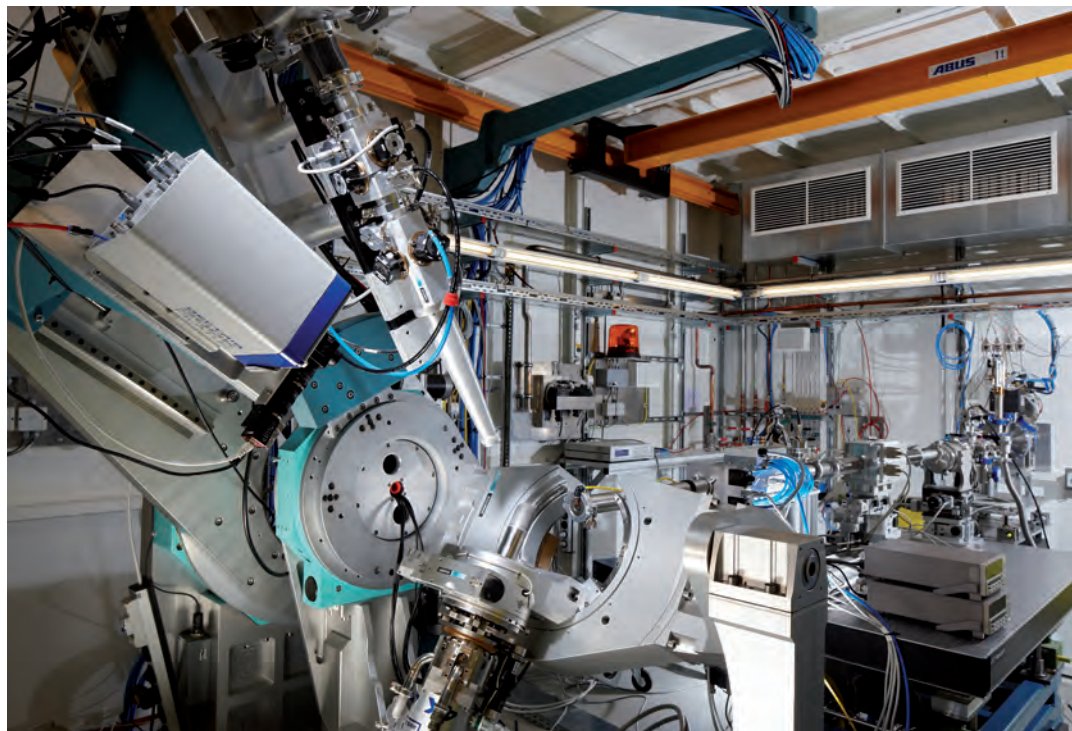


Figure 1

Experimental hutch EH1 for resonant X-ray scattering at beamline P09 at PETRA III.

- A new setup for high resolution fast *in situ* X-ray reflectivity experiments at the high resolution beamline P08.
- The implementation of wave-front preserving channel-cut optics for the coherence beamline P10.

As for detectors, the following developments can be reported on:

- At the soft X-ray beamline P04 a PERCIVAL detector was successfully tested and will be made available for users.
- At the high resolution beamline P08 a 1M-Eiger detector, which was procured in the framework of a BMBF 'Verbundforschungsprojekt' of Kiel University, is now available for users.
- At the coherence beamline P10 a Lambda detector (based on a Medipix3 model) has been successfully tested for the first time in the vertical rheology setup.
- At the dynamics beamline P01 an AGIPD detector has been successfully tested by yielding single pulse properties of the undulator radiation.

(See section 'New Technologies and Developments' for more details.)

Within the last call for BMBF 'Verbundforschungsprojekte' many applications for projects at PETRA III were again very successful, as in former calls. In total, 40 projects were approved both for existing beamlines (28 including projects at EMBL beamlines) and the new beamlines within the PETRA III extension project. First steps have been taken to include this new equipment into the PETRA III instrumentation suite.

In addition to the BMBF funded 'Verbundforschung' activities with German universities, several collaboration projects within the Röntgen-Ångström-Cluster (RAC), the Ioffe-Röntgen-Institute (IRI) and a number of individual contracts have been established in 2013. In addition, DESY Photon Science contributes to the 'Science Link' initiative of the European Union, within which eight industry projects have been completed successfully with the measurements being performed at PETRA III. In order to foster industry applications at our facilities, contacts with key-

players in German industry landscape like Airbus, Siemens or BASF have been initiated.

The number of high impact publications resulting from measurements at PETRA III is steadily increasing. Particularly in the field of high pressure research significant progress has been achieved. For example a new hydrogen storage material has been explored. In collaboration with Edinburgh University a new form of iridium hydrate was found which can store three times more hydrogen than systems used before (see Fig. 2). This is a promising route to develop safe and environmentally friendly storage materials for use in fuel-cell applications, for example.

At the resonant scattering beamline P09 the first successful experiments at a magnetic field of 14 T and temperatures as low as 300 mK have been completed. These results shed light on phase transitions in magnetic materials which might lead to new data storage technologies in the future.

At the high resolution beamline P08 the structure factor of a confined liquid film of only 5.0 nm thickness could be measured in a newly developed sample cell. This means some 9 molecules of the confined liquid fit in between the diamond surfaces of the cell. Understanding the structural changes upon confining a film to several layers of molecules will help to understand lubrication in nano-systems.

After a short break in December, PETRA III will resume operation in early January 2014 with four more weeks of beamtime for users. On February 3rd the operation will be stopped for the construction work for the two new experimental halls of the PETRA III extension project. No further operation of PETRA III for users is planned for 2014.

Contact: Hermann Franz, hermann.franz@desy.de
Alexander Kling, alexander.kling@desy.de

PETRA III Extension

The PETRA III Extension project is taking up momentum. Preparatory work on the construction sites of both experimental halls has started in December. Within the project, the storage ring lattice in the arc sections in the North and the East will be modified to accommodate additional insertion device beamlines. This requires the complete removal of the PETRA storage ring including the ring tunnel in that area to make space for two new experimental halls on either side of the present Max von Laue experimental hall at PETRA III. Both new halls may accommodate up to five beamlines, with one beamline making use of the adjacent long straight section. All new beamlines, P21-P25 in hall East and P61-P65 in hall North, will be serving experimental techniques in the hard X-ray regime.

In the North, the straight section is already filled by a 40 m long array of damping wigglers which produce an extremely hard and powerful X-ray beam which will be the source for beamline P61. In the East, the 108 m long straight section will be modified to accommodate up to three insertion devices – including a 4 m long in-vacuum undulator – for the Swedish high-energy X-ray materials science beamline P21.

The newly planned beamline P66 will cover the VUV range and continue the very successful time-resolved luminescence spectroscopy activities of the DORIS beamline Superlumi. It will be the only beamline at a bending magnet source at PETRA III and the experimental station will be located in a small separate hutch on top of the ring tunnel between the FLASH II and PETRA III Max von Laue experimental halls (see section on ‘Facts and Numbers’ at the end of this report).

The civil construction of the extension halls had to be postponed because of unexpected difficulties with the call for tender procedure and – accordingly – the schedule of the PETRA III user operation had to be re-adjusted. The machine shutdown is now planned for February 3rd, 2014. In the following weeks the storage ring will be completely removed in the arc sections of the new experimental halls and subsequently the concrete tunnel will be demolished. Earth moving activities on the construction site already started at the end of 2013.

Every effort will be made to keep the mandatory PETRA III shutdown as short as possible. The extent and complexity of the project requires considerable time until the machine can be re-installed, which will start in August 2014. It is expected that the installation of the storage ring and the first part of the beamline frontends will be completed by the end of 2014. Commissioning of the machine is planned to start in January 2015 and user operation in the Max von Laue hall is hoped to resume in early spring 2015. After the machine restart, the completion of the new experimental halls and the implementation of the experiment infrastructure and beamlines will continue in parallel to the user operation at the beamlines P01 to P14.

The preparation of the machine reconstruction is progressing according to plan. Quite a number of new components have been delivered and are currently being assembled, tested and

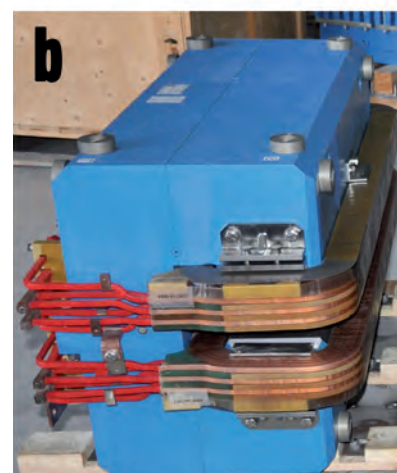


Figure 2

Components and instrumentation for the new sections of the storage ring:

- a) magnet power supplies, being assembled in the North
- b) and c) dipole and quadrupole magnets for the new DBA sections
- d) fast amplifiers for orbit feedback system
- e) storage ring vacuum chamber.

calibrated. Similarly, the assembly of frontend girders for the beamlines has started and these activities take place in the former DORIS experimental hall where the old beamlines have been removed to make space for the new instrumentation.

The detailed planning for the phase-1 beamlines, namely XAFS stations P64 and P65, is in an advanced stage. Their frontends



Figure 1

View of the former DORIS experimental hall where new instrumentation such as beamline frontends for the PETRA III extension are being assembled.



will already be completed during the long machine shutdown to allow beamline commissioning in summer 2015. The phase-2 beamlines P21-24 are expected to follow in 2016. In these cases, additional shorter machine shutdowns will be required to complete the frontend sections. The technical design reports of beamlines P21 and P23 have been reviewed and the detailed design phase has begun. Out of the phase-3 beam-

lines, only the damping wiggler beamline P61 is currently funded. Beamlines P25, P62 and P63 will not be implemented within the current project phase up to 2017.

Contact: Wolfgang Drube, wolfgang.drube@desy.de
Michael Bieler, michael.bieler@desy.de



Figure 3
Layout of the experimental hall and beamlines of PETRA III East.



Figure 4
Layout of the experimental hall and beamlines of PETRA III North.

European XFEL.

Underground construction completed, building components in full swing

In 2013, progress continued on construction of the European XFEL facility and research instrumentation. At mid-year, civil construction reached a major milestone with the completion of underground construction. In 2013 the installation of the accelerator complex began with the setup of the electron gun. Further work on undulators, instruments, and software helped the facility make major steps forward.

On 6 June, European XFEL welcomed 300 guests into the facility's experiment hall and tunnels in Schenefeld to celebrate the completion of underground construction. Following three years of nonstop work, civil construction of the 5.8 kilometres of tunnels and various underground facilities, including the 4500 square metre experiment hall, were completed. Current progress focuses on the installation of technical infrastructure in tunnels and the work on surface buildings. The buildings above shafts and the complex at Osdorfer Born were tendered and their construction is well underway. Meanwhile, below, workers continue installation of the technical infrastructure that will support the accelerator complex and X-ray beamlines in the tunnel. European XFEL is preparing calls for tender for the large lab and office building above the experiment hall in Schenefeld, of which the construction shall start early 2014. Across all

construction sites, from Bahrenfeld to Schenefeld, a number of environmental compensation measures were also implemented this year.

Once operational, the instruments in the experiment hall will address a wide range of scientific areas, with complex demands on space and infrastructure within the hall. These demands are augmented by the need to co-locate high precision optical laser systems that will be synchronized at the femtosecond level with the X-ray pulses coming from the FEL undulators. During 2013 significant progress was made with the planning of the hutch layout, with the general infrastructure as well as the instrument-specific technical infrastructure. The process also involves not only the instrument groups, but also all other contributors such as civil construction, general technical infrastructure, safety, synchronization, transport and a number of outside planning companies supplementing the internal planning resources. As a result of these planning efforts, the tender for the SASE1 instrument hutches is expected early in 2014. After construction and installation of the general infrastructure in the experiment hall, the SASE1 instruments themselves will be installed starting late in 2015. The hutches and infrastructure installation for the other SASE beamlines will follow closely behind.

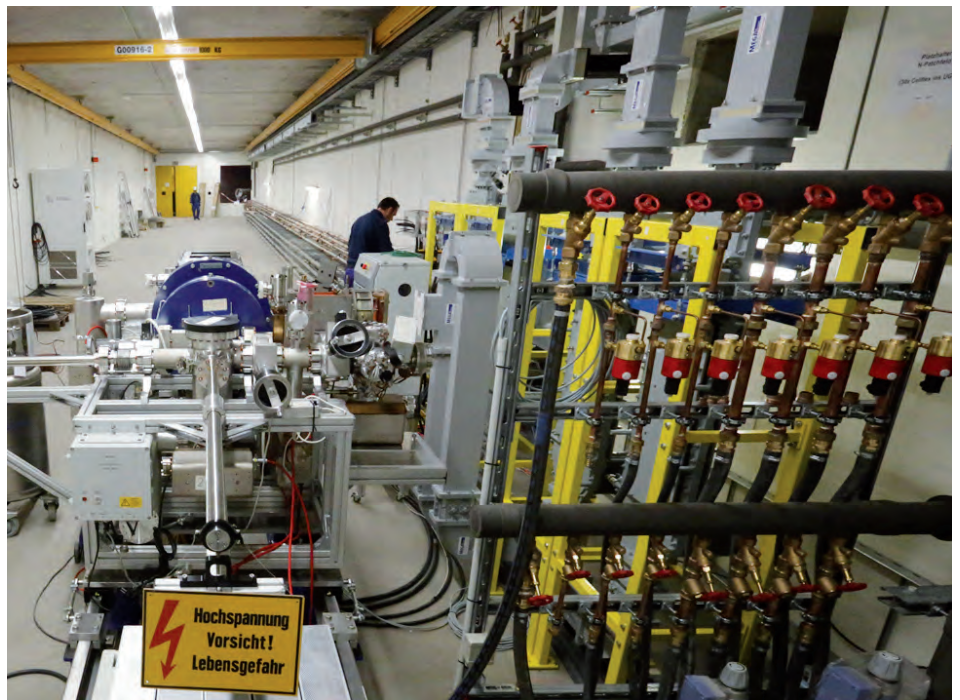


Figure 1

Undulators continue to be tuned. Out of the total 92 undulators, 65 have been calibrated so far.

Figure 2

The European XFEL's electron gun was installed in late 2013 and is currently in the middle of RF tests.



The six scientific instruments also moved forward a great deal. Four of the instruments—FXE, MID, SPB, and SQS—now have completed and published technical design reports (TDRs), which can be accessed on the European XFEL website. The goal is to install the first instruments in the experiment hall by the end of 2015. The other two instruments, SCS and HED, have published conceptual design reports (also available on the European XFEL website) and are on track to finish their TDRs soon.

With the further development of the instruments, contributions to various parts of the accelerator complex have continued to pour in. To date, over 560 million euro of in-kind contributions (IKCs) from 21 institutes in 9 countries have been agreed upon to be delivered to European XFEL, with many of those contributions currently being delivered and tested. DESY, the European XFEL's largest shareholder, is managing construction, commissioning, and operation of the accelerator complex. Accelerator components from 8 different countries are coming in and serial production for all linear accelerator components is either running or ramping up. However, the delivery of RF couplers has turned out to be a time critical bottleneck and contributes to the schedule challenges for the serial production of the accelerator modules. Warm and cold testing of completed accelerator modules began this year. All of the 3 vertical cryostats for cavity testing at the Accelerator Module Test Facility (AMTF) are in use, and so far over 110 cavities have been tested and accepted. Other infrastructure elements such as magnets, cavity tuners, klystrons, pulse modulators, and power electronics are either in production phase or will be shortly. Additionally, radiation safety, access control, and alignment systems are being installed.

The team at DESY has installed the electron gun and is in the process of commissioning it. During 2014 still many components of the injector will be installed, in parallel with initial operation of the electron gun.

Meanwhile, the European XFEL undulator group continued to calibrate the 5 m long undulator segments. By the end of 2013, 65 segments, out of total 92 segments, have been tuned and calibrated to match the tight requirements. In mid-2013 and due to space restrictions in the undulator assembly hall, the group started moving the calibrated undulator segments to an off-site storage area. All undulators are due to be completely calibrated by 2015 and will be installed shortly thereafter.

To control the many parts of the European XFEL, the data management and controls group (DAQ) has developed a new software framework. Called Karabo, the framework will provide the users and operation crews both mechanical control and digital data acquisition of all X-ray systems of the European XFEL facility. The system further includes an interface to the accelerator control system, developed by DESY. Scientists both within and outside European XFEL are working to fine-tune Karabo's capabilities over the next two years.

With its 27 000 flashes per second, European XFEL will be unique among the world's X-ray free-electron laser sources. The new research facility, which is expected to start user operation in 2016, is one of the largest and most ambitious European research projects to date. The non-profit limited liability company European X-Ray Free Electron Laser Facility GmbH (European XFEL GmbH) grew from 145 employees in December 2012 to 196 employees as of December 2013. At present, 12 countries are participating in the project: Denmark, France, Germany, Greece, Hungary, Italy, Poland, Russia, Slovakia, Spain, Sweden, and Switzerland. The governments of the partner countries designate shareholders who form the European XFEL Council, which decides on important issues related to the company and the project. European XFEL and DESY closely collaborate on construction, commissioning, and operation of the facility on the basis of a long-term agreement.

Contact: Massimo Altarelli, massimo.altarelli@xfel.eu





New Technologies and Developments.

- Spin your sample **102**
- X-ray glimpses for PERCIVAL **104**
- Sub-meV resolution at PETRA III **105**
- Flux for fluorescence **106**
- Smooth and stable **108**
- Feel a pulse **110**

Spin your sample.

A new setup for high resolution *in situ* X-ray reflectivity experiments at beamline P08

X-ray reflectivity (XRR) is a non-destructive technique used in chemistry, physics, and materials science to characterize surfaces, thin films (from several to 500 nm) and multilayers [1-4]. In particular, parameters such as thickness, interface roughness, and layer density can be obtained with accuracies of better than 0.1 nm in thickness and roughness determination and 1 % in density calculation. In most cases XRR of solid samples is acquired by performing a $\theta/2\theta$ angular scan. In this case a monochromatic X-ray beam is used while both, the sample (θ) and the detector (2θ) are scanned stepwise. To determine the film parameters accurately the scan angular resolution should be high (small step width) and the q -range large where q is the wave vector transfer which directly depends on θ with: $q = 4\pi \sin\theta/\lambda$.

As to its high sensitivity in the characterization of thin films, XRR is a promising method for *in situ* investigations of dynamic phenomena such as the growth of thin films, polymerization processes, protein adsorption, interdiffusion and annealing processes in multi layer systems, etc. However, up to now the time resolution achieved is strongly limited by the data acquisition method itself: The $\theta/2\theta$ scans imply accelerating, decelerating and backlashing of the scanned motors as well movements in forth and back directions which prevent continuous capturing of the reflectivity data. Recently, typical time resolutions of the

order of a few minutes have been achieved for reflectivity in a q -range of 0 - 0.5 \AA^{-1} [5-7].

Instead of scanning 2θ it is possible to use a position sensitive detector and only scan the incident angle θ . Still drawbacks of the stepwise scanning of the incident angle limit the use of this method for *in situ* studies. Alternative approaches exist. One is to use a white X-ray beam and an energy dispersive detector. However, the heat load on the sample due to the white beam is tremendous and samples can easily be damaged. Furthermore X-ray sources such as X-ray tubes and undulator sources cannot deliver high intensity white beam with uniform flux over the energy distribution. Finally, the time resolution and q -resolution are strongly limited by the energy resolution and the dynamic range of the detector [8, 9]. Another approach is to generate a strongly focused X-ray beam and to make use of the divergence of the beam for an angular dispersive reflectivity [10]. Here the q -space and resolution are restricted by the maximum opening angle of the focused beam. Also the strong focusing means high flux density at the sample which is not advantageous for polymer or biological samples [11].

We propose a new method based on the fast rotation of a slightly tilted sample (see Fig. 1 and 2). The sample is placed on top of a bias-cut cylinder (with bias-cut angle ϕ) mounted on a wobble-free piezo driven rotation. The piezo drive is tilted to

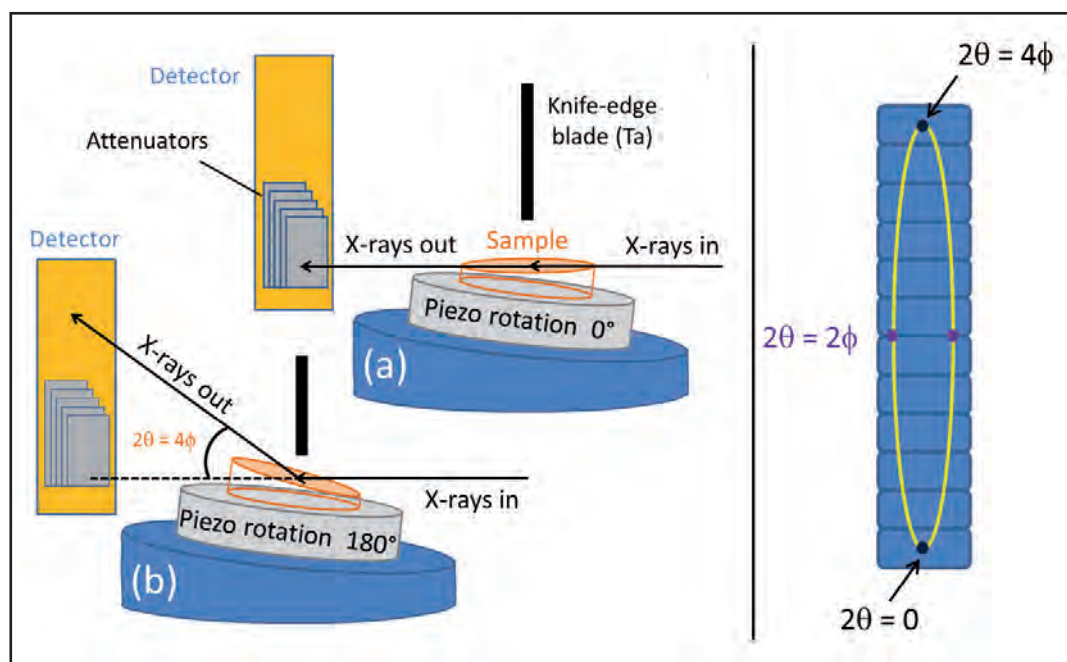


Figure 1

Left: Schematic view of the setup.

(a) Piezo rotation = 0°, $\theta = 0^\circ$

(b) Piezo rotation = 180°, $\theta = 2\phi$.

Right: The reflected intensity has an ellipsoidal shape on the detector sensitive area.

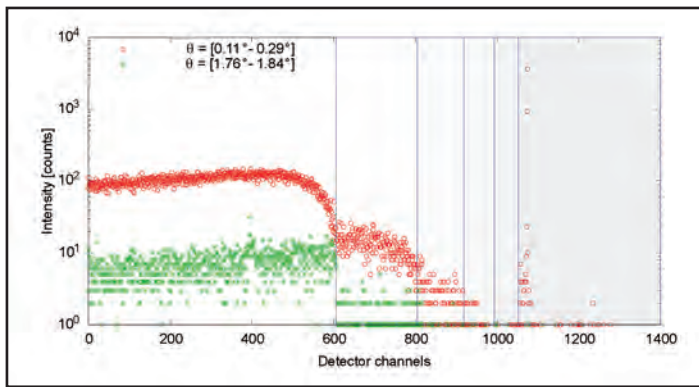


Figure 2

Raw files (Mythen detector) corresponding to an incident angle θ varying from 0.11° (channel 1072) to 0.29° (channel 1069) – see red 'o' – and from 1.76° (channel 415) to 1.84° (channel 385) – see green 'x'. The higher background contribution at smaller incident angles (red 'o') can easily be observed at channels < 600 where no attenuators are used. The attenuator foils are indicated by the gray boxes.

a constant angle of ϕ so that the piezo rotation axis is by ϕ off the vertical axis. A moderately focused X-ray beam comes horizontally. By rotating the piezo drive, the incident angle changes between 0 and 2ϕ . No other motors are moved, no motors are scanned. The position sensitive detector remains static. Since the intensity of a reflectivity scan varies over several orders of magnitude when varying the incident angle, a set of attenuators of different thicknesses is mandatory. In our case we use Fe thin foils. They are positioned just in front of the detector. Their number and positions can be optimized depending on the configuration (sample, energy, and detector). Additionally, a knife-edge blade (Ta) is used to reduce the contribution from air scattering. It is placed just above the sample.

Fast data acquisition (Mythen Detector from Dectris) is performed while the piezo drive is rotating at a frequency of 0.1 to 2 Hz. Actually the exposure time chosen for the data acquisition turns out to be a critical parameter: Long exposure times spoil the signal to noise ratio due to the high background contributions associated to the small incident angles (see red symbols in Fig. 2). Therefore, a complete reflectivity is recorded over several frames of short exposure times (typically 0.05 to 0.1 s) i.e. integration over small angular range to prevent from a too high background contribution and ensure a good signal to noise ratio. In this way complete reflectivity scans are recorded within a few seconds without interruption or downtime between each complete scan.

A python script is used to generate a full reflectivity scan from the short exposures. The script extracts the *in situ* reflectivity data from the multiple detector files. The algorithm is based on the following steps: 1) filtering of the data, 2) attenuation correction – to make allowance for the presence of the attenuators, and 3) speed correction – to take into account the fact that the different channels of the detector are unequally illuminated in time, a direct consequence of the elliptical trajectory described by the reflected beam on the detector sensitive area (Fig. 1). As an illustration Fig. 3 shows a reflectivity scan obtained for a polystyrene thin film ($d \sim 570 \text{ \AA}$). The complete scan was recorded

within 1s (20 frames, exposure time of 0.05 s) at the high resolution diffraction beamline P08 (PETRA III) [12] at an energy of 18 keV and a primary beam intensity of 10^{11} photons/sec. The beam size was (H x V) $200 \mu\text{m} \times 30 \mu\text{m}$. The q-values spans from 0 to 0.4 \AA^{-1} and the intensity drops down to roughly 6.5 orders of magnitude from the primary beam.

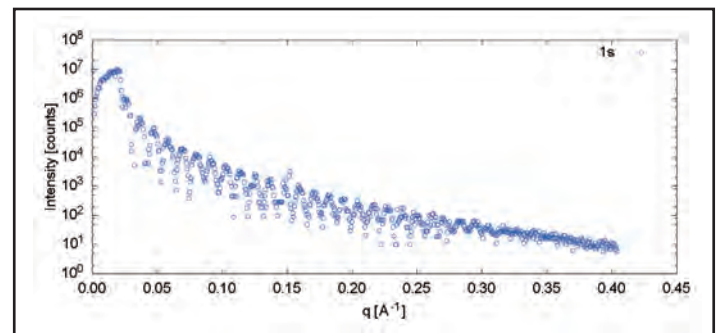


Figure 3

Reflectivity scan obtained for a polystyrene thin film recorded at P08 in 1s.

Outlook

Our new approach for performing fast reflectivity measurements already showed promising results and will open up a new route to perform *in situ* reflectivity studies. Two bias-cut sample stages (with bias angle of about 1° and about 2° respectively) are already available so that, at the X-ray energy of 18 keV, the q-ranges of $0 - 0.4 \text{ \AA}^{-1}$ and $0 - 0.8 \text{ \AA}^{-1}$ are accessible. Two additional sample stages with different cuts as well as a sample stage heating module will be manufactured. Depending on the specimen under study, the q-range investigated and the spatial resolution required the primary X-ray beam energy can be adapted within the range of 14 - 20 keV. A systematic study of experiment parameters such as the piezo rotation speed and the detector exposure time is foreseen and will help us to understand the influence of these parameters on the quality of the collected data and the time resolution achieved.

Contact: Adeline Buffet, adeline.buffet@desy.de

Authors

A. Buffet¹, M. Lippmann¹, K. Pflaum¹ and O. Seeck¹

¹. Deutsches Elektronen-Synchrotron DESY, Notkestrasse 85, D-22607 Hamburg, Germany

References

1. V. Holy, et al., *Phys. Rev. B.* **47**, 15896 (1993)
2. Jens Als-Nielsen, *Elements of Modern X-Ray Physics*, Wiley, New York, (2001)
3. J. Daillant, A. Gibaud, *X-Ray and Neutron Reflectivity: Principles and Applications*. Springer (1999)
4. M. Tolan, *X-Ray Scattering from Soft-Matter Thin Films*, Springer, (1999)
5. T. Hosokai et al., *APL* **97**, 063301 (2010)
6. N. Zotov et al., *Adv. Eng. Mat.* **13** (6) 475 (2011)
7. A. G. Richter et al., *Langmuir* **29**, 5167 (2012)
8. C.-H. Lee et al., *Nucl. Instrum. Methods Phys. Res. A* **467-468**, 1073 (2001)
9. T. H. Metzger et al., *Nucl. Instrum. Methods Phys. Res. A* **350**, 398 (1994)
10. A. Naudon et al., *J. Appl. Cryst.* **22**, 460 (1989)
11. A. Meents et al., *PNAS* **107**, 1049 (2010)
12. O. H. Seeck et al., *J. Synchrotron Rad.* **19**, 30 (2012)

X-ray glimpses for PERCIVAL.

First X-rays for the soft X-ray imager prototype sensor recorded at beamline P04

With the increased brilliance of state-of-the-art Synchrotron radiation sources and the advent of Free-Electron Lasers enabling revolutionary science with Extreme Ultra Violet (EUV) to X-ray photons an urgent need for suitable photon imaging detectors arises. Requirements include high frame rates, very large dynamic range, single-photon counting capability with low probability of false positives, and (multi)-megapixels. PERCIVAL (“Pixelated Energy Resolving CMOS Imager, Versatile and Large”) is being developed to address this need for the soft X-ray regime. Its monolithic active pixel sensor (MAPS) will be back-thinned to access its primary energy range of 250 eV to 1 keV with target efficiencies above 90 %. According to preliminary specifications, the roughly 10 x 10 cm², 3700 x 3500 pixel CMOS sensor will operate at frame rates up to 120 Hz and use multiple gains within its 27 μm pixels to measure 1 to ~ 10⁵ simultaneously arriving photons. Small-scale front-illuminated prototype systems are in hand and are undergoing detailed characterization with optical photons in the laboratory. In May 2013, such PERCIVAL prototype chips saw first X-rays at P04 in a parasitic user configuration.

PERCIVAL is currently being developed by a collaboration of DESY, RAL, Elettra, and DLS to address the dire need for high sensitivity, high dynamic range, high rate, large area imagers for the soft X-ray regime for experiments at both synchrotrons and FELs. Currently, small scale front-illuminated prototype systems (160 x 210 pixels) are undergoing functional testing in the laboratory. In May 2013, such front-illuminated prototype test sensors were exposed to X-rays up to 2 keV at the P04 beamline at PETRA III.

Fig. 2 shows an image of an attenuated 900eV P04 beam, recorded with a PERCIVAL prototype sensor. The calculated photon intensity resulting from a preliminary sensor calibration corresponds to the known incident photon intensity to within a factor of two. Two apparently brighter rows are evident within the illuminated sensor area. This artefact arises because the sensor is front-illuminated, and the metal layers are thick enough to result in significant absorption at 900 eV. As the sensor shall be back-thinned and back-illuminated to optimize soft X-ray response, this effect will not be relevant to the final sensor’s operation – pixel quantum efficiency should be uniform and above 90 % for the full energy range of the imager.

We expect first back-thinned prototype chips in early 2014, and a first large scale imager under commissioning in early 2015.

Contact: Cornelia Wunderer, cornelia.wunderer@desy.de



Figure 1

PERCIVAL test sensor (7 x 12 mm²) on interface board (blue) mounted with in-vacuum readout electronics in its chamber.

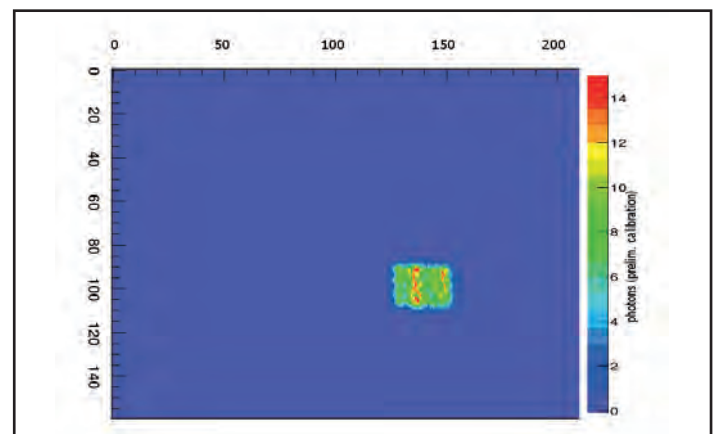


Figure 2

Image of the collimated beam recorded with a second variant of the PERCIVAL prototype chip. This image shows a pre-collimated beam of 900 eV with image intensity units (according to a preliminary calibration) corresponding to the number of photons recorded per pixel.

Authors

C. B. Wunderer¹, A. Marras¹, M. Bayer¹, G. Cautero³, S. Farina³, P. Gasiorek², L. Glaser¹, P. Goettlicher¹, N. Guerrini², S. Lange¹, J. Marchal⁴, B. Marsh², R. Menk³, T. Nicholls², F. Pithan¹, F. Scholz¹, I. Sedgwick², J. Seltmann¹, I. Shevyakov¹, S. Smoljanin¹, L. Stebel³, N. Tartoni⁴, R. Turchetta², J. Viehhaus¹, M. Viti¹, Q. Xia¹, H. Yousef³, M. Zimmer¹, H. Graafsma^{1,5}

1. Deutsches Elektronen-Synchrotron DESY, Notkestrasse 85, D-22607 Hamburg, Germany
2. Rutherford Appleton Laboratory RAL/STFC, Didcot, UK
3. Elettra Sinchrotrone Trieste, Italy
4. Diamond Light Source, Didcot, UK
5. Midsweden University, Östersund, Sweden

Sub-meV resolution at PETRA III.

Nuclear resonance scattering with ^{119}Sn at beamline P01

Nuclear resonance scattering similar to Mössbauer spectroscopy yields information on atomic, magnetic and electronic properties of the solid state. In addition, the vibrational density of states is directly accessible by nuclear inelastic scattering. Due to the outstanding properties of third generation synchrotron radiation sources, the technique allows to perform the measurements under extreme conditions, e.g. high pressure, surfaces and very small samples. A drawback of the method is the limited number of so called Mössbauer isotopes with energy of the nuclear resonances distributed in the energy range between 5 and 100 keV. The application of the method to a new Mössbauer transition often requires the development of new X-ray optics.

A new high resolution monochromator was built at the P01 beamline to perform nuclear resonance scattering with the ^{119}Sn Mössbauer transition at 23.879 keV. It was elaborated according to the conventional “nested” design [1] and consists of two channel-cut crystals with Si (6 4 2) and Si (12 12 12) reflections chosen for the outer and inner crystals (Fig.1). The crystals have been manufactured in the DESY Photon Science crystal laboratory. A heating element was installed on the 3rd crystal in order to compensate the difference in lattice parameters between 2nd and 3rd crystals occurring due to the heat load and gradient in the Si slab. The application of about 10 mW heating power leads to an increase of flux by a factor 4. The monochromator provides a bandpass of 0.72(5) meV (Fig. 2) and a flux of 1.9×10^9 photon/sec. The achieved degree of monochromatization is $\Delta E/E = 3 \times 10^{-8}$.

The efficiency of the monochromator has been tested by measurements of the nuclear inelastic scattering (see Fig. 3) of a polycrystalline foil of β -Sn enriched by the resonant ^{119}Sn isotope. The high efficiency of the measurements leads to the possibility to use the monochromator for studies of the lattice dynamics and electronic structure of compounds of scientific interest even with a natural abundance of ^{119}Sn isotope (8.6 %). Examples of such compounds are the phase change materials SnSb_2Te_4 and $\text{Ge}_{11}\text{Te}_{60}\text{Sn}_4\text{Au}_{25}$ [2] and the thermoelectric material SnTe [3]. Besides application to nuclear resonance scattering, the monochromator can be used for the applications where high level of monochromatization is required, i.e. for high resolution topography [4].

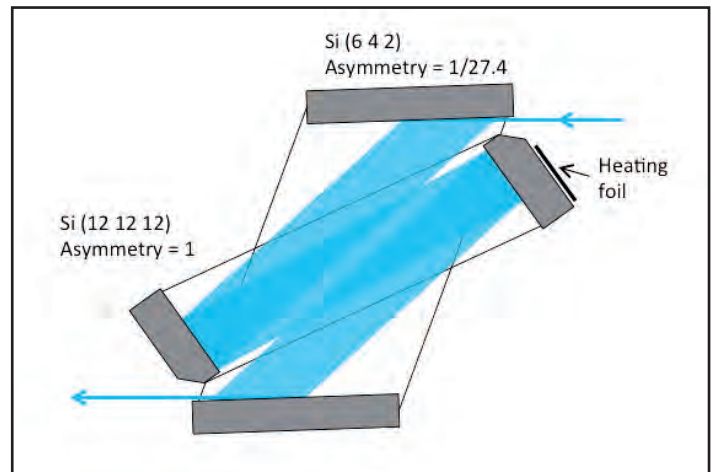


Figure 1

Sketch of the monochromator.

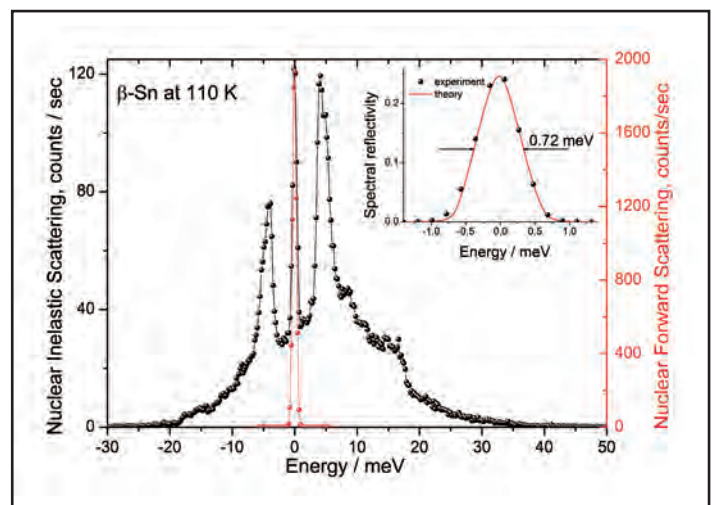


Figure 2

Nuclear inelastic scattering measured with a β -Sn foil enriched by the ^{119}Sn isotope. The red colour shows the instrumental function measured by nuclear forward scattering, which is shown in details in the inset together with the theoretical calculation.

Authors

I. Sergeev¹, H.-C. Wille¹ and K. Schlage¹

1. Deutsches Elektronen-Synchrotron DESY, Notkestrasse 85, D-22607 Hamburg, Germany

References

1. A. I. Chumakov et al., *Phys. Rev B* 58, 254 (1998).
2. M. Wuttig and N. Yamada, *Nature Materials* 6, 824 (2007).
3. Q. Zhang et al., *PNAS* 110, 13261 (2013).
4. J. P. Sutter et al., *J. Synchrotron Rad.* 13, 278 (2006).

Contact: Ilya Sergeev, ilya.sergeev@desy.de

Flux for fluorescence.

The multilayer monochromator at beamline P06



Figure 1

Multilayer Monochromator installed inside the P06 optics hutch.

The Beamline P06 features the Microprobe (XRF, XRD and XAS mapping) and Nanoprobe (Scanning coherent diffraction imaging, Nano-XRF, ptychography) endstations. For the X-Ray fluorescence technique high photon flux is crucial, especially for fast/dynamic XRF trace element mapping. This option is implemented for the Microprobe endstation using a Multilayer Monochromator (ML-Mono) (Fig. 1).

The desired energy range of the ML-Mono is 5 – 88 keV. This range is covered by two multilayer coatings, NiC and Pd/B₄C; additionally an Iridium stripe can be used. The large energy range in combination with 21 mm beam offset (due to radiation protection) demands for a large linear axis of the second optic (3.7 m maximum distance between the multilayer pair). As the ML-Mono is used in white beam the optical components have to be cryocooled.

The monochromator system has been mainly designed at DESY Zeuthen in close collaboration with the colleagues in Hamburg. The vessel and the mechanical stages were purchased from external vendors, smaller components have been manufactured at DESY workshops. The monochromator was assembled at DESY Zeuthen and then moved to the DESY Hamburg site for final testing and installation at the beamline.

The vessel is 4.8 m long and 1.7 m high. Four ion getter pumps (500 l/s each) are mounted on top to sustain a pressure of 3×10^{-7} mbar during operation. The first multilayer substrate has the following degrees of freedom: Lateral, Height, Pitch and Roll.

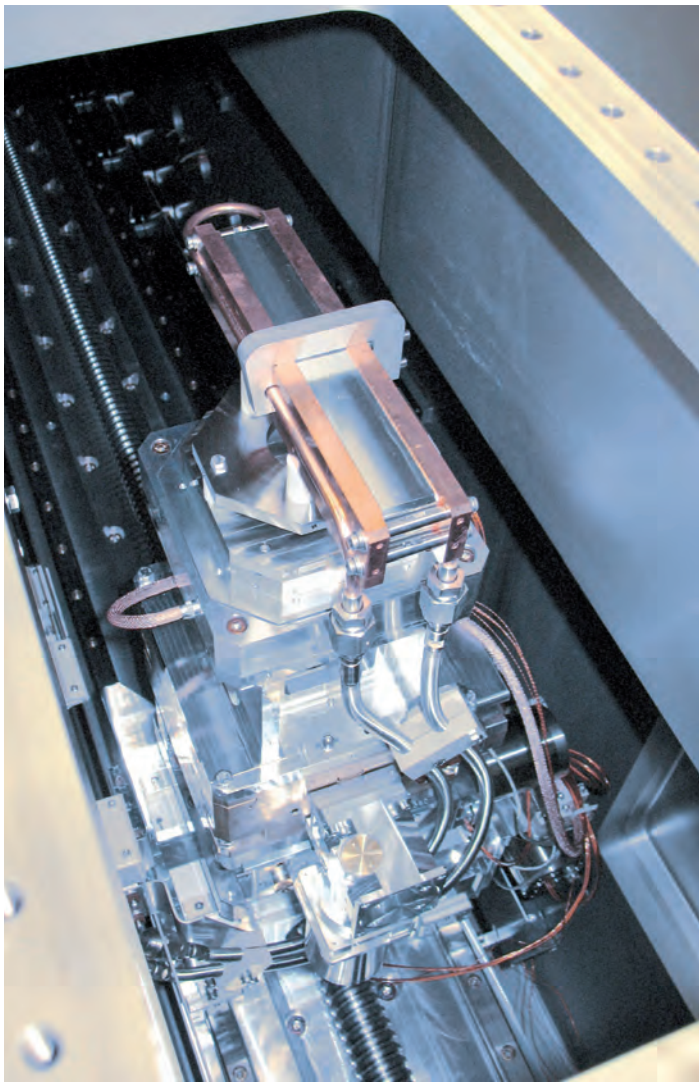


Figure 2
2nd multilayer optic with linear travel range of approx. 3.5 m (aluminium dummy instead of ML mirror is shown).

This is realized by mechanical stages with stepper motors. Furthermore, a 3 axis piezo driven stage allows for pitch, roll and height fine adjustment. For the second multilayer substrate the roll stage is omitted as one roll stage on the first substrate is sufficient for beam position adjustment. The distance between the two substrates can be changed from 225 mm up to 3.7 m by moving the second substrate with a linear stage. The pitch angle of the optics can be varied from 0.16 to 2.7 degree. All axes are controlled by a Beckhoff PLC which is connected to the Tango interface of the beamline control system.

A cryo-cooler is used for indirect cooling of the two multilayer substrates. The substrates are clamped between two lateral brackets which are traversed by liquid nitrogen. The flowrate at the second substrate can be reduced from 2.5 l/min down to 0.5 l/min to adapt to the different heat load at first and second multilayer.

Large effort has been spent on the quality of the substrates (Si (100)) to provide high quality for the multilayers. For the optical clear aperture of 195 x 20 mm the remaining radius of curvature is larger than 125 km. Slope errors were measured as 0.15 μ rad RMS tangential and 0.57 μ rad RMS sagittal. Furthermore, a surface roughness of 0.11 nm RMS has been achieved. The deposited Pd/B₄C multilayer (AXO, Dresden) shows a period thickness of 2.52 nm and the Ni/C multilayer a value of 3.22 nm. The Pd/B₄C system has a peak reflectivity of 43 % (Cu K α) for the single multilayer and a resolution of 1.55 % ($\Delta\theta/\tan(\theta)$). The Ni/C multilayer reaches 67.5 % reflectivity and 1.98 % ($\Delta\theta/\tan(\theta)$) resolution.

Using the ML-Mono the flux is 30 times larger compared to the high heat load monochromator (Si (111) and Si (311)) which is also installed at this beamline. This increase in flux is important for the fast/dynamic XRF trace element mapping station.

Contact: Gerald Falkenberg, gerald.falkenberg@desy.de
Jan Horbach, jan.horbach@desy.de

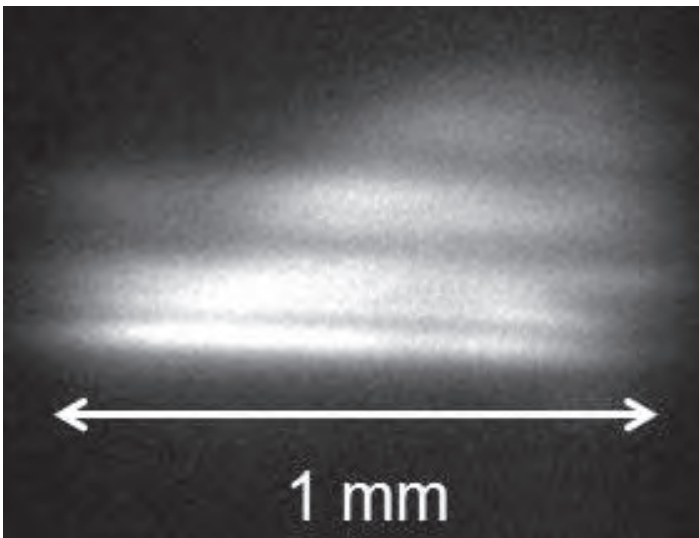


Figure 3
Pd/B₄C beam measured with an X-ray eye at 57 m behind the ML-Mono (11.8 keV, 3rd harmonic).

Authors

Jan Horbach¹, Horst Schulte-Schrepping¹, Gerald Falkenberg¹, Hartmut Lüdecke², Alexander Donat²

1. Deutsches Elektronen-Synchrotron DESY, Notkestraße 85, D-22607 Hamburg, Germany
2. Deutsches Elektronen-Synchrotron DESY, Platanenallee 6, D-15738 Zeuthen, Germany

Smooth and stable.

Wave front preserving channel-cut optics for the coherence beamline P10

Monochromators are key components of many hard X-ray undulator beamlines. The high heat load double crystal monochromators of PETRA III fulfil three important tasks: i) to provide high monochromaticity (e.g. $\Delta E/E \approx 10^{-4}$ for Si (111)), ii) to separate the monochromatic beam from white beam and *Bremsstrahlung* radiation by at least 20 mm in vertical direction and iii) to protect downstream components from the heat load of the undulator beam (up to 600 W/mm²). The high heat load requires active cryogenic cooling of both monochromator crystals. Inevitably cryocooling induces *independent* vibrations of both crystals, thus leading to motions of the X-ray beam in the vertical direction and increasing the vertical effective source size.

One solution to reduce such directional vibrations of the monochromatized X-ray beam is to use a channel-cut crystal at the high heat load monochromator. Channel-cut crystal optics is made from a single slab of silicon by cutting a channel which separates both diffracting crystal surfaces. This rigid design prevents independent angular motions of the crystal diffraction planes and produces a directional stable beam. Basically, channel-cut crystals transfer spatial vibrations into small variations in energy space.

However, the homogeneity or smoothness of the wavefront is another characteristic feature of the X-ray beam. This is especially important for coherent X-ray scattering applications like X-ray photon correlation spectroscopy (XPCS) and coherent diffraction imaging (CDI). The quality of the wavefront is directly coupled to the surface roughness of the crystal optics. Usually channel-cut crystal surfaces cannot be polished to required specifications, since the surfaces are not easily accessible. Here, we characterized the performance of a polished channel-cut crystal installed at the P10 monochromator.

Fig. 1 shows a photo of the first cryogenically cooled copper crystal holder. The holder offers two positions to install crystals. The lower position is occupied by a highly polished Si (111) crystal and the channel-cut is installed at the upper position.

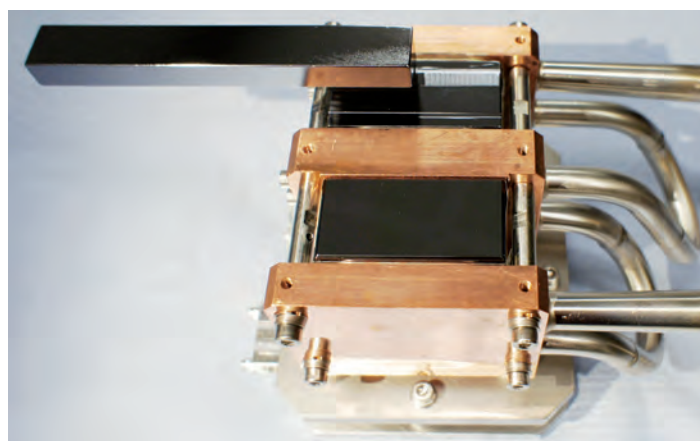


Figure 1
Channel-cut crystal (top slot) and first crystal of standard crystal pair (bottom slot) mounted on the copper block heat exchanger of the P10 monochromator.

The diffraction plane is vertical, and switching from the crystal pair to the channel-cut is performed by horizontal translation of the UHV chamber. This configuration allows to either use the standard crystal pair or channel-cut crystal. An oriented oversized crystal blank was prepared at the Optics Laboratory at DESY, cutting and fine polishing of crystal surfaces was done by Holm Silizium Bearbeitung. The quality of surface polishing of the channel-cut crystal was first evaluated by surface X-ray diffraction mapping measurement at P10. The channel-cut was positioned in the first experimental hutch of P10 at a distance of 71.5 m from the undulator source. A high resolution X-ray camera (PCO Edge, with $\sim 1 \mu\text{m}$ resolution) positioned 22 m behind the channel-cut was used to collect beam profile images at different positions across the crystal surface. These scans covered the full accessible channel-cut crystal surface of 9.5 mm horizontally and 47 mm vertically using monochromatic X-ray beam with a photon energy of 7.9 keV. The resulting surface map is shown in Fig. 2 and confirms the high quality of both crystal surfaces of the channel-cut monochromator. Large areas

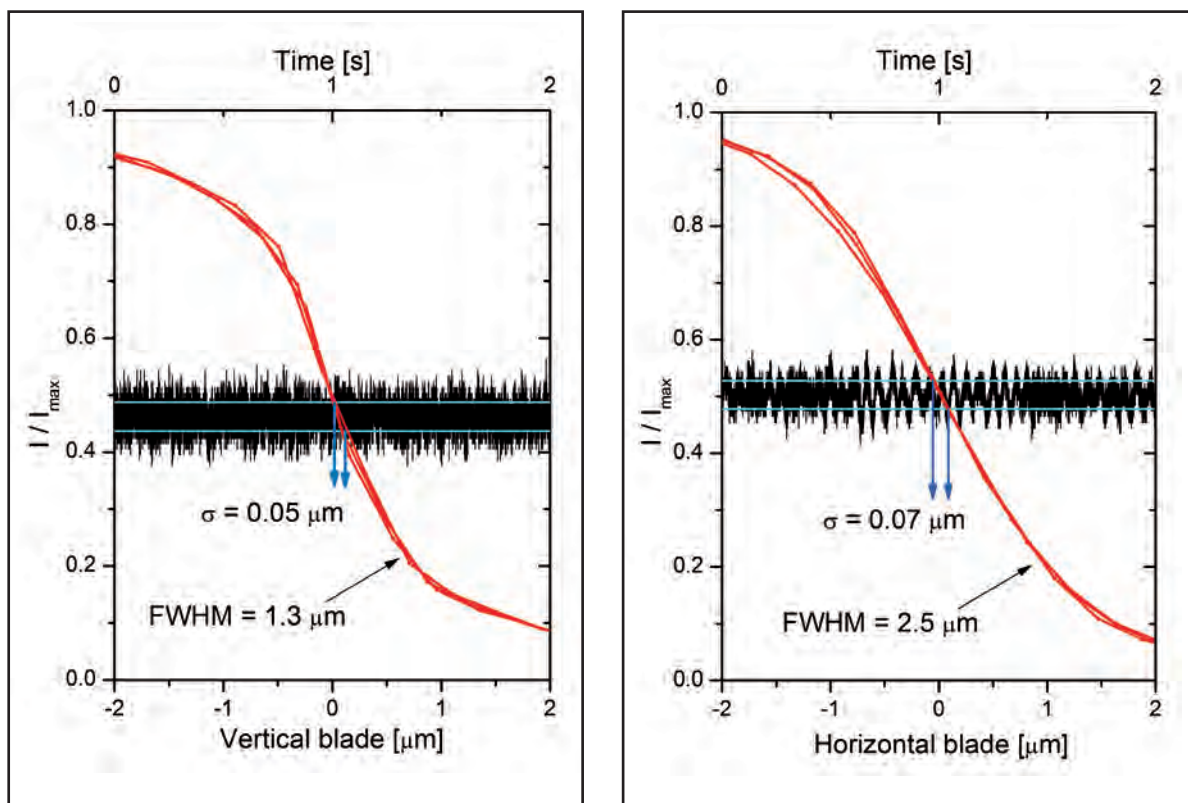


Figure 3

Time dependence of the measured oscilloscope signal (I/I_{\max}) overlaid with knife-edge scans in vertical (left) and horizontal (right) directions.

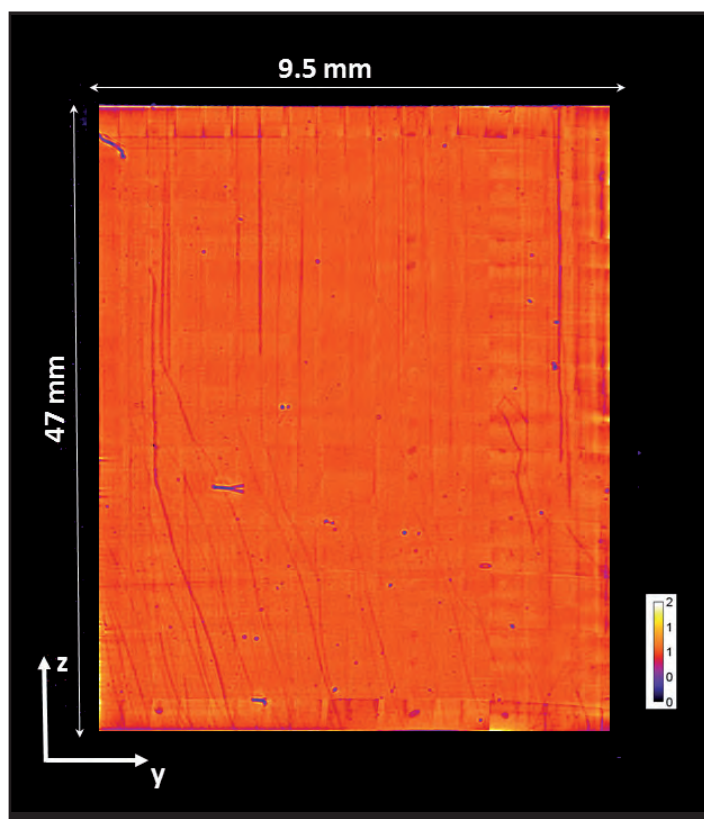


Figure 2

Surface X-ray diffraction map of the P10 channel-cut crystal measured at a photon energy of 7.9 keV.

of the surface are artefact free, only a few mainly longitudinal lines are visible, thus guaranteeing preservation of the beam wavefront. Afterwards the channel-cut crystal was installed in the UHV chamber of the P10 monochromator located in the optics hut at 38.5 m distance from the source.

Measurements of the beam stability after the channel-cut were performed using focusing optics based on compound refractive lenses (CRLs). Using the CRL transfocator located at 86 m from the source, the beam was focused to a spot of 1.3 μm in vertical and 2.5 μm in horizontal direction. Slit blades were inserted to cut 50 % of incident intensity for stability measurements. The transmitted intensity was monitored using a storage oscilloscope. Fig. 3 shows the time dependence of the measured signal and the exceptional stability of the channel-cut beam. An angular stability of less than 50 nrad (sigma-value) is observed in the vertical direction.

Contact: Michael Sprung, michael.sprung@desy.de
Horst Schulte-Schrepping, horst.schulte-schrepping@desy.de

Authors

M. Sprung¹, J. Heuer¹, A. Zozulya¹, I. Sergeev¹, A. Shabalin¹, I. Besedin¹, I. A. Vartanyants¹ and H. Schulte-Schrepping¹

¹. Deutsches Elektronen-Synchrotron DESY, Notkestrasse 85, D-22607 Hamburg, Germany

Feel a pulse.

Pulse energy monitor for the European XFEL

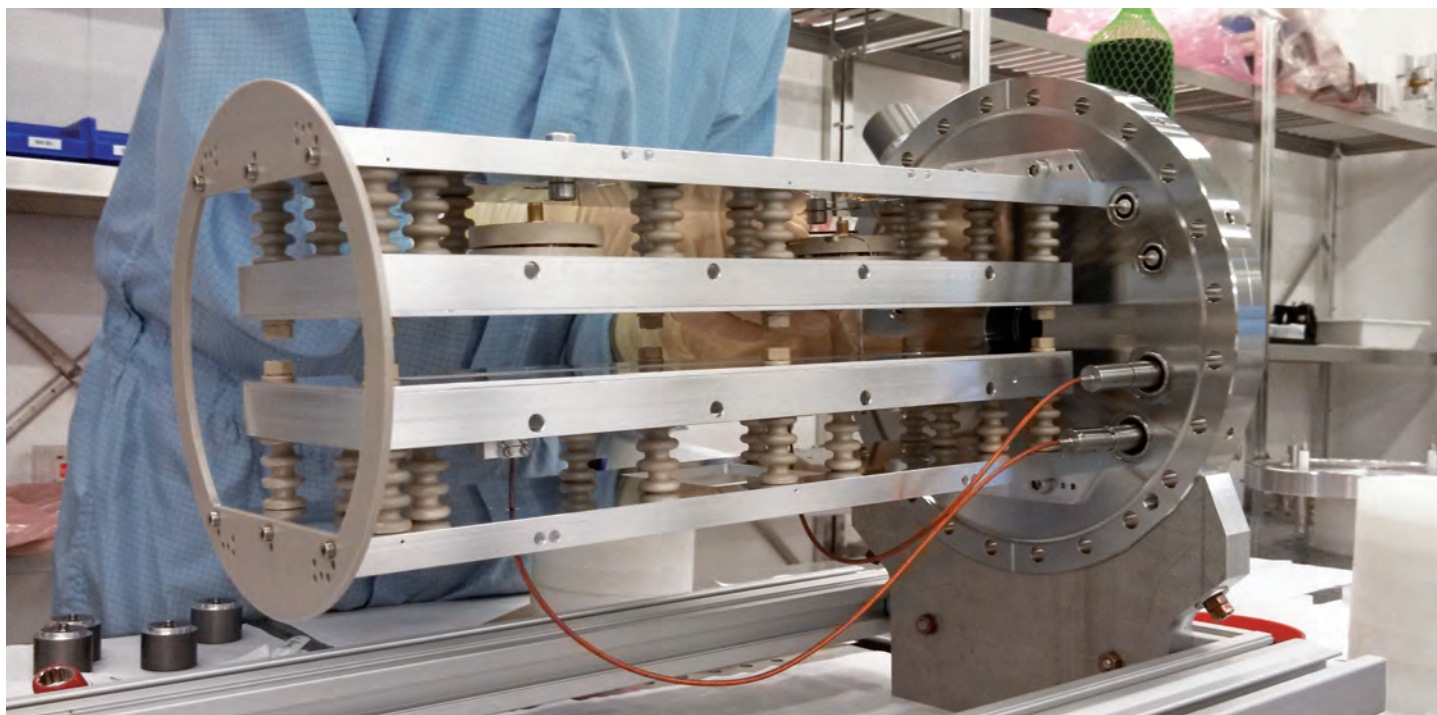


Figure 1
X-ray gas-monitor detector for the European XFEL.

Most Free-Electron Laser (FEL) user experiments need online information about important beam parameters, such as the photon flux, respectively the energy content in the radiation pulse. This requires the use of diagnostic tools which operate in parallel and in a non-destructive way. Furthermore, due to the SASE-specific shot-to-shot fluctuations, it is mandatory to use pulse-resolved diagnostics. Today at FLASH, gas-monitor-detectors (GMDs) are operated as a permanent part of online photon diagnostics measuring the photon flux of the highly intense and strongly pulsed VUV radiation in absolute terms [1]. The detector is based on the atomic photoionization of a rare gas or Nitrogen at low particle density in the range of 10^{11} cm^{-3} which is about five orders lower than for classical ionization chambers. The advantages are obvious: the detector is virtually indestructible and almost transparent.

Furthermore, different GMD versions have been used for intensity measurements at different laser facilities worldwide over the past few years [e.g. 1-5]. The detectors were calibrated with synchrotron radiation in the PTB laboratories at the storage ring facilities BESSY II and Metrology Light Source MLS in Berlin, respectively.

For the European hard X-ray FEL (XFEL) an upgraded version of the GMD with an extended energy as well as dynamic range has been developed over the last 4 years. In contrast to the FLASH device, this so-called XGMD as shown in Fig. 1 and Fig. 3 combines the FLASH detection scheme with an open electron multiplier which is located behind a small slit in an ion Faraday cup. A small fraction of the created ions hits on the multiplier with an amplification factor of up to 10^6 which makes the device sufficiently sensitive for the hard X-ray regime, where the atomic photoionization cross sections are by orders of magnitude lower than in the VUV and soft X-ray spectral range.

Photon energy (keV)	XGMD (μJ)	CR (μJ)	XGMD to CR ratio
4.4	$32.9 \pm 6.2 \%$	$32.3 \pm 1.1 \%$	$1.02 \pm 6.3 \%$
5.8	$106.6 \pm 5.7 \%$	$104.2 \pm 1.2 \%$	$1.02 \pm 5.8 \%$
9.6	$93.9 \pm 6.5 \%$	$95.3 \pm 2.4 \%$	$0.99 \pm 6.9 \%$
13.6	$40.8 \pm 7.1 \%$	$42.2 \pm 2.6 \%$	$0.97 \pm 7.6 \%$
16.8	$1.1 \pm 40 \%$	$0.96 \pm 3.1 \%$	$1.15 \pm 40 \%$

Table 1
Average pulse energy of SACLA for different photon energies as measured with the XGMD and the CR and ratios between these two detectors measurements.

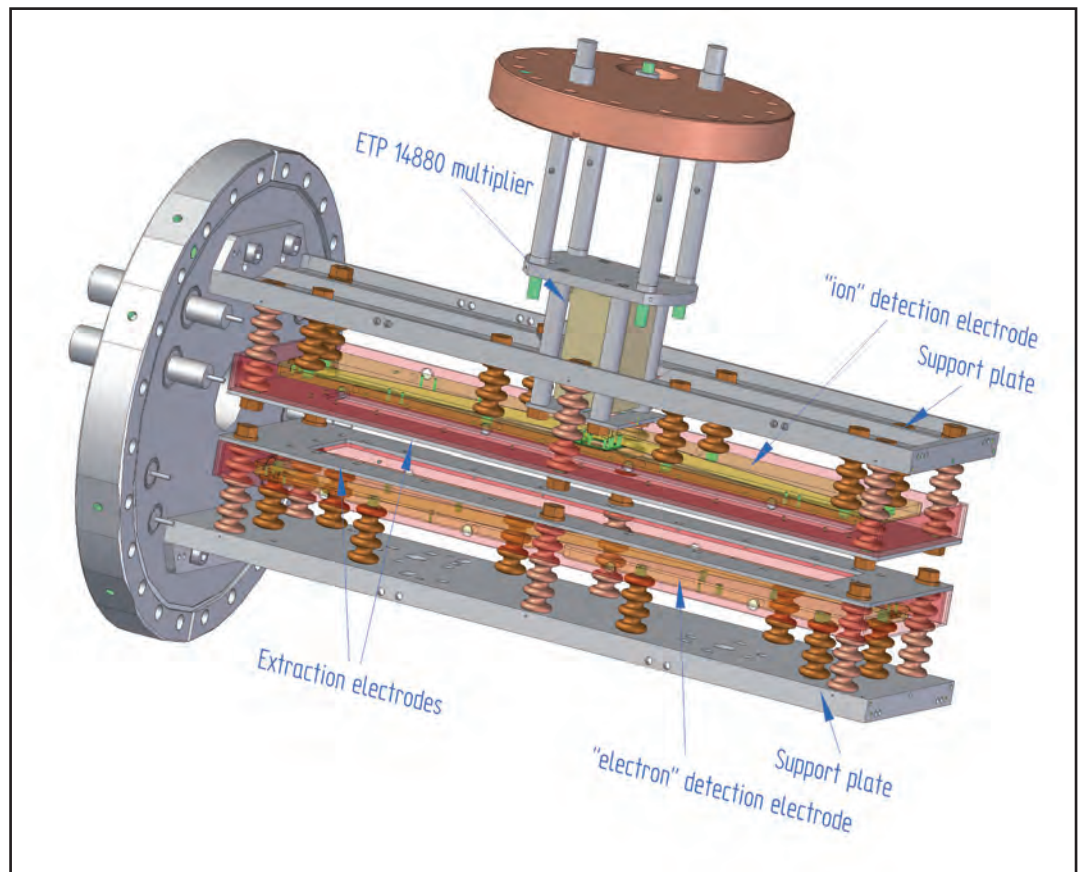


Figure 3

Schematic view of the X-ray gas-monitor detector for the European XFEL with functional details.

In collaboration with colleagues from the Japanese Research Center RIKEN, the Japanese metrology institute AIST/NMIJ and the Physikalisch-Technische Bundesanstalt (PTB) first successful tests of this device have been performed recently at the Japanese hard X-ray laser SACLA [5]. Here, we have measured the pulse energies in the energy range from 4.4 keV to 16.8 keV by means of two independent methods, using a cryogenic radiometer (CR) and the XGMD. A nearly perfect agreement was achieved as shown in Table 1 and Fig. 2.

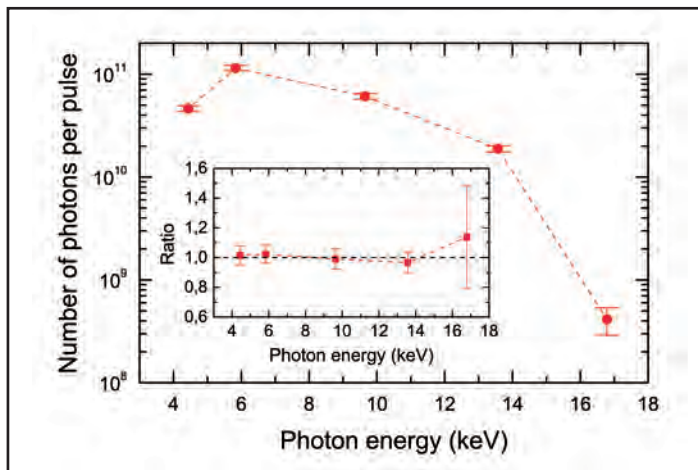


Figure 2

Average number of photons per pulse as measured with the XGMD and ratios between measurements by the XGMD and the CR.

Contact: Kai Tiedtke, kai.tiedtke@desy.de
 Andrey Sorokin, andrey.sorokin@desy.de

Authors

K. Tiedtke¹ and A. Sorokin¹

¹. Deutsches Elektronen-Synchrotron DESY, Notkestraße 85, D-22607 Hamburg, Germany

References

1. K. Tiedtke et al., "Gas-detector for X-ray lasers", *J. Appl. Phys.* **103**, 094511 (2008).
2. N. Saito et al., "Radiometric comparison for measuring the absolute radiant power of a free-electron laser in the extreme ultraviolet", *Metrologia* **47**, 21 (2010).
3. M. Kato et al., "Measurement of the single-shot pulse energy of a free electron laser using a cryogenic radiometer", *Metrologia* **47**, 518 (2010).
4. T. Leitner et al., "Shot-to-shot and average absolute photon flux measurements of a femtosecond laser high-order harmonic photon source", *New J. Phys.* **13**, 093003 (2011).
5. M. Kato et al., "Pulse energy measurements at the hard X-ray laser in Japan", *Appl. Phys. Lett.* **101**, 023503 (2012).

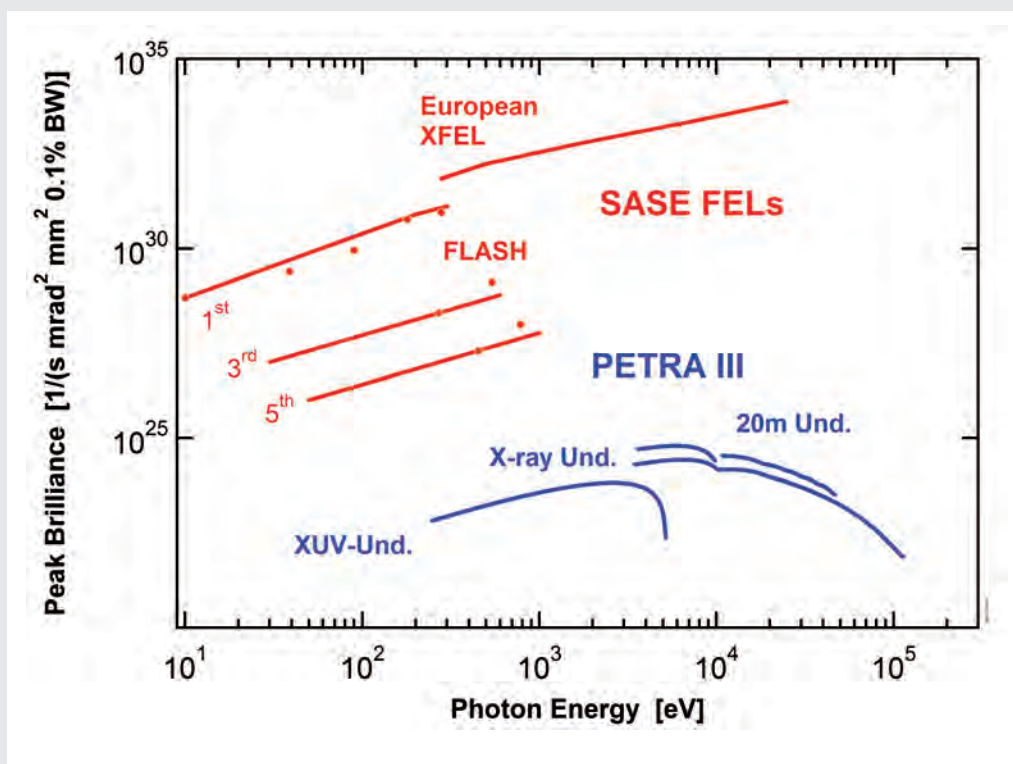
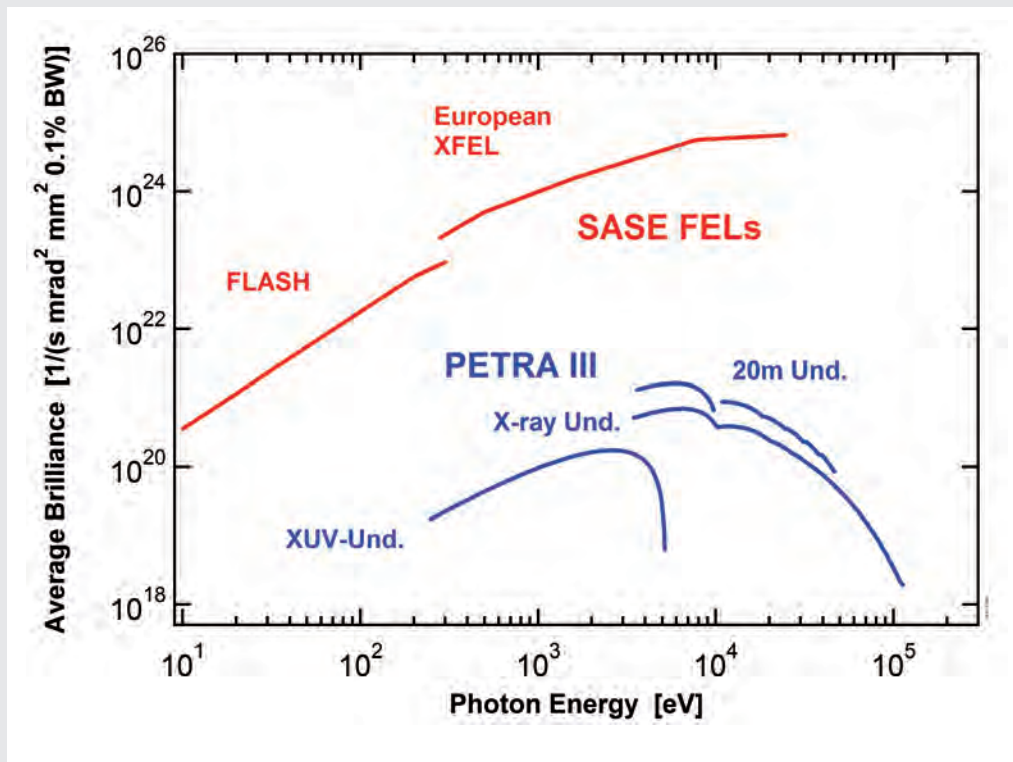




Facts and Numbers.

> Light source characteristics	114
> Beamtime statistics	115
> FLASH beamlines and parameters	116
> PETRA III beamlines and parameters	119
> Committees	122

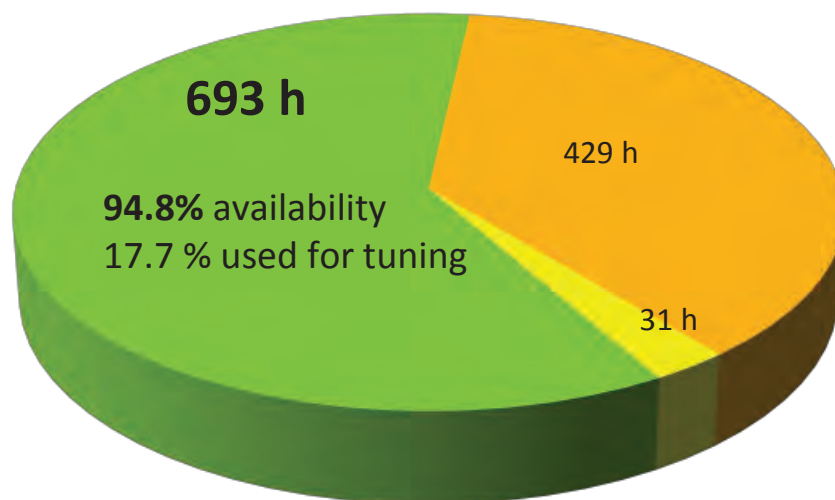
Light source characteristics.



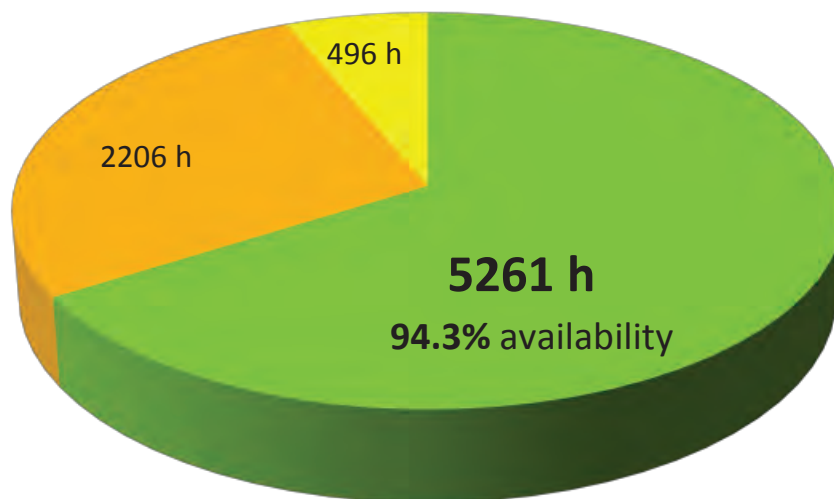
Average and peak brilliance values for FLASH, PETRA III and the European XFEL. Peak brilliance values are given for the optimum bunch charge at the respective photon energies. Dots represent experimentally measured values at FLASH.

Beamtime statistics 2013.

FLASH



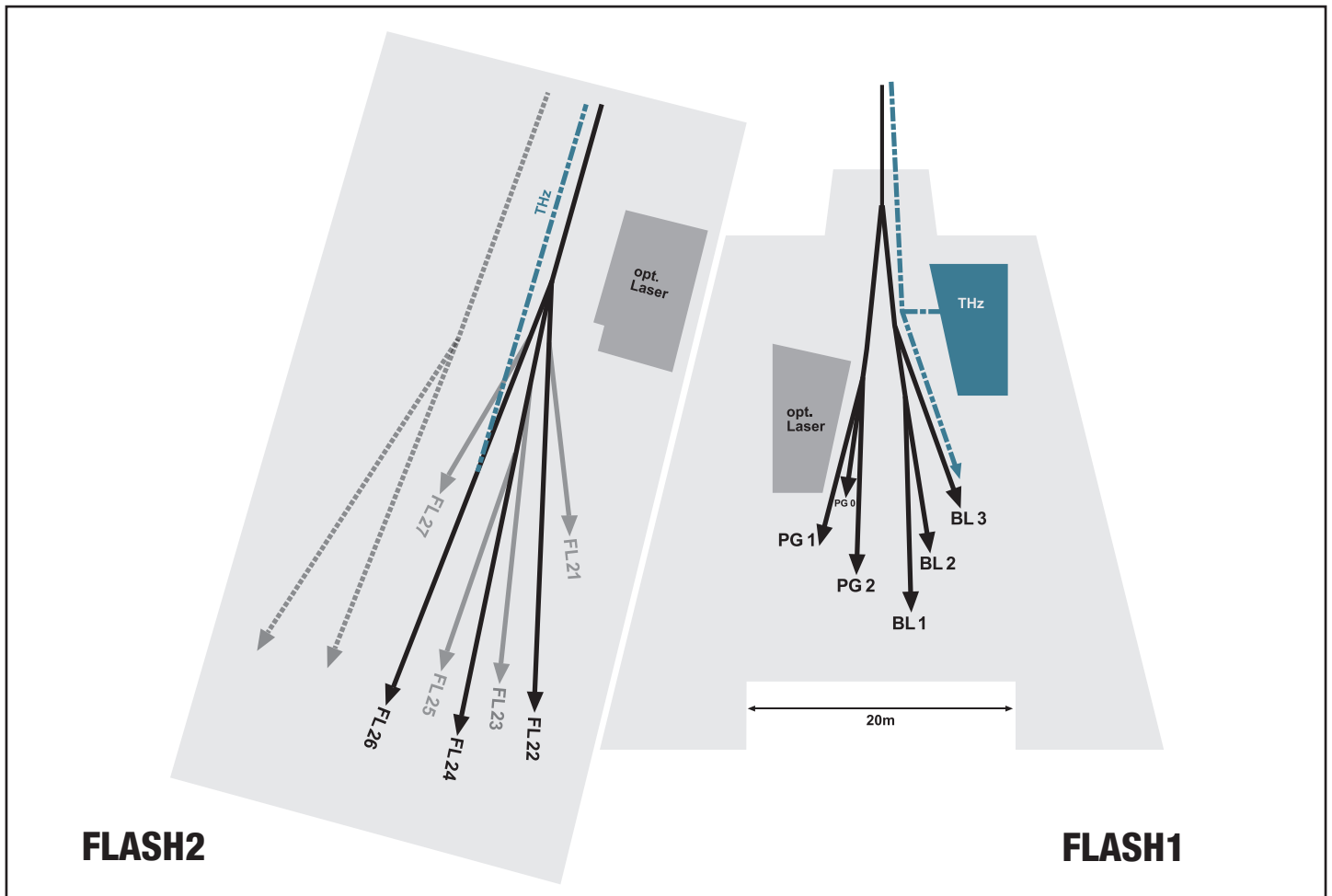
PETRA III



■ User beamtime ■ Machine studies/test runs ■ Maintenance

Operation periods 2013

FLASH	2013: 02.01.-17.02.
PETRA III	1/2013: 28.01.-01.07.
	2/2013: 22.07.-19.12.



Machine parameters FLASH

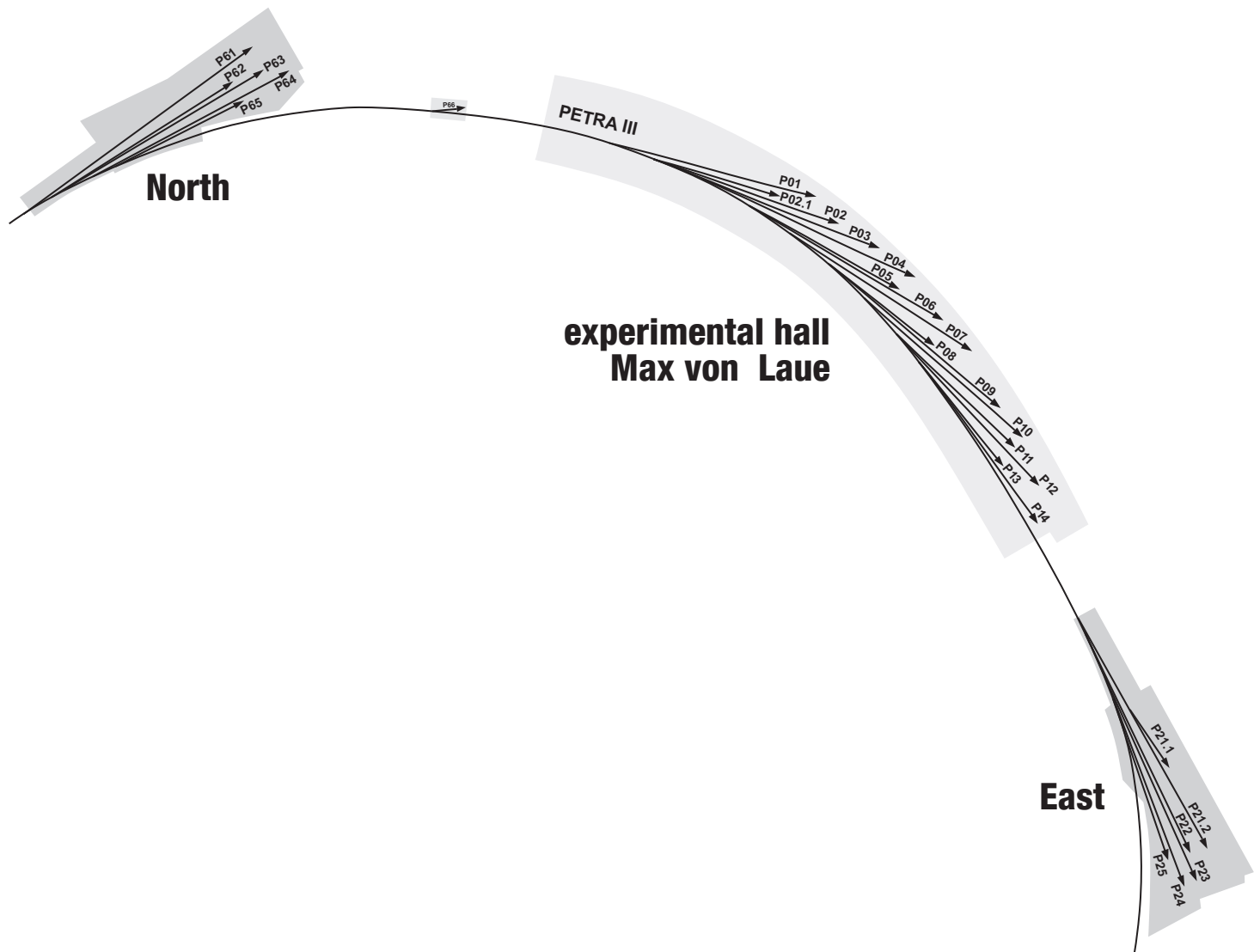
Electron energy (max.)	1.25 GeV
Length of the facility	315 m
Normalized emittance	1.5 mm mrad (rms)
Emittance	0.6 nm rad (rms)
Bunch charge	0.1 – 1 nC
Peak current	1 – 2 kA
Bunches per second (typ. and max.)	300 and 6000

Lasing parameters

Photon energy (max.)	301 eV (fundamental)
Wavelength (min.)	4.12 nm (fundamental)
Pulse duration (FWHM)	50 – 200 fs
Peak power	1 – 3 GW
Bunch energy (average)	up to 500 μ J
Photons per bunch	$10^{11} - 10^{13}$
Average brilliance	$10^{17} - 10^{21}$ photons/sec/mm ² /mrad ² /0.1%
Peak brilliance	$10^{29} - 10^{31}$ photons/sec/mm ² /mrad ² /0.1%

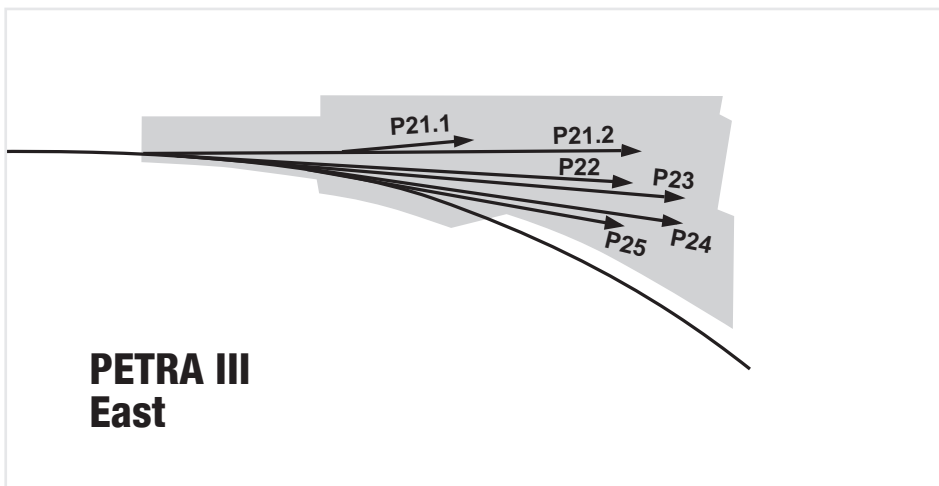
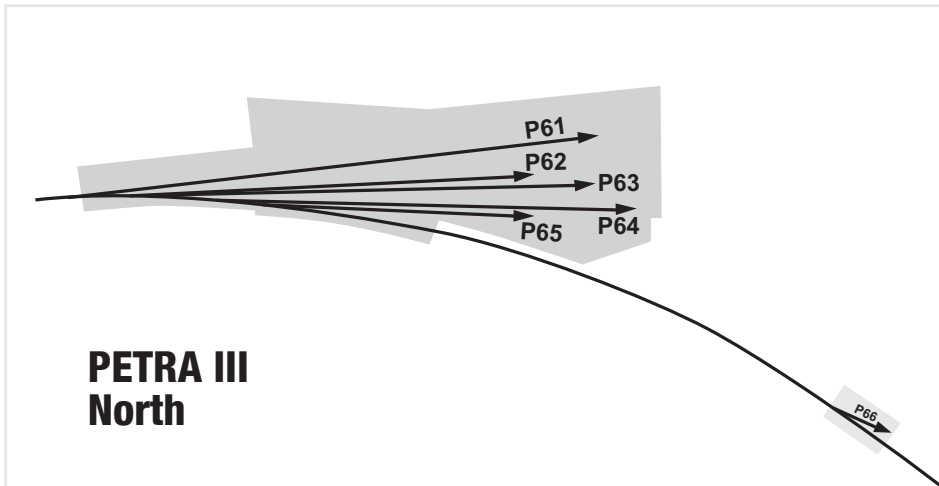
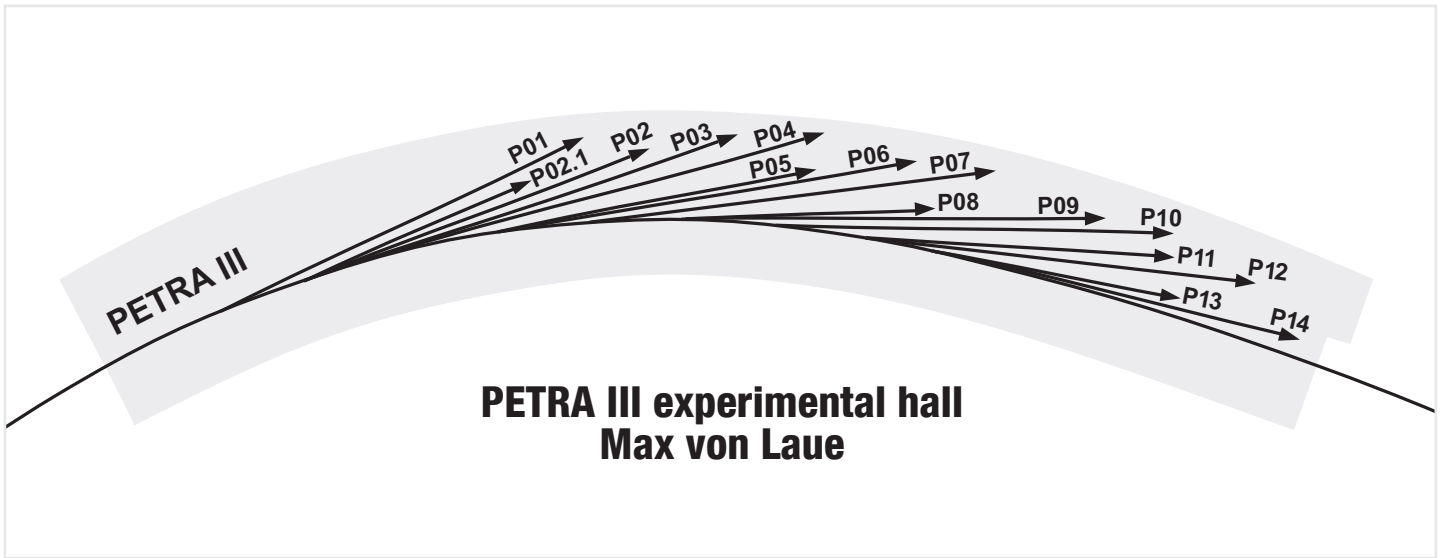
FLASH beamlines

FLASH1	
BL 1	non-monochromatic FEL photons Kirkpatrick-Baez (KB) focusing optics (available fall 2014) FEL focal spot of $\sim 3 \mu\text{m} \times 4 \mu\text{m}$ FWHM <i>TU Berlin</i> split-and-delay unit for XUV pump - XUV probe experiments (planned, up to ns delay) <i>TU Berlin</i> optional pump-probe experiments using FLASH1 optical laser system permanent endstation (available fall 2014): multipurpose CAMP chamber with two pnCCD detectors, electron and ion spectrometers and collinear incoupling optics for optical laser optional supersonic gas jet (as sample) <i>CFEL- Max Planck ASG</i>
BL 2	non-monochromatic FEL photons focused to $\sim 20 \mu\text{m}$ /unfocussed beam size $\sim 5\text{-}10 \text{ mm}$ (FWHM, depending on wavelength) XUV beam splitter with variable delay (-3 ps to 15 ps) for photon diagnostics and XUV pump - XUV probe experiments <i>Univ. Münster</i> optional pump-probe experiments using FLASH1 optical laser system about 3m x 4m footprint for user-provided endstation
BL 3	non-monochromatic FEL photons, spectral range: $>4.5 \text{ nm}$ (carbon coated optics) focused to $\sim 20 \mu\text{m}$ /unfocussed beam size $\sim 5\text{-}10 \text{ mm}$ (FWHM, depending on wavelength) optional pump-probe experiments using FLASH1 optical laser system optional pump-probe experiments using THz radiation (unique to BL3): - tunable: $10\text{-}230 \mu\text{m}$; up to $100 \mu\text{J/pulse}$; $\sim 10\%$ bandwidth, - broadband at $200 \mu\text{m}$, up to $10 \mu\text{J/pulse}$; $\sim 100\%$ bandwidth - synchronized and phase stable to X-ray pulses (down to 5 fs) - delivered to the experiment via vacuum beamline as: (i) ultra-high vacuum ($\sim 10^{-8} \text{ mbar}$), shorter delay between THz and X-ray ($\sim 4 \text{ m}$ path difference), can accommodate up to 0.3 m wide setup; (ii) high vacuum (pressure $\sim 10^{-6} \text{ mbar}$), longer delay between THz and X-ray ($\sim 7 \text{ m}$ path difference); can accommodate up to 2 m wide setup about 3m x 4m footprint for user-provided endstation
PG1	high resolution plane grating XUV monochromator (SX 700 type, $<10^{-4}$ bandwidth, carbon coated optics): - variable combination of photon flux and resolution (from high flux to high resolution) - controlled temporal-spectral properties at moderate resolution for pump-probe experiments - high photon flux with harmonic filtering Kirkpatrick-Baez (KB) refocusing optics, FEL focal spot of $5 \mu\text{m}$ (vertically) <i>Univ. Hamburg</i> permanent endstation: two-stage VUV-Raman spectrometer for high-resolution measurements close to Rayleigh line <i>Univ. Hamburg</i>
PG2	uses the same monochromator as PG1 $50 \mu\text{m}$ focus XUV beamsplitter with variable time delay ($\pm 6 \text{ ps}$) for time resolved studies <i>Univ. Hamburg</i> optional pump-probe experiments using FLASH1 optical laser system about 3m x 4m platform for user-provided endstation
FLASH1 optical/NIR laser system for pump-probe experiments	
<ul style="list-style-type: none"> - 10 Hz bursts with 1 MHz (maximum 400 pulses/burst), 70 fs and $10 \mu\text{J}$ - 10 Hz, up to 20 mJ/pulse - 10 Hz, tunable $\sim 400\text{-}2000 \mu\text{m}$, up to $100 \mu\text{J}$ - delivered to the experiment via high-vacuum beamline - synchronized to FEL pulses down to $\sim 100 \text{ fs}$ 	
FLASH2 - extension under commissioning -	
FL22	wavelength range: $6 - 40 \text{ nm}$ with 6σ , up to 80 nm with 3σ acceptance
FL24	wavelength range: $4 - 16 \text{ nm}$ for the fundamental with 6σ acceptance, for harmonics down to 0.8 nm grazing incidence (1.8°) split-and-delay unit with $\pm 12 \text{ ps}$ delay <i>Univ. Münster</i>
FL26	wavelength range: $6 - 40 \text{ nm}$ with 6σ , up to 80 nm with 3σ acceptance permanent endstation: - split multilayer mirror & reaction microscope (REMI) for time-resolved spectroscopy - grazing incidence delay-line and refocusing optics for a second experiment in-line behind the REMI (under development) <i>MPI-K Heidelberg</i>
All FLASH beamlines provide online photon diagnostics for intensity, wavelength, and beam position; fast shutter, aperture and filter sets.	
We would like to acknowledge all contributions to instrument development and operation provided within the framework of BMBF Verbundforschung and the Ioffe-Röntgen-Institute (IRI).	



Machine parameters PETRA III

Electron energy	6.08 GeV
Circumference of the storage ring	2304 m
Number of buckets	3840
Number of bunches	960, 60, and 40
Bunch separation	8 ns, 128 ns, and 192 ns
Electron beam current	100 mA (top-up)
Horizontal positron beam emittance	1.0 nmrads (rms)
Coupling factor	0.7%
Vertical electron beam emittance	0.007 nmrads (rms)
Electron beam energy spread	0.1% (rms)
Horizontal x vertical beam size at 5 m undulator (high β section)	141.5 x 4.9 μm
Horizontal x vertical beam size at 5 m undulator (low β section)	34.6 x 6.3 μm



PETRA III beamlines

PETRA III		
Beamline and instruments		Operated by
P01	Dynamics 10(20)m U32 4.5 – 40 keV	DESY
	Nuclear resonant scattering	DESY
	Non-resonant IXS	DESY
	X-ray Raman scattering	DESY
P02.1	Powder diffraction 2m U23 60 keV	DESY
	Time resolved powder diffraction	DESY
	High resolution powder diffraction	DESY (in commissioning)
P02.2	Extreme conditions 2m U23 10 - 62 keV	DESY
	Laser heated diamond anvil cells	DESY
	General purpose high pressure	DESY
P03	Micro- and Nano SAXS / WAXS 2m U29 8 - 23 keV	DESY
	Micro-small and wide angle scattering	DESY
	Nano-beam scattering and diffraction	DESY
P04	Variable polarization soft X-rays 5m UE65 200 - 3000 eV	DESY
	UHV diffractometer	DESY
	Photon-Ion spectrometer (PIPE)	DESY
	Ultra-high resolution photoelectron spectroscopy (ASPHERE)	DESY
	Soft X-ray absorption spectrometer	DESY
	Nano focus apparatus for spatial and time resolving spectroscopy	DESY
P05	Micro- and nano-imaging 2m U29 8 - 50 keV	HZG
	Micro-tomography	HZG
	Nano-tomography	HZG (in commissioning)
P06	Hard X-ray microprobe 2m U32 8 - 60 keV	DESY
	Micro-probe	DESY
	Nano-probe	DESY
P07	High energy X-ray materials science 2m U29 (planned: 4m U19) 50 - 200 keV	HZG / DESY
	Multi-purpose triple-axis diffractometer	DESY
	Heavy load diffractometer	HZG
	Grain mapper	HZG (in commissioning)
	High energy tomography	HZG
P08	High resolution diffraction 2m U29 5.4 - 29.4 keV	DESY
	High resolution diffractometer	DESY
	Liquid surface diffraction	DESY
P09	Resonant scattering and diffraction/HAXPES 2m U32 2.7 - 50 keV	DESY
	High precision psi-diffractometer	DESY
	Heavy load diffractometer	DESY
	Hard X-ray photoelectron spectroscopy	DESY
P10	Coherence 5m U29 4 - 20 keV	DESY
	X-ray photon correlation spectroscopy (4 - 20 keV)	DESY
	Vertical rheometer (8 keV)	DESY
	Coherent imaging (8 - 15 keV)	DESY
P11	Macromolecular diffraction and imaging 2m U32 6 - 35 keV	DESY / MPG / HZI
	Macromolecular crystallography	DESY
	Imaging of biological structures (2.4 - 10 keV)	DESY (in commissioning)

Beamline and instruments		Operated by
P12	Bio SAXS 2m U29 4 - 20 keV	EMBL
	Solution small-angle scattering	EMBL
P13	Macromolecular crystallography I 2m U29 4 - 16 keV	EMBL
	Macromolecular crystallography	EMBL
P14	Macromolecular crystallography II 2m U29 10 keV	EMBL
	Macromolecular crystallography	EMBL
PETRA III Extensions East and North		
Beamline and instruments		Operated by
P21.1	Swedish high-energy materials science beamline (side branch) 2m U29 50, 80, 100 keV	tbd (Sweden) / DESY
	Broad band diffraction	tbd / DESY (planned 2016/17)
P21.2	Swedish high-energy materials science beamline 4m IVU21 40 - 150 keV	tbd (Sweden) / DESY
	Diffraction and imaging	tbd / DESY (planned 2016/17)
P22	Nano X-ray spectroscopy (India-motivated beamline) 2m U32 2.4 - 30 keV	DESY
	Hard X-ray photoelectron spectroscopy (relocated from P09)	DESY (planned 2016)
	Tbd	
P23	Russian-German nano-diffraction beamline 2m U32 5 - 35 keV	DESY
	Nano-XRD, in situ and complex environments	DESY (planned 2016)
	Tbd	
P24	Chemical crystallography Undulator (tbd) 8 - 45 keV	DESY
	Single crystal diffraction in complex sample environments	DESY (planned 2016)
	Small molecule crystallography	DESY (planned 2016)
P25	Education & testing Short undulator (tbd)	DESY (not yet funded)
P61	High-energy materials science 40 m damping wiggler 50 - 200 keV / pink beam	DESY / HZG
	High-energy engineering materials science	HZG (planned)
	Extreme conditions in large volume press	DESY (planned 2016/17)
P62	Small-angle X-ray scattering Short undulator (tbd) 4 - 40 keV	DESY
	SAXS, WAXS, USAXS	DESY (planned 2019)
P63	Tbd	DESY (not yet funded)
	Tbd	
P64	Time-resolved X-ray absorption 2m U32 4 - 44 keV	DESY
	Time-resolved in situ XAFS, QEXAFS, bioXAFS	DESY (planned 2015)
P65	X-ray absorption Short U32 4 - 44 keV	DESY
	Ex situ and in situ XAFS of bulk samples	DESY (planned 2015)
P66	Superlumi Bending magnet 4 - 40 eV	DESY
	Time-resolved luminescence spectroscopy	DESY (planned 2016)
<p><i>We would like to acknowledge all contributions to instrument development and operation provided within the framework of BMBF-Verbundforschung, the Röntgen-Ångström-Cluster (RAC), the Ioffe-Röntgen-Institute (IRI), and the Ruprecht-Haensel-Laboratory (University of Kiel).</i></p>		

Committees 2013.

Photon Science Committee PSC – advises the photon science management

Markus Drescher (chair)	Universität Hamburg, D
Melissa A. Denecke (vice chair)	University of Manchester, UK
Stefan Eisebitt	Technische Universität, Berlin, D
Gwyndaf Evans	Diamond Lights Source Ltd., Oxford, UK
Maya Kiskinova	Sincrotrone Trieste, I
Franz Pfeiffer	Technische Universität München, D
Henning Friis Poulsen	DTU Fysik, Lyngby, DK
Harald Reichert	ESRF, Grenoble, F
Jean-Pierre Samama	Synchrotron Soleil, F
Bernd Schmitt	PSI, Villigen, CH
Lucia Incoccia-Hermes (PSC secretary)	DESY, Hamburg, D

Laser Advisory Committee LAC (shared between DESY and the European XFEL)

Uwe Morgner (Chair)	Universität Hannover, D
Giulio Cerullo	Politecnico di Milano, I
Patrick Georges	CNRS, F
Alfred Leitenstorfer	Universität Konstanz, D
Robert Schoenlein	LBL, USA
William E. White	SLAC, Menlo Park, CA, USA
Andreas Galler (European XFEL LAC secretary)	European XFEL GmbH, Hamburg, D
Lucia Incoccia-Hermes (DESY LAC secretary)	DESY, Hamburg, D

Project Review Panels (PRP)

PRP1: VUV- and Soft X-Ray

Michael Meyer	European XFEL GmbH, Hamburg, D
Luc Patthey	PSI Villigen, CH
Jens Viefhaus (PRP Secretary)	DESY, Hamburg, D

PRP2: X-Ray Spectroscopy

Ralph Claessen (starting 2014)	Julius-Maximilians-Universität Würzburg, D
Melissa A. Denecke	University of Manchester, UK
Joerg Evers	MPI für Kernphysik, Heidelberg, D
Raphael Hermann	FZ Jülich, D
Lutz Kipp	Christian-Albrechts-Universität, Kiel, D
Sebastian Schoeder	Synchrotron Soleil, F
Christina Strelt	Technische Universität Wien, A
Joseph Woicik	NIST, Gaithersburg, MD, USA
Wolfgang Drube (PRP secretary)	DESY, Hamburg, D

PRP3: X-Ray Diffraction/Scattering – Hard Condensed Matter

Denis Andraut	Université Clermont-Ferrand, F
Thomas Beale	Durham University, Durham, UK
Lars Ehm	Stony Brook University, Stony Brook, NY, USA
Peter Hatton	Durham University, Durham, UK
Markus Huecker	Brookhaven National Lab., Upton, NY, USA
Helmut Klein	Universität Göttingen, D
Ulrich Schwarz	MPG Dresden, D
Sergio Speziale	GFZ Potsdam, D
Urs Staub	PSI, Villigen, CH
Peter Wochner	MPI für Metallforschung, Stuttgart, D
Hermann Franz (PRP secretary)	DESY, Hamburg, D

PRP4: X-Ray Diffraction/Scattering – Engineering Materials Science

Jens Gibmeier	Karlsruher Institut für Technologie KIT, D
Jozef Keckes	Montanuniversität Leoben, A
Svea Mayer	Montanuniversität Leoben, A
Walter Reimers	Technische Universität Berlin, D
Guillermo Requena	Technische Universität Wien, A
Gerold Schneider	Technische Universität Hamburg-Harburg, D
Bernd Schönfeld	ETH Zürich, CH
Carsten Siemers	Technische Universität Braunschweig, D
Axel Steuwer	MAX IV Laboratory, Lund, SE
Martin Müller (PRP secretary)	HZG, Geesthacht, D
Ralf Röhlberger (DESY representative)	DESY, Hamburg, D

PRP5: X-Ray Diffraction/Scattering – Soft Materials, Bulk	
Francisco José Baltá-Calleja	CSIC, Madrid, ES
Wim de Jeu	RWTH Aachen, D
Uwe Klemradt	RWTH Aachen, D
Yongfeng Men	Changchun Inst. of Applied Chemistry, CN
Michael Paulus	Technische Universität Dortmund, D
Christine M. Papadakis	Technische Universität München, D
Joachim Wagner	Universität Rostock, D
Rainer Gehrke (PRP secretary)	DESY, Hamburg, D
PRP6: X-Ray Diffraction/Scattering – Soft Materials, Surfaces and Interfaces	
Gerald Brezesinski	MPG, Potsdam, D
Moshe Deutsch	Bar-Ilan University, Ramat Gan, IL
Tiberio A. Ezquerro (starting 2014)	CSIC, Madrid, ES
Thomas Gutschmann	Leibniz-Zentrum Borstel, D
Hyunjung Kim	Sogang University, Seoul, Korea
Mark Schlossmann	University of Illinois, Chicago IL, USA
Frank Schreiber (starting 2014)	Universität Tübingen, D
Oliver Seeck (PRP Secretary)	DESY, Hamburg, D
PRP7: Imaging	
Oliver Bunck (starting 2014)	PSI, Villigen, CH
Koen Janssens (starting 2014)	University Antwerpen, BE
Hendrik Kuepper (starting 2014)	Universität Konstanz
Bert Müller	University Basel, CH
Michael Nickel	Friedrich-Schiller-Universität Jena, D
Stefan Vogt	APS, Argonne, USA
Gerald Falkenberg (PRP secretary)	DESY, Hamburg, D
Felix Beckmann (HZG representative)	HZG, Geesthacht, D
PRP8: Methods and Instrumentation	
Rolf Follath	PSI, Villigen, CH
Tim Salditt	Universität Göttingen, D
Anatoly Snigirev	ESRF, Grenoble, F
Horst Schulte-Schrepping (PRP secretary)	DESY, Hamburg, D
PRP11: Soft X-Ray – FEL Experiments (FLASH)	
Massimo Altarelli	European XFEL GmbH, Hamburg, D
Chris Jacobsen	APS, Argonne, USA
Steven Johnson	ETH Zürich, CH
Maya Kiskinova	Sincrotrone Trieste, I
Jonathan Marangos	Imperial College London, UK
Ronald Redmer	Universität Rostock, D
Jan-Michael Rost	MPI, Dresden, D
Bernd Sonntag	Universität Hamburg, D
Urs Staub	PSI, Villigen, CH
Kiyoshi Ueda	Tohoku University, Sendai, J
Gwyn P. Williams	Jefferson Laboratory, Newport News VA, USA
Josef Feldhaus (PRP secretary)	DESY Hamburg,
DESY Photon Science User Committee DPS-UC	
Peter Müller-Buschbaum (Chair)	Technische Universität München, D
Thomas Möller	Technische Universität Berlin, D
Markus Perbandt	Universität Hamburg, D
Christian Schroer	Technische Universität Dresden, D
Joachim Wollschläger	Universität Osnabrück, D
Komitee Forschung mit Synchrotronstrahlung KFS	
representative of the German synchrotron radiation and FEL user community	
Wilfried Wurth (chair)	Universität Hamburg, D
Christian Schroer (vice chair)	Technische Universität Dresden, D
Andreas Schreyer	Helmholtz-Zentrum Geesthacht, D
Stefan Eisebitt	Technische Universität Berlin, D
Peter Müller-Buschbaum	Technische Universität München, D
Irmgard Sinning	Universität Heidelberg, D
Claus M. Schneider	Forschungszentrum Jülich, D
Eckart Rühl	Freie Universität Berlin, D
Rainer Fink	Universität Erlangen-Nürnberg, D
Jan-Dierk Grunwaldt	Karlsruher Institut für Technologie KIT, D
Lutz Kipp	Universität Kiel, D
Dietmar Manstein	Medizinische Hochschule Hannover, D

Photographs and Graphics:

Reiner Becker Architekten, Berlin

Lars Berg, Hamburg

CFEL

DESY

EMBL

European XFEL GmbH

HZG

Jörg Harms, MPSD/CFEL

Heiner Müller-Elsner, Hamburg

Reimo Schaaf, Hamburg

Thomas Scheler, University of Edinburgh

Universität Hamburg

Jan Wilken, Hamburg

Figures of the Research Highlights were reproduced by permission from authors or journals.

Acknowledgement

We would like to thank all authors and all those who helped in the creation of this annual report. ●

Imprint

Publishing and Contact:

Deutsches Elektronen-Synchrotron DESY
A Research Centre of the Helmholtz Association

Hamburg location:

Notkestr. 85, 22607 Hamburg, Germany
Tel.: +49 40 8998-0, Fax: +49 40 8998-3282
desyinfo@desy.de

Zeuthen location:

Platanenallee 6, 15738 Zeuthen, Germany
Tel.: +49 33762 7-70, Fax: +49 33762 7-7413
desyinfo.zeuthen@desy.de

Photon Science at DESY

Tel.: +49 40 8998-2304, Fax: +49 40 8998-4475
photon-science@desy.de
photon-science.desy.de

www.desy.de

ISBN 978-3-935702-84-3

Online version:

photon-science.desy.de/annual_report

Realization:

Wiebke Laasch, Ralf Röhlsberger, Daniela Unger

Editing:

Lars Bocklage, Rainer Gehrke, Lucia Incoccia-Hermes, Wiebke Laasch, Tim Laarmann, Emma McBride, Wolfgang Morgenroth, Elke Plönjes, Ralf Röhlsberger, Horst Schulte-Schrepping, Daniela Unger, Martin von Zimmermann

Layout: Britta Liebaug

Printing: Heigener Europrint, Hamburg

Copy deadline: December 2013

Reproduction including extracts is permitted subject to crediting the source.



Deutsches Elektronen-Synchrotron A Research Centre of the Helmholtz Association

The Helmholtz Association is a community of 18 scientific-technical and biological-medical research centres. These centres have been commissioned with pursuing long-term research goals on behalf of the state and society. The Association strives to gain insights and knowledge so that it can help to preserve and improve the foundations of human life. It does this by

identifying and working on the grand challenges faced by society, science and industry. Helmholtz Centres perform top-class research in strategic programmes in six core fields: Energy, Earth and Environment, Health, Key Technologies, Structure of Matter, Aeronautics, Space and Transport.

www.helmholtz.de